

Abstract Booklet of the 14th edition of the

International Workshop on Advanced Infrared Technology and Applications, AITA 2017

and of the 8th IWASPND E WORKSHOP

Sept. 27th - Sept 29th, 2017, Québec City (Canada)



Conference officially hosted by



Workshop organized by:

*Canada Research Chair on Multipolar Infrared Vision Infrarouge Multipolaire (MIVIM)
of the Electrical and Computer Engineering Department*

X.P.V. Maldague, Editor

publié par:

X. Maldague
É. du CAO
38, Chemin du Cap-aux-Oies
Les Éboulements (Québec)
CANADA
G0A 2M0

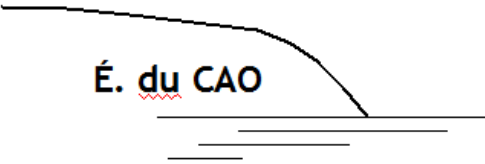
Copyright © 2017 par X. Maldague. Tous droits réservés. X. Maldague ne peut être tenu responsable pour l'authenticité, l'exactitude ou les conséquences éventuelles résultant de l'usage des renseignements publiés dans ce volume. Les opinions et affirmations publiées dans ce volume ne reflètent pas nécessairement l'opinion de X. Maldague. Les produits ou services publicisés ou mentionnés dans ce volume ne sont pas endossés par X. Maldague.

Copyright © 2017 by X. Maldague. All rights reserved. X. Maldague is not responsible for the authenticity, accuracy of information herein or for any outcomes resulting from reliance thereon, and published opinions and statements do not reflect necessarily the opinion of X. Maldague. Products or services that are advertised or mentioned do not carry the endorsement or recommendation of X. Maldague.

ISBN 978-2-9809199-5-4

Dépôt légal - Bibliothèque nationale du Québec, 2017
Dépôt légal - Bibliothèque et Archives Canada, 2017

Imprimé au Canada
Printed in Canada

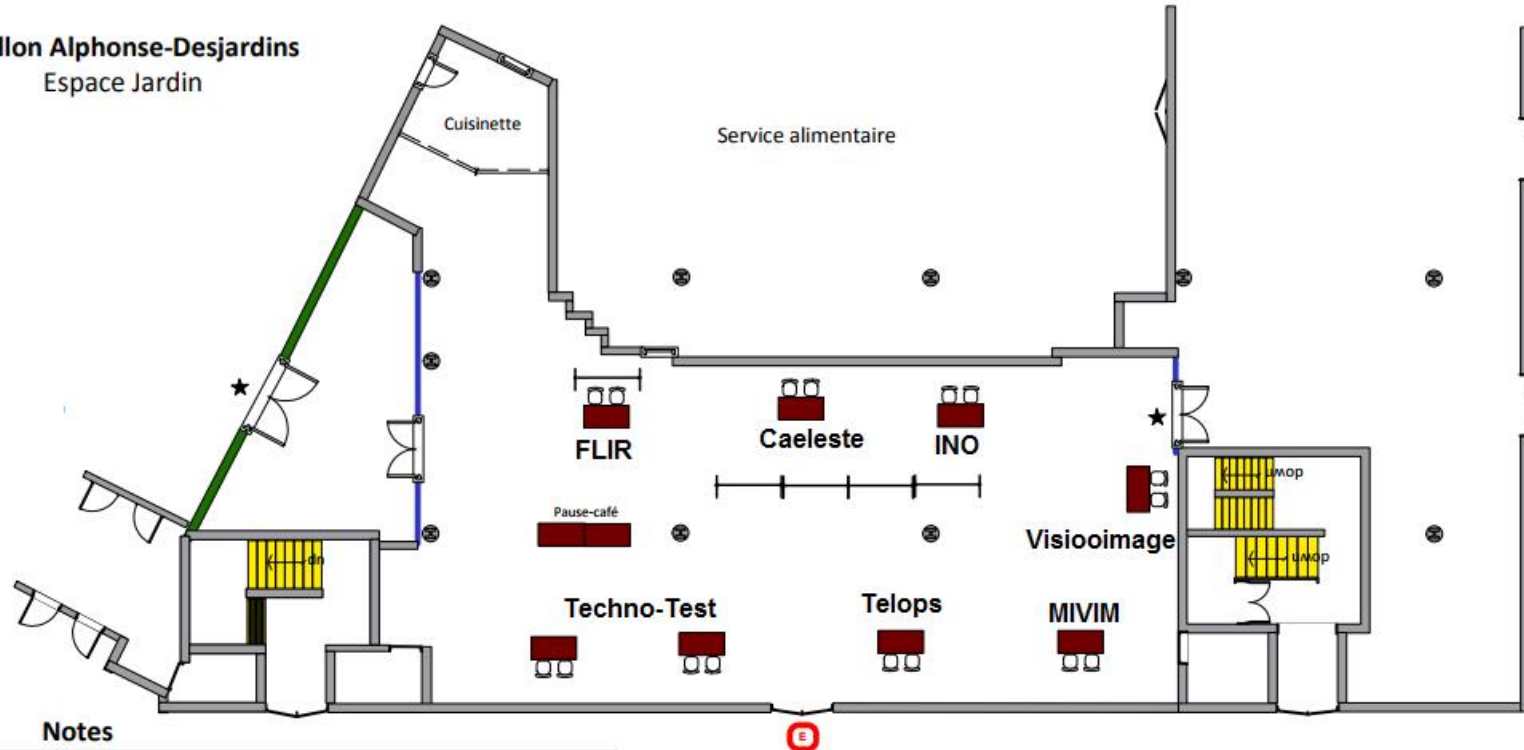


É. du CAO

à la frontière des connaissances
at the cutting edge of knowledge



Pavillon Alphonse-Desjardins
Espace Jardin



Notes

Caeleste
FLIR
InfraTec
INO
MIVIM
Techno-Test
Telops
Visioimage

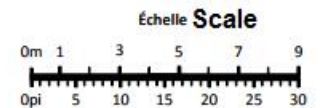


Table of contents

Keynotes

| | |
|---|----|
| <i>Paolo Bison, Federico Cernuschi and Stefano Boldrini</i> IR thermography applied to assess thermophysical properties of Thermal Barrier Coatings | 14 |
| <i>Prof. Roman Maev and Dr. Dmitry Gavrilov</i> Cultural Heritage, an IR Perspective | 18 |
| <i>Prof. A. Mandelis</i> Principals and Non-Invasive Biomedical, Dental and Engineering Materials NDI Applications | 19 |

Applications

| | |
|---|----|
| <i>Magdi Mossoba</i> Application of Infrared Spectroscopy to Food Safety using Cryogenic Trapping, Chemical Imaging, and Portable Devices | 21 |
| <i>Hui Huang, Laura Liu and Michael Ngadi</i> Non-Destructive Evaluation of Fat Attributes of Pork Loin using NIR Images of Rib End | 25 |
| <i>Munetaka Ryu, Hidetoshi Sakamoto, Yoshifumi Ohbuchi, Tsuyoshi Yoshida and Yasunori Nakamura</i> Development of Furnace Wall Automatic Inspection..... | 29 |
| <i>A. Taram, C. Roquelet, Ph. Meilland, Th. Dupuy, C. Kaczynski, JL. Bodnar, Th. Duvaut</i> Induction Heating Thermography for Crack Detection in Spot Welds..... | 33 |

Biothermophotonics Invited Session

| | |
|--|----|
| <i>Boris Majaron, Nina Verdel, Ana Marin, Luka Vidovič and Matija Milanič</i> Quantitative Characterization of Human Skin by Combined Photothermal Radiometry and Optical Spectroscopy | 35 |
| <i>Nima Tabatabaei</i> Infrared Imaging Technologies for Early Detection of Dental Caries..... | 39 |
| <i>Perry Xiao, Xu Zhang and Christos Bontozoglou</i> Advances in Opto-Thermal Skin Measurements..... | 40 |

Detectors

| | |
|---|----|
| <i>Antoni Rogalski, Małgorzata Kopytko and Piotr Martyniuk</i> Performance prediction of p-i-n HgCdTe long wavelength infrared HOT photodiodes | 42 |
| <i>Yong-Gang Zhang, Yi Gu, Xing-You Chen, Ying-Jie Ma, Xue Li, Xiu-Mei Shao, Hai-Mei Gong and Jia-Xiong Fang</i> IGA-rule 17 for performance estimation of wavelength extending InGaAs photodetectors: validity and limitations | 45 |
| <i>Dr. Sven-A. Wode</i> Active spatial resolution enhancement for cooled IR cameras | 49 |
| <i>Ajit Kumar Kalgi, Dirk van Aken, Bart Dierickx, S. Veijalainen, K. Liekens, W. Verbruggen, P.Hargrave, R.Sudiwala, M.Haiml, H. Hoehnemann</i> Multiple shutter mode radiation hard IR detector ROIC | 50 |

Environment

| | |
|--|----|
| <i>Marija Strojnik, Beethoven Bravo-Medina, Guillermo Garcia-Torales and Michelle K. Scholl</i> Extra-solar planet detection: review of indirect and direct methods..... | 57 |
|--|----|

| | |
|--|-----|
| <i>Bakhram Gaynullin, Maksym Bryzgalov, Christine Hummelgard, Claes Mattsson, Henrik Rodjegard and Goran Thungstrom</i> Pressure characterization and resolution limits' investigation of high accuracy NDIR Methane sensor for environmental applications. | 61 |
| <i>Moulay Akhloufi, Tom Toulouse, Lucile Rossi and Xavier Maldague</i> Three-dimensional infrared-visible framework for wildland fires | 65 |
| <i>Chan Park, Sungho Lee, J.S. Oh, I. Yuk, J.Lee, M.Chun, K.Kim, H.Oh, U.Jeong, N.Hwang, B. -H.Park, H.Lee, G.N.Mace, K.R. Sokal, L.Prato, D.T. Jaffe</i> IGRINS: Design, Performance and Plan for the Gemini Telescope | 69 |
| <i>Chao Ni, Yuanhao Wang, Yuting Lu, Fengzhi Tan and Yuan Li</i> Rapid and nondestructive quantitative determination of total flavonoids in Cyclocarya paliurus leaves by near-infrared reflectance spectroscopy | 73 |
| <i>Cinzia Lastri, Stefano Baronti, Giulio Coluccia, Donatella Guzzi, Demetrio Labate, Enrico Magli, Micael Miranda, Vanni Nardino, Lorenzo Palombi, Ivan Pippi, Alessandro Zuccaro Marchi and Valentina Raimondi</i> IR camera for NEO detection based on Compressive Sensing technologies..... | 89 |
| <i>Thibaud Toullier, Jean Dumoulin and Laurent Mevel</i> Comparison of Thermocouples Surface Measurements and Infrared Thermography for Transport Infrastructure Thermal Monitoring | 93 |
| <i>Bushra Jalil, Davide Moroni and Maria Antonietta Pascali</i> Power Lines Inspection via Thermal and Infrared Imaging | 97 |
| <i>Fernando López and Xavier Maldague</i> Determination of Energetic Parameters of Building Rooftops by Aerial Infrared Thermography..... | 101 |
| <i>Kazuhisa Nakasho , Carlos Cuadra , Hirokazu Madokoro , Nobuhiro Shimoi</i> Infrared Thermography Applied for Robust Image Processing to Examine Historical Wooden Buildings | 104 |
| <i>Guzzi Donatella, Stefano Baronti, Daniela Coltuc, Florin Garoi, Iuliana Iordache, Demetrio Labate, Cinzia Lastri, Vanni Nardino, Micael Miranda, Ivan Pippi, Alessandro Zuccaro Marchi and Valentina Raimondi</i> Compressive sensing and space applications in the SWIR-FIR spectral range | 108 |

Image Processing

| | |
|---|-----|
| <i>Nobuhiro Shimoi, Carlos Cuadra, Kazuhisa Nakasho and Hirokazu Madokoro</i> Active Image Processing for Wooden Traditional Structure using IR Cameras | 113 |
| <i>Michal Švantner, Lukáš Muzika, Tomáš Chmelík and Jiří Skála</i> Quantitative evaluation of active thermography using contrast to noise ratio | 117 |
| <i>Jeroen Peeters, Bart Ribbens, Boris Bogaerts, Seppe Sels, Joris Dirckx and Gunther Steenackers</i> Optimized setup modification for automated active thermography | 121 |
| <i>Hossein Memarzadeh Sharifipour, Bardia Yousefi and Xavier P V Maldague</i> Skeletonization and Reconstruction Based on Graph Morphological Transformations..... | 125 |
| <i>Moulay Akhloufi and Axel-Christian Guei</i> DeepSIRF - Super-resolution infrared face images using Deep Convolutional Generative Adversarial Networks | 129 |
| <i>Julien Fleuret, Lei Lei, Changjian Shui, Clemente Ibarra-Castanedo, Xavier Maldague and Hai Zhang</i> An Improved Algorithm for Detection and Segmentation of Defects..... | 133 |

Medical

| | |
|---|-----|
| <i>Mario D'Acunto</i> Near IR Biological Transparency Window and Theranostics Strategies | 137 |
| <i>Bardia Yousefi, Hossein Memarzadeh Sharifipour, Mana Eskandari, Clemente Ibarra Castanedo, Xavier P V Maldague and Denis Laurendeau</i> Incremental Low Rank Noise Reduction for Thermal Monitoring of Human Body Using Infrared Imagery | 140 |
| <i>Bushra Jalil, Valentina Hartwig, Ovidio Salvetti, Davide Moroni, Zunera Jalil, Antonio Benassi, Antonio L'abbate, Letizia Guiducci, Laura Pistoia, Tommaso Minutoli Tegrimi, Antonio Quinones-Galvan and Giorgio Iervasi</i> Near Infrared and Thermal Imaging of Normal and Obese Women During Oral Glucose Tolerance Test (OGTT) | 144 |

NDT

| | |
|--|-----|
| <i>Marc Genest and Gang Li</i> Induction Thermography of Steel Coupons with Crack | 149 |
| <i>Frank Billy Djupkep Dizeu, Denis Laurendeau and Abdelhakim Bendada</i> Quantitative Nondestructive Testing Using Infrared Thermography: An Inverse Geometry Problem | 153 |
| <i>Matthew Bondy, Dmitry Gavrilov, Inna Seviaryna and Roman Maev</i> Practical Application of Acoustic and Thermographic Methods for Analysis of Impact Damage to Composite Avionic Parts | 157 |
| <i>Abdoulahad Thiam, Jean-Christophe Kneip, Eugen Cicala, Yannick Caulier and Jean-Marie Jouvard</i> Using numerical experimental design for crack detection by active thermography | 161 |
| <i>Alexandrine Huot, Frédérick Marcotte, Kamel Mouhoubi and Jean-Luc Bodnar</i> Using Active Infrared Thermography for Characterizing Types of Ballistic Impacts | 165 |
| <i>Takahide Sakagami, Daiki Shiozawa, Yu Nakamura, Shinichi Nonaka and Kenichi Hamada</i> Detection of Fatigue Damage in Short Carbon Fiber Reinforced Plastics Using Thermoelasticity | 168 |
| <i>Louis-Daniel Thérroux, Jacques Lewandowski, Benoit Masson, Jean-François Vandenrijt and Marc Georges</i> Practical simulation of delamination in composites for thermography NDT | 172 |
| <i>Hai Zhang, Stefano Sfarra, Ahmad Osman, Udo Netzelmann, Clemente Ibarra-Castanedo, Stefano Perilli, Fabrizio Sarasini and Xavier Maldague</i> Eddy Current Pulsed Thermography for Basalt-Carbon Hybrid Composites Subjected to Ballistic Impacts: A Numerical and Experimental Study | 176 |
| <i>Yui Izumi, Yoshiaki Mizokami, Akira Moriyama and Takahide Sakagami</i> Detection of back-surface crack based on temperature gap measurement using infrared thermography | 179 |
| <i>Daiki Shiozawa, Tsuyoshi Inagawa, Takaya Washio and Takahide Sakagami</i> Effect of mean stress on phase difference of dissipated energy | 183 |
| <i>Henrique Fernandes, Stefano Sfarra, Hai Zhang, Clemente Ibarra-Castanedo and Xavier Maldague</i> Fiber Orientation Detection on Fiber Reinforced Polymers Moulded with Randomly-Oriented Strands | 187 |
| <i>Marco Ricci, Giuseppe Silipigni, Stefano Laureti, Luca Senni, Riccardo Tomasello and Pietro Burrascano</i> Optimal Design of Chirp Excitations for Pulse Compression Thermography | 191 |
| <i>E.T. Delegou, M. Krokida, N.P. Avdelidis, A. Moropoulou</i> An Empirical mathematical Model Developed for Pulsed Thermography Analysis on Marble Surfaces | 195 |

Techniques

| | |
|---|-----|
| <i>Ruben Usamentiaga, Daniel Garcia, C. Ibarra-Castanedo and Xavier Maldague</i> Metric Measurements on a Plane with an Infrared Camera | 200 |
|---|-----|

Seol-Hee Yi, Ik-Hwan Kwon, Hyun-Chul Jung, Kyeong-Suk Kim and Chung-Ki Hong Measurement of three dimensional surface temperature distribution by hybrid digital holographic imaging system 204

Hector Torres-Ortega, Marija Strojnik, Guillermo Garcia-Torales and Michelle K. Scholl Thermal Chamber for DNA Amplification at Given Temperature (T=62 C): Preliminary Test Results 208

Hector Torres-Ortega, Marija Strojnik, Guillermo Garcia-Torales, Michelle K. Scholl Thermal Bed for DNA Amplification at given Temperature (test case T = 62 C) 212

Thermal Properties

Jonas Allegrini, Dominique Derome and Jan Carmeliet Wind Tunnel Measurements of Local Heat Transfer Coefficients and Local Air Temperatures in an Urban Street Canyon Using IR Thermography 217

Alexey Prosvetov, Christina Trautmann and Marilena Tomut In-plane and through-plane laser flash measurements of thermal diffusivity degradation induced by heavy ion irradiation in thin graphite samples..... 221

Suhyeon Park, Y.B. Ji and Srinath Ekkad Flame Infrared Radiation Measurement at a Model Gas Turbine Combustor 224

Francesco Montagner, Silvia Deambrosis, Enrico Miorin, Giovanni Ferrarini and Paolo Bison Optical temperature measurement of the rotating plate in PVD system 229

J. Robert Mahan, Vinh Q. Nguyen, Nazia B. Munir and Vinh X. Ho MonteCarlo Ray-Trace Diffraction Based On The Huygens-Fresnel Principle..... 232

Posters

Abbasali Saboktakin, Saeid Hedayatrasa, Hosein Moienkhah, Xavier Maldague and Guillermo Rus Carlborg Aircraft Fuselage Testing Using Vibrothermography Technique 237

Bryan García, Andrés-David Restrepo-Giron and Humberto Loaiza-Correa Detection of External Structures of Anti-personnel Mines by Means of Thermographic Inspection of Soil 241

Serge-Olivier Gnessougou, Clemente Ibarra, Xavier Maldague, Alain deChamplain Thermal Diffusivity Measurements with the Flash Method at Different Depths in a Burned Composite Material..... 245

Weike Dong, Zhenqing Song and Long Liu A Novel FPGA-based Data Reconstruction Method for Synchronized Real-time DMD Display with High Frame Rate 246

Mouhoubi Kamel, Taram Abdoulaye, Bodnar Jean-Luc Follow-up of Restoration of Works of Arts of the Patrimony by Infrared Thermography..... 254

Preface

It is our pleasure to welcome you here at Université Laval for the 14th edition of the International Workshop on *Advanced Infrared Technology and Applications*, AITA 2017!

AITA Workshops were born in Italy where most of the Editions took place. In 2007, AITA was hosted in León, Mexico by Prof. Marija Strojnik. Hence, to mark this 10th anniversary, the Program Committee decided to organize AITA 2017 once again in North America, but this time in Quebec City, Canada.

Interestingly 2017 marks also the 150 anniversary of the Canadian Confederation with all kind of celebrations all across the country so it is a unique opportunity to host AITA right here in Canada!

AITA is a forum that brings together researchers in the field of infrared science and technology to exchange knowledge and ideas. Interestingly, the VIIIth edition of the *International Workshop on Advances Signal Processing for NonDestructive Evaluation* (IWASPND, Quebec Workshops) will take place as a simultaneous event.

For the 2017 edition, sessions were divided as follows: Applications, Detectors, Environment, Image processing*, Medical, NonDestructive Testing*, Techniques, Thermal properties, and we also have an invited session organized by Prof. A. Mandelis: Biothermophotonics (*: joint sessions with *VIIIth IWASPND*).

The following invited Keynote Lectures are others program highlights:

- «IR thermography applied to assess thermophysical properties of Thermal Barrier Coatings», Dr. Paolo Bison, CNR - ITC, Italy;
- «Cultural Heritage, an IR Perspective», Dr. Roman Maev and Dr. Dmitry Gavrilov, University of Windsor, Canada;
- «Photothermal Coherence Tomography (PCT): «Principals and Non-Invasive Biomedical, Dental and Engineering Materials NDI Applications »
 Dr. Andreas Mandelis, University of Toronto, Canada.

The «Under 35 Paper Award» competition will take place during the Workshop. This Award is named after Ermanno Grinzato who passed away in 2012. Mr. Grinzato was AITA cochairman for a long time and was a very well-known scientist in the thermography community. Additional Workshop highlights are a Poster session, a Vendor Session, an Exhibit with the following Companies participating: Caeleste, FLIR, InfraTec, INO, TechnoTest, Telops, Visioo-Image.

The social program includes a Reception and a Visit, Cocktail and Banquet at «Aquarium de Québec». For this last event, we thank Telops for their generous support.

As usual, a selection of the received papers will be published in a peer-review journal: *OSA Applied Optics*.

Finally, the website: <http://aita2017.gel.ulaval.ca>
 will be maintained active for future references. The website includes the Workshop
 Booklet with all the abstracts in .PDF format. This way to proceed was found more
 convenient and environmentally friendly.

As partners in the success of this week, was the help of the Program Committee,
 Scientific Committee, Organizing Committee, Université Laval, including my own
 Electrical and Computing Engineering Department and staff. The participation of our
 exhibitors is also appreciated. I would like also to point out the dedicated work of all
 our student staff and particularly of our assistant, Mr. Patrick Deschênes Labrie.

I will conclude these remarks by wishing to all a fruitful Workshop, full with great talks,
 great discussions, meetings of old and new faces! I would like also to thank you all for
 your participation which is essential to the success of AITA 2017.

Enjoy AITA 2017, enjoy beautiful Québec City, Canada!

Xavier Maldague
 Chair, AITA 2017

Committees

Program Committee

General Chair

- L. Ronchi Abbozzo, Fondazione Giorgio Ronchi, Firenze, Italy

Cochairs

- X. Maldague, Electrical and Computing Engineering Dept., Quebec City, Canada
- P. Bison, CNR-ITC, Padova, Italy
- M. D'Acunto, CNR-ISM, Rome, Italy
- D. Moroni, CNR-ISTI, Pisa, Italy
- V. Raimondi, CNR-IFAC, Firenze, Italy
- A. Rogalski, Military University of Technology, Warsaw, Poland
- T. Sakagami, Kobe University, Kobe, Japan
- M. Strojnik, CIO, León, Guanajuato, Mexico

Scientific Committee

- D. Balageas, Onera, Chatillon, France
- C. Corsi, Alenia-Creo, L'Aquila, Italy
- E Derekiak, University of Arizona, Tucson, USA
- C.T. Elliott, Heriot-Watt University, Edinburgh, Scotland
- C. Maierhofer, BAM, Germany
- C. Meola, Univ. of Naples, Naples, Italy
- I. Pippi, CNR-IFAC, Firenze, Italy
- H.N. Rutt, Southampton University, Southampton, United Kingdom
- O. Salvetti, CNR-ISTI, Pisa, Italy
- J.L. Tissot, ULIS, Veurey Voroize, France
- V.P. Vavilov, Tomsk University, Tomsk, Russia
- H. Zogg, ETH, Zurich, Switzerland

Organizing Committee

- Xavier Maldague, chair, Université Laval, Canada
- Hakim Bendada, Université Laval, Canada
- Clemente Ibarra-Castanedo, Université Laval, Canada
- Marc Genest, National Research Council Canada, Canada
- Roman Maev, University of Windsor, Canada
- Andreas Mandelis, University of Toronto, Canada
- Stefano Sfarra, University of L'Aquila, Italy
- Nicolas P. Avdelidis, National Technical University of Athens, Greece

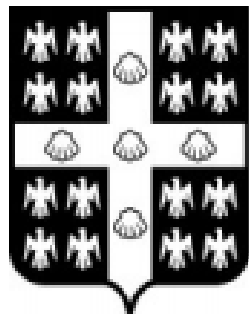
Technical Secretariat - AITA2017

- Mr. Patrick Deschênes Labrie
Department of Electrical and Computer Engineering
Université Laval, Québec, Canada, G1V 0A6
Phone : ++ 1 418 656-2962
Fax : ++ 1418 656-3159
Email : Quebec@gel.ulaval.ca

Keynote Lecture

AITA 2017

Québec City, Canada
September 27th - 29th, 2017



UNIVERSITÉ
LAVAL

IR thermography applied to assess thermophysical properties of Thermal Barrier Coatings

Paolo Bison^{1*}, Federico Cernuschi² and Stefano Boldrini³

^{1*} CNR-ITC, C.so Stati Uniti 4, 35127 Padova, Italy

² RSE, via Rubattino 54, 20134 Milano, Italy

³ CNR-ICMATE, C.so Stati Uniti 4, 35127 Padova, Italy

^{1*} Tel: +39-049-829-5735, E-mail: paolo.bison@itc.cnr.it

In this paper some photothermal and thermographic techniques are applied to determine the thermophysical properties of porous ceramic materials. Laser Flash experiments in a controlled atmosphere allow to evaluate the thermal conductivity and its dependence on the microporosity of the material under test. IR thermography, thanks to its imaging capabilities, can determine the conductivity anisotropy of Thermal Barrier Coatings. The semitransparency of materials is considered and the measurements process is modeled to improve the accuracy.

Introduction

Ceramic thermal barrier coatings (TBCs) are applied for protecting hot path components of gas turbines. Such a refractory ceramic porous layer deposited on the surfaces of the metallic materials of vanes, blades, transition pieces and combustion chambers, reduces the temperature on the metallic substrates of 30°C – 100°C depending on the thickness and on the specific properties of the coating. The state-of-the-art material of TBC is Yttrium oxide partially stabilized Zirconium (YPSZ) oxide (7-8 wt.% $Y_2O_3+ZrO_2$) deposited onto the components either by Air Plasma Spray (APS) or by Electron Beam Physical Vapour Deposition (EB-PVD) [1]. To estimate the effective insulation performances of TBCs, the thermo-physical characterisation is required because, apart from lattice properties of the material, the low thermal conductivity of TBCs strongly depends on the specific microstructural features related to the deposition process. Moreover, the microstructure is affected by the service condition of coated components. The exposure to high temperature promotes sintering phenomena within the TBC by micro-crack healing, neck formation and by reducing the very fine porosity, making the TBC less strain

compliant and more thermally conductive (see Fig.1).

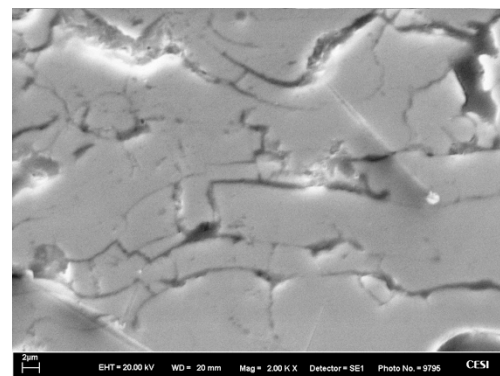
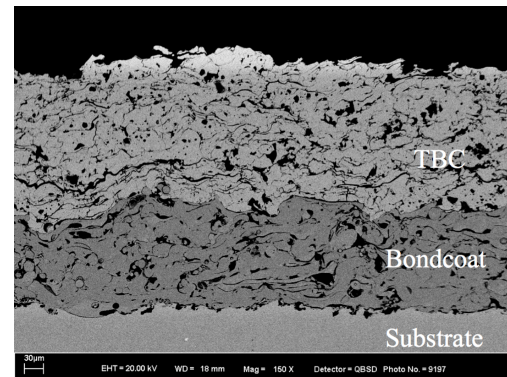


Fig. 1. (top) TBC top layer showing the typical microstructure with nearly spherical and lamellar pores which both are specifically induced by the Air Plasma Spray deposition technique. (bottom) Lamellar pores between zirconia splats.

To study these phenomena, the thermal diffusivity of aged or serviced TBC samples is often and often investigated. Today, Laser Flash (LF) is considered one of the standard technique for measuring the thermal diffusivity of solids. This method consists in heating the front face of a sample by a short laser pulse and in detecting the temperature rise on its rear surface.

For porous materials, the kind of gas filling the pores can play a key role on the thermal diffusivity evaluation. In particular, the contribution of the atmosphere is strictly dependent on the specific microstructural features of the porous sample under investigation such as porosity content, orientation and morphology.

Thus, if thermal diffusivity measurements are performed varying the gas type and/or its pressure, in principle they would allow to estimate the overall porosity content, the shape factor and the relative content of pores and their orientation with respect to the heat flux of TBCs, by applying suitable effective thermal conductivity models [2].

IR thermography and anisotropy

Depending on the deposition techniques and parameters, the TBC exhibits different kinds of microstructures that affect its thermal conductivity. As a response to a temperature gradient, the flow of heat in the TBC depends, both in magnitude and orientation, on the percentage of porosity, the shape of the pores and their orientation. A technique able to determine the thermal diffusivity in a non-contact and non-destructive way, using IR thermography to follow the surface temperature evolution of samples is described. A pulsed spot of heat with spatial Gaussian shape is delivered on the surface of the sample by a lamp. Thermography follows the diffusion of the spot as a function of time allowing the determination of the in-plane diffusivity and the in-depth as well [3]. The experimental scheme is shown in Fig. 2.

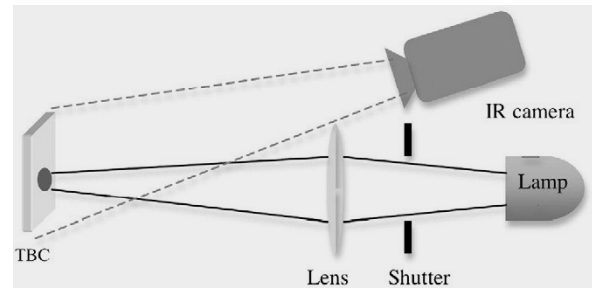


Fig. 2. Experimental set-up or the measurement of TBC anisotropy by IR thermography.

Examples of the signals obtained by this technique are given in Fig. 3, where the temperature evolution for the in-depth conductivity evaluation is shown (top) and the time evolution of the width of the Gaussian spot is also shown (bottom) allowing the in plane conductivity evaluation.

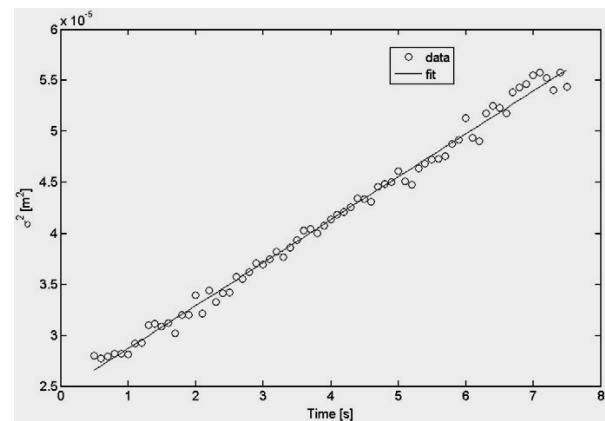
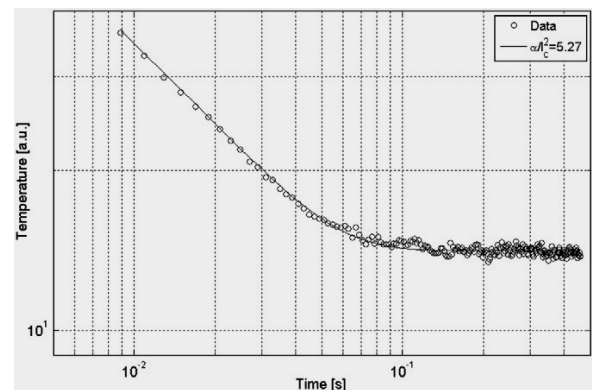


Fig. 3. (top) Temperature vs. time in bi-logarithmic scale for in-depth thermal diffusivity evaluation. The continuous line shows the best fitting curve. (bottom) Experimental Gaussian spot widening parameter as a function of time (O) and the corresponding best fitting line (–) for in-plane thermal diffusivity evaluation.

Semitransparency

ZrO₂ is semitransparent to near IR radiation that is typically delivered by the laser in the laser flash equipment. Moreover, the characterization of TBCs at high temperatures is particularly interesting as the typical working temperature of gas-turbine is >1000 °C. At these temperatures heat transfer is no more limited to conduction and the radiative heat transfer becomes paramount. The evaluation of effective heat conduction is carried out in this work by laser flash equipment and IR thermography as well, describing at the same time common practices and countermeasures to minimize the discrepancies from the commonly used models to analyze data. The effects of blackening surfaces by a thin layer of graphite is considered. The role of heat conduction and radiation is also taken into account trying to separate each contribution. Experiments are carried out at ambient temperature by means of a thermographic camera and at higher temperature in vacuum until 1200 °C. Data are treated according to classical scheme taking into account the exchange with the environment. Successively the data are considered by using the possibility of radiative exchange between the two blackened sides [4] of the sample (see Fig. 4 top). The possibility of simultaneous heating of the two sides of the sample, due to the semitransparency of the material to the laser shot is considered, giving rise to a new model that explains in some conditions anomalous immediate heating of the side facing the detector (see Fig. 4 bottom).

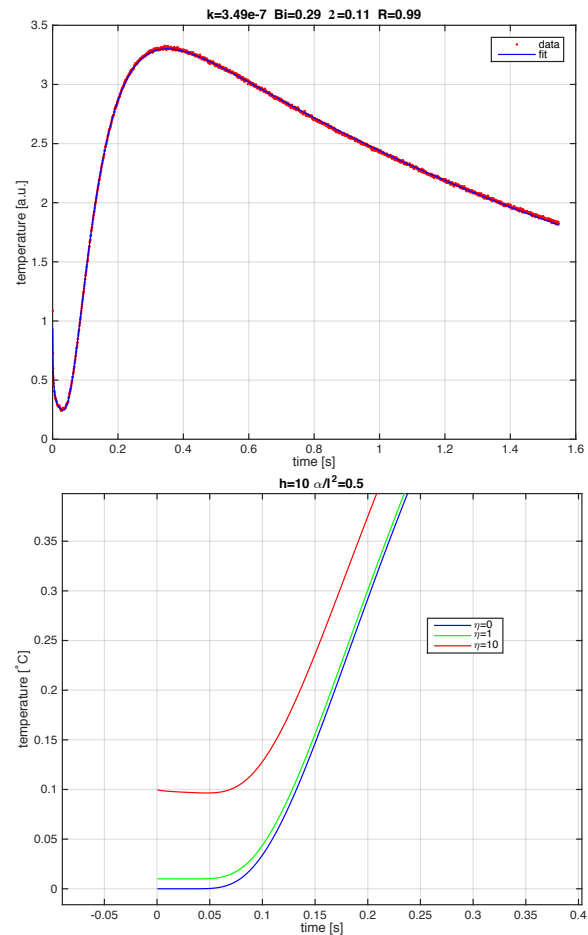


Fig. 4. (top) The Mehling model describes the jump of the temperature signal of the laser flash experiment immediately after the shot by a radiative exchange between the two blackened sides of the sample. (bottom) The large increase of temperature on the side facing the detector can be explained by a semitransparency of the material to the laser shot that simultaneously heat the side facing the laser and the back side as well.

References

1. W. Beele, G. Marijnissen and A. Van Lieshout, The Evolution of Thermal Barrier Coatings – Status and Upcoming Solutions for Today’s Key Issues, Surf. Coat. Technol., 120-121 (1999), pp. 61-67.
2. F. Cernuschi, P.G. Bison, S. Martinetti and P. Scardi, Thermophysical, mechanical and microstructural characterization of aged free-standing plasma-sprayed zirconia coatings, Acta Materialia 56 (2008) 4477–4488.
3. P. Bison, F. Cernuschi and S. Capelli, A thermographic technique for the simultaneous estimation of in-plane and in-depth thermal diffusivities of TBCs, Surface & Coatings Technology 205 (2011) 3128–3133.
4. H. Mehling, G. Hautzinger, O. Nilsson, J. Fricke, R. Hofmann, and O. Hahn. Thermal diffusivity of semitransparent materials determined by the laser-flash

method applying a new analytical model. International
Journal of Thermophysics, 19(3), 1998.

Cultural Heritage, an IR Perspective

Roman Gr. Maev

Dr. Sc., Ph.D., P. Phys., Prof.

The Institute for Diagnostic Imaging Research, University of Windsor,
 Ontario N9B 3P4 Canada

Innovations in advanced High Resolution Imaging Technologies and Methods have resulted in unique applications for non-destructive investigations of surface and subsurface microstructures in the conservation of cultural and environmental heritage. It has become the preferred approach even in cases where microanalysis sampling is permitted. The synergy between experts in science and the cultural arts leads to continuous development and evolution of novel scientific methods, their applications in the field of preservation, reconstruction and diagnostics of museum, and archeological objects. High-resolution imaging diagnostics, in particular, is a powerful and significant method that can revolutionize the analysis, study and conservation of art-objects.

Modern art science is unthinkable without such instruments as near-infrared photography, spectroscopy, as well as thermography. They allow for seeing what is concealed by layers of materials, determine composition of artistic paints, and verify authenticity of pieces of art, which makes these methods indispensable.

The goal of this invited talk is to revisit the subject of analysis of art and highlight the importance of infrared radiation for non-destructive diagnostics for preservation of objects of cultural heritage.

Photothermal Coherence Tomography (PCT): Three-Dimensional Imaging Principles and Non-Invasive Biomedical, Dental and Engineering Materials NDI Applications

Andreas Mandelis (*)

Center for Advanced Diffusion-Wave and Photoacoustic Technologies (CADIPT), Dept. of Mechanical and Industrial Engineering, Univ. of Toronto, Toronto M5S3G8, Canada

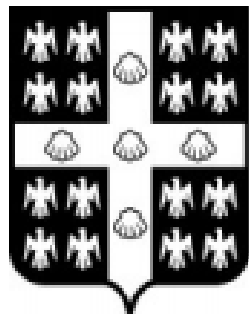
Abstract. Energy transport in diffusion-wave fields is gradient driven and therefore diffuse, yielding *depth-integrated* responses with poor axial resolution. Traditional diffusion-wave techniques, controlled by the physics of parabolic diffusion and depth-limited by the thermal diffusivity, can only produce depth-integrated planar images as they are unable to generate depth-resolved three-dimensional subsurface imaging. This talk will present a new imaging paradigm developed in the CADIPT for enabling parabolic thermal-wave fields to exhibit energy localization akin to propagating hyperbolic wave-fields like ultrasound. This approach when used with a mid-IR camera results in *depth-selective* (or depth-resolved) photothermal imaging that not only improves axial resolution allowing for deconvolution of individual responses to superposed axial source distributions (tomography), but also greatly enhances depth range thereby opening a new dynamic imaging field of subsurface PCT, the thermal analog to Optical Coherence Tomography (OCT). The talk will present the physical principles of Truncated-Correlation Photothermal Coherence Tomography (TC-PCT) and examples of applications to engineering materials non-destructive imaging (NDI), non-invasive dental caries diagnosis and small animal biotissue imaging.

(*) With Konesh Sivagurunathan and Pantea Tavakolian

Applications

AITA 2017

Québec City, Canada
September 27th - 29th, 2017



UNIVERSITÉ
LAVAL

APPLICATION OF INFRARED SPECTROSCOPY TO FOOD SAFETY USING CRYOGENIC TRAPPING, CHEMICAL IMAGING, AND PORTABLE DEVICES

M. Mossoba

US Food and Drug Administration, 5001 Campus Drive, College Park, MD 20740 USA
magdi.mossoba@fda.hhs.gov

Matrix isolation-Fourier transform infrared (FTIR) spectroscopy allowed the detection of trace levels of chemical contaminants or constituents eluting from a chromatographic column such as glucosinolates in *Brassica* vegetables and cyclic fatty acid monomers in frying oils. Mid-IR chemical imaging (IRCI) was applied as a read-out tool for the analysis of DNA microarrays in which hybridized spots had been selectively augmented with nanogold-silver to facilitate spectral detection on glass slides. IRCI was used to identify catfish species and analyze virulence genes of food bacterial pathogens. Portable NIR and/or FTIR devices were applied to the rapid screening of extra virgin olive oils for authenticity, the determination of fatty acids in marine oil omega-3 dietary supplements, and the prediction of *trans* fat content of fast foods for verification of label declarations.

Introduction

For decades, infrared (IR) spectroscopy has been successfully used to fingerprint chemical compounds, identify functional groups, and discriminate between isomers. These experiments were carried out on IR instrumentation that usually required milligram quantities of analytes. However, several technological advances led to the development of commercial Fourier transform infrared (FTIR) spectrometers coupled to capillary gas chromatographs. This progress allowed the on-line measurement of FTIR spectra at cryogenic temperatures for sub-nanogram-level analytes eluting from a capillary gas chromatographic column [1].

Food misbranding [2] in general and the need to identify pathogenic bacteria [3] in foods have led to an increased interest in developing confirmatory deoxyribonucleic acid (DNA)-based methods. A new methodology was developed and applied in our laboratory that was based on DNA microarrays coupled with

mid-infrared chemical imaging (IRCI) in the external reflection mode for detection.

In April 2016, a US Congressional Committee expressed concerns related to reports of the high prevalence of imported olive oil products sold in the US that are adulterated or mislabeled. Such fraudulence include the mixing of extra virgin olive oil (EVOO) with lower grades of olive oil and the addition of seed oils to EVOO which could adversely impact the health of consumers who are allergic to seed oils. FDA was directed to assess the authenticity of imported olive oils in order to verify accuracy in product labeling and to ensure consumer confidence and safety. Therefore, there has been an urgent need for authoritative testing standards and rigorous analytical methods to determine olive oil quality and purity [4-6]. In recent years there has also been an interest in miniaturizing benchtop spectrometers to portable devices, which would allow for the routine screening of test samples in the field [7].

The potential benefits of long-chain omega-3 polyunsaturated fatty acids (PUFA) found in

fish oil are well documented. The high demand for dietary supplements containing fish oil has led to the development of a wide variety of fish, algal, and krill oils omega-3 products. While the determination of marine oil PUFA can be obtained by chromatographic methods with high selectivity and sensitivity, they are time-consuming and laborious. To overcome these limitations, a portable attenuated total reflection (ATR)-FTIR spectroscopic device in conjunction with partial least squares regression (PLSR) was applied to the rapid prediction of PUFA in marine oil dietary supplements [8].

In August 2016, the US Food and Drug Administration (FDA) ruled that partially hydrogenated oils (PHO), the major dietary source of industrially-produced *trans* fat (TF), were no longer “generally recognized as safe (GRAS)” for any use in human food. Consequently, to verify TF label declarations for regulatory purposes, a rapid screening procedure was recently developed using a portable ATR-FTIR device in conjunction with PLSR for the rapid prediction of low concentrations of TF (<1% of total fat) and for quality control of raw material and processed foods.

Application of gas chromatography-cryogenic trapping-FTIR spectroscopy

Trace levels of individual compounds and isomers in complex mixtures of food matrices could be identified by capillary gas chromatography (GC)-cryogenic trapping-FTIR spectroscopy [1]. After the GC separation is completed, each GC peak is sequentially placed in the path of the IR beam for reflection-absorption measurement. Several minutes of post-GC-run FTIR spectral data acquisition resulted in improved signal-to-noise ratios.

Ethyl carbamate (EC) is an animal carcinogen and a natural product in fermentation processes that may be present in alcoholic beverages and foods. GC- matrix isolation (MI)—FTIR allowed

the identification and quantification of EC at the ppb levels in foods.

Concern over the extreme toxicity to laboratory animals of the pollutant 2,3,7,8,-tetrachlorodibenzo-p-dioxin (2378-TCDD) prompted the application of GC-MI-FTIR to the determination of 2378TCDD at the 15 to 45 picogram/gram level in fish extracts and discrimination between TCDD isomers.

Increased consumption of *Brassica* vegetables is recommended due to their association with reduced risk of some alimentary track cancers. GC-MI-FTIR was used to separate and unequivocally characterize glucosinolate products from rutabaga and Brussels sprouts.

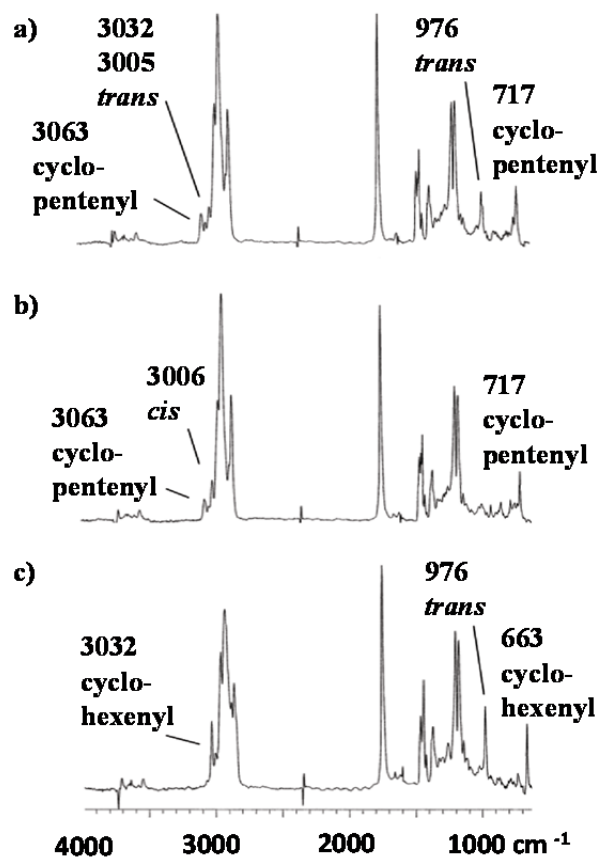


Fig. 1. Sharp MI-FTIR spectral bands observed at 4 cm^{-1} resolution for methyl ester derivatives of C18 cyclic fatty acid monomers having structures consistent with (a) a cyclopentenyl ring and a *trans* double bond, (b) a cyclopentenyl ring and a *cis* double bond, and (c) a cyclohexenyl ring and a *trans* double bond. The *cis* or *trans* double bonds are along the hydrocarbon chain.

The capability of GC-MI-FTIR for lipid analysis (Fig. 1) was also demonstrated for low levels of complex cyclic fatty acid methyl ester mixtures isolated from frying linseed and sunflower oils. The size of the unsaturated fatty acid ring in cyclic fatty acid methyl esters was established, and it was possible to differentiate between a *cis* double bond in a five-membered ring (717 cm^{-1}) and one in a six-membered ring (663 cm^{-1}) as well as the configuration of a double bond along the fatty acid chain.

Application of mid-infrared chemical imaging

IRCI in the external reflection mode was applied to the detection of nanostructure-based DNA microarrays printed on glass slides [2,3]. Alkyl amine-modified oligonucleotide probes were immobilized on slides prefunctionalized with succinimidyl ester groups. This procedure entailed the binding of gold-nanoparticle-streptavidin conjugates to biotinylated DNA targets. Hybridization was visualized by the enhancement of gold nanoparticles with silver metal. The adlayer of silver, which was selectively bound only to hybridized spots in a microarray, formed the external reflective infrared substrate that was needed for the detection of DNA hybridization by IRCI (Fig. 2).



Fig. 2. Schematic illustration (not to scale) of the probe-target DNA duplex structure that enabled detection by IRCI.

Using IRCI it was possible to discriminate between diffuse and specular external reflection modes (Fig. 3).

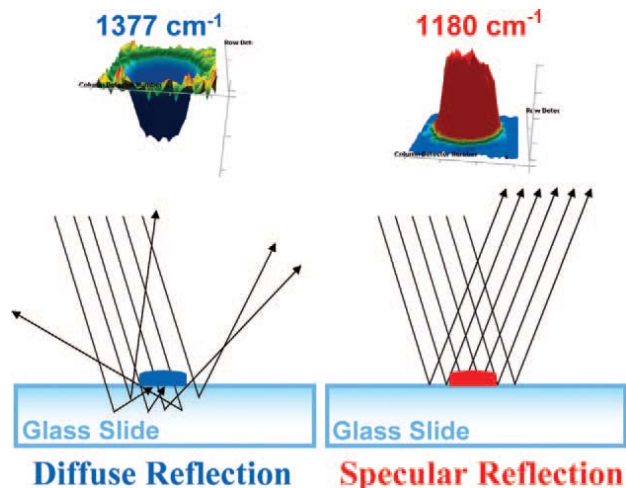


Fig. 3. Schematic diagrams representing diffuse and specular external reflection modes and the corresponding, vastly different chemical images observed at wavenumbers associated with these two distinct phenomena.

Applications of IRCI included the analysis of five virulence genes in samples of the bacterium *Clostridium perfringens* and the identification of catfish species [2,3]. Several families of catfish species are aquacultured around the world. However, only those from the family Ictaluridae can be labeled as catfish in the US; non-Ictalurid species, if marketed as catfish, would be considered misbranded (Fig. 4).

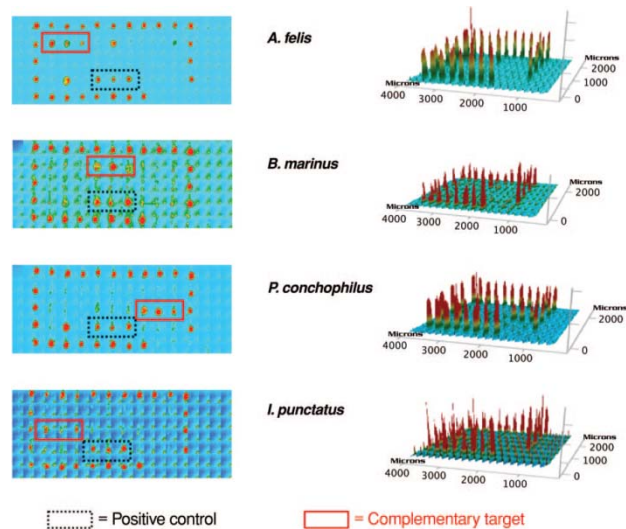


Fig. 4. Panels show two-dimensional (left) and three-dimensional (right) IR images for hybridized spots in DNA microarrays for four catfish species. Spot diameter is approximately $120\text{ }\mu\text{m}$.

DNA microarrays coupled with IRCI were successfully applied to the discrimination among seven species of catfish.

Application of NIR and FTIR portable devices

To detect economically motivated adulteration of olive oil and address food safety vulnerabilities, rapid, screening methods were developed to authenticate EVOO using benchtop FT-NIR spectrometers and a NIR handheld device [4-7].

For the first time, FT-NIR spectroscopic methodologies in conjunction with univariate and multivariate chemometric analyses were recently developed and applied to commercial EVOO products to rapidly predict whether they are authentic, of lower quality, or potentially mixed with refined olive oil or other vegetable oils [4-7]. Without any sample preparation, spectra of authentic reference EVOO, refined olive oils, potential adulterants consisting of edible oils, EVOO spiked with adulterants, and 93 commercial olive oil products were rapidly measured using a fiber optic probe and disposable transmission tubes. Based on chemometric data analyses, of the commercial products labeled EVOO that were analyzed, approximately a third satisfied the requirements identified for authentic EVOO products, and were classified as belonging to the class of authentic EVOO. These findings were consistent with previously published data based on the results of two accredited sensory panels.

The performance of a portable ATR-FTIR device in conjunction with PLS regression (PLSR) was evaluated and successfully applied to the rapid prediction of omega-3 PUFA in marine oil dietary supplements [8]. Overall findings of PUFA composition were consistent with label declarations as well as values determined by chromatography. Similarly, low levels of TF in diverse sets of neat edible fats and oils and fast food lipid extracts were rapidly predicted using portable ATR-FTIR and PLSR for concentrations as low as approximately 0.1% and 0.3% of total fat, respectively. We also successfully transferred

PLSR models developed with the benchtop ATR-FTIR spectrometer to the portable FTIR device.

Conclusion

Advances in IR technology and instrumentation and the development of chemometrics algorithms has allowed the application of IR spectroscopy to the analysis of food composition, detection of trace levels of food contaminants, and rapid prediction of potential food adulteration, mislabeling or misbranding.

References

1. M. Mossoba, G. Reedy. FTIR and hyphenated FTIR techniques for the analysis of foods in *Spectral Methods in Food Analysis*, M. Mossoba (ed.), Marcel Dekker, New York, 1999.
2. S. Handy, V. Chizhikov, B. Yakes, S. Paul, J. Deeds, M. Mossoba. Microarray chip development using IR imaging for the identification of catfish species, *Appl. Spectros.* Vol. 68, N. 12, pp. 1365-1373, 2014.
3. M. Mossoba, S. Al-Khaldi, B. Schoen, B. Yakes. Nanoparticle probes and IRCI for DNA microarray detection, *Appl. Spectrosc.*, Vol. 64, N. 11, pp. 1191-1198, 2010.
4. H. Azizian, M. Mossoba, A. Fardin-Kia, P. Delmonte, S. Karunathilaka, J. Kramer. Novel, rapid identification and quantification of adulterants in EVOO using NIR spectroscopy and chemometrics, *Lipids*, Vol. 50, N. 1, pp. 705-718, 2015.
5. M. Mossoba, H. Azizian, A. Fardin-Kia, S. Karunathilaka, J. Kramer. First Application of Newly Developed FT-NIR Spectroscopic Methodology to Predict Authenticity of Extra Virgin Olive Oil Retail Products in the USA, *Lipids*, Vol. 52, N. 5, pp. 443-455, 2017.
6. S. Karunathilaka, A. Fardin-Kia, C. Srigley, J. Chung, M. Mossoba. Nontargeted, rapid screening of EVOO products for authenticity using NIR spectroscopy in combination with Conformity Index and multivariate statistical analyses, *J. Food Sci.*, Vol. 81, N. 10, C2390-C2397, 2016.
7. S. Karunathilaka, A. Fardin-Kia, C. Srigley, J. Chung, M. Mossoba. Rapid screening of commercial EVOO products for authenticity: Performance of a handheld NIR device, *NIR News*, February, pp. 9-14, 2017.
8. S. Karunathilaka, M. Mossoba, J. Chung, E. Haile, C. Srigley. Rapid prediction of fatty acid content in marine oil omega-3 dietary supplements using a portable FTIR device and PLSR analysis, *J. Agri. Food Chem.*, Vol. 65, N. 1, pp. 224-233, 2017.

NON-DESTRUCTIVE EVALUATION OF FAT ATTRIBUTES OF PORK LOIN USING NIR IMAGES OF RIB END

H. Huang¹, L. Liu², M. O. Ngadi³

¹ Ocean College, Zhejiang University, Hangzhou, China hhuang1@126.com

² Department of Bioresource Engineering, McGill University, Quebec, Canada li.liu5@mcgill.ca

³ Department of Bioresource Engineering, McGill University, Quebec, Canada
 Michael.ngadi@mcgill.ca

The purpose of this study was to investigate the possibility of rapid and non-destructive evaluation of fat attributes – intramuscular fat (IMF) content and marbling score (MS) of pork loin using NIR hyperspectral images (900-1700 nm) of rib end. Pattern analysis techniques were applied to extract spectral and image features from the rib end of the pork loin. Correlation analysis was used to select optimal features which have strong predictive potential for fat attributes. Multiple linear regression was exploited to build prediction models based on the selected features and leave-one-out cross validation was employed to test the robustness of the established models. The promising results indicated the great potential of using NIR hyperspectral images of rib ends for non-destructive evaluation of fat attributes of pork loin.

Introduction

Quality is a concern for all pork cuts, especially pork loin which is the most valued primal cut. Fat attributes, i.e. intramuscular fat (IMF) content and marbling score (MS), are one of the most measurements for pork loin quality. IMF content is defined as the total quantity of scattered flecks of fat within the meat muscle, while marbling is the visible intermingling of fat with lean in a muscle [1]. Fat level of pork loin strongly influences the cooking quality (flavor and juiciness), consumer satisfaction, and health issues. A typical commercial pork loin contains about 12 or 13 ribs. IMF content and MS of the whole loin are either chemically or visually assessed between the 3rd and 4th last ribs as per the NPPC standard [2], which entails cutting the loin and results in decreases of commercial values. In addition, the preference of fat attribute levels may vary from one locale to another. It is important to classify pork loins into different fat

levels and distribute them according to the demands of specific markets.

In the last decade, imaging techniques such as computer vision and hyperspectral imaging has been studied for the objective assessment of pork fat attributes [1, 3-7]. The extensive research has shown that hyperspectral imaging with the assistant of image processing and machine vision techniques has great potential to predict IMF content and MS [1, 5-7]. However, most of the studies focused on evaluating fat attributes of pork chops which are the cross-section cuts along pork loin, instead of the whole loin. The possibility of evaluating fat attributes for the whole loin needs to be investigated. Availability of objective and non-destructive evaluation of fat attributes for the whole loin would be an asset for the pork industry.

The aim of the present study was to investigate the potential of non-destructive evaluation of fat attributes of pork loin using the NIR hyperspectral images of the rib end. Specific objectives were to (1) extract spectral and image

features of the rib end using pattern analysis techniques, (2) identify the optimal features for modeling, and (3) establish suitable models for quantitative assessment of IMF content and MS using NIR images of rib end.

Materials and Methods

Sample preparation

In this study, 24 pigs were slaughtered at a local commercial slaughterhouse. The loin joint of *Longissimus dorsi* at 24 h post-mortem was dissected from pigs, packed in refrigerated boxes and transported to the laboratory of Hyperspectral Imaging, McGill University, Montreal, QC, Canada. The loin between the 3rd last and the 4th last ribs (denoted as LS 3 in Fig. 1) and the last piece between the 2nd last rib and posterior (rib end) were sliced as sampling location in Fig. 1.

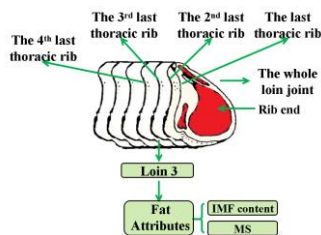


Fig. 1. Sampling scheme of the pork loin.

Hyperspectral imaging system

A laboratory hyperspectral imaging system was established for this study. It consisted of a spectrograph in the NIR range of 900 – 1700 nm (Headwall Photonics Inc. USA), a cooled InGaAs camera, a conveyer, two tungsten halogen lamps (50 W), a sample holder, and an enclosure, as shown in Fig. 2.

Hyperspectral image acquisition and normalization

The last loin slice was placed on the wood board with rib end upward toward the camera. After scanning on a rib end, an output *hypercube* of 350 pixels× 320 pixels× 167 wave bands was constructed.

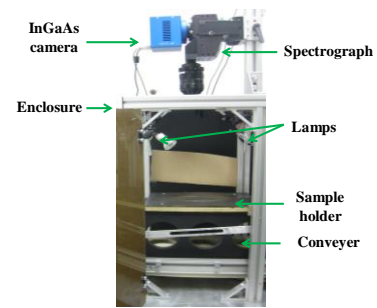


Fig.2. The hyperspectral imaging system.

All hypercubes, i.e. spectral images, need to be corrected from the dark current of the camera prior to the further processing and analysis. To correct the spectral images, a dark image B and a white image W were obtained by covering the lens with a cap and by taking an image from a standard white reference, respectively. The relative reflectance I was calculated by

$$I = \frac{I_0 - B}{W - B}, \quad (1)$$

where I_0 was the original spectral image. The normalized images were used for the subsequent image analysis.

Analytical determination of fat attributes

The MS of each pork loin was assessed with the corresponding LS3 by technicians using NPPC standard charts [2]. MS of two surfaces of each LS3 was evaluated. The average MS value of two surfaces was used as the referenced MS value of the corresponding loin.

Right after evaluation of MS, all samples were carefully trimmed to remove peripheral and intermuscular fat as well as the connective tissue and surrounding muscles. Samples were freeze-dried and ground. A ground meat sample of known weight was used for determining the intramuscular fat (IMF) content in accordance with Official Method 960.39 [8]. IMF content (%) at the 3rd / 4th last ribs was determined and expressed as percentages of total crude fat content in dry weighted pork.

Image segmentation

The main purpose of image segmentation was to isolate the interested meat part from the background and the residual adhering fat as

well as the connective tissue after bone removal. The selected loin part was defined as the region of interest (ROI). In this study, ROI segmentation was operated automatically using the method described in [5]. Spectral images between 940-1650 nm were used for further image processing and analysis due to the low signal-to-noise ratio in the two ends of the spectral range 900-1700 nm.

Feature extraction

The reflectance mean spectrum (**MR**) was determined by averaging the reflectance value of all pixels in the raw ROI of rib end and used as spectral features. The first derivative of **MR** (**DMR**) was also calculated.

An isotropic Gabor filter (GF1) and an oriented Gabor filter (GF2) [9] were used to extract useful texture information to facilitate the prediction of pork IMF content and MS. Mean spectra from GF1-processed and GF2-processed ROI were recorded and denoted as **MG1** and **MG2**, respectively. The first derivatives of **MG1** and **MG2**, i.e. **DMG1** and **DMG2**, were calculated

The wide line detector [10] was applied to the ROI of hyperspectral images to detect fat flecks which can be regarded as kind of line patterns. The proportion of lines (**PL**) was calculated as the ratio of the total number of pixels in detected lines in a ROI over the total number of pixels in the corresponding ROI.

Multivariate analysis

Multivariate regression analysis was applied to select optimal image feature and vital wavelengths for modeling. The total of 24 samples were divided into two groups, i.e. the calibration set ($N_c = 18$ samples) and the prediction set ($N_p = 6$ samples).

Since different spectral and image features were extracted from NIR images of rib ends, selection of optimal image feature is necessary to determine the optimal feature for prediction models. Pearson's correlation coefficient was applied to evaluate the linear dependence

between different image features and IMF content / MS. Stepwise regression procedure was carried out to identify optimal wavelengths that are most essential on the attribute prediction.

Multiple linear regression (MLR) models were built with optimal features from calibration sets. Leave-one-out cross validation was applied to the calibration models to test their robustness. The performance of MLR models were evaluated by following statistical values: R values of calibration (R_c), cross validation (R_{cv}) and prediction (R_p); root mean square error ($RMSE$) of calibration ($RMSE_c$), cross validation ($RMSE_{cv}$) and prediction ($RMSE_p$).

Results and Discussion

Measured mean values for IMF content and MS of total 24 pork loins at LS3 were 6.63% and 2.86, respectively. Standard deviation of for IMF content and MS of total 24 pork loins at LS3 were 3.79% and 0.77, respectively. Larger variability presented in the reference data affect the robustness and stability of predictive models positively.

The typical NIR images of rib end and the corresponding ROI are shown in Fig. 3.

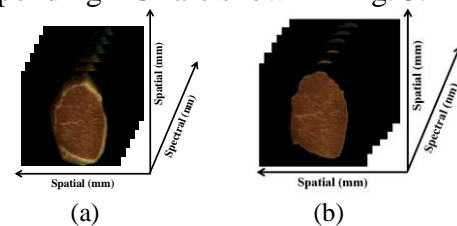


Fig. 3. The HSI before and after ROI segmentation.

Pearson's correlation coefficients (R) between IMF content/ MS and different features from rib ends were calculated. Maximum values of correlation coefficient between IMF content/ MS and different features from rib ends are listed in Table 1.

The texture-spectral feature **DMG2** which provided highest correlation coefficient to IMF content/ MS were used as the variables for prediction of corresponding attributes. Stepwise procedure was applied to **DMG2** using optimal parameter set to simplify the independent

variables to several vial wavelengths. The used key wavelengths for prediction of IMF content and MS are listed in Table 2.

| Features | IMF content (%) | MS |
|-------------|-----------------|------|
| MR | 0.63 | 0.25 |
| DMR | 0.86 | 0.40 |
| MG1 | 0.67 | 0.23 |
| DMG1 | 0.87 | 0.61 |
| MG2 | 0.75 | 0.34 |
| DMG2 | 0.90 | 0.56 |
| PL | 0.85 | 0.44 |

Table 1. Maximum values of correlation coefficients between different features and fat attributes

| Fat attributes | | IMF content (%) | MS |
|-------------------------|----------|---------------------------|-----------------------------------|
| Para- meters | σ | 3 | 15 |
| | f | 0.1 | 0.125 |
| | θ | 0 | 90 |
| Key wavelengths (nm) | | 1198, 1222, 1289, 1610 | 1164, 1246, 1414, 1519, 962 |

Table 2. Optimal parameter sets of **DMG2** and selected key wavelengths by stepwise

The ability of the NIR spectra-based feature for predicting fat levels in pork is based on the vibrational responses of chemical bonds including in the NIR region. Since composition of IMF and marbling in pork is lipid, the NIR spectra produced by the C-H stretch second overtones for fatty acids in 1100-1400 nm would explain the adoption of wavelengths in this range in Table 2 [11]. Different wavelengths were identified for MS compared to IMF content, which could be attributed to the basic differences between the conventional measurements of the two quality attributes (chemical vs. visual).

Table 3 shows modeling results in both training and testing set for prediction of IMF content and MS. The MLR models produced promising performance for prediction of either IMF content or MS, which indicated that the two fat attributes of the pork loin could be evaluated by several NIR images of the rib end.

| Fat attributes | | IMF content (%) | MS |
|------------------|-------------|-----------------|------|
| Cali-bration | R_c | 0.97 | 0.95 |
| | $RMSE_c$ | 0.89 | 0.18 |
| Cross Validation | R_{cv} | 0.97 | 0.94 |
| | $RMSE_{cv}$ | 1.64 | 0.25 |
| Prediction | R_p | 0.90 | 0.97 |

| | $RMSE_p$ | 0.92 | 0.13 |
|--|----------|------|------|
|--|----------|------|------|

Table 3. MLR models and performance for predicting IMF content/ MS at the 3rd / 4th last ribs

Conclusion

This study investigated the potential of using NIR hyperspectral images of pork rib end for non-destructive prediction of IMF content and marbling score of the whole loin. The promising results in this study make it possible to identify fat levels of pork loin using the images of rib end non-destructively, which would make it practical to inspect each pork loin and distribute them to specific markets.

References

1. J. Qiao, M.O. Ngadi, N. Wang, C. Gariépy, S.O. Prasher. Pork quality and marbling level assessment using a hyperspectral imaging system. *Journal of Food Engineering*, 83, 10-16, 2007.
2. NPB (National pork board). *Pork quality standards*. Des Moines, IA USA, 2002.
3. L. Faucitano, P. Huff, F. Teuscher, C. Gariépy, J. Wegner. Application of computer image analysis to measure pork marbling characteristics. *Meat Science*, 69(3), 537-543, 2005.
4. J.H. Liu, X. Sun, J.M. Young, L.A. Bachmeier, R. Somers, S.B. Schauunaman, D. Newman. Using machine vision technology to determine pork intramuscular fat percentage. *Journal of Animal Science*, 94(supplement2), 67-67, 2016.
5. L. Liu, M. Ngadi, S. Prasher, C. Gariépy. Objective determination of pork marbling scores using the wide line detector. *Journal of Food Engineering*, 110(3), 497-504, 2012.
6. H. Huang, L. Liu, M. Ngadi. Recent developments in hyperspectral imaging for assessment of food quality and safety. *Sensors*, 14(4), 7248-7276, 2014.
7. H. Huang, L. Liu, M. Ngadi, C. Gariépy, S. Prasher. Near-Infrared Spectral Image Analysis for Pork Marbling Detection. *Applied Spectroscopy*. 68(3), 332-339, 2014.
8. AOAC. Official methods and analysis. Association of Official Analytical Chemist. EUA. 2000.
9. L. Ma, T. Tan, Y. Wang, D. Zhang. Personal identification based on iris texture analysis. *IEEE Trans. Pattern Recognition and Machine Intelligence*, 25(12), 1519-1533, 2002
10. L. Liu, D. Zhang, J. You. Detecting wide lines using isotropic nonlinear filtering. *IEEE Trans. Image Processing*, 16(6), 1584-1595, 2007.
11. J. Shenk, M. Westerhaus, J. Workman. Application of NIR spectroscopy to agricultural products. Handbook of Near Infrared Analysis. New York, USA. 383-431, 1992.

Development of Furnace Wall Automatic Inspection

M. Ryu¹, H. Sakamoto², Y. Ohbuchi¹, T. Yoshida⁴, Y. Nakamura⁵

¹ Graduate School of Engineering, Kumamoto University, 2-39-1, Kurokami, Chuo-ku, Kumamoto-shi, Kumamoto, 860-8555, Japan, 161d8559@st.kumamoto-u.ac.jp

² Graduate School of Science and Engineering, Doshisha University, 1-3, Tataramiyakodani, Kyotanabe-shi, Kyoto, 610-0394, Japan, hsakamot@mail.doshisha.ac.jp

³ The Institute of Professional Engineers, 2-3-5, Takasunishi, Wakamatu-ku, Kitakyusyu-shi, Fukuoka, 808-0146, Japan, tuyoshi-yoshida@nifty.com

⁴ Osaka Sangyo University, 3-1-1, Nakagaito, Daitou-shi, Osaka, 574-0013, Japan

The purpose in this study is the development of non-contact 3D inspecting system for the inner wall of incinerator. In this incinerator, the system by using the non-contact 3D sensor is developed in order to inspect easily, safety and high-precisely. In this study, Kinect sensor is used. This sensor is much cheaper than other sensors and its sensitivity is enough to inspect the incinerator wall conditions. As the experimental results, it was demonstrated that the inner part of incinerator can be inspected by Kinect. Moreover, advanced measurement evaluations other than the furnace wall inspection can be executed by using ROS and PCL, etc. The incinerator wall inspection machine built into the 3D measurement system is being developed now.

Introduction

In this study, the system which inspect the detect of furnace wall is developed. The target is submerged combustion type waste fluid incinerator which process the waste fluid exhausted by plant. The present state of inspection is that the worker set up scaffolding, and inspect by visual observation without using inspection device. In this inspection, it is dangerous and severe work because inside of incinerator is dark and high temperature, and inspection precision is low because it is inspected by visual observation. There is already device which inspect the furnace wall in the market, but the device cost is very high and the cost per performance is low. It is difficult in a small, medium size company to introduce the inspection device.

The purpose is to develop the high cost performance system which can inspect the furnace wall with safety, easily and highly-

precision condition by using sensor. The sensor can be bought for approximately 200\$ with enough precision. Thus, we use this sensor in this study. Moreover, this study is being requested by the company which have plant and submerged combustion type waste fluid incinerator, and developed system will be used in this plant in the future.



Fig. 1. Present state of inspection [1].

There is a submerged combustion type waste fluid incinerator in the waste fluid processing equipment. This gushes the high temperature combustion gas generated by combustion in the liquid all at once, and is the liquid processing equipment of the combustion gas bubble to

which the heat conduction and the absorption of the combustion gas element are effectively carried out by direct contact with gas and liquid. The 3D model of submerged combustion type waste fluid incinerator and the real picture of interior of this incinerator are shown in Fig. 2.

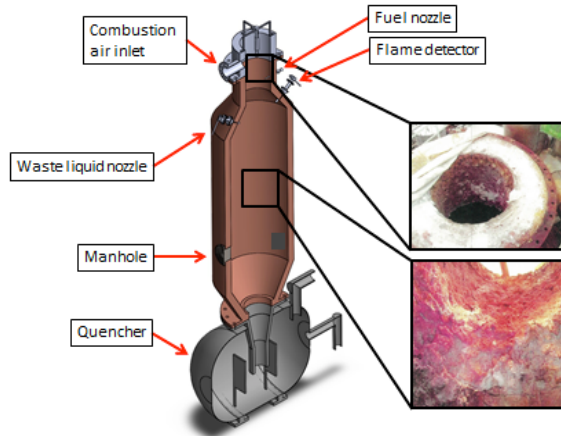


Fig. 2. Submerged combustion type waste fluid incinerator.

Methods

The main contents of this paper are the design of the inspection machine system, the development of control system and data processing in sensor.

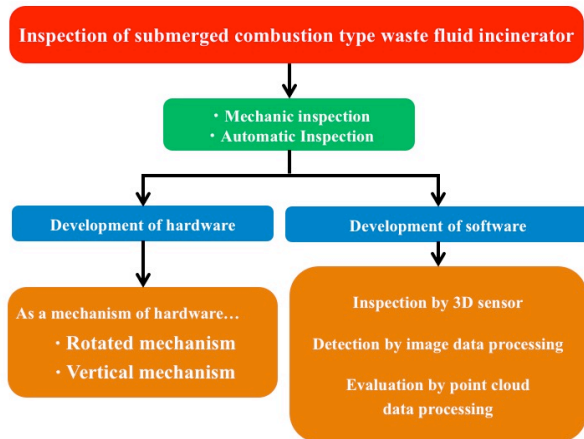


Fig. 3. Flow of the development

In development of device, it is thought that rotated mechanism and vertical mechanism is introduced to this device, in order to inspect the interior of incinerator. In this device, the internal whole of incinerator can be inspected

by rotational motion and linear motion. The sensor used in this study have depth sensor and distance information between sensor and target. The existence of defect can be detected by comparing the distance information by the control of this sensor. By processing the data acquired by the sensor, detailed measurement and evaluation can be done.

The Kinect sensor is put on the market by Microsoft Co. LTD., which has the RGB camera, IR camera and the depth sensor. The RGB camera and the depth sensor function of this device are applied to the inspection system on the surface of the furnace wall [2].

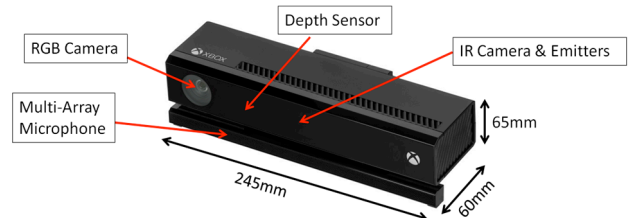


Fig. 4. Kinect sensor.

ROS is used as a software platform for developing applications.

Here, ROS is defined in ROS Wiki as follows: “ ROS (Robot Operating System) provides libraries and tools to help software developers create robot applications. It provides hardware abstraction, device drivers, visualizers, message-passing, package management, and more.” [3].

OpenCV (Open Source Computing Vision Library) is software library which have the functions of Image processing, Structural Analysis, Pattern Recognition, and so on.

By using cv_bridge package, ROS Image messages and OpenCV Images are converted [4].

"PCL" is abbreviation of "Point Cloud Library" and this software is a large-scale 3D point cloud operating open source program. The function of the model making, the filtering, registration and the object detecting is used in this study.

The Kinect sensor is connected to a PC and used, and software is executed in order to control on a PC. As a platform to develop and execute the software, ROS is used. By using OpenCV and PCL on ROS, Kinect is controlled, and image and point cloud data is processed. By this system, the detect of furnace wall is inspected and evaluated. The relation of system is shown in Fig. 5.



Fig. 5. Relation of system.

Result and Discussion

In order to experiment with Kinect, pseud-model of incinerator was made. The target incinerator is made by brick, so this pseud-model was mainly made by brick. The size of a brick is $215 \times 100 \times 60$ mm. The brick displayed lengthwise assumes it the wall of the incinerator. The part which the brick fell out of means a defect. The pseud-model of incinerator is shown in Fig. 6.



Fig. 6. Pseud-model of incinerator.

The RGB color image obtained by Kinect is shown in Fig. 7 [5]. When it is really used in incinerator, the RGB color image is obtained by lighting up the inside with a light. The presence of the defect is inspected by this function. The display of Kinect Fusion is shown in Fig. 8. Then Kinect Fusion is the function to build 3D model by depth information, IR information and other factors measured by Kinect [6].



Fig. 7. Color image.



Fig. 8. Kinect Fusion

The process of measurement and detection by using Kinect and OpenCV is shown below:

- I. Calculate the average distance between the sensor and target
- II. Measure the center distance of sensor
- III. The center distance is compared with the average distance
- IV. It is considered the crack if there are 0.1m or more difference of these distances
- V. The information about distance is displayed in the terminal

Average distance, the distance of center and distance of crack are obtained. The capture of result and the output of distance are shown in Fig. 9 and Table 1.

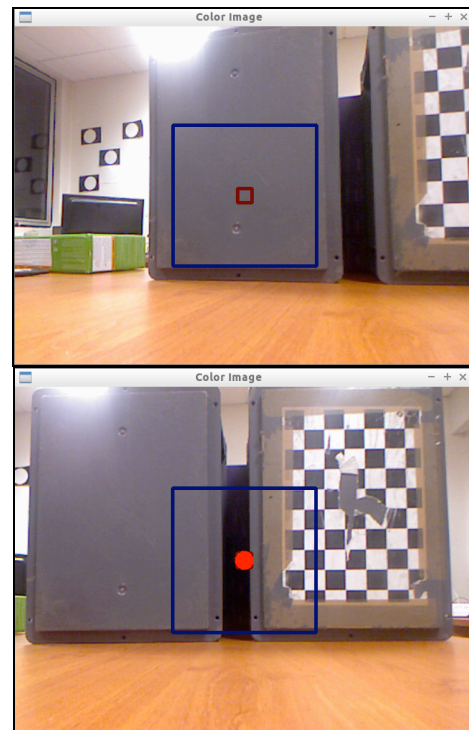


Fig. 9. Measurement and detection

| | Normal | Defect |
|---------------|--------|--------|
| Average[m] | 0.557 | 0.521 |
| Distance[m] | 0.562 | 0.772 |
| Difference[m] | 0.005 | 0.251 |

Table 1. Result of output

In a design of the inspecting system, the program using PCL was made.

The algorithm included in PCL as follows.

- Visualization ... Visualizing of the 3D data
- Filtering ... Processing the point cloud.
- Registration ... Aligning the point cloud
- Mesh ... Creating the mesh model

is used to process the data obtained by Kinect [7].

The result of output 3D model obtained by the Kinect Fusion as a 3D point cloud model, is shown in Fig. 10. The detailed inspection can be done by output in 3D point cloud model [8].



Fig. 10. Point cloud data.

The 3D point cloud data which were processed by Voxel Grid Filter is shown in Fig. 11. Then Voxel Grid Filter, one of the library included in the PCL, control the interval of the point cloud data by downing the sampling processing [9]. After this process, it becomes easy to control this data.

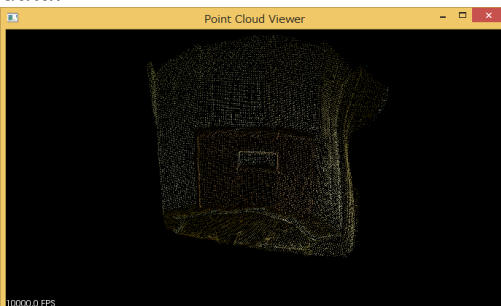


Fig. 11. Voxel grid filter

Conclusion

- The system which inspect the inner incinerator wall state by using the Kinect sensor, the ROS and the OpenCV was developed.
- The 3D model of the inspected incinerator was made by using the PCL.
- The inspection device will be developed, which has the Kinect and the data processing systems.

References

1. 1975 Kyosei industry Co.,Ltd. (2017) Demolition construction of the chimney : Chimney construction – Kyosei industry Co, Ltd. <http://www.entotsu.biz/subdivision.htm> (accessed 2017-5-22).
2. Miles Hansard, Seungkyu Lee, Ouk Choi, Radu Horaud.” Time of Flight Cameras: Principles, Methods, and Applications”. Springer Science & Business Media. 2012.
3. ROS (2016). ROS Wiki. <http://wiki.ros.org/>. (accessed 2016-12-8).
4. OpenCV team (2017). OpenCV library <http://opencv.org/> (accessed 2017-5-22).
5. Kaoru Nakamura, Tsukasa Sugiura, Tomohiro Takata, Tomoaki Ueda (2015). KINECT for Windows SDK Programing corresponding to Kinect for Windows v2 sensor. SHUWA SYSTEM CO.,LTD. 480p.
6. D.Pagliari, F.Menna , R.Roncella , F.Remondino , L.Pinto .” KINECT FUSION IMPROVEMENT USING DEPTH CAMERA CALIBRATION”. The International Archives of the Photogrammetry, Remote Sensing and Spatial Information Sciences, Volume XL-5. 2014
7. PointClouds.org (2017). PCL-Point Cloud Library. <http://www.pointclouds.org/> (accessed 2017-1-23).
8. Hiroshi Masuda (2013). Current Status of Large-Scale Point Processing Captured by Terrestrial Laser Scanner. The Japan Society for Precision Engineering. Vol.79, No.5, 384-387.
9. PointClouds.org (2017). Documentation – Point Cloud Library (PCL). http://pointclouds.org/documentation/tutorials/voxel_grid.php (accessed 2017-5-22).

Induction Heating Thermography for crack detection in spot welds

A. Taram^{1,2}, C. Roquelet¹, Ph. Meilland¹, Th. Dupuy¹, C. Kaczynski¹, JL. Bodnar², Th. Duvaut²

¹ ArcelorMittal Maizieres Research, Voie Romaine 57280 Maizières-lès-Metz, Cedex, France
abdoulaye.taram@arcelormittal.com, cyrielle.roquelet@arcelormittal.com
thomas.dupuy@arcelormittal.com

² GRESPI, UFR Sciences Exactes et Naturelles, BP 1039, 51687 Reims cedex 02, France
jean-luc.bodnar@univ-reims.fr, thierry.duvaut@univ-reims.fr

Abstract

Induction heating thermography is a nondestructive inspection which has been used successfully to detect cracks in metallic material. The technique consists in using eddy current to produce heat in the material and used an infrared camera to monitor the surface temperature distribution. The presence of defects or cracks will perturb the heat distribution. The technique is fast and efficient for cracks detection. However, it is more convenient for electrical conductive material.

The purpose of this paper is to use induction heating thermography for welding defects detection.

The sequence of images captures by the infrared camera is processed using pulsed phase thermography technique. Phase image completed with supplementary filtering operation allow outlining defects. The result was confirmed with confocal microscopy inspection.

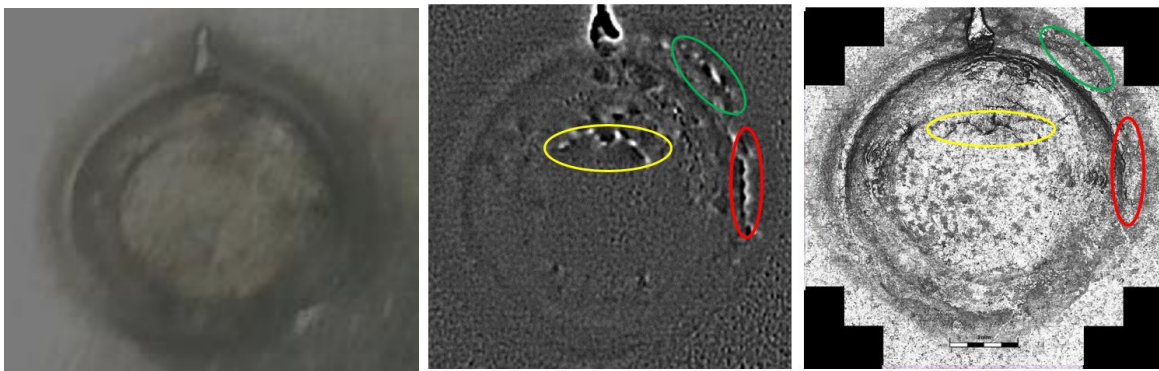
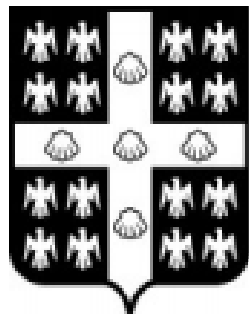


Figure 1: Cracks detection on resistance spot weld (Left: sample; Middle: Thermography inspection; Right: Confocal result)

Biothermophotonics Invited Session

AITA 2017

Québec City, Canada
September 27th - 29th, 2017



UNIVERSITÉ
LAVAL

QUANTITATIVE CHARACTERIZATION OF HUMAN SKIN BY COMBINED PHOTOTHERMAL RADIOMETRY AND OPTICAL SPECTROSCOPY

B. Majaron^{1,2}, N. Verdel,¹ A. Marin,² L. Vidovič,¹ M. Milanič^{1,2}

¹Jožef Stefan Institute, Ljubljana, Slovenia

²Faculty of Mathematics and Physics, University of Ljubljana, Slovenia

boris.majaron@ijs.si, nina.verdel@ijs.si, ana.marin@fmf.uni-lj.si,
 luka.vidovic@ijs.si, matija.milanic@fmf.uni-lj.si

We are combining two optical techniques, pulsed photothermal radiometry (PPTR) and diffuse reflectance spectroscopy (DRS), for noninvasive assessment of structure and composition of human skin *in vivo*. The analysis involves simultaneous multi-dimensional fitting of the measured PPTR signals and DRS spectra with predictions of a numerical model of light transport in the involved strongly scattering tissues - inverse Monte Carlo. Applying a four-layer skin model, representing the epidermis, papillary and reticular dermis, and subcutis yields an very good match between the experimental and modeling data. The assessed parameter values (i.e., the layer thicknesses, chromophore contents, scattering properties, etc.) lie within anatomically and physiologically plausible intervals.

Introduction

Pulsed photothermal radiometry (PPTR) involves measurements of transient dynamics in mid-infrared (IR) emission from sample surface after exposure to a single light pulse. Beside the assessment of optical or thermal properties of homogeneous samples, light-induced temperature depth profiles can also be determined from such radiometric signals [1–3].

Quantitative assessment of structural properties and composition of multi-layered tissue structures, such as human skin, however, requires solving an additional inverse problem of light transport in scattering-dominated medium. This process relies on several assumptions, such as the scattering properties of the tissue layers, which may however vary with anatomical location, person's age, gender, lifestyle (smoking), etc.

Because PPTR analysis doesn't allow for unique extraction of all relevant skin

characteristics, we combine PPTR with another optical technique, diffuse reflectance spectroscopy (DRS) in the visible spectral range. This considerably improves the accuracy and robustness of the inverse analysis. While PPTR is highly sensitive to depth distribution of the selected absorbers, DRS namely enables spectral differentiation between various chromophores in human skin (e.g., oxy- and deoxy-hemoglobin, melanin, adipose, etc.).

Methods

Selected test sites in healthy volunteers were irradiated with individual 1 ms light pulses at $\lambda = 532$ nm, emitted from a medical-grade laser (DualisVP by Fotona, Ljubljana, Slovenia). At the effective spot size of ~ 5 mm, the radiant exposure was ~ 0.30 J/cm.² Prior to measurement, the superficial layer of dried-out epidermal cells (*stratum corneum*) was removed by tape-stripping to enable unobstructed heat diffusion all the way to the skin surface [2,4].

Mid-IR emission from the tissue surface was recorded with a fast IR camera (SC7500 by FLIR; $\lambda = 3.5\text{--}5.1\ \mu\text{m}$; see Fig. 1) at a typical rate of 1000 frames per second.

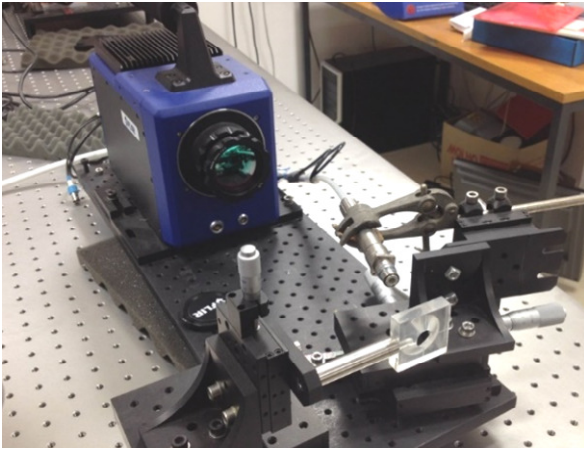


Fig. 1. Experimental setup for PPTR measurements, consisting of a fast mid-IR camera with a 50 mm objective, optical fiber for delivery of light pulses from a 532 nm laser, beam-shaping optics, and an aperture for positioning of the test site.

One-dimensional PPTR signals were obtained from the acquired radiometric record (Fig. 2) by lateral averaging over the area of interest (typically $1.5 \times 1.5\ \text{mm}^2$) and subtracting the baseline value. The manufacturer provided calibration system was used for conversion of raw signal values to radiometric temperature scale [3,4].

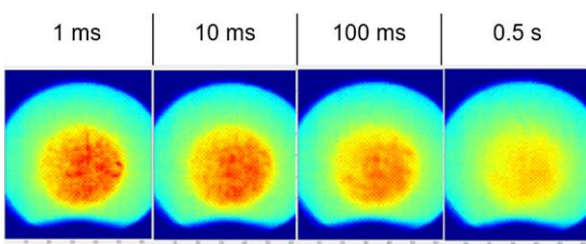


Fig. 2. Typical IR images of the skin test site at different times after pulsed irradiation (indicated above the images). The lateral dimension equals 1 cm and the indicated radiometric temperatures range from 30 to 35 °C (shown in deep blue and red, respectively).

The DRS were measured within the visible spectral range ($\lambda = 400\text{--}700\ \text{nm}$) using an integrating sphere with an internal light source (ISP-REF by Ocean Optics, Dunedin, FL) and a

fiber-connected compact optical spectrometer (USB4000, Ocean Optics) [4,5]. Prior to analysis, a typical measurement artefact called single-beam substitution error was removed from each acquired DRS using an algebraic correction, developed earlier using theoretical analysis and experimental verification [5].

The structure and composition of the selected test site is assessed by fitting the measured PPTR signals and DRS spectra with corresponding predictions from a dedicated numerical model of light and heat transport in human skin. This is performed by objective multi-dimensional minimization of the residual norm, using the nonlinear least-squares algorithm implemented as a function `lsqnonlin` in Matlab Optimization Toolbox (Mathworks Inc., Natick, MA, USA).

The optical model of skin assumes four optically homogeneous layer, representing the epidermis, papillary and reticular dermis, and subcutis (adipose). The refractive index is set to $n = 1.45$ for the epidermis, 1.37 for dermis, and 1.34 for subcutis. Determination of the absorption coefficient in each layer in relation to the fractional contents of specific absorbers was described elsewhere [4,6].

Light transport and energy deposition in skin during the PPTR measurements are simulated using the well established weighted-photon Monte Carlo (MC) technique [7]. The 532 nm laser pulse is divided into 10^7 energy packets ("photons") and their quasi-random tortuous paths through the scattering medium are followed until they deposit all the initial energy or escape through the skin surface. Due to the large computational complexity, this process is parallelized using CUDA technology and run on a high-performance graphics card.

By considering also the thermal properties of the involved skin layers, the obtained laser-induced energy deposition profiles are then converted into the corresponding temperature profiles. And from these, the consequent PPTR signals are computed by accounting for partial

absorption of the IR emission contributions from subsurface tissue layers [3,4]. The initial 1.5 seconds of the PPTR signals are used in the analysis.

The DRS spectra are simulated using the same MC algorithm. However, in order to control the computational load, the diffuse reflectance values are fitted at only 13 wavelengths from 410 to 600 nm, carefully selected by considering the absorption spectra of melanin, oxy-, and deoxy-hemoglobin (see Fig. 3b)[6].

Results

Figure 3 presents a PPTR signal (a) and diffuse reflectance spectrum (b) as measured on the inner forearm of a healthy male (age 54; *orange solid line*). The above described analysis yields a good match between the measured and best fitting model data (*dashed*) for both techniques.

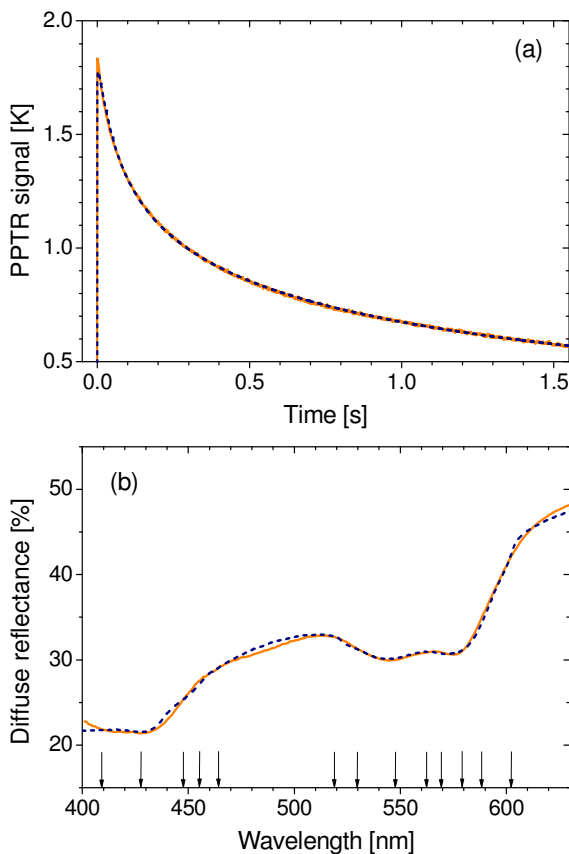


Fig. 3. PPTR signal following pulsed irradiation at 532 nm (a) and DRS spectrum in the visible (b) as measured in a healthy volunteer. Solid curves are experimental data, dashed and best fits from our model.

The obtained epidermal and dermal thicknesses, chromophore concentrations, and blood oxygenation levels (Tbl. 1) are within physiologically and anatomically plausible ranges and in agreement with literature data [8].

Specifically, allowing the reduced scattering coefficient of the epidermis and dermis to be fitted simultaneously with the other parameters, according to the customary ansatz

$$\mu'_s(\lambda) = a \left(\frac{\lambda}{500 \text{ nm}} \right)^{-b} \quad (1)$$

leads to improved match and more realistic values as compared to the approach where the dependence (1) is fixed according to average data from literature [9]. It is namely known (or at least speculated) that these properties can vary individually, tentatively depending on person's age, gender, lifestyle, anatomical location, etc. Similarly, the amplitude of scattering in subcutis (A) is also fitted individually [10].

| Model variable | Fitted value |
|--------------------------|-----------------|
| d_{epi} [mm] | 0.12 |
| d_{der} [mm] | 0.81 ± 0.14 |
| m [%] | 1.2 |
| b_{pap} [%] | 2.4 ± 0.1 |
| b_{ret} [%] | 2.7 ± 0.1 |
| S_{pap} [%] | 33 ± 3 |
| S_{ret} [%] | 59 ± 3 |
| A [-] | 0.65 ± 0.03 |
| a [mm^{-1}] | 7.1 ± 0.1 |
| b [-] | 2.4 ± 0.1 |

Table 1. The assessed parameters of our four-level model of human skin: Epidermal and dermal thickness (d_{epi} and d_{der}), melanin fractional volume (m), blood contents in the papillary and reticular dermis (b_{pap} and b_{ret} , respectively), oxygen saturation levels in the same layers (S_{pap} , S_{ret}), scattering amplitude in subdermal adipose (A), and scattering amplitude and power in epidermis and dermis (a , b). The presented values are averages from five inverse analysis runs and the corresponding standard deviations (where significant).

The obtained result was verified by imaging the same test site with a commercial multi-photon microscopy system (MPTflex, JenLab, Jena, Germany) [11]. Our analysis of the obtained cross-sectional images indicated an epidermal thickness of 0.10 ± 0.02 mm, in very good agreement with the presented result.

Conclusion

Combining pulsed photothermal radiometry and diffuse reflectance spectroscopy with inverse analysis based on numerical modeling (MC) of light transport in strongly scattering tissues enables noninvasive characterization of human skin in terms of the thicknesses of its characteristic layers, chromophore contents, and also scattering properties *in vivo*. In our group, we are currently using such values as a baseline in several on-going studies aiming at quantitative assessment of hemodynamics in healthy human skin [11], healing dynamics of incidentally acquired bruises (*hematomas*) [13], the effects of aesthetic laser treatments, etc.

Acknowledgements

This work was financed by The Slovenian Research Agency (ARRS) through grants P1-0192, P1-0389, PR-07590, and PR-04360. The authors thank Fotona (Ljubljana, Slovenia) for lending us the clinical laser system.

References

1. T.E. Milner, D.M. Goodman, B.S. Tanenbaum, et al. Depth profiling of laser heated chromophores in biological tissue by pulsed photothermal radiometry, *J. Opt. Soc. Am.*, vol. A 12, pp. 1479–1488, 1995.
2. B. Majaron, W. Verkruyse, B.S. Tanenbaum, et al. Combining two excitation wavelengths for pulsed photothermal profiling of hypervascular lesions in human skin, *Phys. Med. Biol.*, vol. 45, pp. 1913–1922, 2000.
3. M. Milanič, I. Serša, B. Majaron. A spectrally composite reconstruction approach for improved resolution of pulsed photothermal temperature profiling in water-based samples, *Phys. Med. Biol.*, vol. 54, pp. 2829–2844, 2009.
4. L. Vidovič, M. Milanič, B. Majaron. Objective characterization of bruise evolution using photothermal depth profiling and Monte Carlo modeling, *J. Biomed. Opt.*, vol. 20, pp. 017001-1–11, 2015.
5. L. Vidovič, B. Majaron. Elimination of single-beam substitution error in diffuse reflectance measurements using an integrating sphere, *J. Biomed. Opt.*, vol. 19, pp. 027006-1–9, 2014.
6. M. Milanič, B. Majaron. 3D Monte Carlo model of pulsed laser treatment of cutaneous vascular lesions, *J. Biomed. Opt.*, vol. 16, pp. 128002-1–12, 2011.
7. L. Wang, S. L. Jacques, L. Zheng. MCML-Monte Carlo modeling of light transport in multi-layered tissues, *Comput. Methods Programs Biomed.*, vol. 47, pp. 131–146, 1995.
8. S. L. Jacques. Optical properties of biological tissues: a review, *Phys. Med. Biol.* vol. 58, pp. R73–R61, 2013.
9. N. Verdel, A. Marin, L. Vidovič, et al. In vivo characterization of structural and optical properties of human skin by combined photothermal radiometry and diffuse reflectance spectroscopy, *Proc. SPIE*, vol. 10037, pp. 100370H-1–9, 2017. (BiOS 2017, San Francisco, CA)
10. P. Naglič, L. Vidovič, M. Milanič, et al. Applicability of diffusion approximation in analysis of diffuse reflectance spectra from healthy human skin, *Proc. SPIE* vol. 9032, 90320N, 2013. (Biophotonics Riga 2013, Riga, Latvia, 2013).
11. M. Balu, C. B. Zachary, R. M. Harris, et al. In vivo multiphoton microscopy of basal cell carcinoma, *JAMA Dermatol.*, vol. 151, pp. 1068-1074, 2015.
12. N. Verdel, A. Marin, L. Vidovič, et al. Analysis of hemodynamics in human skin using photothermal radiometry and diffuse reflectance spectroscopy, *Proc. SPIE*, vol. 10412, 2017. (ECBO 2017, Munich, Germany, 2017)
13. A. Marin, N. Verdel, L. Vidovič, et al. Assessment of individual bruising dynamics by pulsed photometric radiometry and inverse Monte Carlo analysis, *Proc. SPIE*, vol. 10412, 2017. (ECBO 2017, Munich, Germany, 2017)

Invited Paper as part of the «AITA Biothermophotonics Invited Session»

INFRARED IMAGING TECHNOLOGIES FOR EARLY DETECTION OF DENTAL CARIES

Nima Tabatabaei

*York University, Department of Mechanical Engineering, Toronto, Canada
Nima.Tabatabaei@Lassonde.YorkU.ca*

Worldwide, 60–90% of school children and nearly 100% of adults have dental cavities. The prevalence of dental cavities imposes significant financial and societal burdens on families, governments, and health care systems. A case in point is the total dental expenses for U.S. children aged 5–17 years in 2009 which was estimated at \$20 billion, accounting for 17.7% of all health-care expenses among this age group. The prevalence of dental caries suggests that the current standard of care in Dentistry is not effective. As such, Dentistry is undergoing a paradigm shift away from surgical treatment of caries to a model of early caries diagnosis and management (i.e., preventive Dentistry). However, preventive Dentistry is only effective if practiced on caries at early stages of development. Yet, existing clinical detection tools and techniques such as x-ray and visual/tactile inspection are not sensitive enough to detect early decay or monitor its progression.

In this invited talk, I will present two infrared optical imaging technologies for detection of early dental caries, named optical coherence tomography (OCT) and thermophotonic lock-in imaging (TPLI). OCT is an interferometric imaging technology which detects caries by sensing the enhanced optical scattering at caries sites. TPLI, on the other hand, is a lock-in thermography technology which utilizes the enhancement of light absorption at early caries site for detection.

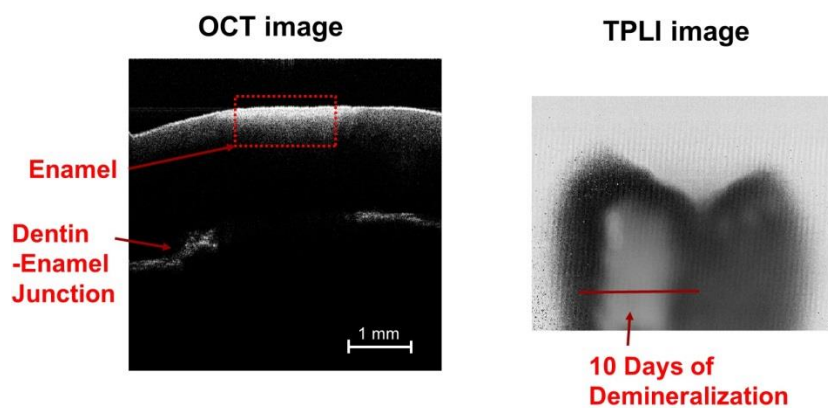


Figure 1. Detection of caries on smooth surfaces by optical coherence tomography (left) and thermophotonic lock-in imaging (right).

A systematic comparison between the detection performance of OCT and TPLI will be presented. The comparative study is carried out through imaging of inception and progression of artificially-induced early caries in human teeth using an acidified gel. The comparison results of key performance parameters such as early caries detection threshold, maximum inspection depth, detection sensitivity, and imaging time will be presented and discussed.

Advances in Opto-Thermal Skin Measurements

X. Zhang, C. Bontozoglou, P. Xiao

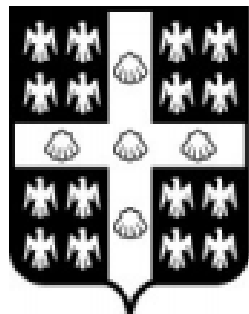
**School of Engineering, London South Bank University, 103 Borough Road, London SE1 0AA,
UK. xiaop@lsbu.ac.uk**

Opto-Thermal Transient Emission Radiometry (OTTER) is an infrared remote sensing technique that has been used in skin hydration, skin pigments, skin topically applied substances penetrate measurements etc. In this paper, we will present the latest developments of the OTTER technology, including high speed sampling, multiple wavelengths detection, enhanced depth profiling algorithms, multiple topically applied substances measurements, as well as hair measurements. We will first present the theoretical background, then followed by the experimental results.

Detectors

AITA 2017

Québec City, Canada
September 27th - 29th, 2017



UNIVERSITÉ
LAVAL

Performance prediction of p-i-n HgCdTe long wavelength infrared HOT photodiodes

A. Rogalski, M. Kopytko, and P. Martyniuk

Institute of Applied Physics, Military University of Technology, 2 Kaliskiego Str., 00-908 Warsaw, Poland

Infrared system performance is highly scenario dependent and requires the designer to account for numerous different factors when specifying detector performance. It means that a good solution for one application may not be as suitable for a different application.

HgCdTe is currently the most prevalent material system used in high performance infrared detectors. Its position is conditioned by three key features:

- tailorable energy band gap over the 1–30- μm range,
- large optical coefficients that enable high quantum efficiency, and
- favorable inherent recombination mechanisms that lead to high operating temperature.

Moreover, the specific advantages of HgCdTe are ability to obtain both low and high carrier concentrations, high mobility of electrons, and low dielectric constant. The extremely small change of lattice constant with composition makes it possible to grow high quality layered and graded gap structures. As a result, HgCdTe can be used for detectors operated at various modes [photoconductor, photodiode or metal-insulator-semiconductor (MIS) detector].

Despite these advantages, there are several drawbacks associated with HgCdTe devices. Being a II-VI semiconductor with weaker ionic Hg-Te bonds and high Hg vapor pressure, HgCdTe is soft and brittle and requires extreme care in growth, fabrication, and storage. The commonly growth of HgCdTe epitaxial layers is more challenging than for typical III-V materials, resulting in lower yields and higher costs. HgCdTe material exhibits relatively high defect densities and surface leakage currents that adversely affect performance, particularly for LWIR devices. Also composition uniformity is a challenge for HgCdTe devices, particularly for LWIR devices, leading to variability in cut-off wavelength. In addition, $1/f$ noise causes uniformity to vary over time, what is difficult to correct via image processing. As a result, LWIR HgCdTe detectors can only be fabricated in small FPAs.

Important advantage of T2SLs is the high quality, high uniformity and stable nature of the material. In general, III-V semiconductors are more robust than their II-VI counterparts due to stronger, less ionic chemical bonding. As a result, III-V-based FPAs excel in operability, spatial uniformity, temporal stability, scalability, producibility, and affordability – the so-called “ibility” advantages [1]. The energy gap and electronic properties of T2SLs are determined by the layer thicknesses rather than the molar fraction as is the case for HgCdTe. The growth of T2SLs can be carried out with better control over the structure and with higher reproducibility. The spatial uniformity is also improved, since the effects of compositional change due to flux and temperature non-uniformity are not as important as they are in ternary/quaternary bulk materials.

From a performance perspective, III-V diffusion current limited FPAs can operate at levels that approach that of HgCdTe, but always with a required lower operating temperature. It should be however insist, that ultimate cost reduction for an IR system will only be achieved by room temperature operation of depletion current limited FPAs with pixel densities that are fully consistent with background- and diffraction-limited performance due to system optics. In this context a long SR lifetime of HgCdTe mandates the use of this material systems for room-temperature operation. Kinch predicted that large area ultra-small pixel diffraction-limited and background-limited photon detecting MW and LW HgCdTe FPAs operating at room temperature will be available within the next ten years. Unfortunately, it will be rather difficult to improve SR lifetime to overcome the disadvantage of large InAs/GaSb T2SL's depletion dark currents. Better situation is observed in Ga-free InAs/InAsSb T2SLs due to large values of carrier lifetimes, including SR lifetime.

In the paper the performance of $\text{P}^+\text{-v-N}^+$ LWIR HgCdTe HOT photodiode, with the n-type absorber doping sufficiently low to allow a full depletion at moderate bias, is theoretically predicted. For low doping HgCdTe, the way to achieve very low carrier concentration in the detector absorber region is to apply sufficient reverse bias to fully deplete it, what is shown in Fig. 1(a). In such conditions, free carrier and Auger recombination is eliminated. If generation-recombination (G-R) currents are adequately low, the detector performance is limited by the background.

To predict the detector performance, the n-type doping of the $\text{P}^+\text{-v-N}^+$ device absorber [see Fig. 1(b)] is chosen to be sufficiently low to allow a full depletion at moderate bias. The absorber layer is surrounded by a wider bandgap, highly doped contact layers to suppress dark current generation from these regions and to suppress tunneling current under reverse bias. Thus, the $\text{P}^+\text{-v-N}^+$ device is essentially p-i-n diode.

The parameters taken in calculations for $\text{P}^+\text{-v-N}^+$ diode designed for LWIR range are presented in Fig. 1(b). Bottom illumination was used for the spectra response calculations. We have assumed more realistic device that includes doping and compositional grading at interfaces, and also a graded HgCdTe composition in the absorber layer from $x_{\text{Abs}} = 0.19$ to 0.21. The gradient of Cd alloy composition in the absorber layer was adjusted in order to maintain a constant peak wavelength at the temperature of operation in comparison to the device with constant Cd alloy composition in the absorber layer, $x_{\text{Abs}} = 0.2$.

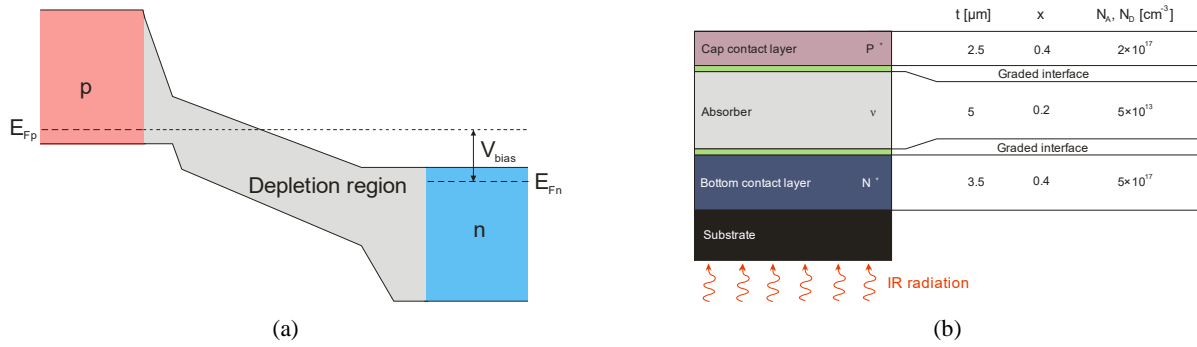


Fig. 1. p-i-n photodiode: (a) band diagram for reverse bias photodiode; (b) P⁺-v-N⁺ HgCdTe photodiode architecture and structural parameters used in modeling.

The generation-recombination current of a fully depleted detector can be estimated by following expression

$$J_{GR} = q \frac{n_i}{\tau_{SR}} W_{dep}, \quad (1)$$

where W_{dep} is the width of depletion region, and τ_{SR} is the Shockley-Read-Hall lifetime.

Figure 2 gathers the trap levels reported for Hg_{1-x}Cd_xTe detectors obtained using different methods of characterizations [2]. The data scattering is significant. The electron trap levels being found follow commonly observed trap level trends $E_T = 0.35E_g(x)$ and $E_T = 0.75E_g(x)$. The trend line $0.75E_g(x)$ is well supported for $x \geq 0.29$ (the uppermost ellipse). The trend line $0.35E_g(x)$ is strongly supported by experiments in the low x -regime $x < 0.35$.

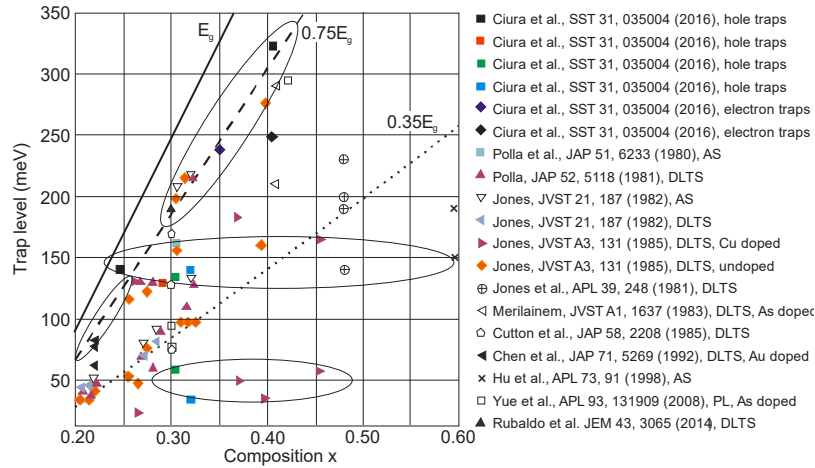


Fig. 2. The trap levels detected in HgCdTe detectors. The lines indicate the characteristic trends in the data. Ellipses gather the particular groups of the traps (after Ref. 1).

The kinetics of SRH mechanism is strongly dependent on the density of SRH centres, N_T , both associated with Hg-vacancies and dislocations. The impact of the density of SRH centres on the SRH carrier lifetime was carried out for uniform (constant composition $x = 0.2$ in the absorber region) LWIR P⁺-v-N⁺ photodiode. Figure 3(a) shows the SRH carrier lifetime as a function of the position of the SRH energy level, calculated for the non-biased LWIR ($x = 0.2$) n-type material doped at the level of $5 \times 10^{13} \text{ cm}^{-3}$. The SRH energy level associated with the mercury vacancy has been changed from $0.25E_g$ to $0.75E_g$ above the valence band. Calculations have been done for the product of $\sigma_n N_T = \sigma_p N_T$ between 10^{-3} cm^{-1} and 10^{-5} cm^{-1} (σ_n and σ_p are the electron and hole captures cross-sections, N_T denotes the mercury vacancy concentration). For example, if one assumes a typical value for the capture cross-section of a neutral centre of 10^{-15} cm^2 , the product of $\sigma_n N_T = \sigma_p N_T = 10^{-4} \text{ cm}^{-1}$ represents the minority carrier lifetime consistent with the density of mercury vacancy of 10^{11} cm^{-3} . The SRH carrier lifetime is inversely proportional to the product of $\sigma_n N_T$ ($\sigma_p N_T$).

Figure 3(b) shows the dependence of the SRH carrier lifetime on dislocation density for LWIR P⁺-v-N⁺ photodiode. The following parameters have been chosen: capture cross section for the dislocation band was set at $2 \times 10^{-15} \text{ cm}^2$ and the mean energy of the dislocation at $0.3E_g$ above the valence band. Taking this value of ionization energy we have obtained good agreement between theoretical predictions and experimental data [3]. The maximum value of the minority carrier lifetime is determined by the Hg-vacancy concentration. For $N_T = 10^{10} \text{ cm}^{-3}$, the critical dislocation density value, below which the minority carrier lifetime does not change with dislocation density is $G_{DIS} = 10^3 \text{ cm}^{-2}$. For $N_T = 10^{12} \text{ cm}^{-3}$, the minority carrier lifetime does not change for dislocation density below 10^5 cm^{-2} . When the impact of the dislocation exceeds the SRH component associated with Hg-vacancies, the minority carrier lifetime is approximately inversely proportional to the dislocation density.

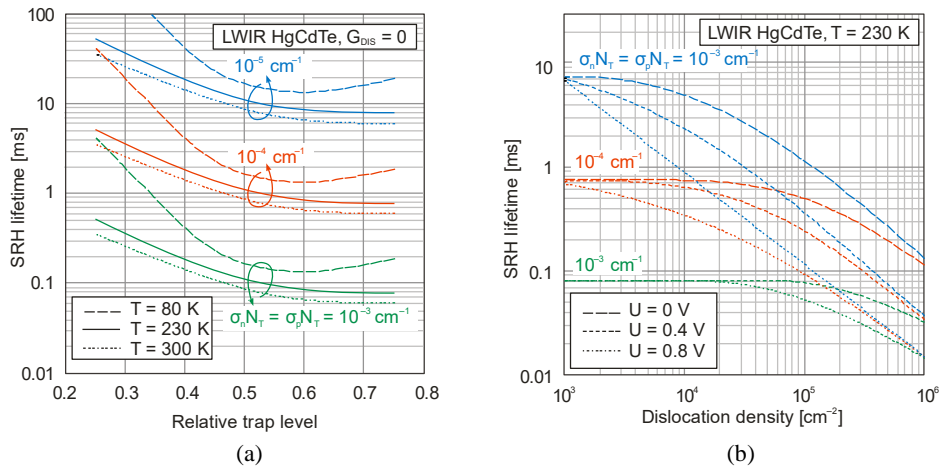


Fig. 3. Dependence of the SRH carrier lifetime in LWIR P⁺-v-N⁺ HgCdTe photodiode: (a) on the position of the trap energy level for an absorber layer with a low donor concentration of $5 \times 10^{13} \text{ cm}^{-3}$ under equilibrium bias conditions and different temperatures; (b) on dislocation density for an absorber layer with a low donor concentration of $5 \times 10^{13} \text{ cm}^{-3}$ in LWIR HgCdTe P⁺-v-N⁺ photodiode at 230 K. Calculations have been done for different product of $\sigma_n N_T$ and $\sigma_p N_T$.

Figure 4 shows simulated current-voltage characteristics for LWIR P⁺-v-N⁺ HgCdTe detector. The calculations have been done for Auger and SRH mechanism. Only Hg-vacancies were assumed as the SRH centers with the capture cross-section of a neutral centre of 10^{-15} cm^2 and energy level at $0.75 E_g$ above the valence band. The dark currents were predicted for varied vacancy concentration from 10^{10} cm^{-3} to 10^{13} cm^{-3} , what gives the product of $\sigma_n N_T$ ($\sigma_p N_T$) varied from 10^{-5} cm^{-1} to 10^{-2} cm^{-1} , respectively. The maximum value of the current responsivity is in the negative resistance region [see Fig. 4(a)]. In the case of good quality HgCdTe alloys, with a reduced number of a structural defects, the Auger-suppression is more efficient. The dark currents might be an order of magnitude lower than for $N_T = 10^{10} \text{ cm}^{-3}$ than for 10^{13} cm^{-3} .

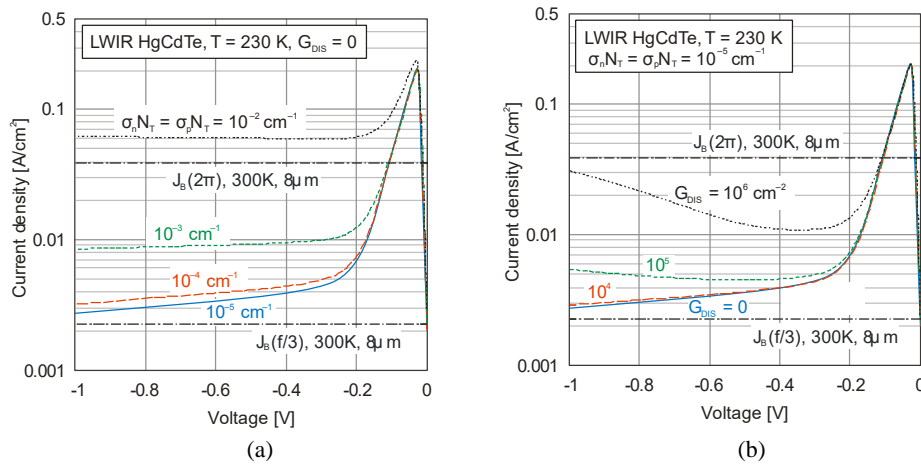


Fig. 4. Calculated current-voltage characteristics for LWIR P⁺-v-N⁺ HgCdTe photodiode. The theoretical prediction was calculated with consideration of Auger processes and SRH mechanism associated with mercury vacancies (a) for different product of $\sigma_n N_T$ and $\sigma_p N_T$ and (b) for $\sigma_n N_T$ and $\sigma_p N_T$ equal 10^{-5} cm^{-1} and dislocations with varied densities. The dark current densities are compared to background flux generation rates through f/3 optics and 2π field of view (FOV).

The influence of dislocations on current-voltage characteristics is shown on Figure 4(b). With increasing dislocation density, the dark current increases what suggests additional leakage channel by the energy levels positioned in the region of the dislocation cores. For $G_{DIS} = 10^6 \text{ cm}^{-2}$, the tunnel-like dark current rapidly increases with reverse voltages above 0.4 V.

In addition, the dark current densities shown in Fig. 4 are compared to background flux generation rates through f/3 optics and 2π field of view (FOV). It can be seen that the theoretically predicted dark current is comparable to that of the background flux current from f/3 optics for photodiodes with 9- μm cutoff wavelength at 230 K.

- [1] D.Z. Ting, A. Soibel, A. Khoshakhlagh, L. Höglund, S.A. Keo, B. Rafol, C.J. Hill, A.M. Fisher, E.M. Luong, J. Nguyen, J.K. Liu, J.M. Mumolo, B.J. Pepper, and S.D. Gunapala, Antimonide type-II superlattice barrier infrared detectors. *Proc. SPIE* 10177, to be published.
- [2] Ciura, L., Kolek, A., Kłębowski, A., Stanaszek, D., Piotrowski, A., Gawron, W., and Piotrowski, J., "Investigation of trap levels in HgCdTe IR detectors through low frequency noise spectroscopy", *Semicond. Sci. Technol.* 31, 035004-1-7 (2016).
- [3] Józwickowski, K., Józwickowska, A., Kopytko, M., Rogalski, A., Jaroszewicz, L.R., "Simplified model of dislocations as a SRH recombination channel in the HgCdTe heterostructures," *Infrared Phys.* 55, 98-107 (2012).

IGA-rule 17 for performance estimation of wavelength extending InGaAs photodetectors: validity and limitations

Zhang Yong-gang^{1*}, Gu Yi¹, Chen Xing-you¹, Ma Ying-jie¹,
Li Xue², Shao Xiu-mei², Gong Hai-mei², Fang Jia-xiong²

¹State Key Laboratory of Functional Materials for Informatics, Shanghai Institute of Microsystem and Information Technology, Chinese Academy of Science, Shanghai 200050, China.
*ygzhang@mail.sim.ac.cn

²Key Laboratory of Infrared Imaging Materials and Detectors, Shanghai Institute of Technical Physics, Chinese Academy of Sciences, Shanghai 200083, China

A thumb of rule, denoted as IGA-rule 17, has been developed to describe the temperature and cutoff wavelength dependent dark currents of wavelength extending InGaAs photodetectors in 2-3 μm band. The validity and limitations of the rule are discussed. This rule is intended as an index for device developer evaluating their technologies in processing, and a simple tool for device user estimating reachable performance at various conditions in their design, as well as an effective bridge between the two.

Introduction

Wavelength extending InGaAs photodetectors (PDs) and focal plane arrays (FPAs) have attracted much attention in numerous applications. Although from catalog data the performance of wavelength extending In_xGa_{1-x}As devices is still slightly inferior to HgCdTe (MCT) device at the same wavelengths, the robustness of the material system and maturity of the growth and processing comparing to MCT makes them a strong competitor. Different from their In_{0.53}Ga_{0.47}As cousin lattice matched to InP substrate, wavelength extending In_xGa_{1-x}As devices need higher Indium content (x>0.53) so metamorphic structure should be adopted, which leads to their discriminatory features. Besides, this device itself may rely on different technologies including material combinations, structure design, growth methods, processing flow, etc. How to evaluate those technologies is an intractable problem for the device developer. Furthermore, device users may not care about related technologies but dependent performances. A convenient communication bridge between the two is expected. Based on accumulated device data from different categories including our works, a trial has been made to meet the needs.

IGA-rule 17

Equation (1) was used to describe the dark current behavior of wavelength extending In_xGa_{1-x}As (x>0.53) photodetectors, in which J_s is saturation dark current density, λ_c and T is cutoff wavelength and operation temperature, others have their conventional meaning. In this equation two fitting parameters of C' and J₀ were introduced, which is proved to be an effective indicator to evaluate different technologies [1].

$$J_s = J_0 e^{-C' \frac{1.24q}{k} \times \frac{1}{\lambda_c T}} \quad (1)$$

Several groups of device data at 1.9-2.6 μm cutoff wavelength range and from room temperature (RT) to below 200 K were collected to extract the fitting parameters. The data are from Judson [2], Hamamatsu [3] and two of our works with superlattice electron barrier [4] or n-on-p [5] structures respectively. The saturation dark current density J_s is calculated from listed zero resistance area product R₀A data using J_s=kT/qR₀A, supposing in this temperature range and low bias condition the dark current is diffusion

dominated. From the data fitting, parameters of C' and J_0 for each category are extracted as listed in table 1. From equation (1), J_0 represents the current density at $T=\infty$, so in table 1 another more direct and meaningful parameter J_1 , which is defined as the dark current density at 300 K and cutoff wavelength of 2.4 μm , was also listed. The J_1 could be calculated directly from J_0 and C' .

| Categories & wavelengths | C' | J_0 (A/cm ²) | J_1 (A/cm ²) |
|---------------------------|--------|----------------------------|----------------------------|
| Judson 1.9-2.6 Ref.[2] | 0.6195 | 23.89 | 1.013E-4 |
| Hamamatsu 1.9-2.6 Ref.[3] | 0.7570 | 277.0 | 7.548E-5 |
| SIMIT 2.61 Ref.[4] | 0.7041 | 308.9 | 2.421E-4 |
| SIMIT 2.40 Ref.[5] | 0.7282 | 819.2 | 2.423E-4 |

Table 1. Fitted parameters from different categories including our works, under the frame of IGA-rule 17.

$$J_s = 300 \times e^{-0.75 \times \frac{1.24q}{k} \times \frac{1}{\lambda_c T}} \quad (2)$$

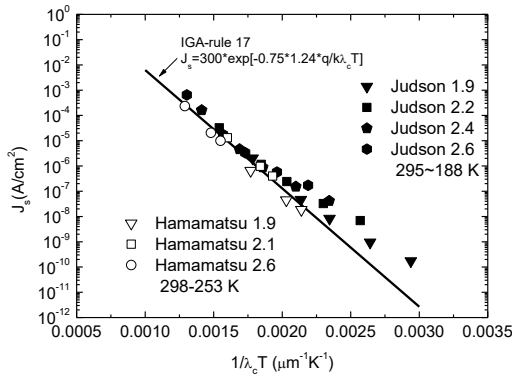


Fig. 1. Plotting of dark current density versus reciprocal cutoff wavelength temperature product of Judson [2] and Hamamatsu [3] wavelength extending photodiodes, solid line shows IGA-rule 17.

From above data, IGA-rule 17 is established as equation (2) to depict the cutoff wavelength and operation temperature dependent dark current of wavelength extending InGaAs PDs, for simplicity C' and J_0 are setting to be 0.75 and 300 A/cm² reasonably, which may represents

state of the art performance of those devices currently, corresponding to $J_1 \approx 1 \times 10^{-4}$ A/cm² of 2.4 μm PD at RT. Figures 1 and 2 plotted the J_s versus $1/\lambda_c T$ of the data from different categories including our works, as well as IGA-rule 17 line. Notice that the Hamamatsu data are only collected in temperature range from RT to 45 K below, other data in this narrow temperature range also fits the trend well. From which the validity of this thumb of rule is confirmed.

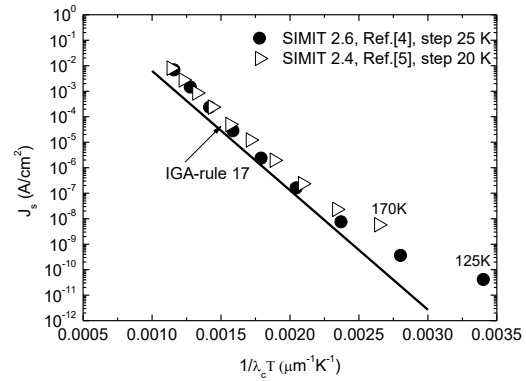


Fig. 2. Plotting of dark current density versus reciprocal cutoff wavelength and temperature product of our works [4-5], solid line shows IGA-rule 17.

Performance estimation using IGA-rule 17

Under the frame of IGA-rule 17, not only the dark current but also the important figures of merits $R_0 A$ and peak detectivity $D_{\lambda p}^*$ could also be estimated more precisely using equation (1) in conjunction with equation (3) and (4). In the estimation of detectivity, approximation of external quantum efficiency $\eta \approx 0.55$ and $\lambda_p \approx 0.9 \lambda_c$, or $\eta \lambda_p = 0.5$, was supposed.

$$R_0 A = \frac{kT/q}{J_0} e^{C' \frac{1.24q}{k} \times \frac{1}{\lambda_c T}} \quad (3)$$

$$D_{\lambda p}^*(R_0 A) = \frac{\eta \lambda_p q}{hc} \sqrt{\frac{R_0 A}{4kT}} \approx \frac{\lambda_c q}{4hc} \sqrt{\frac{R_0 A}{kT}} \quad (4)$$

$$E_g(x, T) = 1.52 - 1.575x + 0.475x^2 + \left(\frac{5.8}{T+300} - \frac{4.19}{T+271}\right) 10^{-4} T^2 x - \left(\frac{5.8}{T+271}\right) 10^{-4} T^2 \quad (5)$$

In calculation, the temperature coefficient of the cutoff wavelength λ_c needs to be considered. For $\text{In}_x\text{Ga}_{1-x}\text{As}$, the bandgap energy E_g could be calculated according to its composition and temperature [6]. By using equation (5), the cutoff wavelengths at different composition x and temperature T are plotted as shown in Fig. 3, where possible small difference between the band edge wavelengths of the materials and real cutoff wavelengths of the devices are neglected. The calculated saturation current density, as well as R_0A and peak detectivity $D^*_{\lambda_p}$, are shown in Fig.4.

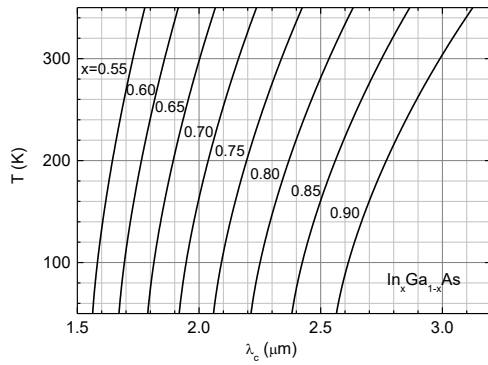


Fig. 3. Cutoff wavelength versus operation temperature of wavelength extending InGaAs photodetector using high Indium $\text{In}_x\text{Ga}_{1-x}\text{As}$ as the absorption layer.

$$\frac{J_s(T_2)}{J_s(T_1)} = e^{-C' \frac{1.24q}{k} \left(\frac{1}{\lambda_c'' T_2} - \frac{1}{\lambda_c' T_1} \right)} \quad (6)$$

$$\frac{R_0A(T_2)}{R_0A(T_1)} = \frac{T_2}{T_1} e^{C' \frac{1.24q}{k} \left(\frac{1}{\lambda_c'' T_2} - \frac{1}{\lambda_c' T_1} \right)} \quad (7)$$

$$\frac{D^*_{\lambda_p}(T_2)}{D^*_{\lambda_p}(T_1)} = \frac{\lambda_p''}{\lambda_p'} e^{\frac{C' 1.24q}{2k} \left(\frac{1}{\lambda_c'' T_2} - \frac{1}{\lambda_c' T_1} \right)} \quad (8)$$

In practice, people may want to deduce the performance of the device at different cutoff wavelengths and temperatures from known or measured data at specific conditions, such as at RT. In this case, a more convenient way could be adopted still under the frame of IGA-rule 17. Equations (6)-(8) show the formulas for calculation. From those formulas it could be seen that, for estimating the performances of

the devices at certain temperature and wavelength from known data, the only needed parameter is the exponential factor C' . In the calculation of detectivity, ratio of peak wavelength λ_p could be substituted directly by cutoff wavelength λ_c without big error. To determine state of the art performance of wavelength extending InGaAs photodetector currently, $C'=0.75$ could be used.

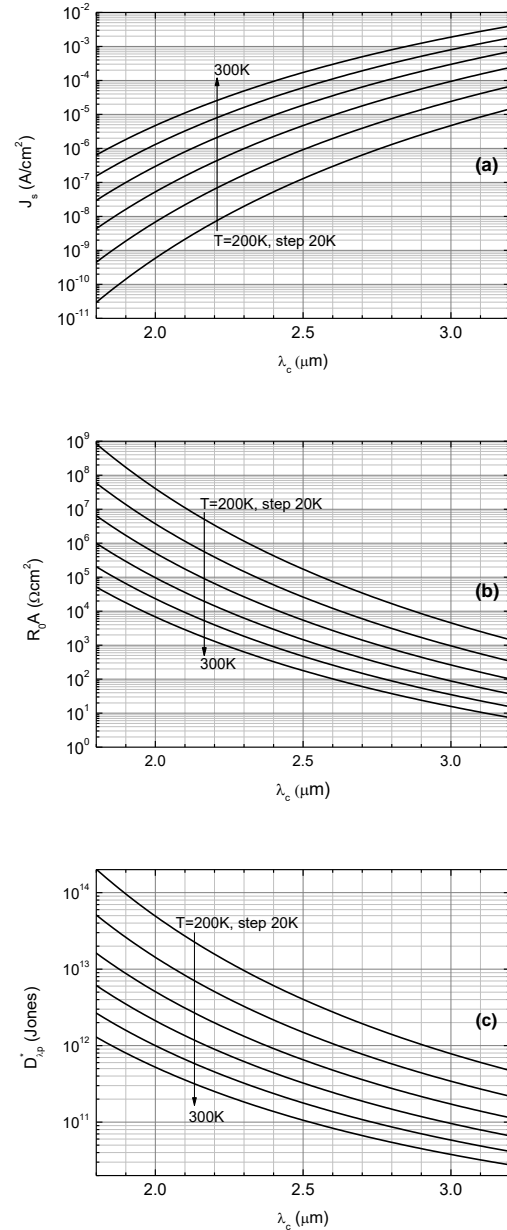


Fig. 4. Calculated IGA-rule 17 performance dependence of cut-off wavelength at different operation temperatures. (a): dark current density, (b): R_0A , (c): peak detectivity.

Discussions

The form of IGA-rule 17 of equation (1) is similar to the well know MCT-rule 07 a decade ago [7]. However, at the same wavelength range three more ambiguous parameters are needed as shown in equation (9) in MCT-rule 07 to force the data alone the line seemingly.

$$J_s = J_0 e^{C \frac{1.24q}{k} \times \frac{1}{\lambda_c T} \times [1 - (\frac{\lambda_s}{\lambda_c} - \frac{\lambda_s}{\lambda_t})^P]} \quad (9)$$

From above data analysis it could be realized that, in IGA-rule 17 the C' is a key index and could be linked to different dark current mechanisms [8]. In general the saturation current density of a pn junction diode obeys $J_s \propto \exp(-E_g/nkT)$, where $n=1$ and $n=2$ correspond to diffusion or generation-recombination(G-R)/Ohmic leakage mechanism respectively. Compared with equation (1), $C' \approx 1/n$ could be deduced. For IGA-rule 17, $C' \approx 0.75$ or $n \approx 1.33$ means the dark current is still diffusion dominated but G-R or Ohmic leakage play important rule. Also, from Fig.1 and Fig.2 it could be noticed that, at lower temperature the data points have the trends deviating from IGA-rule 17 line. At even low temperatures, the diffusion and G-R current decreased dramatically, in this case other mechanism such as surface recombination or tunneling with $n > 2$ becomes dominant. For wavelength extending InGaAs PDs with metamorphic structures, this is congruous. Therefore, IGA-rule 17 with fixed $C' \approx 0.75$ currently is only suitable for certain temperature range such as 200-300 K, fortunately it just fits the most commonly used operation temperature range of RT to thermal-electric cooling for those devices. Although IGA-rule 17 is derived from the data of PDs, it is also suitable for FPAs with the same technology.

Conclusion

In conclusion, a thumb of rule to evaluate the performance and related technologies of wavelength extending InGaAs PDs and FPAs has been demonstrated. With two meaningful

fitting parameters and limited around 2-3 μm wavelength band and 200-300 K temperature range, the validation of this rule, denoted as IGA-rule 17 temporarily, is confirmed definitely.

Acknowledgments

This work was supported by the National Key Research and Development Program of China (No. 2016YFB0402400), the NSFC program (Nos. 61675225, 61605232, 61405232), and the Shanghai Sailing/Rising-Star Program (Nos. 15YF1414300 /17QA1404900).

References

1. Y. G. Zhang, Y. Gu, X. Y. Chen, Y. J. Ma, X. Li, X. M. Shao, H. M. Gong, J. X. Fang, "An effective indicator for evaluation of wavelength extending InGaAs photodetector technologies," *Infrared Physics & Technology*, **83**, 45-50 (2017)
2. <http://www.teledynejudson.com/prods/Documents/PB4206.pdf>
3. http://www.hamamatsu.com/resources/pdf/ssd/g1218_1_series_kird1117e.pdf
http://www.hamamatsu.com/resources/pdf/ssd/g1218_2_series_kird1118e.pdf
http://www.hamamatsu.com/resources/pdf/ssd/g1218_3_series_kird1119e.pdf
4. Y. Gu, L. Zhou, Y. G. Zhang, X. Y. Chen, Y. J. Ma, S. P. Xi, Hsby Li, "Dark current suppression in metamorphic $\text{In}_{0.83}\text{Ga}_{0.17}\text{As}$ photodetectors with $\text{In}_{0.66}\text{Ga}_{0.34}\text{As}/\text{InAs}$ superlattice electron barrier," *Appl. Phys. Express*, **8**, 022202 (2015)
5. Y. G. Zhang, Y. Gu, Z. B. Tian, A. Z. Li, X. R. Zhu, K. Wang, "Wavelength extended InGaAs/InAlAs/InP photodetectors using n-on-p configuration optimized for back illumination," *Infrared Phys. & Tech.* **52**, 52-56(2009)
6. S. Paul, J. B. Roy, P. K. Basu, "Empirical expressions for the alloy composition and temperature dependence of the band gap and intrinsic carrier density in $\text{Ga}_x\text{In}_{1-x}\text{As}$," *J. Appl. Phys.*, **69**, 827-829 (1991)
7. W. E. Tennant, D. Lee, M. Zandian, E. Piquette, M. Carmody, "MBE HgCdTe technology: a very general solution to IR detection, described by "rule 07", a very convenient heuristic," *J. Electronic Materials*, **37**, 1406-1410 (2008)
8. X. Li, H. M. Gong, J. X. Fang, X. M. Shao, H. J. Tang, S. L. Huang, T. Li, Z. C. Huang, "The development of InGaAs short wavelength infrared focal plane arrays with high performance," *Infrared Phys. & Tech.* **80**, 112-119 (2017)

Abstract for AITA 2017 in Quebec/Canada

Vendor or Scientific presentation

Presenter:

Dr. Sven-A. Wode
Business Develop Manager
InfraTec GmbH Infrarotsensorik und Messtechnik
Germany

Title of presentation: Active spatial resolution enhancement for cooled IR cameras.

Typically spatial resolution (iFOV) of (IR) cameras with a given FPA size (in terms of pixels) can be influenced by using macroscopic and microscopic lenses. With such a solution the overall field of view (FOV) will be reduced by nature. To achieve both small iFOV and large FOV at the same time an FPA detector with a higher amount of pixels usually is needed. This solution depends on the general availability of such detectors and most probably it will result in a more expensive solution. This paper describes an opto-mechanical solution which increases the iFOV still keeping the FOV of a given FPA detector. The gain of spatial resolution will be presented with examples as well as the possible influence of such enhancement to other performance data of the system. The realization of the opto-mechanical resolution enhancement will be presented as a reliable and an affordable alternative to usually expensive solutions.

Headquarters

InfraTec GmbH
Infrarotsensorik und Messtechnik
Gostritzer Straße 61 – 63
01217 Dresden / GERMANY

Phone +49 351 871-8630
Fax +49 351 871-8627
E-mail thermo@InfraTec.de
www.InfraTec.eu

USA office

InfraTec infrared LLC
5048 Tennyson Pkwy.
Plano TX 75024 / USA

Phone +1 844-226-3722 (toll free)
E-mail thermo@InfraTec-infrared.com
www.InfraTec-infrared.com

Multiple shutter mode radiation hard IR detector ROIC

A.K.Kalgi¹, B.Dierickx¹, D. Van Aken¹, S.Veijalainen¹, K.Liekens¹, W. Verbruggen¹, P. Hargrave², R. Sudiwala², M. Haiml³, H. Hoehnemann³

¹Caeleste, Hendrik Consciencestraat 1 b, 2800 Mechelen, Belgium, ²Cardiff University. ³AIM Micro Systems GmbH
ajit.kalgi@caeleste.be

A generic radiation hard IR detector readout IC (ROIC) for cryogenic temperature operation with an array size of 320 (H) x 1080 (V) that is capable to interface with long wave (>10 μ m) to short wave (<2 μ m) IR detector focal plane arrays is implemented. It operates at over 20 fps in four shutter modes: integrate while read (IWR), integrate then read (ITR), rolling shutter (RS) and non-destructive readout (NDR) or Fowler sampling. The 20 μ m pixel contains a capacitive trans-impedance amplifier (CTIA) with 3 in-pixel sample and hold (S&H) capacitors. Programmable integration capacitors provide dual gain full well of 10ke- and 50ke- for a voltage swing of 2 V. The read noise is < 35e-, measured at room temperature. The reset and integrated signal values of the CTIA are converted to differential signals in the column-based correlated double sampling (CDS) stage. Devices are manufactured in XFAB-XS018 technology.

Introduction

An infrared imager typically consists of a detector diode array (realized in HgCdTe (MCT), GaAs etc) pixel to pixel bonded onto the ROIC (realized in silicon) through Indium bumps [1]. The detector diodes convert the incident IR radiation to proportional quantity of electrons. For a high-sensitivity at longer wavelengths, detectors are realized with narrow bandgap semiconductor materials. The narrow bandgap of the detectors results in high dark current, unless they are cooled down to cryogenic temperatures. In addition to above requirements, certain applications might require the device to be operated at extreme radiation conditions.

The above-mentioned detector characteristics requires the design of readout electronics that is compatible with cryogenic operation and is radiation hard. The cryogenic operation also implies that the chip operates with very low power consumption. In most cases this is compatible with the requirement for very long integration times [2].

The narrow bandgap of the detector requires very accurate and stable biasing. The transients on the detector bias voltage results in image artifacts which are difficult to calibrate. In that respect CTIA based pixels are superior over other topologies: the CTIA's feedback maintains an accurate and stable bias voltage on the detector [3][4], with additional measures to minimize the transients. The architecture of our CTIA enables the readout of both 'P over N' or 'N over P' detector diode types.

The yield of the non-Silicon detectors is much lower than the CMOS ROIC yield. The defect detectors could be excess dark current generation center or worse a short between their bias terminals. The defect detectors can also bloom the neighboring detectors. An in-pixel programmable switch between the bump pad and virtual ground of the CTIA allows to disconnect the defect detectors from the ROIC.

Many integration modes are available: IWR, ITR and RS. Non-destructive readout is possible as well and is often the choice in deep space astronomy where integration times are extremely long and very low read noise must be reached.

The ROIC is implemented with the specification shown in Table 1.

| | |
|--------------------------------------|--|
| Array size | 4x320 (H) X 1080 (V) |
| Pixel pitch | 20 μm |
| Integration modes | Integrate While Read (IWR) Integrate Then Read (ITR) Rolling shutter (RS) Non-Destructive Readout (NDR) |
| Radiation hardness | TID, SEU, SEL |
| Programmable Integration capacitance | 8 fF 40 fF |
| Diode compatibility | P over N N over P |
| Pixel readout rate | 20 MHz |
| Operating temperature | 40 K - 80 K |
| Technology | 0.18 μm XFAB |

Table 1: Specifications

In the following sections pixel topology, pixel noise analysis, layout for radiation hardness is discussed. Test pixels for measurements without the detectors being bonded and some measurement results are followed.

Pixel topology

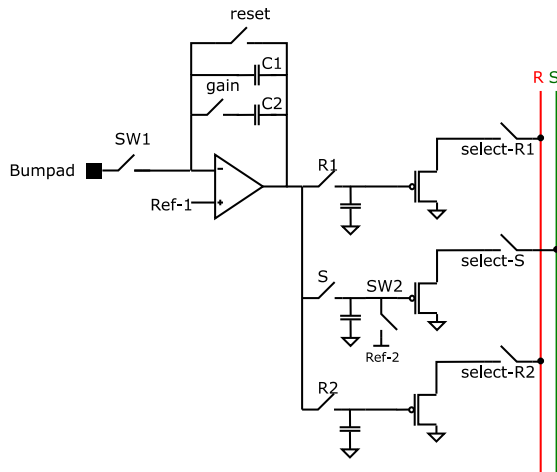


Figure 1: Schematic of pixel

Figure 1 is the schematic representation of the pixel. The detector is bonded on the bump pad and connects to the virtual ground of the amplifier through switch 'SW1'. The 8fF integration capacitor 'C1' is designed to contain 10Ke-. An additional 32fF capacitor 'C2' can be connected by programming switch 'gain'. The reset voltage of the amplifier can be sampled on capacitors connected through

switch 'R1' and 'R2'. The integrated amplifier output signal can be sampled on capacitor connected through switch 'S'. The signal sampling capacitor is discharged before sampling via switch 'SW2'.

The sampled voltages on the capacitor are buffered onto the columns through PMOS source followers.

All the switches are complementary in nature to overcome the reduced signal handling range of NMOS/PMOS only switches at cryogenic temperatures.

Pixel operation

The operation of the pixel in IWR mode is shown through the timing diagram in Figure 2. IWR mode requires the use of the pixel's all three S&H capacitors. ITR and RS operation can be achieved with only 2 S&H capacitors.

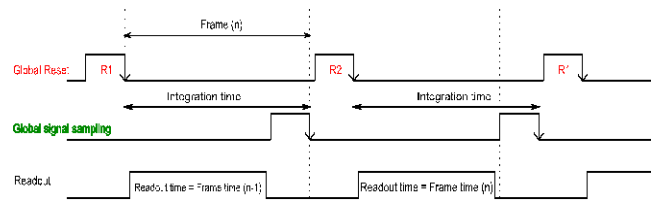


Figure 2: Timing diagram of IWR mode

The chip is globally reset and the reset level is sampled on the capacitor connected through the 'R1' switch. During the integration time, the previously sampled integrated signal is readout, shown as 'Frame time(n-1)'. After the frame readout, the signal sampling capacitor is pre-charged and the integrated voltage at the output of the amplifier is sampled. The pixel is reset again and the new reset level is sampled on the capacitor connected through switch 'R2'. The readout of the sampled frame is done while the pixels are in integration.

Similarly, the ITR and RS mode follows with usage of capacitor 'R1' and 'S'.

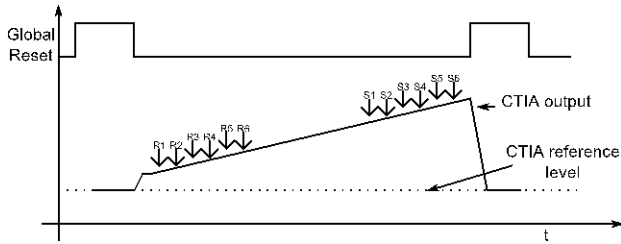


Figure 3: Non-destructive readout (NDR)

The timing of Non-destructive readout is shown in Figure 3. The sequence starts with a pixel reset. The CTIA output is read out consecutively with or without using the S&H stages. The minimum time difference between two readouts is a frame time if all the pixel rows are read. ‘n’ reset frames and ‘n’ signal frames are readout during one integration time and subsequent signal processing is done off-chip. In this mode, zero, one or all the three S&H capacitors can be connected in parallel as load to the CTIA. This reduces the bandwidth of the amplifier and impacts the total integrated noise at its output.

Noise analysis

The overall noise of the pixel shown in Figure 1 including the detector has multiple contributions, as: dark current shot noise of the detector, resistive and capacitive coupling of detector bias noise, and the noise due to ROIC. The CTIA operation noise can be separated in 2 contributions: reset noise and integration noise [5].

1) Reset noise

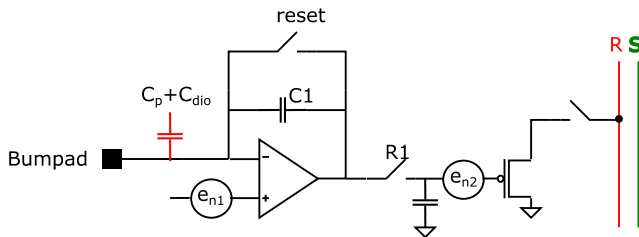


Figure 4: Simplified pixel schematic with dominant noise sources

When the reset switch and R1 are toggled, the amplifier noise (represented here as e_{n1}) is sampled on the S&H capacitance. The noise is partly flicker noise of the amplifier and partly

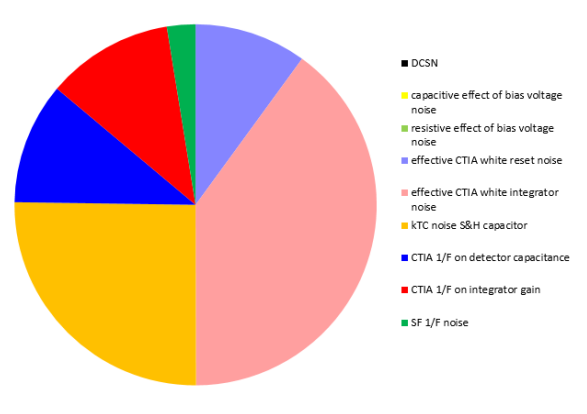
thermal noise. The noise is also sampled on the virtual ground node to an amount related to the total capacitance on that node. In practice this node capacitance is thought of as C_p (parasitic capacitance) + C_{dio} (detector capacitance). For a ROIC without detector $C_{dio} = 0$.

2) Integration noise

After integration, the signal at the output of the CTIA is sampled on the signal sampling capacitor. The noise sampled in this phase consists of the amplified noise (e_{n1}) [$gain=(C_p+C_{dio}+C_1)/C_1$] and the amplified reset noise [$gain=(C_p+C_{dio})/C_1$].

When the signal value is subtracted from reset value through the in-column CDS operator, the thermal noise components are square-summed whereas the correlated noise (sampled reset noise from virtual ground node) is cancelled.

The overall noise contributions from different sources are shown in Figure 5. The pixel noise at the detector node is about 26 e-RMS. The thermal noise component scales down with the temperature, hence the noise at cryogenic temperature is lower than room temperature. Similar calculations show that the ROIC only noise at 77K is 15 e-RMS.



| CDS Applied | | CVFout [V/e] | |
|---|----------|---------------|--------------------------|
| BREAKDOWN | | 3.11E-05 | |
| noise source | CVF | at source [V] | Eq Detecto eq Output [V] |
| DCSN | | 0.0 | 0.00E+00 |
| capacitive effect of bias voltage noise | | 0.0 | 0.00E+00 |
| resistive effect of bias voltage noise | | 0.0 | 0.00E+00 |
| effective CTIA white reset noise | 1.82E-05 | 9.31E-05 | 5.1 1.59E-04 |
| effective CTIA white integrator noise | 1.82E-05 | 3.72E-04 | 20.4 6.35E-04 |
| KTC noise S&H capacitor | 1.82E-05 | 2.35E-04 | 12.9 4.02E-04 |
| CTIA 1/F on detector capacitance | | | 5.6 1.73E-04 |
| CTIA 1/F on integrator gain | 1.82E-05 | 1.05E-04 | 5.8 1.80E-04 |
| SF 1/F noise | 1.82E-05 | 2.37E-05 | 1.3 4.06E-05 |
| total noise | | | 26.0 8.09E-04 |

Figure 5: All noise contributions, nominal operation

Pixel layout

It is known as one of the effect that when transistors are exposed to radiation, charges are trapped in the shallow trench isolation (STI) and form a channel from drain to source of the transistor underneath STI. The channel causes a leakage current between drain and source of transistor resulting in increased power consumption and loss of signals levels. The radiation damage can be mitigated by techniques like enclosed transistor layout and H-gate transistor layout [6].

The H-gate transistor layout technique is followed in the layout of this ROIC because it is compact compared to enclosed transistor of similar sizes and the layout extraction of enclosed transistor is difficult for verification.

The layout snapshot of a 2x2 pixel arrangement is shown in the Figure 6. The location of amplifier and source followers are indicated in the layout. Only the active area, poly and metal 1 are shown. The 2x2 layout of Top metal (M6) and MIM capacitors are shown in Figure 7. The MIM S&H capacitors are implemented as double MIM between M4-M5-M6 of 150 fF each.

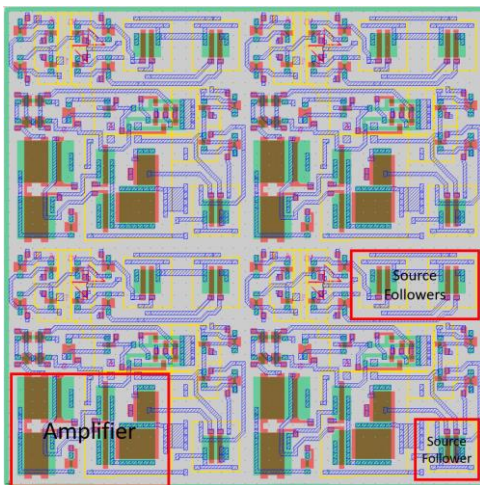


Figure 6: 2x2 pixel layout of BOL layers

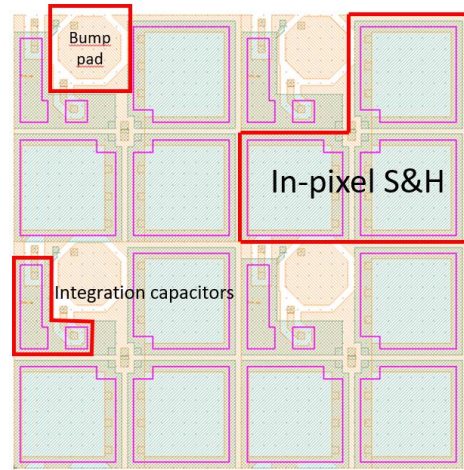


Figure 7: 2x2 layout of Top metal and MIM capacitors

Parasitic extraction

The dense pixel layout results in an unwanted coupling between different nodes of the pixels or even between neighbouring pixels [7]. It is foreseen that the coupling capacitance is less than 1% of the node capacitance. The parasitic extraction was done on a small array of 3x3 to study the coupling capacitance is shown in Figure 8.

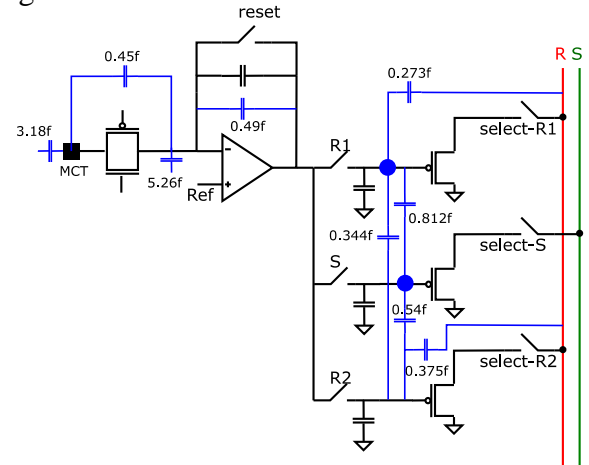


Figure 8: Extracted parasitic capacitors

The ROIC is and should be insensitive to visible light. The functionality of the pixels without detectors can only be measured by injecting a current at the detector node through a resistor or capacitor in certain test pixels as shown in Figure 9.

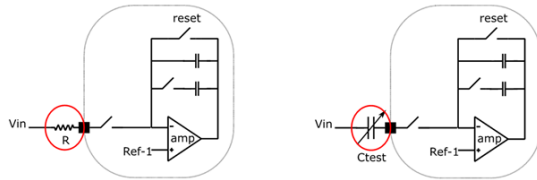


Figure 9: Test pixels

The pixels in the topmost row are test pixels and are provided with on-chip resistive and capacitive inputs.

The pixels with resistive input saturate depending on the voltage ‘ V_{in} ’ w.r.t reference voltage ‘ $Ref-1$ ’. If $V_{in} > 'Ref-1'$ then the output of amplifier saturates to VSS while it saturates to VDD if $V_{in} < 'Ref-1'$.

The pixels with capacitive input shows responses depending on the ΔV change on ‘ V_{in} ’, the value of the capacitor ‘ C_{test} ’ and integration capacitor (C_{int}).

$$\text{Output} = \Delta V * C_{test}/C_{int}$$

Measurement results

The ROIC is tested at room temperature without bonding the detectors.

1) Laser Illumination

The ROIC is light insensitive. However, due to the diodes at the source and drain of the switches at the virtual ground the ROIC is sensitive to high illumination. A laser line is shined across the sensor and images are captured. This test serves to prove the working of the peripheral and driving circuits.

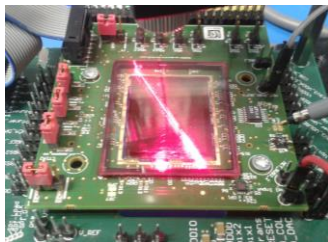


Figure 10: Test setup

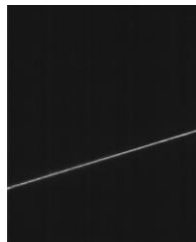


Figure 11: Captured image

2) Testpixel measurements

As described above, the pixel with capacitive input is used to measure the response of the pixels. The measurement results are shown in Figure 12. The input capacitor ‘ C_{test} ’ are designed to have 8 fF, 32 fF, 64 fF, 128 fF, 256 fF, 512 fF. The input voltage is changed in varying steps and the output is plotted. It can be seen from the plot that pixel responds linearly over the entire range.

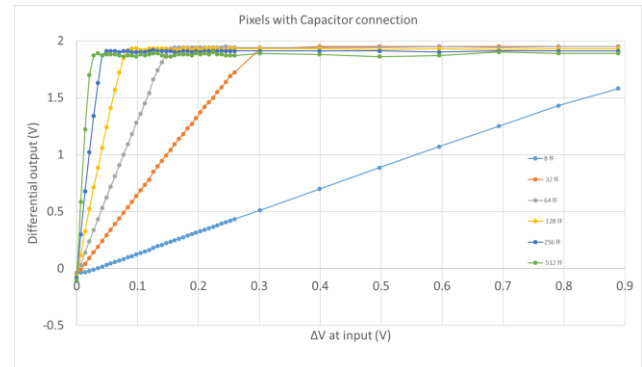


Figure 12: Capacitive input test pixels measurement

3) Noise measurement

The noise measurements of pixels always in reset and under nominal operation in ITR readout mode is shown in Figure 13. The measured noise of the pixels in reset is between 24 to $32e^{-}_{RMS}$ and under nominal operation it is between 30 to $42e^{-}_{RMS}$. It was predicted to be $26e^{-}_{RMS}$ under nominal operation. At 77K these values will drop to about $15-20e^{-}_{RMS}$.

The higher noise than the prediction is because the noise contributions from the downstream electronics (column S&H, column amplifier and output amplifier) is not considered in calculations. The useful output voltage range is 0.5V-2.5V (supply=3.6 V) at cryogenic temperature.

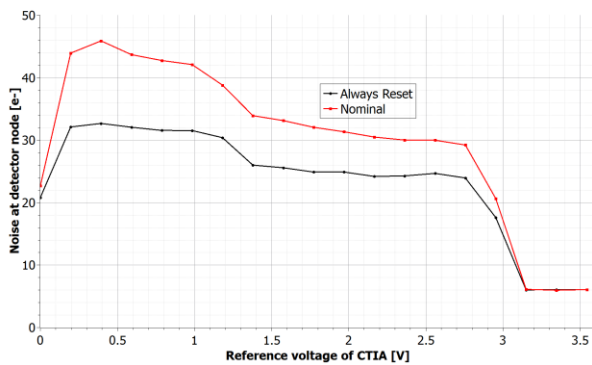


Figure 13: Noise in e- at detector node vs reference voltage

Acknowledgment

The author and all the collaborators thank European Space Agency for sponsoring the work and aiding in materialization of the concepts.

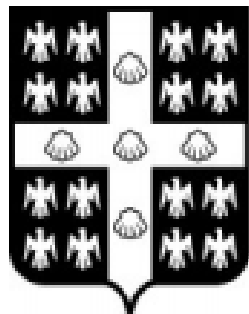
References

1. C.C. Hsieh, C.Y. Wu. "Focal plane arrays and CMOS readout techniques of Infrared imaging systems". IEEE circuits and systems for video technology, Aug 1997.
2. P. Merken, Y. Creten, J. Putzeys, T. Souverijns, C. Van Hoof. "A low noise, low power readout electronics circuit at 4 K in standard CMOS technology for PACS/Herschel". SPIE 2004.
3. F. Guellec, O. Boulade, C. Cervera, V. Moreau, O. Gravrand, J. Rothman, J-P Zanatta. "ROIC development at CEA for SWIR detectors: Pixel circuit architecture and trade-offs" ICSO 2014.
4. B. Fieque, E. Sanson, L. Martineau, P. Chorier, O. Boulade, V. Moreau. "Infrared ROIC for very low flux and very low noise applications". Sensors, systems and next generation satellites XV, Oct SPIE 2011
5. D.A. Van Blerkom. "Analysis and simulation of CTIA based pixel reset noise" SPIE 2011.
6. B. Dierickx. "Radiation hard design in CMOS image sensors". Workshop on CMOS active pixel sensors for particle tracking. CPIX 14. Bonn.
7. G. Finger, J. Beletic, R. Dorn, M. Meyer, L. Mehrgan, A.F.M. Moorwood, J. Stegmeier. "Conversion gain and interpixel capacitance of CMOS hybrid focal plane arrays". Experimental Astronomy, Vol. 19, Issue 1-3, pp. 135-147.

Environment

AITA 2017

Québec City, Canada
September 27th - 29th, 2017



UNIVERSITÉ
LAVAL

Extra-solar planet detection: review of indirect and direct methods

Marija Strojnik¹, Beethoven Bravo-Medina², Guillermo Garcia-Torales², and Michelle K. Scholl³

¹Optics Research Center, AP 1-948, CP 37000, Leon, Gto., Mexico

²Departamento de Electronica, Universidad de Guadalajara, Av. Revolucion 1500, C. P. 44840 GDL, Jalisco, Mexico

³Alenka Associates, P. O. Box 27488 Tempe, AZ 85285, USA

mstrojnik@gmail.com, msbbravom@hotmail.com

We review indirect and direct methods used in the detection of a planet outside our solar system. Within the last 20 years this research has concentrated initially on visible radiation, and then on IR. We favor placing the observatory on the far side of the Moon where the stray-light noise radiation from the Earth, near-Earth objects, and the Sun is avoided.

1. Planet detection problem

We are interested in the direct detection of a planet next to a bright star. Figure 1 illustrates the geometry for the detection of a planet outside our solar system. The Earth-/interferometer-based coordinate system is displaced from the nearby planetary system along the optical axis, Z-axis. The nearby star, Estrella, and its planet, the Tierra, emit spherical waves.

After free-space propagation, spherical waves become plane waves. They are tilted if they originate at an off-axis point, as at the Tierra [1]. Today, over 3500 planets have been detected [2]. The great majority have been discovered with indirect methods.

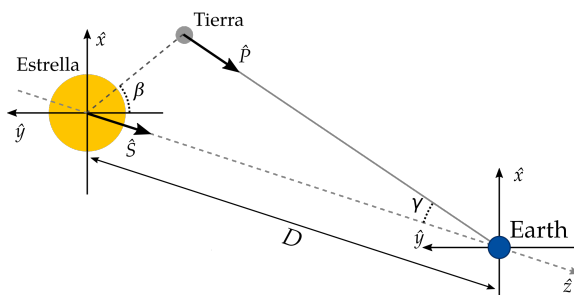


Fig. 1. Geometry for the detection of a planet outside our Solar system. The Earth-/interferometer-based coordinate system is displaced from the nearby planetary system along the optical axis, Z-axis. The nearby star, Estrella, and its planet, the Tierra, emit spherical waves. After free-space propagation, spherical waves become plane waves. They are tilted if they originate at an off-axis point, such as Tierra.

So far, only 72 planets have been discovered with direct methods.

II. Indirect techniques

The main indirect detection techniques are gravitational microlensing, transit light curves, and spectroscopic radial velocity.

The principle of gravitational micro-lensing [3, 4] is illustrated in Fig. 2. We detect a planet when a short-duration peak in the incidence modifies the spatial resolution. This technique is applicable to planets with large orbits, separated by more than 1 arcsec in angular separation from the star.

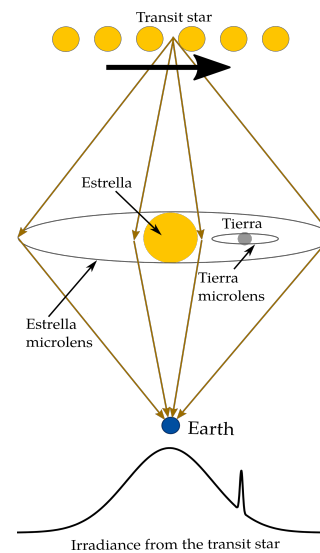


Fig. 2. In microlensing, both the star and the planet act as a microlens on the radiation emitted from the star transiting behind the planetary system. A small peak is observed due to a planet.

III. Interferometric techniques

The main interferometric techniques are narrow-angle astrometry [5–7], differential phase [8, 9], precision phase closure [9], and nulling interferometry [11–14].

The narrow angle astrometry is actually an indirect detection technique; nonetheless, it is usually included with the interferometric techniques. We measure the changes in the position of the center of mass of the Estrella-Tierra system while the Tierra orbits around the Estrella. See Fig. 3.

The displacement of the center of mass of the solar system is measured with respect to another star. The radiation from both stars is captured by the interferometer: the resultant interferogram provides information about the relative position of the Estrella with the Tierra with respect to the reference star.

The basic parameters of this method take into consideration the proper motion and the parallax of both stars. A statistically significant discrepancy in the measured information confirms the existence of a Tierra. While the Tierra orbits its Estrella, part of the time it speeds toward the Estrella and part of the time it travels directly away from it.

Correspondingly, the radiation is modified by the Doppler shift toward shorter and longer wavelengths. This is the basis of the radial velocity technique, illustrated in Fig. 4.

In the differential phase method (shown in Fig. 5), the Estrella radiation interferes with itself to generate a fringe pattern. When the Estrella radiation is reflected off the Tierra, the reflected light is incident onto the interferometer with different phase than the phase coming directly from the Estrella. The resultant fringe pattern is displaced due to phase shift. The generated phase shift is a function of wavelength, because the radiation ratio between the planet and the star depends on wavelength. Therefore, a change in the measured phase shift at several wavelengths confirms the presence of a Tierra.

The phase closure method is a variant of the differential phase method. It uses a three-aperture interferometer to obtain three differential phase measurements. It is presented in Fig. 6. The sum of three differential phases is the closure phase. This quantity is immune to the atmospheric phase delays, because three differences are taken between three optical paths through the atmosphere [15, 16].

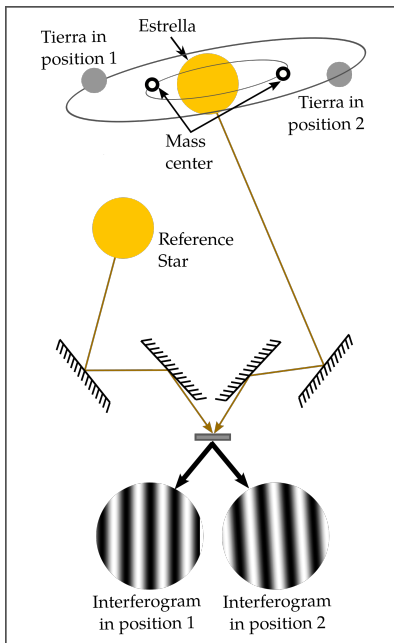


Fig. 3. Narrow angle astrometry.

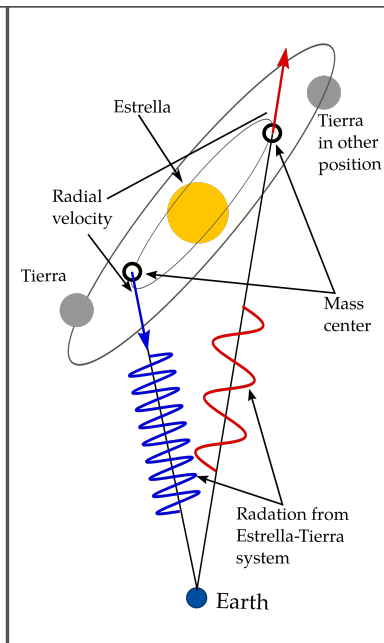


Fig. 4. Radial velocity.

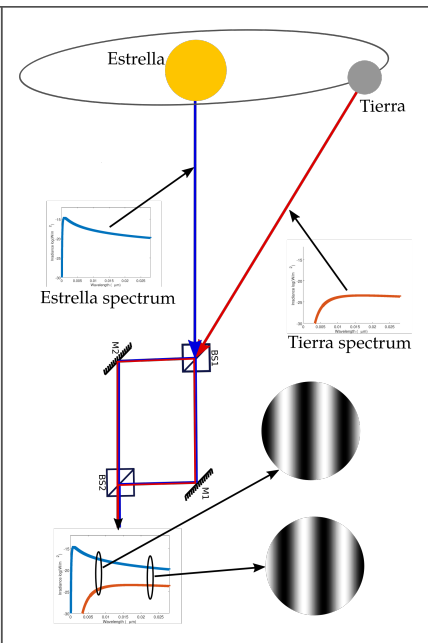


Fig. 5. Differential phase.

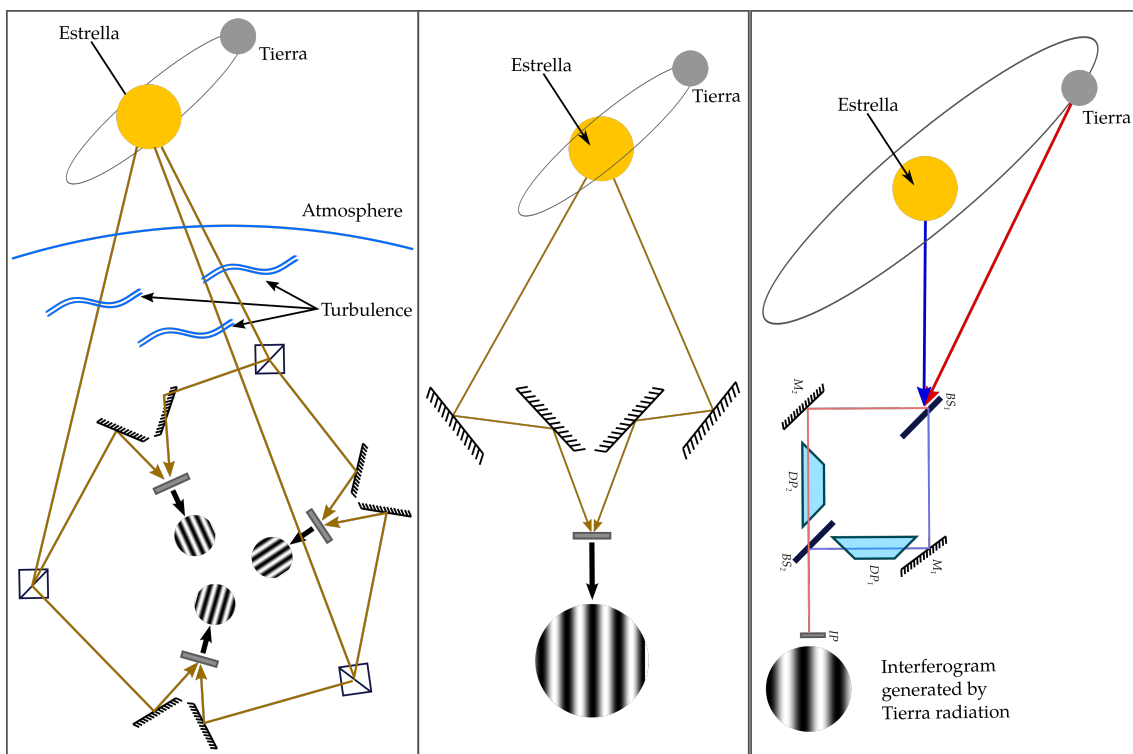


Fig. 6. Phase closure.

Fig. 7. Nulling interferometer.

Fig. 8. Rotational shearing interferometer.

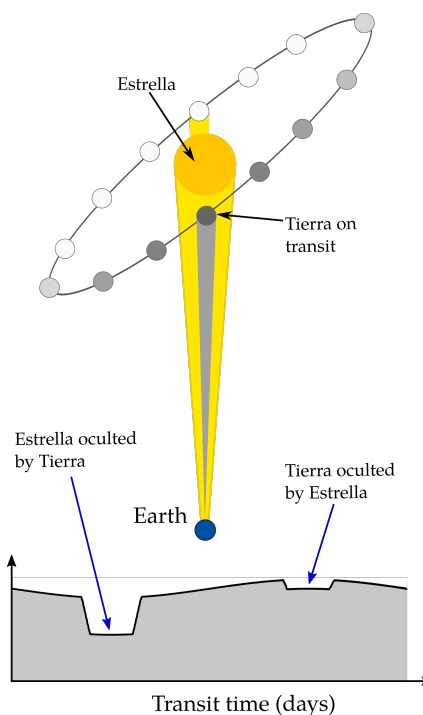


Fig. 9. Transit time.

The nulling interferometry consists of interfering the radiation from the distant solar system with itself. The Estrella radiation is suppressed by destructive interference. This results in a completely black fringe for the radiation emitted from the Estrella. The detectability of the radiation from the Tierra is enhanced.

A rotational shearing interferometer [17, 18] is used to eliminate the cylindrically-symmetric Estrella wave front. It is sensitive to the tilted Tierra wave front.

Most planets have been discovered using the method of transit time (Fig. 9). The technique that NASA is contemplating is based on a coronagraph (see Fig. 10).

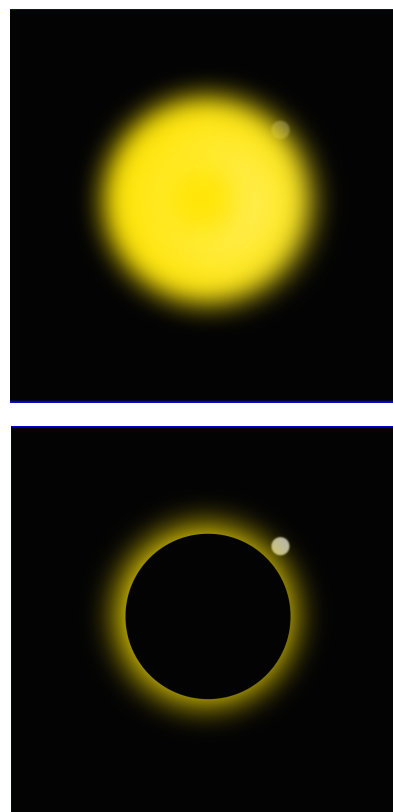


Fig. 10. Coronagraph.

5. Summary

Independently of which of the proposed concepts is eventually implemented, placing the instrument on the far side of Moon has many favorable advantages (Fig. 11). [19]

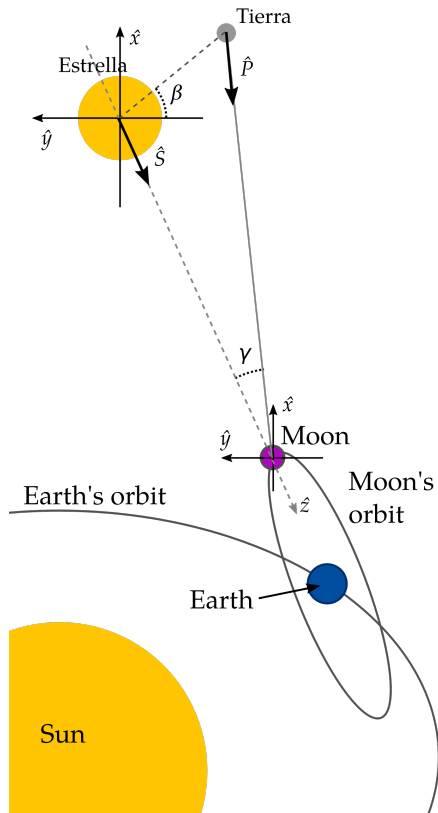


Fig. 11. Placing the planet observatory on the Moon avoids stray light noise from the Earth and near-Earth objects and eliminates Sun illumination.

References

26. M. S. Scholl, "Signal detection by an extra-solar-system planet detected by a rotating rotationally-shearing interferometer," *J. Opt. Soc. Am. A*, **13** (7), 1584- 1592 (1996); <http://dx.doi.org/10.1364/JOSAA.13.001584>.
- E. Team, "The extrasolar planets encyclopaedia," <http://exoplanet.eu/> (2016). Accessed: 2016-09-30.
- A. Gould and A. Loeb, "Discovering planetary systems through gravitational microlenses," *The Astrophysical Journal* **396**, 104–114 (1992).
- A. Bhattacharya, D. Bennett, I. Bond, T. Sumi, A. Udalski, R. Street, Y. Tsapras, F. Abe, M. Freeman, A. Fukui *et al.*, "Discovery of a gas giant planet in microlensing event ogle-2014-blg-1760," arXiv preprint arXiv:1603.05677 (2016).
- M. Shao and M. M. Colavita, "Potential of long-baseline infrared interferometry for narrow-angle astrometry," *Astronomy and Astrophysics* **262**, 353–358 (1992).
- A. Sozzetti, S. Casertano, R. A. Brown, and M. G. Lattanzi, "Narrowangle astrometry with the space interferometry mission. The search for extrasolar planets. I. detection and characterization of single planets," *Publications of the Astronomical Society of the Pacific* **114**, 1173–1196 (2002).
- B. F. Lane and M. W. Muterspaugh, "Differential astrometry of subarcsecond scale binaries at the palomar testbed interferometer," *The Astrophysical Journal* **601**, 1129 (2004).
- B. Lopez and R. G. Petrov, "Direct detection of hot extrasolar planets using differential interferometry," in "From Extrasolar Planets to Cosmology: The VLT Opening Symposium," (Springer, 2000), pp. 565–570.
- R. L. Akeson, M. R. Swain, and M. M. Colavita, "Differential phase technique with the keck interferometer," *Proc. SPIE* **4006**, 321–327 (2000).
- M. Zhao, J. D. Monnier, X. Che, E. Pedretti, and N. Thureau, "Toward direct detection of hot jupiters with precision closure phase," in "Resolving The Future Of Astronomy With Long-Baseline Interferometry," , vol. 487 (2014), vol. 487, p. 185.
- P. M. Hinz, J. R. P. Angel, W. F. Hoffmann, D. W. McCarthy, P. C. McGuire, M. Cheselka, J. L. Hora, and N. J. Woolf, "Imaging circumstellar environments with a nulling interferometer," *Nature* **395**, 251–253 (1998).
- M. P. Cagigal and V. F. Canales, "Exoplanet detection using a nulling interferometer," *Opt. Express* **9**, 36–41 (2001).
- R. Errmann, S. Minardi, L. Labadie, B. Muthusubramanian, F. Dreisow, S. Nolte, and T. Pertsch, "Interferometric nulling of four channels with integrated optics," *Appl. Opt.* **54**, 7449–7454 (2015).
- S. Martin, A. Booth, K. Liewer, N. Raouf, F. Loya, and H. Tang, "High performance testbed for four-beam infrared interferometric nulling and exoplanet detection," *Appl. Opt.* **51**, 3907–3921 (2012).
- E. Ribak, "Phase closure with a rotational shear interferometer," *Appl. Opt.* **26**, 197–199 (1987).
- G. Shoulga and E. N. Ribak, "Toward spectral intensity interferometry," *Appl. Opt.* **56**, A23–A30 (2017).
- M. S. Scholl, "Cancellation of star light generated by a nearby star–planet system upon detection with a rotationally-shearing interferometer," *Infrared Physics & Technology* **40**, 357 – 365 (1999).
- M. Strojnik and G. Paez, "Infrared detection of a planet next to a bright star," *Infrared Physics & Technology* **49**, 312 – 316 (2007).
- M. Strojnik and M. K. Scholl, "Extrasolar planet observatory on the far side of the Moon," *J. Appl. Remote Sens.*, **8** (1), 084982 (2014). doi:10.1117/1.JRS.8.084982.

PRESSURE CHARACTERIZATION AND RESOLUTION LIMITS' INVESTIGATION OF HIGH ACCURACY NDIR METHANE SENSOR FOR ENVIRONMENTAL APPLICATIONS.

B. Gaynullin¹, M. Bryzgalov², C. Hummelgård³, C. Mattsson⁴, H. Rödjegård⁵, G. Thungström⁶

¹ SenseAir AB, Stationsgatan 12, 82060 Delsbo, Sweden bakhram.gaynullin@senseair.com

² SenseAir AB, Stationsgatan 12, 82060 Delsbo, Sweden maksym.bryzgalov@senseair.com

³ SenseAir AB, Stationsgatan 12, 82060 Delsbo, Sweden christine.hummelgard@senseair.com

⁴ MIUN, Holmgatan10, 85170 Sundsvall, Sweden claes.mattsson@miun.se

⁵ SenseAir AB, Stationsgatan 12, 82060 Delsbo, Sweden henrik.rodjegard@senseair.com

⁶ MIUN, Holmgatan10, 85170 Sundsvall, Sweden goran.thungstrom@miun.se

This paper presents characterization of a methane gas sensor. A lab test system for precise control of the environment has been used. It is designed for studying performance of Non Dispersive Infra-Red (NDIR) gas sensors and for investigation of pressure dependence in accuracy demanding applications. The test system described here consists of a hardware test bench, a LabVIEW based software and a calculation algorithm. The lab test-bench provides a highly accurate and stable test environment for characterization. From the data accurate compensation parameters for each specific NDIR sensors can be derived.

Introduction

The progress within Non Dispersive Infra-Red (NDIR) technology has provided relatively low-cost gas sensors with high sensitivity and sub-ppm resolution. The combination of reasonable cost and high sensitivity makes them attractive for implementation in applications where there is a significant demand for large numbers of sensing units such as in environmental research, detailed air quality monitoring, vertical atmosphere concentration profiling, leakage detection, etc. [1].

The development process for such high accuracy sensors includes comprehensive procedures for characterization of sensor performance. One of the most important components of a test procedure is the creation of precisely controlled environments protected from disturbances in the surrounding atmosphere such as gas pressure, humidity and the sensor's targeted gases.

A distinctive feature of the NDIR sensing principle, employing Lambert-Beer law [2]

(fig.1), is the dependence between gas media transmittance and pressure. Variations in measured concentrations due to even small changes of ambient pressure might cause measurement errors exceeding the accuracy requirements.

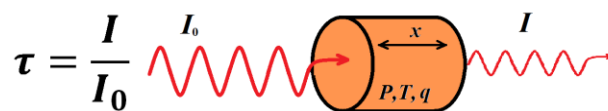


Fig. 1. Graphic representation of Lambert-Beer's law.

Background

The methane sensor is based on the HPP family (High Performance Platform) from SenseAir AB. It is a non-dispersive infra-red sensor operating at 3.5 μm wavelength [3]. The optical path length is 96 cm obtained by 16 passes in 6 cm long White cell [4]. Hence, high resolution is obtained in a small and compact cuvette with a total internal volume of 35 cm³. The optics, including the reflective lenses, is fabricated using plastic molding with integrated thermal

stabilization for low production cost and high performance.

The pressure characterization of CO₂ sensors based on the same HPP platform is described in [5]. Studies of the stability performance and the pressure characterization of the methane sensors include important features which distinguish it from CO₂ sensors:

1. Significantly lower relative absorption of light in the methane spectrum, due to the narrow and widely separated absorption peaks. And hence a higher sensitivity to disturbance from pressure variation, mechanical instabilities and interfering gases.
2. Overlap of methane and water vapor spectra puts stronger requirements for dehumidification of the test environment in order to avoid measurement drift during evaluation.

Test system and methods.

The lab test system consists of a hardware lab test bench (Fig.2), supporting software (developed in LabVIEW) and calculation algorithms.

In order to achieve a reliable and stable environment, the following needs must be ensured:

- Absolute elimination of contaminating leakages from ambient air. For the calculation of the pressure compensation coefficients measurements should be performed in a pressure range from 0.5 up to 1.2 Bar. If the target gas is present in the surrounding air also a minor leakage, or reverse flow, may cause a significant error in the measured gas

concentration.

- Protection against concentration variations due to gas and/or water molecules adsorbed and released from the internal surfaces of the test volume. A closed volume with reduced pressure easily causes detaching of residual molecules which in turn influence the true gas concentration.
- Stable pressure with a tolerance of less than 1 mBar, or 0.1 % of 1.013 Bar.
- Stable temperature with a tolerance of less than 0.5 K of the gas test environment, including elimination of temperature rise due to self-heating.

To the authors' knowledge, there is no cost-efficient sealing method with perfect protection against leakages driven by the pressure difference between the surrounding air (close to 1 Bar) and environment in test volume. For instance, contaminating leakages easily penetrate through wires and cable insulation passing into test volume.

Here, leakage protection is implemented using the physics principle – negative pressure drop – which eliminates the problem in an efficient way. Test bench consists of two volumes – test volume inside a protection volume. Pumping out the gas from the protection volume always maintains a pressure inside the protection volume that is lower than the pressure in the test volume (P3 is lower than P4 in Fig. 2). It is also important to cut-open, and ventilates, all cable insulation within the protective volume in order to avoid unexpected tubing from the outside air to the test volume.

The second issue was solved by implementation

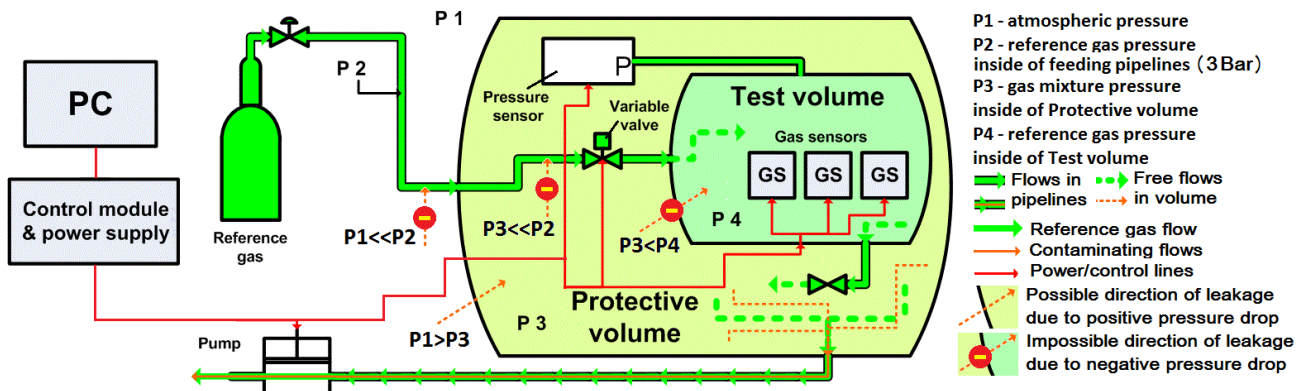


Fig. 2. Pressure characterization lab test bench.

of a reference gas flow (1 liter per minute). Constant flushing of the test volume removes contaminating residues from test objects and internal surfaces.

A control algorithm, based on Fuzzy logic, controls a variable valve and a pump. This maintains a stable pressure with deviation less than 0.2 mBar, while simultaneously flushing reference gas through the system.

Tests and results

Pressure characterization of a sensor first requires a preliminary evaluation of the stability performance. Sensors are susceptible to drift due to internal as well as external factors. Stability performance tests allow discovering and characterization of drift factors and estimation of stability periods within predefined limits.

For evaluation of the stability performance, long term logging in dry nitrogen was performed. First, the test volume was flushed with nitrogen. When the visible drift became negligible a zero calibration procedure was performed. The sensors were thereafter left for 28 hours in test volume with stabilized

temperature, pressure (± 0.2 mBar) and a constant flow of dry nitrogen.

The concentration graph (Fig. 3) has two distinguishable sections in the logged data – “drifting” and “stable”. Due to high sensitivity of the methane sensor to water vapor molecules it is possible to conclude that the measured concentration was fully stabilized first when the test volume was properly cleaned from residual water and hydrocarbon molecules.

The contaminating molecules causing the drift after the initial flushing were most likely released from surfaces inside the test volume.

The test result shows that the stability performance of the sensors itself is high enough for environmental studies, but can only be verified in a highly accurate environment.

Allan deviation is derived using data from the stable part of the logging, allowing evaluation of possible limits of the sensor’s resolution (Fig. 4).

The theoretical resolution limit obtained from these graphs, for this sensor design, may reach as low as 50 ppb.

Pressure characterization tests were performed in gases with mole fractions of 50, 250 and 500 ppm.

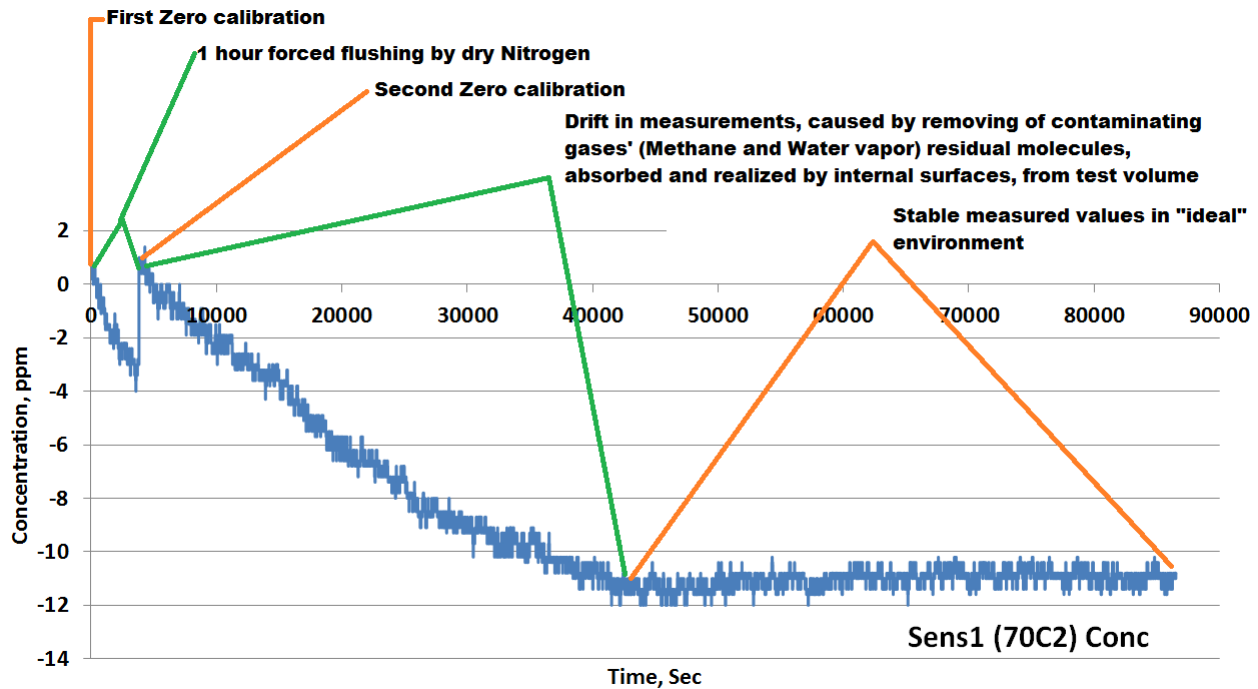


Fig. 3. Test of stability performance.

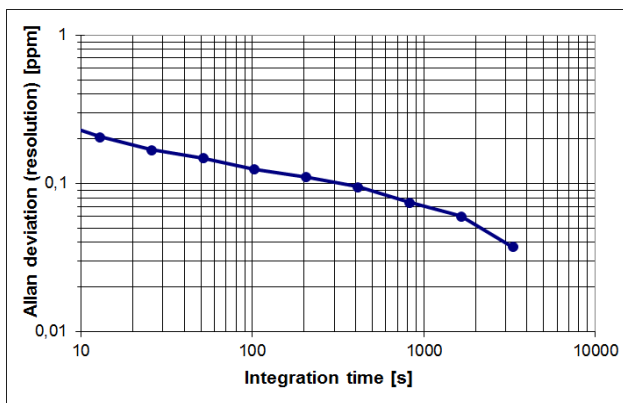


Fig. 4. Allan deviation plot is showing methane sensor resolution at different integration intervals.

Pressure was varied and stabilized in steps between 0.5 and 1.2 Bars and the measured concentration was recorded at each step (Fig. 5). Here, the reference concentration was 250 ppm.

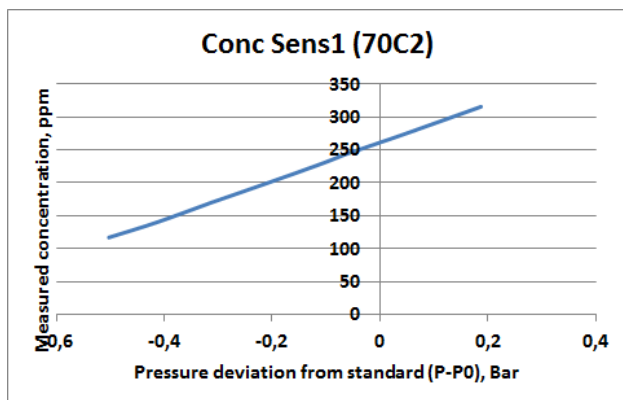


Fig. 5. Measured value using 250 ppm gas concentration vs pressure deviation from standard value.

Pressure dependence derivation

Pressure dependence is illustrated in Fig. 6 and represented in the form:

$$\frac{M_{Conc}}{T_{Conc}} = 1 + A \left(\frac{P - P_0}{P_0} \right) + B \left(\frac{P - P_0}{P_0} \right)^2 + C \left(\frac{P - P_0}{P_0} \right)^3 \quad (1)$$

M_{Conc} – measured molar fraction under variable pressure.

T_{Conc} – true molar fraction value, under standard pressure 1.013 Bar

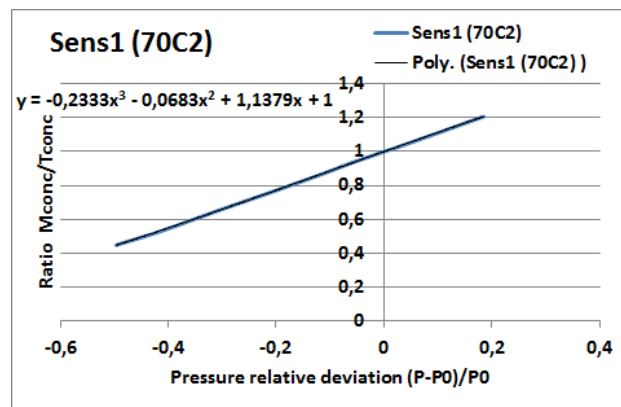


Fig. 6. Methane pressure dependence.

Conclusion

A test system used for studying of sensor stability performance and pressure characterization has been developed and characterized. The system is able to provide an accurate and controllable environment, necessary for evaluation of high accuracy NDIR gas sensors.

In each reproduced environment, the sensors show stable measurement results. Analysis based on the stable data performed by Allan variance approach, allows for determination of theoretical limits for the sensor resolution.

The pressure characterization allows obtaining data for derivation of accurate pressure compensation parameters for normalization of measured data to standard pressure level.

References

1. B. B. Stephens, N. L. Miles, S. J. Richardson, A. S. Watl, and K. J. Davis, "Atmospheric CO2 monitoring with single-cell NDIR-based analyzers", Atmos. Meas. Tech., 4, 2737–2748, 2011
2. <http://www.spectralcalc.com/info/CalculatingSpectra.pdf>
3. C. Hummelgård et al. Low-Cost NDIR based Sensor Platform for sub-ppm Gas Detection Urban Climate 14 (2015) 342-350
4. White, J., 1942. Long optical paths of large aperture. J. Opt. Soc. Amer. 32, 285–288
5. B. Gaynullin et al., "A practical solution for accurate studies of NDIR gas sensor pressure dependence.", IEEE Sensors 2016, Orlando, Florida, Oct. 30 – Nov 3, 2016.

THREE-DIMENSIONAL INFRARED-VISIBLE FRAMEWORK FOR WILDLAND FIRES

M. A. Akhloufi¹, T. Toulouse², L. Rossi², X. Maldague³

¹ Computer Science Department, University of Moncton, Moncton, NB, Canada,
moulay.akhloufi@umoncton.ca

² UMR CNRS 6134 SPE, University of Corsica, France, {toulouse, lrossi}@univ-corse.fr

³ Elect. Comp. Eng., Laval University, Quebec, QC, Canada, xavier.maldague@gel.ulaval.ca

This paper proposes a new three-dimensional infrared-visible framework for wildland and forest fires monitoring and study. The system uses both near infrared and visible spectrum to efficiently segment the fire front and extract its three-dimensional representation. The obtained model can be used in computing important geometrical characteristics that can be useful in the fire propagation models. The proposed framework, uses multiple systems to capture complementary viewpoints of the fire front and register them in a common reference frame using multisensory fusion techniques based on GNSS and IMU data. These last data serve in an inter-stereo calibration procedure that estimate the relative position and orientation of each stereovision system. The results show the efficiency of the proposed system for wildland fires research and firefighting decision support in operational scenarios.

Introduction

Forest and wildland fires represent a major risk worldwide, with an estimated 350 million hectares affected by fires every year [1], resulting in wood loss and other indirect effects such as landslides, desertification, air pollution, destruction of homes and deaths [2-3]. With the climate change and global warming, experts expect an increase in the frequency and size of fires [4-6].

Image processing and computer vision for fire study, has attracted an increasing interest over the last decade. Many techniques were proposed for fire detection, fire segmentation, and the extraction of fire front properties such as position, rate of spread, fire height, fire length, fire inclination angle, fire base width, fire apparent surface and volume [7-10].

Most of the algorithms for fire detection and segmentation use visible spectrum images. In the presence of smoke, the segmentation in the visible spectrum is limited. To overcome this limitation, infrared images can be used [11-15]. However, since the fire has non-uniform

emissions in different spectral bands, the resulting fire area varies depending on the infrared spectral band used during the image capture [11, 16]. This make it difficult to use infrared images alone for fire segmentation when we want to extract measurements from the fire front.

In this paper, we propose a new three-dimensional multimodal stereovision system based on the use of both visible and near infrared spectrum to efficiently segment the fire area and extract the geometrical fire characteristics. The proposed framework, permits the use of multiple multimodal stereovision systems to monitor wildland and forest fires and register them using multisensory fusion (infrared-visual images, GPS, IMU).

Three-dimensional infrared-visible system

The three-dimensional multimodal infrared-visible system is a stereovision system built using two multispectral near infrared-visible cameras. The cameras used are two AD-080GE from JAI [17], a prism based 2CCD multi-spectral (2-channels), that captures the light coming from the scene and split it into two

signals that simultaneously hit the visible and near infrared sensors of the camera. The spectral response of the near infrared sensor shows a peak response around a wavelength of 800nm [17]. The cameras are equipped with a 6mm lens.

The cameras are fixed on a 1m baseline axis (green arrows in figure 1). The cameras are simultaneously triggered for image capture using a radio signal (receptor antenna is shown with the blue arrow in figure 1). In field experiments, the position of the left camera is registered using a centimeter precision GNSS (Leica Viva CS10 [18]). An IMU, for three-dimensional orientation measurements, is fixed on top of the left camera (circled in red in figure 1). In order to reduce possible errors, the IMU and GNSS (GPS) data are averaged over two minutes and used for the 3D points registration.

To calibrate the stereovision and extract the intrinsic and extrinsic parameters an iterative refinement method was used [19]. A 1×1m checker grid is used to calibrate each stereovision system in the field. The calibration parameters permit the extraction of three-dimensional coordinates of feature points extracted from the segmented fire images.



Fig. 1. 3D infrared-visible stereo system

The registration and processing framework

Multiple multimodal infrared-visible stereovision systems can be used for wildland and forest fires monitoring. These systems permit the extraction of a three-dimensional fire front shape. The resulting three-dimensional data can be registered using the proposed framework given by figure 2. Two multimodal systems are used in our experiments. They can be deployed at different positions and capture complementary views of the fire.

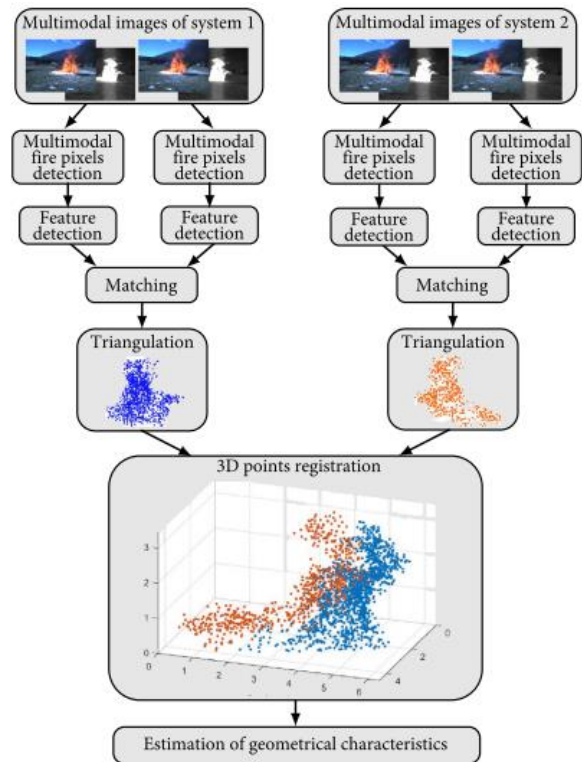


Fig. 2. The multimodal registration framework.

The first step of the proposed framework is a multimodal fire pixels detection (figure 3). This step is important for the accuracy of the following steps. The fire detection is performed in the visible and near-infrared spectrum. For each multimodal image, the probability of a pixel to be considered as fire is computed as the mean of the probabilities in the near-infrared (NIR) and the visible spectrum. The probability in the NIR spectrum is given by:

$$p_{nir}(i) = \begin{cases} \frac{i-t}{2t} + \frac{1}{2} & \text{if } i \leq t \\ \frac{i-t}{2(255-t)} + \frac{1}{2} & \text{otherwise} \end{cases} \quad (1)$$

Where i is the intensity of the pixel, and t the threshold defined by:

$$t = \begin{cases} \mu + 2\sigma & \text{if } \mu + 2\sigma \leq 255 \\ 255 & \text{otherwise} \end{cases} \quad (2)$$

μ and σ respectively the mean and standard deviation of the near-infrared image intensities. The probability $p_{vis}(rgb)$ of the visible spectrum pixel is computed for the pixels labeled as fire using the near-infrared probability above. This probability is based on

the color histogram approach proposed by Philips *et al.* [20]. The pixels having an average infrared-visible probability above 0.5 are considered as fire pixels.

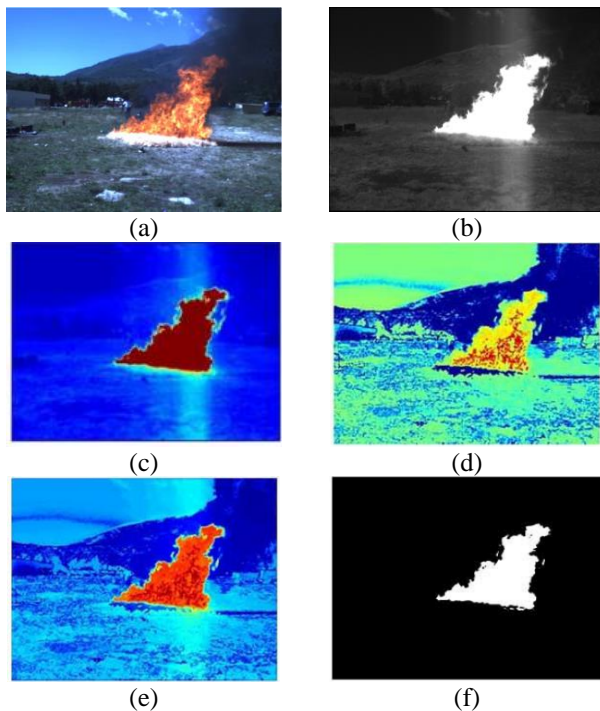


Fig. 3. Multimodal fire pixel detection: (a) Visual spectrum image, (b) near infrared image, (c) $p_{nir}(i)$, (d) $p_{vis}(rgb)$, (e) multimodal average probability, (f) fire pixel labeling

This step is followed by features detection to select the most important points to be used in the stereo matching procedure. The feature detection and the matching procedures are performed in the visible spectrum. In this work, we use a multi-scale oriented patch feature detection approach proposed in [21]. This approach uses an intensity normalized rotationally invariant 8×8 patch to extract salient features.

The stereo matching is performed using ZNSSD correlation measure in stereo rectified images [22] (figure 4).

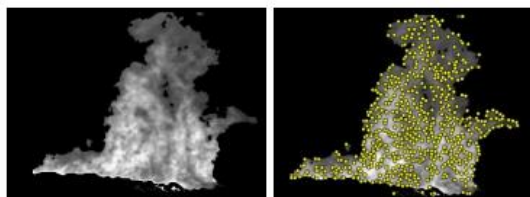


Fig. 4. Example of the result of feature extraction and matching (in yellow the matched points)

The stereo matched points with the calibration data permit the extraction of their three-dimensional coordinates by triangulation [23]. The extracted 3D coordinates are relative to the coordinate system of the left camera. Figure 5 shows the result of a rendered 3D reconstruction of the fire front.

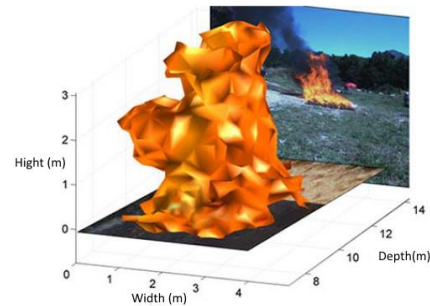


Fig. 5. 3D reconstruction of the fire front

The final step is the registration of 3D images captured by the different infrared-visible stereovision systems (figure 6). Each 3D computed fire points are projected into a common reference using an offline inter-stereo calibration procedure that estimate the relative position and orientation of each stereovision system. This inter-stereo calibration estimates the three-dimensional projection matrix based on the GNSS position and IMU orientation data of the stereo system.

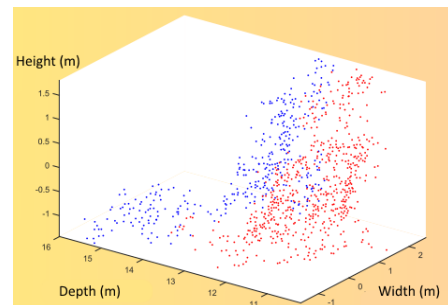


Fig. 6. Registration of 3D fire points captured by two multimodal stereo systems (bleu and red)

Since the fire is a chaotic phenomenon and there is no available tool to measure precisely the fire characteristics, we decided to evaluate the performance of the proposed system using a rigid object with known dimensions. A utility car on which black marks were glued was used for this evaluation. The three-dimensional reconstruction of the vehicle gives an error lower than 5%, which is more than satisfactory for a system designed for forest fires research.

Conclusion

In this work, we propose a new three-dimensional infrared-visible stereovision system for wildland and forest fires monitoring and study. The proposed multimodal system is robust to the presence of smoke and permits the segmentation and extraction of 3D coordinates of fire data. A new multispectral segmentation technique is presented. The proposed framework, uses multiple systems to capture complementary viewpoints of the fire front and register them in a common reference frame. Multisensory fusion based on GNSS and IMU data is used in an inter-stereo calibration procedure that estimate the relative position and orientation of each stereovision system for this purpose.

References

1. B.M. Wotton, C. A. Nock, and M. D. Flannigan. Forest fire occurrence and climate change in Canada. *International Journal of Wildland Fire*, 19(3):253–271, 2010.
2. J.G. Quintiere. *Principles of fire behavior*. Cengage Learning, 1998.
3. F. Raga. The Chilean Forestry Sector and associated risks, Trébol, XIV n.51, Mapfre 2009, <http://www.mapfre.com/mapfrere/docs/html/revistas/trébol/n51/articulo2En.html>, visited May 2017.
4. M. Finneran, "Wildfires: A Symptom of Climate Change". NASA Langley Research Center, <https://www.nasa.gov/topics/earth/features/wildfires.html>, visited May 2017.
5. M.A. Moritz, M.A. Parisian, E. Batillori, M.A. Krawchuk, J. Van Dorn, D.J. Ganz and K. Hayhoe, "Climate change and disruptions to global fire activity". *Ecosphere*, Vol. 3, no. 6, Art. 49, p. 11, June 2012.
6. E. Ferris, "The Hazard of Wildfires". April 19, 2013, <https://www.brookings.edu/blog/up-front/2013/04/19/the-hazard-of-wildfires/>, visited May 2017.
7. N. Cheney, J. Gould. Fire growth in grassland fuels. *International Journal of Wildland Fire* 5(4), 237–247, 1995.
8. N. Cheney, J. Gould, W. Catchpole. The influence of fuel, weather and fire shape variables on fire-spread in grasslands. *International Journal of Wildland Fire* 3(1), 31–44, 1993.
9. J.F. Sacadura. Radiative heat transfer in fire safety science. *Journal of Quantitative Spectroscopy and Radiative Transfer* 93(1), 5–24, 2005.
10. R. Viskanta. Overview of some radiative transfer issues in simulation of unwanted fires. *International Journal of Thermal Sciences* 47(12), 1563–1570, 2008.
11. B. Gouverneur, S. Verstockt, E. Pauwels, J. Han, P.M. de Zeeuw, J. Vermeiren. Archeological treasures protection based on early forest wildfire multi-band imaging detection system. In: *SPIE Security+ Defence*, pp.85,410J–85,410J. International Society for Optics and Photonics, 2012.
12. J.R. Martinez-de Dios, A. Ollero. Wavelet applications to forest-fire monitoring and measurement. In: *Proceedings of the 5th Biannual World Automation Congress*, vol. 13, pp. 221–226. IEEE, 2002.
13. J.R. Martinez-de Dios, L. Merino, F. Caballero, A. Ollero. Automatic forest-fire measuring using ground stations and unmanned aerial systems. *Sensors* 11(6), 6328–6353, 2011.
14. J.R. Martinez-de Dios, L. Merino, A. Ollero. Fire detection using autonomous aerial vehicles with infrared and visual cameras. In: *Proceedings of the 16th IFAC World Congress*, 2005.
15. S. Verstockt, A. Vanoosthuysse, S. Van Hoecke, P. Lambert, R. Van de Walle. Multi-sensor fire detection by fusing visual and non-visual flame features. In: *Image and Signal Processing*, vol. 6134, pp. 333–341. Springer, 2010.
16. Y. Billaud, P. Boulet, Y. Pizzo, G. Parent, Z. Acem, A. Kaiss, A. Collin, B. Porterie. Determination of woody fuel flame properties by means of emission spectroscopy using a genetic algorithm. *Combustion Science and Technology* 185(4), 579–599, 2013.
17. JAI AD-080GE. <http://www.jai.com/en/products/ad-080ge>, visited May 2017.
18. Leica Viva CS10. <http://leica-geosystems.com/products/gnss-systems/carnets-de-terrain/leica-viva-cs15-and-cs10>, visited May 2017.
19. A. Datta, J.S. Kim, T. Kanade. Accurate camera calibration using iterative refinement of control points. In: *IEEE 12th International Conference on Computer Vision Workshops*, pp. 1201–1208. IEEE, 2009.
20. W. Phillips III, N. Shah, N. da Vitoria Lobo. Flame recognition in video. *Pattern recognition Letters* 23(1), pp. 319–327, 2002.
21. M. Brown, R. Szeliski, S. Winder. Multi-image matching using multi-scale oriented patches. In: *IEEE Computer Society Conference on Computer Vision and Pattern Recognition*, vol. 1, pp. 510–517. IEEE, 2005.
22. E. Trucco, A. Verri. *Introductory techniques for 3-D computer vision*, vol. 93. Prentice Hall Englewood Cliffs, 1998.
23. R. Hartley, A. Zisserman. *Multiple view geometry in computer vision*. Cambridge university press, 2003.

IGRINS: Design, Performance and Plan for the Gemini Telescope

S. Lee¹, C. Park¹, J. S. Oh¹, I. Yuk¹, J. Lee¹, M. Chun¹, K. Kim¹, H. Oh¹, U. Jeong¹, N. Hwang¹,
B.-G. Park¹, H. Lee², G. N. Mace², K. R. Sokal², L. Prato³, D. T. Jaffe²

¹ Korea Astronomy and Space Science Institute, 61-1 Hwaam-dong, Daejeon 305-348, South Korea, leesh@kasi.re.kr, chanpark@kasi.re.kr, ojs001@kasi.re.kr, yukis@kasi.re.kr, leejjoon@kasi.re.kr, mychun@kasi.re.kr, kmkim@kasi.re.kr, hyoh@kasi.re.kr, uij@kasi.re.kr, nhwang@kasi.re.kr, bgpark@kasi.re.kr

² Department of Astronomy and McDonald Observatory, University of Texas at Austin, 2515 Speedway, Austin, TX 78712-1205, USA, lee@astro.as.utexas.edu, gmace@astro.as.utexas.edu, ksokal@utexas.edu, dtj@astro.as.utexas.edu

³ Lowell Observatory, 1400 West Mars Hill Road, Flagstaff, AZ 86001, USA, lprato@lowell.edu

The Immersion GRating INfrared Spectrometer (IGRINS) is the first astronomical spectrograph that uses a silicon immersion grating. IGRINS fully covers the H and K band atmospheric transmission windows in a single exposure. It is a compact (0.96m x 0.6m x 0.38m) high-resolution cross-dispersed spectrometer whose resolving power R is 45,000. On the 2.7 m Harlan J. Smith telescope at the McDonald Observatory, the plate scale is 0.27"/pixel on a 2048 x 2048 pixel HAWAII-2RG detector. Since its commissioning in 2014, IGRINS has been fully optimized and its performance has been successfully proven at the McDonald Observatory. Recently, IGRINS has been invited to the 4.3m Discovery Channel Telescope at Lowell Observatory in 2016 and 2017, and is now being prepared for a visit to the 8.1m Gemini South Telescope in April 2018.

Introduction

Immersion gratings break the size-resolving power curve for spectrograph designs [1,2,3,4]. An immersion grating of a given size made from Si has the same resolving-power slit-width product as a front-surface grating that is 3.4 times larger. Use of immersion gratings can therefore reduce cryogenic instrument volumes by an order of magnitude or more for a given resolving power and slit size. Lithographically produced Si immersion gratings also make it possible to have instrument designs with continuous wavelength coverage at high resolving power [5,6]. The lithographic gratings have superbly blazed grooves that give them high efficiency in high orders and the process permits coarse enough rulings to allow entire orders to fit onto a single detector.

IGRINS, the Immersion GRating INfrared Spectrometer, is a joint project of the Korea Astronomy and Space Science Institute (KASI) and the University of Texas (UT) at Austin. It has a resolving power $R=45,000$ and covers all wavelengths between 1.4 and 2.5 microns where the atmosphere transmits with ~ 3.5 pixel sampling of the spectral resolution elements. The instrument has a fixed format and no moving parts within the spectrograph. We describe the instrument design and present performance results from the commissioning runs on the 2.7m Harlan J. Smith telescope at McDonald Observatory [7].

IGRINS on the 2.7m telescope is nearly as sensitive as CRIRES at the 8m Very Large Telescope while IGRINS has more than 30 times the spectral grasp of CRIRES in a single exposure. Proven for its excellent performance,

IGRINS has been invited to the 4.3m Discovery Channel Telescope at Lowell Observatory from September 2016 to February 2017, and to the 8.1m Gemini South Telescope in April 2018. In this paper, we also introduce our recent preparation for the visit to the Gemini Observatory.

Instrument Overview

The IGRINS optical system is designed to cover as large a simultaneous wavelength range as possible while maintaining a spectral resolving power of 45,000. Fig. 1 shows the IGRINS optical design layout.

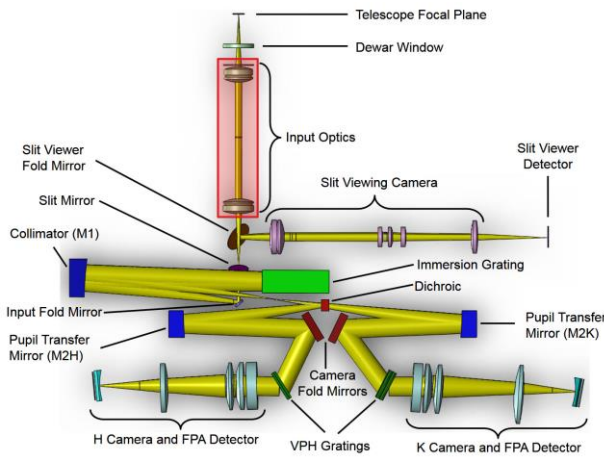


Fig. 1. IGRINS optical design layout.

Apart from the warm calibration system, all of IGRINS resides within a custom-designed, compact (longest dimension < 1 m), cryostat. The cryostat optical bench is an 880 x 520 mm rectangular plate. Fig. 2 displays the optical bench with the components in place. The bench surface was fabricated with high precision (flatness of 13 μm peak to valley). All the optical elements were positioned by locating pins and the compensators have their positions adjustable by using a set of bumpers and shoulder screws.

Based on the detector dark noise requirement, we set the operating temperature to 130 K for the optics and their mounts and to 65 K for the three detectors. Instead of liquid cryogenes, we use a closed-cycled mechanical cooler, a CTI M-1050 two-stage refrigerator system. If the immersion grating temperature changes, variations in the refractive index of silicon may violate our top

level requirements for wavelength stability. We therefore require the immersion grating temperature to remain within 60 mK of its reference temperature.

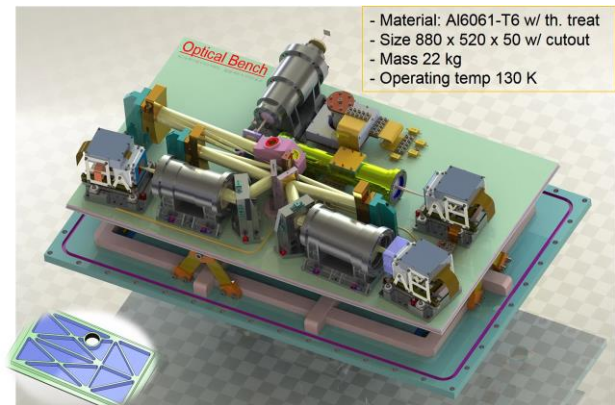


Fig. 2. Optical bench and the components above it.

IGRINS employs three Teledyne H2RG HgCdTe detectors. The H- and K-band spectrograph channels use science-grade 2.5 μm cutoff sensors, while the slit-viewing camera makes use of an engineering-grade sensor. Each detector set is controlled by a SIDECAR ASIC cryogenic board and a JADE2 USB interface card. We measured various characteristic properties of the detectors during the laboratory experiments including readout noise, system conversion gain, signal linearity response, dark current, reference-level stability, etc.

The IGRINS software consists of five functional packages. Housekeeping Package, Slit Camera Package, Data Taking Package, and Quick Look Package software tools are designed to be conducting the observation. After the observation, the obtained data can be reduced by the Pipeline Package (PLP). This package can also be used during the observing night to help an observer to decide on further observing strategies.

Commissioning Runs and Performance

IGRINS has had three commissioning runs on the McDonald Observatory 2.7 m Harlan J Smith telescope in March, May, and July of 2014. The purpose of these runs was to debug the system hardware and software, to measure the instrument performance, to provide a sample dataset for tests of the data reduction software, and to facilitate

planning of future astronomical observing programs.

IGRINS' design resolving power R is 45,000 throughout H and K bands. We used ThAr lines both to determine the instrumental dispersion and to measure the width of the spectral point spread function. The typical measurement of the FWHM of a singlet emission line is about 3.3 pixels. It provides the resolution element of $3.841 \times 10^{-5} \mu\text{m}$ and the resultant resolving power of about 45,000. This is a naturally expected outcome since the installed actual IGRINS slit width is slightly narrower than the designed one.

We have observed more than 100 sample objects with various exposure times during our three commissioning runs. The sample objects cover a broad range of spectral types, from B to M and the sample also includes highly embedded protostars. From these sample data we estimate the observed signal-to-noise ratios (SNR) and compare them with the predictions of our exposure time calculator (ETC). Measured sensitivity from the May commissioning data resulted in 84 % of ETC values on average, and sensitivity from the July data produced 101 % of ETC predictions of SNR. The revised auto-guiding mechanism after the May observing run improved the total instrumental sensitivity performance.

Radial velocity (RV) stability in a spectrograph begins with mechanical stability. Gravitational flexure of the instrument along the main dispersion direction will be the major cause of shifts in line positions. For IGRINS, a one-pixel shift translates to an RV change of 2 km/s. To estimate the possible instrumental flexure, we took a series of ThAr emission lamp spectra in the H and K bands while varying the orientation of the instrument. Table 1 summarizes the average flexures measured between airmass 1 and airmass 3 for different orientations of the slit. The K-band images show larger shifts than the H-band echellograms. This result is consistent with the finite-element analysis of the flexure of the optical bench where the greatest deviations with orientation were in the corner of the bench where the K-band camera resides. The distance from the center of mass is larger for the K-band camera than for the H-band camera. For the telescope

motion along the meridian, north-south slit orientations showed more flexure than measurements with the slit oriented east-west, a result which is consistent with the structural analyses of collimating mirrors and dichroic mount. The average flexure for K band is about 0.4 pixels and this will produce at maximum a shift of 0.1 pixels in the spectral direction during a one-hour exposure. Such a shift would cause a 0.2 km/s RV change if contemporaneous calibration is not applied.

| Slit orientation | H band [pix] | K band [pix] |
|------------------|--------------|--------------|
| East-west | 0.01±0.04 | 0.16±0.04 |
| North-south | 0.08±0.02 | 0.65±0.02 |

Table 1. Instrumental flexure measured between airmass 1 and airmass 3 in pixels.

Planning for IGRINS at Gemini in 2018

IGRINS has been accepted as a visiting instrument to the Gemini South telescope for 3 months in 2018 (April, May, June) with availability for 2 weeks each month. A 15 night observing program has been awarded to the team to be observed in Priority Visitor mode. Additional 30 nights will be supplied to the community in a queue mode supported by Gemini.

In preparation for the Gemini commissioning, KASI will modify and develop a new input optics assembly and support the software and instrument operation while UT is in charge of optical and mechanical engineering.

New input optics, composed of four lens assembly and a cold stop, are required for the f/16 telescope beam to be converted to the f/10 expected at the slit mask (Fig. 3). This is being designed by UT and is implemented and verified by KASI (Fig. 4). The current IGRINS input optics convert a f/8.8 beam to f/10 for the McDonald 2.7 m telescope and the DCT.

In order to mount IGRINS at the Gemini telescope, there are a few mechanical needs; an instrument mount and baffle to mount IGRINS to the instrument support structure (ISS), a new ballast weight assembly (BWA) and hardware for

mounting the electronics rack into the BWA, and an instrument stand to move IGRINS into the Gemini cleanroom and to put it in the preferred orientation for mounting to the telescope.

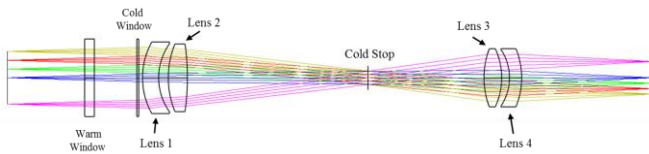


Fig. 3. Optical layout of the input optics which relays f/16 beam from the Gemini telescope to f/10 beam.

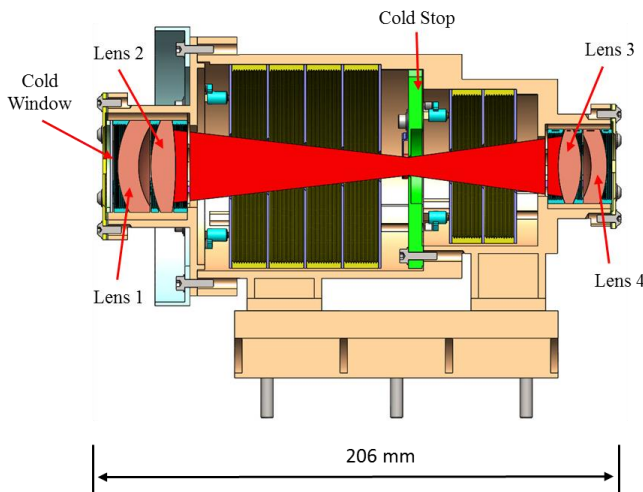


Fig. 4. Design of the input optics barrel assembly for the Gemini telescope.



Fig. 5. IGRINS on the 4.3m Discovery Channel Telescope at Lowell Observatory. The cryostat is the gold box on the left. The three protruding blue boxes contain the Teledyne JADE2 USB interface cards. The CTI cold head and vacuum pump fitting are at the center of the side facing the reader. To the right is the electronics rack which holds the three detector computers and other auxiliary hardware. The black metal box

between the cryostat and telescope rotator is the calibration unit.

Conclusion

The IGRINS hardware fabrication and parts assembly for the optical and mechanical components were finished by the end of 2013. We confirmed that IGRINS met its intended design goals through the commissioning runs at the McDonald Observatory 2.7 m Harlan J Smith telescope. During those observations, we debugged the system hardware and software, measured the instrument performance and provided a sample dataset for tests of the data reduction software and for facilitating plans of future astronomical observing programs. Proven for its excellent performance, IGRINS has been invited to the 4.3m Discovery Channel Telescope at Lowell Observatory in 2016 and 2017 (Fig. 5), and is now being prepared for a visit to the 8.1m Gemini South Telescope in April 2018.

References

1. H. Dekker. An immersion grating for an astronomical spectrograph, Instrumentation for Ground-Based Optical Astronomy, L. B. Robinson, ed. (Springer-Verlag, Berlin), pp.183-188, 1988.
2. G. Wiedemann, D. E. Jennings. Immersion grating for infrared astronomy, Appl. Opt., Vol. 32, pp. 1176-1178, 1993.
3. D. T. Jaffe, L. D. Keller, O. A. Ershov. Micromachined silicon diffraction gratings for infrared spectroscopy, Proc. SPIE, Vol. 3354, pp. 201-212, 1998.
4. J. P. Marsh, D. J. Mar, D. T. Jaffe. Production and evaluation of silicon immersion gratings for infrared astronomy, Appl. Opt., Vol. 46, pp. 3400-3416, 2007.
5. M. Gully-Santiago, W. Wang, C. Deen, D. T. Jaffe. Near-infrared metrology of high-performance silicon immersion gratings, Proc. SPIE, Vol. 8450, 2012.
6. W. Wang, M. Gully-Santiago, C. Deen, D. J. Mar, D. T. Jaffe. Manufacturing of silicon immersion gratings for infrared spectrometers, Proc. SPIE, Vol. 7739, 2010.
7. C. Park, et al. Design and early performance of IGRINS (Immersion Grating Infrared Spectrometer), Proc. SPIE, Vol. 9147, 91471D, 2014.

Rapid and nondestructive quantitative determination of total flavonoids in *Cyclocarya paliurus* leaves by near-infrared reflectance spectroscopy

Chao Ni^a, Yuanhao Wang^{b*}

^a College of Mechanical and Electrical Engineering, Nanjing Forestry University, Nanjing, China

^b College of Light Industry and Chemical Engineering, Dalian Polytechnic University,

Dalian, China

ABSTRACT

Total flavonoids content is an important quality index of *Cyclocarya paliurus* leaf. The feasibility of quantifying the total flavonoids content at the wavelength range of 10,000 – 4000 cm^{-1} for rapid and nondestructive determination in *Cyclocarya paliurus* leaf using near-infrared spectroscopy (NIR) combined with chemometric techniques was investigated. 54 leaves in different growth environment were used to spectra acquisition and total flavonoid determination. The chemometric methods, namely partial least square regression (PLS), principal component regression (PCR) and stepwise multiple linear regression (SMLR), were applied in the current research. Coefficient of cross-validation, root mean square error of cross-validation (RMSECV) and external validation were used to evaluate the quantitative analysis model and to test the calibration model. The results indicate that NIRS can have a good

quantification (correlation coefficient: 0.9415; RMSECV = 0.109) of total flavonoids in *Cyclocarya paliurus* leaves with preprocessing MSC+SD+SG(7,3) of raw NIRS and using the PLS method to establishment of the model with the wavelength range of 5000 – 4225 cm^{-1} .

Keywords: *Cyclocarya paliurus*; near-infrared spectroscopy; total flavonoids; quantitation

1. INTRODUCTION

Cyclocarya paliurus is mainly found in the mountainous regions in the tropics and subtropics [1]. It was called “sweet tea tree” in Chinese and its leaves have traditionally been used by indigenous people for the treatment of hypertension and diabetes [2] because of it contains several triterpenoids [3], flavonoids [4] steroids [5] and some other compounds. Moreover, many other therapeutic effects of *Cyclocarya paliurus* leaves have also been reported, such as the improvement of mental efficiency [6], antihypertensive action [7] and immunomodulation [8], et al. As a result, *Cyclocarya paliurus* leaves have a food resource for maritime people for a long time [9], and have also been used for drug formulations in traditional Chinese medicine [10]. Flavonoids are found to be the main active compounds in *Cyclocarya paliurus* leaves [11], which have many biological activities, such as preventing hyperglycemia, diabetes mellitus, hypertension and coronary heart disease. However, the content of flavonoids in *Cyclocarya paliurus* leaves is affected by genetic, cultural, harvesting, and environmental factors that occur during the growing period. So, it is an important quality index to evaluate the quantity of *Cyclocarya paliurus* leaves according to the

content of flavonoids. There are many techniques for extracting and determining the content of flavonoids, including the extraction process of heating, boiling, refluxing and the quantitative determination process of spectrophotometer using the aluminum chloride colorimetric method [12], high-performance liquid chromatography (HPLC) [9]. These methods require several hours or even days for the extraction process and a large volume of solvent, and may result in a loss of flavonoids due to hydrolysis, ionization and oxidation during extraction [13] and determination.

Compared with the traditional chemical methods, near-infrared spectroscopy (NIRS) has been used for raw material testing, product quality control [14] and process monitoring because of its advantages, such as non-destructive manner [15][16], speed and convenience. So, NIR combined with

chemometrics has attracted considerable attention in chemical content analysis. NIR is the region in the electromagnetic spectrum that consists of radiation from 780 nm to 2500 nm (4000 cm^{-1} to $12\,820\text{ cm}^{-1}$). The energies arising from this spectral range mainly correspond to the vibrational transitions due to superior harmonics (overtones) and combination bands. It has been employed to determine the active ingredient content of plants, such as ganoderma [17], leaf rape [14], ginkgo biloba leaf [18], *Cyclopia subternata* [19] and *Hoodia gordonii* [20]. As far as we know, no previous studies have been reported on the applications of NIR spectroscopy on the direct determination of chemical content in *Cyclocarya paliurus* leaves using NIR spectroscopy.

The aim of the present study was to develop a quantity determination of total

flavonoids in *Cyclocarya paliurus* leaves by NIRS technique in order to permit rapid and accurate quantification.

2. MATERIALS AND METHODS

2.1. Leaf samples

The *Cyclocarya paliurus* leaves (Fig.1) were collected from different trees and different growth environment, such as the location, ages and leaf area, etc in Muchuan, Jiangxi Province, China. The leaves were air-dried before NIR spectra measurement and the appearance of the leaves is basically complete and flat. All chemical reagents were of analytical purity grade and were purchased from YINDAXIGUI Chemical Reagent Corporation (Shanghai, China). Spectra collection and total flavonoids, determination were carried out on the same day.



Fig.1. Some samples of *Cyclocarya paliurus* leaves

2.2. Chemical Analyses of total flavonoids in *Cyclocarya paliurus* leaves

The content of total flavonoids was determined by spectrophotometer using the aluminum chloride colorimetric method [11]. Briefly, 1.0 g of a sample was placed in

a soxhlet extractor and refluxed with 75% methanol for 2 h at 80 °C. The extract was evaporated to dryness in a rotary vacuum evaporator at 40 °C and then dissolved with methanol. Exactly 0.3 mL of 5% NaNO₂ was added to a 1 mL extract in a 10 mL volumetric flask, and the mixture was kept for 5 min at room temperature. Addition of 0.3 mL of 10% AlCl₃·6H₂O to the mixture, which was incubated for another 5 min, was followed by the addition of 2 mL of 1 M NaOH. After 15 min of incubation at room temperature for color development, the absorbance at 415 nm was measured. Total flavonoids content (0.22% - 3.01%) was calculated using the standard rutin curve.

2.3. NIR spectral measurement and pre-treatment

All NIR spectra of *Cyclocarya paliurus* leaves were measured using an Antaris II Fourier transform near-infrared (FTNIR) analyzer (Thermo Nicolet, Madison, WI) equipped with an InGaAs detector and controlled by TQ Analyst version 7.2 (Thermo Nicolet) from 4,000 to 10,000 cm⁻¹ in diffuse reflectance mode. An NIR integrating sphere diffuse reflectance accessory (Bruker Optics Inc., Ettlingen, Germany) was also used. The spectra were collected from three different spots at the center of the leaf. The ambient air temperature was kept around 22-28 °C and the humidity was kept at a steady level in the laboratory. The spectra were digitalized at approximately 8 cm⁻¹ interval in the Fourier transform. A reference spectrum was taken before measuring each sample. To increase the signal-to-noise ratios, both reference and sample spectra were measured with scan number 32, and each spectrum was averaged

from two parallel measurements.

In order to reduce the systematic noise, such as baseline variation, light scattering, path length differences [21] and enhance the contribution of the chemical composition, Mathematical pre-treatments are necessary to perform. In this study, the combined optimization processes were implemented via multiplicative scatter correction (MSC), the first-derivative (FD), second-derivative (SD) and standard normal variable transformation (SNV). MSC was used to modify the additive and multiplicative effects in the spectra [22]. First and second derivatives were used to reduce peak overlap and remove constant and linear baseline drift, respectively [23]. SNV is a mathematical transformation method of the $\log(1/R)$ spectra used to remove slope variation and to correct for scatter effects [24]. Savitzky-Golay (SG) smoothing technique was also used in order to remove the noise from the data and to improve the signal to noise ratio. The smoothing window size and the number of polynomials were selected by the TQ Analyst software for 7 and 3, and the SG smoothing processing method is represented as SG (7, 3).

2.4. Quantitative Modeling

The partial least square (PLS) regression, stepwise multiple linear regression (SMLR) and principal component regression (PCR) were used for the modeling and prediction. The modeling was performed using TQ Analyst version 7.2 (Thermo Nicolet). To build a robust PLS model, all 54 samples were divided into a calibration and a validation set for building the PLS regression, SMLR and PCR models and a

validation set (10 samples) as the validation set for external validation by Kennard-Stone (K-S) method. According to the NIR spectrum distribution in the PC space, 10 samples were selected as the validation set for external validation, and the remaining 44 samples were taken as the calibration set for building the PLS regression, SMLR and PCR models. The 10 validation samples were within the concentration range of the calibration samples. The performances of these regression models were evaluated using the correlation coefficient (R^2) and root mean square error of cross-validation (RMSECV), which was determined via leave-one-out cross-validation (LOO-CV). For the validation set, the relative error of prediction was used to estimate the prediction of the developed models.

3. RESULTS AND DISCUSSION

3.1. Preliminary Data Analysis

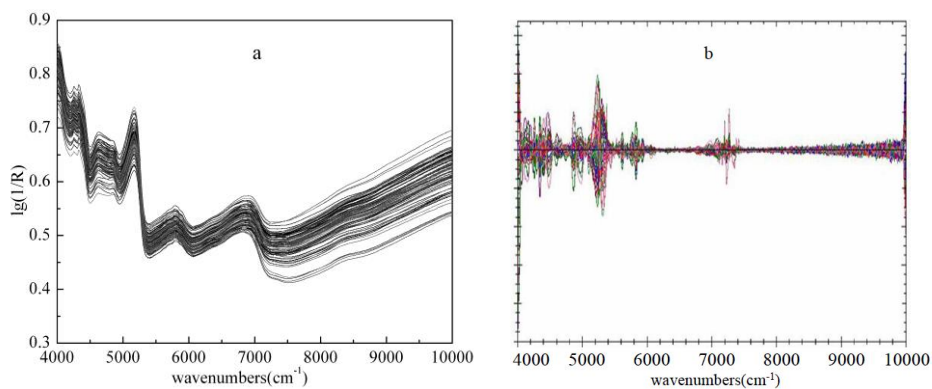


Fig. 2. The raw near infrared reflectance spectrum (a) and 2st derivative (b) of *Cyclocarya paliurus* leaves

Average raw and second derivative near-infrared transmittance spectra of *Cyclocarya paliurus* leaves samples are shown in Fig. 2. It can be seen from Fig. 2 that all the spectra had similar characters and more absorption peaks in the region of 7500 – 4000 cm^{-1} . 7500 – 5500 cm^{-1} region was related to C-H first overtone stretch vibration

modes in CH₃ and CH₂ groups [17]. It can be seen from Fig.2a that there is no distinct dissimilarities can be observed from the original spectra. In order to enhance the spectral features of samples, spectral pretreatment method of 2st derivative was used. The spectral differences associated with different samples became more apparent during region of 6000-4000 cm⁻¹, as shown in Fig.2b.

3.2. Quantitative Analyses of total flavonoids

3.2.1. Selection of the raw spectral data pretreatment methods

All 54 samples were divided into two sets, namely a calibration (44 samples) and a prediction (10 samples) set by Kennard-Stone method. The calibration-set samples were used to establish the PLS model in the experiment. Each calibration data set was used as the calibration set for the prediction, and the remaining data sets were employed for testing the PLS model. To extract complete and accurate information from the spectral data and, as much as possible, eliminate the influence of derivatives, a preprocessing method must be carried out. RMSECV was used as a comparison criterion to evaluate the preprocessing result of the model. The parameters of the PLS model using different processing methods are listed in Table 1.

Table 1. Results of the partial least squares regression calculation of samples for the different pretreatments

| Processing | RMSECV(%) | Correlation coefficient |
|---------------------------|--------------|-------------------------|
| Raw spectra | 0.123 | 0.9316 |
| MSC | 0.117 | 0.9286 |
| FD + SG(7,3) | 0.129 | 0.9237 |
| SD + SG(7,3) | 0.139 | 0.9127 |
| MSC + SD + SG(7,3) | 0.114 | 0.9325 |
| SNV + SD + SG(7,3) | 0.127 | 0.9265 |

FD, first-derivative; MSC, multiplicative scatter correction; RMSECV, root mean square error of cross-validation; SD, second-derivative; SG, Savitzky-Golay; SNV, standard normal variable transformation.

It was found that different mathematical treatments had different influence on the prediction result of the model. A comparison of the R^2 and RMSECV shows that the optimal processing for total flavonoids is the use of MSC+SD+SG (7,3) processing method. This may be due to the fact that the Multiple Scatter Correction (MSC) and Savitzky-Golay (7,3) pretreatment can eliminate the noise caused by the specular reflection and nonuniformity in the near infrared diffuse reflectance spectra, and to eliminate the non reproducibility of the baseline and the spectra of the diffuse reflectance spectra. In addition, two order derivative processing can strengthen the characteristic information of polysaccharide in the spectrum, so that the characteristic information is more obvious. After the best pretreatment of the raw spectra, the correlation coefficient and RMSECV are 0.9325 and 0.114%, respectively.

3.2.2 Chemometrics methods and wavelength-range Options

Chemometrics methods of partial least squares regression (PLS), principal component regression (PCR) and stepwise multiple linear regression (SMLR) were used to build quantitative correction model for NIR spectra. It will make no contribution to the models if the spectral regions with high noise to signal ratio or little correlation with the chemical characteristics. Thus it is important to select the optimum wavelength range for building best predictive model. Selection of the optimum wavelength range for best predictive model was done by PLS analysis by TQ analyst V 7.2. The correlation coefficient and variance were used to determine the wavelength-range options for building the models.

Based on the suggested region by TQ analyst software, different wavelength ranges

with different prediction performance were obtained, which included ranges of 4225 – 5000 cm^{-1} , 5200 – 6000 cm^{-1} and 4225 – 6000 cm^{-1} (Fig.3). The performance of the NIR calibration models of PLS and PCR with these ranges are presented in Table 1. There are obvious differences in 4225 cm^{-1} , 4900 cm^{-1} , 5300 cm^{-1} , 5610 cm^{-1} and 5820 cm^{-1} bands in Fig.3. These points are suitable for building SMLR model. Moreover, raw spectra without any processing method were used to build the models.

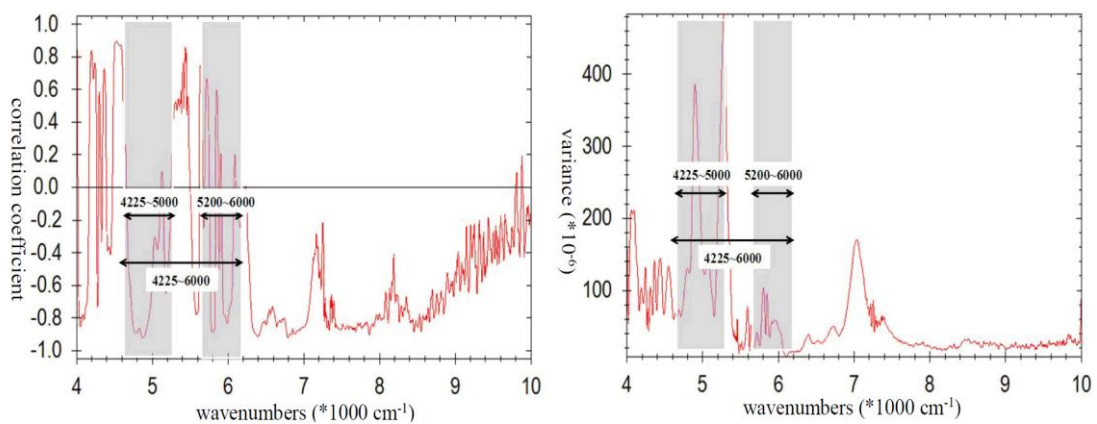


Fig. 3. Correlation of coefficient (a) and variance (b) in relation to wavenumbers

The results of the different wavelength ranges are listed in Table 2. By comparing different modeling methods of PLS, PCR and SMLR, the chemometrics method of PLS regression is the best quantification models of total flavonoids. After comparing the RCV (coefficient of cross-validation) and RMSECV, the optimal region for best predictive model of total flavonoids were clearly at 4225 - 5000 cm^{-1} range with a lowest RMSECV of 0.109% and was therefore used for further analysis.

Table 2. Results of the models for the different methods

| Methods | Region | RMSECV(%) | RCV |
|---------|--------------------------|--------------|---------------|
| PLS | 4000-10000 | 0.140 | 0.9016 |
| | 4225-5000 | 0.109 | 0.9415 |
| | 5200-6000 | 0.124 | 0.9241 |
| | 4225-6000 | 0.122 | 0.9256 |
| PCR | 4000-10000 | 0.146 | 0.8924 |
| | 4225-5000 | 0.132 | 0.9125 |
| | 5200-6000 | 0.133 | 0.9125 |
| | 4225-6000 | 0.139 | 0.9047 |
| SMLR | 4250,4900,5300,5610,5820 | 0.118 | 0.9311 |
| | 4900, 5300,5610,5820 | 0.128 | 0.9179 |

PCR, principal component regression; PLS, partial least squares regression; SMLR, stepwise multiple linear regression; RCV, coefficient of cross-validation; RMSECV, root mean square error of cross-validation.

3.2.3 Determination of the optimum factor numbers.

To avoid the insufficient fitting (underfitting) and rupture (overfitting) of the predictions of the other samples, the optimum number of factors for the models was determined using the leave-one-out cross validation (LOO-CV) method. The effects of different latent variables on the cross validation of the root mean square error (RMSECV) are studied. The relational graph of the RMSECV values against the LV numbers is shown in Fig. 4. Evidently, RMSECV decreased as the number of factors increased. When the number of latent variables of the calibration model of PLS analysis was 7, the RMSECV value was the smallest. The RMSECV value tends to be stable with the increase of the principal component. When the PC numbers exceeded 7, the RMSECV increased. Therefore, 7 is the optimal option for the model.

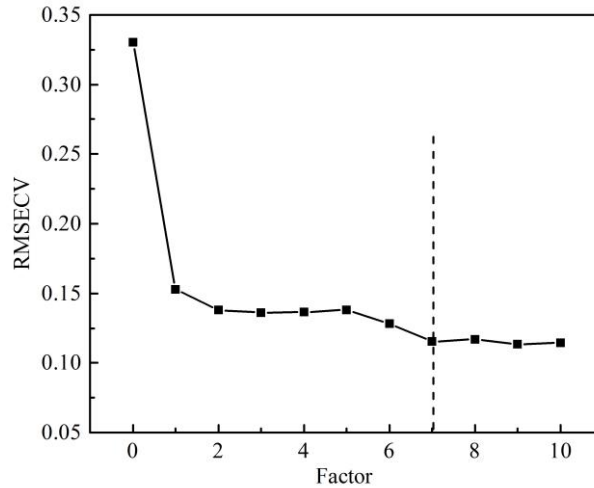


Fig. 4. Variation of the rootmean square error of cross-validation (RMSECV) with the principal component number for the model

4. Calibration results

4.1. The result by the NIR spectroscopy technique

The PLS model for polysaccharides was developed under the best conditions of selecting 4,225 - 5,000 cm^{-1} range and the best spectra pre-treatments of MSC + SD + SG(7,3) processing method. Fig.5 show the result by the NIR spectroscopy technique on the whole sample set of polysaccharides. The correlation coefficient for the polysaccharides model was 0.9415 while the RMSECV was 0.109%, which indicated that the calibration performance of the models were quite good and accurate.

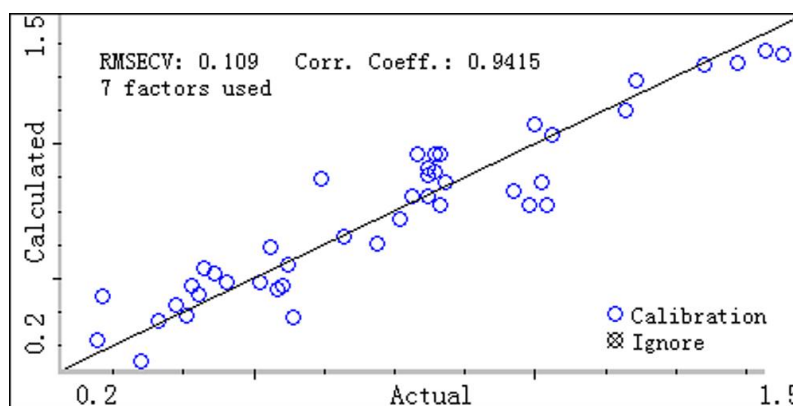


Fig. 5. The correlation between predicted value and chemical value of the PLS model for polysaccharides (“Corr. Coeff” in the figure means the determination coefficient “ R^2 ”).

4.2. External validation

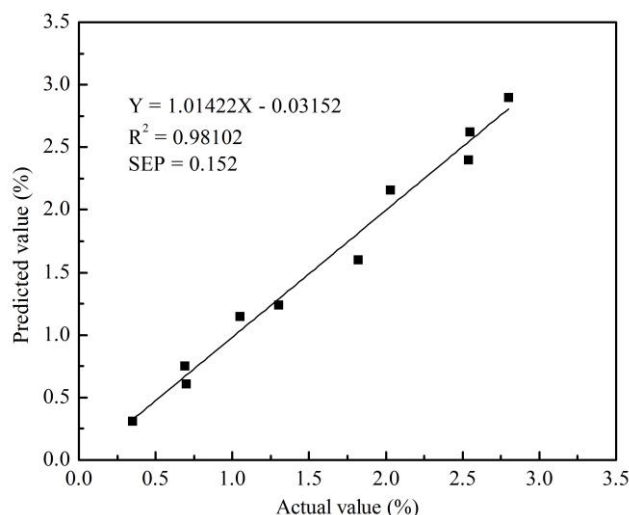


Fig. 6. Results of the predicted concentrations with the reference values

The prediction set was used to test the calibration model. Correlation coefficient and SEP were used to evaluate the result. Figure 6 shows the result of the predicted values and it shows that the correlation coefficient and SEP of the model are 0.98102 and 0.0152. Eight prediction samples of the validation results show that the model prediction values are accurate. Thus, the established model is reliable for predicting the flavonoids content in *Cyclocarya paliurus* leaves.

5. CONCLUSIONS

A new method for the quantitative analysis of total flavonoids in *Cyclocarya paliurus* leaves was developed using the NIR spectrum. Preprocessing MSC+SD+SG (7,3) of raw NIRS with the PLS method can be efficiently utilized in the rapid and accurate quantitative analysis of flavonoids. The correlation coefficient and RMSECV

of the PLS model are 0.9415 and 0.109, respectively. External validation results show that the model is accurate and that its correlation coefficient and SEC of the model are 0.98102 and 0.0152. Therefore, the NIR diffuse reflectance spectroscopy can provide a feasible way for quantitatively determining total flavonoids in *Cyclocarya paliurus* leaves.

ACKNOWLEDGMENTS

The authors are thankful for the National Natural Science Fund of China (31570714), Scientific Research Fund of Liaoning Provincial Education Department (L2014223) and Youth Foundation of Dalian Polytechnic University (QNJJ201303).

REFERENCES

- [1] Xie MY, Li L, Nie SP. Determination of speciation of elements related to blood sugar in bioactive extracts from *Cyclocarya paliurus* leaves by FIA-ICP-MS. *Eur Food Res Technol* 2006;223:202-209.
- [2] Li S, Li J, Guan XL. Hypoglycemic effects and constituents of the barks of *Cyclocarya paliurus* and their inhibiting activities to glucosidase and glycogen phosphorylase. *Fitoterapia* 2011;82:1081-1085.
- [3] Jiang ZY, Zhang XM, Zhou J, Qiu SX, Chen JJ. Two new triterpenoid glycosides from *Cyclocarya paliurus*. *J Asian Nat Prod Res* 2006;8:93-98.
- [4] Fang SZ, Yang WX, Chu XL. Provenance and temporal variations in selected flavonoids in leaves of *Cyclocarya paliurus*. *Food Chem* 2011;24:1382-1386.
- [5] Xie JH, Shen MY, Xie MY. Ultrasonic-assisted extraction, antimicrobial and antioxidant activities of *Cyclocarya paliurus* (Batal.) Iljinskaja polysaccharides. *Carbohydr polym* 2012;89:177-184.

- [6] Wang J, W K. Fatigue-alleviating effect of polysaccharides from *Cyclocarya paliurus* (Batal) Iljinskaja in mice. *Afr J of Microbiol Res* 2012;6:5243-5248.
- [7] Fan DM, Ye LJ, Luo Y. Development of Microsatellite Loci for *Cyclocarya paliurus* (Juglandaceae), A Monotypic Species in Subtropical China. *Appl Plant Sci* 2013;1:221-223.
- [8] Xie JH, Liu X, Shen MY. Purification, physicochemical characterisation and anticancer activity of a polysaccharide from *Cyclocarya paliurus* leaves. *Food Chem* 2013;136:1453-1460.
- [9] Birari RB, Bhutani KK. Pancreatic lipase inhibitors from natural sources: unexplored potential. *Drug discovery today* 2007;12:879-889.
- [10] Xie MY, Wang YX, Yi X. A study on the structure and contents of flavonoids in the leaves of *Cyclocarya paliurus*. *Chinese J Anal Chem* 2003;32:1053-1056.
- [11] Amir M, Mujeeb M, Khan A. Phytochemical analysis and in vitro antioxidant activity of *Uncaria gambir*. *International Journal of Green Pharmacy* 2012;6:67-70.
- [12] Bao J, Cai Y, Sun M. Anthocyanins, flavonols, and free radical scavenging activity of Chinese bayberry (*Myrica rubra*) extracts and their color properties and stability. *J Agric Food Chem* 2005;53:2327-2332.
- [13] Li H, Chen B, Yao S. Application of ultrasonic technique for extracting chlorogenic acid from *Eucommia ulmoides* Oliv. *Ultrason sonochem* 2005;12:295-300.
- [14] Font ., Río-Celestino M, Cartea E. Quantification of glucosinolates in leaves of leaf rape (*Brassica napusspp pabularia*) by near-infrared spectroscopy. *Phytochemistry* 2005;66:75-185.
- [15] Hom NH, Becker HC, Möllers C. Non-destructive analysis of rapeseed quality by NIRS of small seed samples and single seeds. *Euphytica* 2007;153:27-34.
- [16] Menesatti P, Antonucci F, Pallottino F, Raccuzzo G, Allegra M. Estimation of plant nutritional status by Vis-NIR spectrophotometric analysis on orange leaves. *Biosyst Eng* 2010;105:448-454.
- [17] Chen Y, Xie MY, Zhang H. Quantification of total polysaccharides and triterpenoids in *Ganoderma lucidum* and *Ganoderma atrum* by near infrared spectroscopy and chemometrics. *Food Chem* 2012;135:268-275.

- [18] Shi JY, Zou XB, Zhao JW. Determination of total flavonoids content in fresh Ginkgo biloba leaf with different colors using near infrared spectroscopy. *Spectrochim Acta A* 2012;94:271-276.
- [19] Maicu MC. Optimisation of retention of Mangiferin in Cyclopia Subternata during preparation for drying and storage of green honeybush and development of Nir Spectroscopy Calibration models for rapid quantification of Mangiferin and Xanthone contents. *Ugeskrift for Laeger* 1971;133:296-9.
- [20] Vermaak I, Hamman J, Viljoen A. A rapid spectroscopic method for quantification of P57 in Hoodia gordonii raw material. *Food Chem* 2010;120:940-944.
- [21] He Y, Li XL, Deng XF. Discrimination of varieties of tea using near infrared spectroscopy by principal component analysis and BP mode. *J Food Eng* 2007;79:1238-1242.
- [22] Naes T, Isaksson T, Fearn T, Davis T. *Multivariate calibration and classification*. Chichester, UK: NIR Publications; 2002. p. 34-45.
- [23] Osborne BG, Fearn T, Hindle P. *Practical NIR spectroscopy with applications in food and beverage analysis*. Harlow, Essex, UK: Longman Scientific and Technical; 1993. p. 21-24.
- [24] Chen QS, Zhao JW, Zhang HD. Feasibility study on qualitative and quantitative analysis in tea by near infrared spectroscopy with multivariate calibration. *Anal Chim Acta* 2006;572:78-81.

IR camera for NEO detection based on Compressive Sensing technologies

C. Lastrì¹, S. Baronti¹, G. Coluccia², D. Guzzi¹, D. Labate³, E. Magli², M. Miranda⁴,
V. Nardino¹, L. Palombi¹, I. Pippi¹, A. Zuccaro Marchi⁴, V. Raimondi¹

¹ CNR – IFAC, Via Madonna del Piano 10, 50019 Sesto Fiorentino, Italy
Tel.: +39 055 5226379, v.raimondi@ifac.cnr.it

² Politecnico di Torino – DET, Corso Duca degli Abruzzi 24, 10129 Torino, Italy

Tel.: +39 011 090 4195, enrico.magli@polito.it

³ Leonardo-Company S.p.A., Via Officine Galileo 1, 50013 Campi Bisenzio (FI), Italy

Tel: +39 055 89526, demetrio.labate@leonardocompany.com

⁴ ESA-ESTEC, Keplerlaan 1, NL-2200AG Noordwijk, The Netherlands
Tel.: +31 71 5658254, alessandro.zuccaro.marchi@esa.int

Compressive Sensing (CS) techniques are well suited to the infrared (IR) spectral range where they can be exploited in order to reduce payload budgets, data throughput and costs. This paper presents the preliminary study of a new CS-based instrument concept for space applications. The payload was designed for on-board detection of Near Earth Object (NEO). Although some technologies needed for the payload development are not yet completely mature, the results of simulations are very promising.

Introduction

Compressive Sensing (CS) theory has provided a basis for a different approach to data acquisition, overcoming the Shannon-Nyquist sampling theorem. CS predicts that a signal can be recovered from fewer measurements than those requested by the sampling theorem, provided that prior knowledge about the signal's sparsity is available [1]. In the past years, several prototypes have been developed to demonstrate such theory [2-4]. The single-pixel camera of Rice University has also been followed by a commercialization of a SWIR camera employing CS techniques [5]. In the single-pixel camera, a single photodetector element is used for imaging instead of an array detector [2]. CS essentially relies on the use of a 2-D Spatial Light Modulator (SLM) - which physically performs the scalar product between a random pattern and the incoming light - and of an optical assembly that concentrates the radiation on a single-element detector. This characteristic can be beneficial in the infrared (IR) spectral range, where 2-D detectors have a poor

performance in comparison with single-element detectors or are very expensive or not available. Recently, the European Space Agency (ESA) has funded the *Optical CS Technologies for Space Applications* (OCS-TECH) project in order to investigate the potential of CS-based optical instrumentation for space applications and to demonstrate the existence of substantial advantages - with respect to a traditional system - in terms of resources required for its development. The first step consisted in a review of space applications that could benefit from CS technique. Among these applications, some were selected for a preliminary design of a CS-based optical payload. In particular, this paper reports the results of the preliminary design of a CS-based camera working in the MIR for the on-board detection of NEO.

Background

A NEO is a small Solar System body whose orbit intersects or nearly intersects Earth orbit; therefore, they have a non-null (even if very small) probability of hitting our planet. A NEO

is considered as a Potential Hazardous Object (PHO) if its diameter is at least 100 m - 150 m and it is estimated to pass at less than 0.05 AU from the Earth. Nowadays it is widely known that collisions in the past have taken place, probably causing catastrophic events. For this reason, several space agencies have planned programs for the detection and tracking of NEOs, such as: the Lincoln Near-Earth Asteroid Research (LINEAR), European Near Earth Asteroids Research (EURONEAR), and the Near-Earth Object WISE (NEOWISE) projects. Although devoted to different space science applications, also other programs are able to detect NEO: among these, the Spitzer Space Telescope (SST) and the Arecibo Observatory Planetary Radar System. Most of these programs observe the sky in the visible; nevertheless, IR observation can provide valuable information on NEOs [6]. One of these is the Wide-field Infrared Survey Explorer (WISE) mission designed to survey the entire sky in four IR wavelength bands (3.4 μm , 4.6 μm , 12 μm and 22 μm) [7]. WISE consists of a 40-cm telescope in a Sun-synchronous low-Earth orbit. The survey began on January 2010, but after nine months the cryogen tanks were exhausted. After that time, the first two channels (W1 and W2) continued to operate, and a four-month survey (known as the NEOWISE Post-Cryogenic Mission) was undertaken. The WISE short-wavelength channels employ 4.2- μm and 5.4- μm cutoff HgCdTe arrays with 1024 \times 1024 pixels. The NEOWISE project, funded by NASA's Planetary Science Division, harvests measurements of asteroids and comets from images collected by the WISE spacecraft [8].

Instrument concept

The instrument here proposed was conceived as a CS-counterpart of the WISE instrument. It is a CS-based panchromatic camera for sky observation, devoted to on-board detection of NEOs, with a single channel centered at 4 μm , and with 2- μm FWHM, which roughly corresponds to the W1 channel of the WISE instrument. The schematic diagram of the

proposed optical payload is reported in Fig.1. while Fig. 2 shows a detail of the single pixel architecture: L1 is the collecting optics, SLM is the digital micromirror array, L2 is the condenser optics and SPD is the single pixel detector in the MIR spectral region.

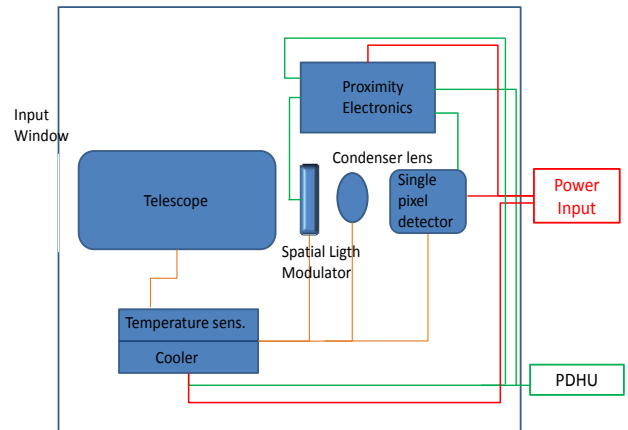


Fig.1: Schematic diagram of the proposed payload.

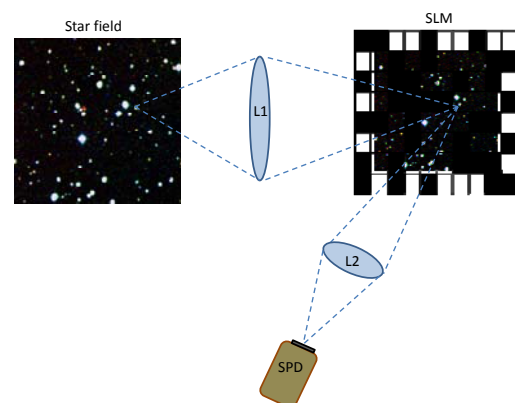


Fig. 2: Diagram of a single pixel CS-based camera for sky observations.

The payload is made up of the following main elements: a 50-cm telescope, a 512x512 pixel SLM, a condenser lens, a single pixel detector, a proximity electronic board, a temperature controller and coolers. Finally, a processing unit (PDHU) and a power supply unit complete the block diagram of the payload.

The main advantages offered by this CS architecture consist in the use of a single pixel detector and in the possibility to apply techniques deriving from CS theory directly on board. The last characteristic permits to obtain information on the NEO presence directly in

the measurements domain, without reconstructing the images. The very sparse acquisition domain represented by star fields would permit to achieve high compression ratios, yet maintaining a good quality of the retrieved information and consequently a considerable downlink bandwidth reduction. The main drawbacks are the limits posed by the working temperature of the SLM, which must be higher than 233°K. For this reason, the working spectral range of the instrument was set in the range 3-5 μm in order to cope with the issues raised by the background emission at such temperature. Actually, it should be taken into account that this application is very critical from this point of view: due to the low level of the signal of interest, the system should be cooled to cryogenic temperatures in order to reduce the unwanted background contribution. Presently, the only cryogenic SLM devices are Micro Shutter Arrays [9], but they have a frame rate (3-4 Hz) too low to fulfil the requirements of this application. A cryogenic DMD (minimum working temperature: 162°K) is under development at LAM-CNRS and EPFL [10, 11], but its size of 32x64 micromirrors is too small for the purposes of this CS-instrument. Commercial DMD can work at a temperature higher than 233°K [10].

Data simulation and processing

After the definition of the instrument main characteristics and the preliminary optical design, data simulations were performed in order to evaluate the photon flux reaching the detector and to assess the ability to detect NEOs. Images from the WISE database were used as a basis for image simulation [12]. Two images from the detector W1 were chosen: one with a very large star and few small objects (Fig. 3a) and the other with many objects of different extension and energy (Fig. 3b). In these images four “synthetic” NEOs were added. The NEOs were simulated as spherical objects at a given temperature by using the Black Body spectral radiation curve. The distances taken into account for the simulations were: 0.5 AU, 0.75 AU, and 1 AU. The

detection limit was set at 20 photons. Considered that the lowest working temperature of commercial DMD devices is 233 °K, only large and hot objects (i.e. 50-km diameter and 500-°K temperature) can be detected because of the DMD emissivity.

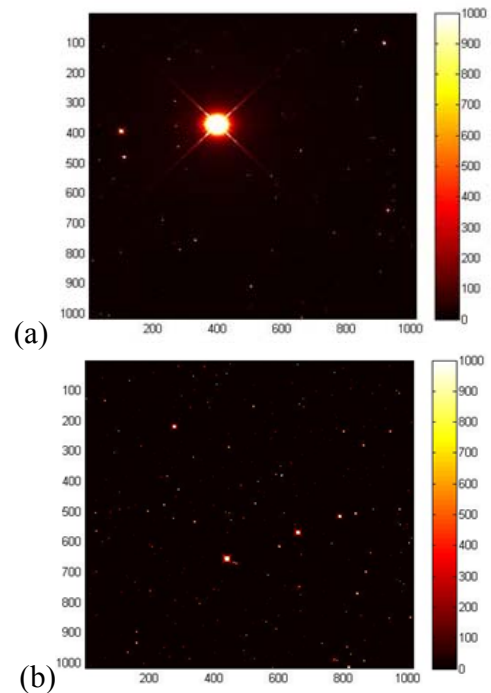


Fig. 3: Images used for the data simulations: (a) image with a very large star and few small objects, and (b) image with many objects of different extension and energy. Data are in Digital Numbers.

If a cryogenic device were available as SLM (cooling temperature at 150° K), the system could detect also NEO characterized by a lower temperature and smaller dimensions, as reported in Table 1. In this case, the SLM was supposed to be cooled at 150° K, while the detection limit was still set at 20 photons.

| Distance | NEO minimum diameter | NEO temperature |
|----------|----------------------|-----------------|
| 0.5 AU | 21 km | 300 °K |
| 0.5 AU | 3.5 km | 400 °K |
| 1 AU | 15.5 km | 350 °K |
| 1 AU | 7 km | 400 °K |

Table 1: NEOs detection limits with the system cooled at 150 °K.

The acquisition process was tested using simulated images and software procedure that mimics the CS acquisition, using as sensing matrix a Block Circulant with Circulant Blocks (BCCB) Bernoulli random matrix, which allows efficient encoding and decoding via the two-dimensional discrete Fourier transform. Starting from simulated acquisition, the images reconstructed by keeping only 10% of samples using Orthogonal Matching Pursuit (OMP) [13] exhibit a satisfying quality (Fig. 4).

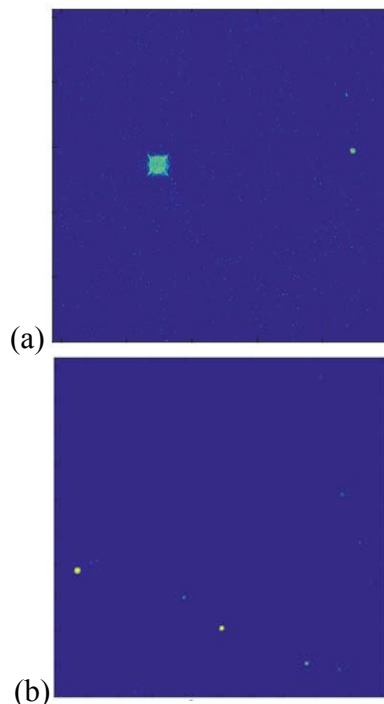


Fig. 4: Reconstruction from 10% samples using BCCB sensing matrix and OMP: (a) image with a very large star and few small objects, and (b) image with many objects of different extension and energy.

Conclusions

A CS-based instrument working in the MIR spectral region for NEO detection was designed at Preliminary Design level. Data simulations and CS algorithms - based information retrieval showed a good performance for the on-board detection of NEOs. The major limit for the development of such instrument is posed by the working temperature of high-modulation speed commercial SLMs, which presently can work at a temperature not lower than 233°K. New perspectives can be opened by the development

of SLMs able to work at cryogenic temperature, which are currently under development.

Acknowledgements

The OCS-TECH project (ITT AO/1-8235/15/NL/RA) was funded under ESA ESTEC contract n.4000116423/15/NL/BJ/gp. The view expressed in this publication can in no way be taken to reflect the official opinion of the European Space Agency.

References

1. R. Baraniuk. Single-pixel imaging via compressive sensing, *IEEE Trans. Signal Process.* 83-91, (2008).
2. <http://dsp.rice.edu/research/compressive-sensing>.
3. F. Magalhaes, et al. A compressive sensing based transmissive single-pixel camera, *International Conference on Applications of Optics and Photonics*, SPIE Vol.8001, (2011).
4. M. Abolbashari, et al. High dynamic range compressive imaging: a programmable imaging system, *Opt. Eng.* 51(7), 071407, (2012).
5. <http://inviewcorp.com/products/shortwave-infrared-swir-cameras>.
6. E. F. Tedesco, K. Muinonen, and S. D. Price. Space-based infrared near-Earth asteroid survey simulation. *Planetary and Space Science* 48.9 (2000): 801-816.
7. E. L. Wright, et al. The Wide-field Infrared Survey Explorer (WISE): mission description and initial on-orbit performance. *The Astronomical Journal* 140.6 (2010): 1868.
8. A. Mainzer, et al. Preliminary results from NEOWISE: An enhancement to the wide-field infrared survey explorer for Solar System science. *The Astrophysical Journal* 731.1 (2011): 53.
9. M. J. Li, A. D. Brown, A. S. Kutyrev, H. S. Moseley, V. Mikula, "JWST microshutter array system and beyond", *Proc. SPIE*, pp. 7594, 2010
10. Zamkotsian, Frederic, et al. "Micromirror arrays designed and tested for space instrumentation." *Optical MEMS and Nanophotonics (OPT MEMS)*, 2010 International Conference on. IEEE, 2010.
11. F. Zamkotsian, P. Lanzoni, A. Liotard, T. Viard, V. Costes, P.-J. Hebert, "Programmable wide field spectrograph for earth observation", *Proc. ICSO 2014*, Tenerife, Canary Islands, Spain, International Conference on Space Optics 7 - 10 October 2014
12. <http://irsa.ipac.caltech.edu/applications/wise/>
13. A. Tropp and A. C. Gilbert. (2007). Signal recovery from random measurements via orthogonal matching pursuit, *IEEE Transactions on Information theory* 53, 4655–4666.

COMPARISON OF THERMOCOUPLES SURFACE MEASUREMENTS AND INFRARED THERMOGRAPHY FOR TRANSPORT INFRASTRUCTURE THERMAL MONITORING

T. Toullier^{1,2}, J. Dumoulin^{1,2}, L. Mevel^{1,2}

¹ Ifsttar, COSYS-SII, Route de Bouaye, F-44340, Bouguenais, France

² Inria, Équipe I4S, Campus de Beaulieu, F-35042 Rennes, France

This study is intended to the evaluation and improvement of instrumentation solutions for long term monitoring of new generation of transport infrastructures. A test site has been instrumented with thermocouples and an infrared thermographic system coupled with the monitoring of environmental parameters. A spatial reconstruction method is proposed. Measured data acquired on site and post-processed are analyzed through time. Finally, obtained results are commented and perspectives are proposed.

Introduction

Studies around new deicing or controlled temperature structures are conducted under the 5th Generation Road (R5G) project of IFSTTAR. In order to control such structures, new thermal monitoring solutions *in-situ*, low cost and robust are needed. The aim of this study is to evaluate and improve thermal instrumentation solutions for long-term monitoring. First studies on uncooled infrared cameras has been made on open traffic structures [4], with promising results. If thermocouples or even optics fibers meet the expectation of thermal monitoring, the instrumentation can be complex, with a risk of breaking during the operation. On the contrary, infrared thermography seems more simple to deploy and offers a temperature measurement on multiple points at the same time.

However, in such application context, additional measurements are needed in order to convert the radiative fluxes (in digital levels) to temperature. In fact, the computation of the temperature will depend on spatial and meteorological parameters and also on the own characteristics of the observed object. Therefore, a multi-sensor system has been instrumented in order to improve this conversion

process [3]. Thanks to the development of new technologies and more efficient computation power (GPGPU), acquisition means enable the synchronization and the coupling of data in order to make the best use of infrared measurements. Nevertheless, camera positioning will have an impact on the temperature computation. Indeed, the projection of the 3D scene causes a non-constant resolution on the image. In such context, we study an infrared spatial calibration method by using the geometry of the scene which is applied to outdoors measurements. Then, thermographic infrared temperature measurements are compared with thermocouples measurements located at the structure's surface. The comparison is analyzed and commented. Finally, we propose to quantify the difference between the two methods in dynamic state.

Test site and related instrumentation

An experiment has been conducted on an instrumented road concrete section. Our measurement system gathers the temperature from the surface thermocouples, a weather station and fluxes at small and large wavelength. In parallel, the whole section is monitored with a FLIR SC655 thermal infrared camera (640 X 480 LWIR FPA).

The flux received by the thermal camera depends on its surrounding environmental conditions and also the thermo-optics properties of the measurement scene [4, 6]. Furthermore, the camera is placed on a mast, leading to a non-constant spatial sampling of the surface of the monitored scene. In such configuration, the radiation flux attenuated by the atmosphere depends on the position of the measurement point in the scene (Fig. 1).

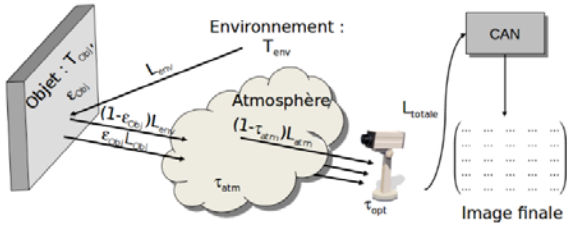


Figure 1. Illustration of the fluxes received by the camera
First, we can express for each point of the infrared image the total radiance L_{tot} by using the simplified radiometric equation to retrieve the flux received by the camera (Eq. 1)

$$L_{tot}^{i,j} = \epsilon_{obj} \tau_{atm} \tau_{opt} L_{obj}^{i,j} + (1 - \epsilon_{obj}) L_{env} \tau_{atm} \tau_{opt} + (1 - \tau_{atm}) L_{atm} \tau_{opt} + L_{opt} (1 - \tau_{opt}) \quad (1)$$

From this equation, we can retrieve the self-radiative contribution of our object. As mentioned before, the weather station is used to compute the environmental quantities from equation 1. The reflected, optics and atmospheric radiance values are computed by injecting some knowledge about the monitored objects, components of the infrared system and atmospheric conditions. For example, the atmospheric transmission τ_{atm} is function of the point within the image, external temperature and relative humidity.

Prior to the experiment, a thermal calibration is performed in order to retrieve the temperature as a function of the digital level associated to the radiance for each pixel of the image, following the equation 2.

$$T_{obj} = \frac{B}{\log\left(\frac{R}{L_{obj}}\right) + F} \quad (2)$$

Where R , B and F are calibration constants. Equation 1 shows the strong interaction between our measurement system and the environment.

The uncertainty due to the estimation of transmittance, emissivity and atmospheric radiances will influence the final result in a non-negligible way [2]. As shown by [8] in their simulation, solar flux, sky temperature or even rainfall are all parameters that can be a source of error when converting infrared measurements into temperature. Camera's position will also influence the calculation of the temperature which depends on the angle and the distance between the camera and the observed object. In the following, we propose a method for calibrating the image in order to extract at best thermal data to make a comparison with the thermocouples measurements.

Camera resectioning

In order to solve the simplified radiometric equation, the knowledge of spatial parameters is needed. The Direct Linear Transformation (DLT) [5] algorithm has been used on the measurements on site. The objective is to get the correspondences between the original coordinates and the image coordinates (Fig. 2).

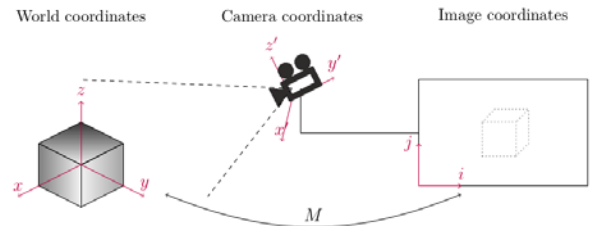


Figure 2. Illustration of a scene setup

We want to find the matrix M so that for every couple $(x, X) \in \mathbb{R}^2 \times \mathbb{R}^3$:

$$x = MX \quad (3)$$

M can be expressed in homogeneous coordinates as:

$$M = \begin{pmatrix} f & s_k & c_x \\ 0 & af & c_y \\ 0 & 0 & 1 \end{pmatrix} \begin{pmatrix} 1 & 0 & 0 & 0 \\ 0 & 1 & 0 & 0 \\ 0 & 0 & 1 & 0 \end{pmatrix} \begin{pmatrix} R_{3 \times 3} & 0_{3 \times 1} \\ 0_{1 \times 3} & 1 \end{pmatrix} \begin{pmatrix} I_3 & T_{3 \times 1} \\ 0_{1 \times 3} & 1 \end{pmatrix} \quad (4)$$

This system has 11 degrees of freedom, so it is necessary to know at least the coordinates associated to 6 points in order to solve it. Those 6 points are normalized so that:

- The barycenter of the two sets of points are at the origin

- The points are in average around the unit ball in their space in euclidian norm.

Therefore, two normalization matrices (U and V) are defined:

$$\hat{X}_i = UX_i, \hat{x}_i = Vx_i \quad (5)$$

The Levenberg-Marquardt algorithm is used to minimize the geometric error (Eq. 6) [1]. In order to approach the solution, the algorithm is initialized with the result of a singular value decomposition.

$$\min \sum_{1 \leq i \leq N} d(\hat{x}_i, M\hat{X}_i) \quad (6)$$

The jacobian matrix for the Levenberg-Marquardt algorithm is analytically calculated (Eq. 7)

$$J_M = \frac{\partial(\hat{u} - u, \hat{v} - v, 1 - s)}{\partial(f, a, c_x, c_y, s_k, t_x, t_y, t_z, w_x, w_y, w_z)} \quad (7)$$

Where $T = (t_x, t_y, t_z)$ and $W = (w_x, w_y, w_z)$ are respectively the translation and the rotation matrices. W is obtained with the Rodrigues rotation formula.

Once calibrated, a distance map and an angle map are computed and can be injected to our computation model (Fig. 3). This distance map is not yet integrated into the computation of the atmospheric transmission but we can note that regarding our setup (12m at maximum) the distance has a low impact on the final result, compared to the environmental conditions (relative humidity evolution through time for example). Those two maps enable us to perform geometrical transformations on the images and compare them with the thermocouples measurements.

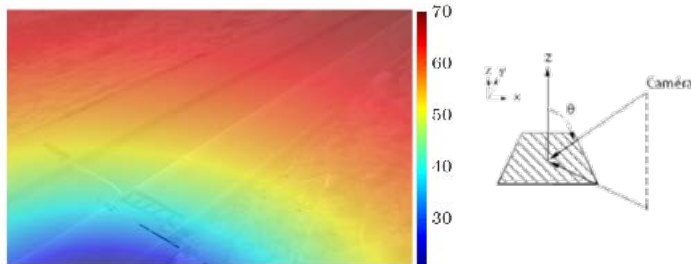


Figure 3. Angle map (degrees) and the angle definition
The result of image rectification is given in figure 4.

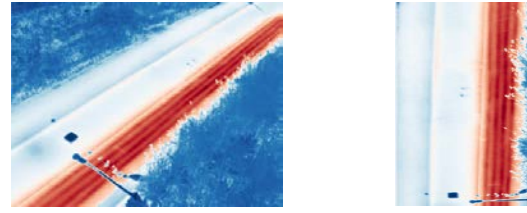


Figure 4. Original image (left) and rectified image (right)

Results analysis

The Figure 5 shows a comparison of two measured signals, one with surface thermocouple and the other one by data extraction on the rectified image with the model presented in the previous section. After calibration, the thermocouples position on the image enables us to extract the temperature values on the image sequence to recreate the thermal signal for a given period. A statistical comparison of the two times signals shows that the signals can be relatively close (expected value of $0.70^{\circ}C$ and standard deviation of $0.69^{\circ}C$), the difference is not null and can be important on specific periods of time (for example due to the presence of hydrometeors).

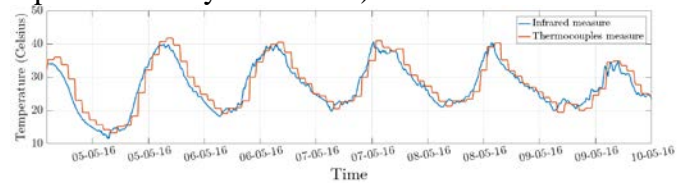


Figure 5. Infrared measurements compared to thermocouples measurements

To analyze more deeply the differences and evaluate the robustness of the infrared measure, the Dynamic Time Warping (DTW) algorithm has been used [7]. This algorithm optimizes the alignment of two temporal observations by minimizing the distance between every points. The computed distance gives information on the similitude of the two signals. By computing the distance DTW locally between the thermocouple and infrared measure, we can see the impact of the outdoor conditions on the infrared measurement.

To do so, let $X = (x_i)$ and $Y = (y_j), 1 \leq i \leq N, 1 \leq j \leq M$ be our two observations. We initialize the matrix dtw such as:

$$dtw(i,j) = \begin{cases} \infty & \text{if } i=0 \text{ or } j=0 \\ 0 & \text{if } i=j=0 \end{cases} \quad (8)$$

The distance DTW is then computed in dynamic programming by defining a cost function $c(x_i, y_j)$

$$dtw(i, j) = c(x_i, y_i) + \min \begin{cases} dtw(i-1, j-1) \\ dtw(i-1, j) \\ dtw(i, j-1) \end{cases} \quad (9)$$

For $1 < i < N, 1 < j < M$ and $|i - j| < w$ where w represents the maximum temporal tolerance between the two signals. In our case, the DTW distance has been computed by narrowing a region of interest with a sliding window. We have defined a six hours observation window and admitted a maximal offset between the signals (w) of ± 2 hours. The cost function chosen was the euclidian distance. Finally, the final value was divided by the size of our observation window in order to get an average value. This method helps us to quantify the difference between the different methods for a given period, and close experimental conditions.

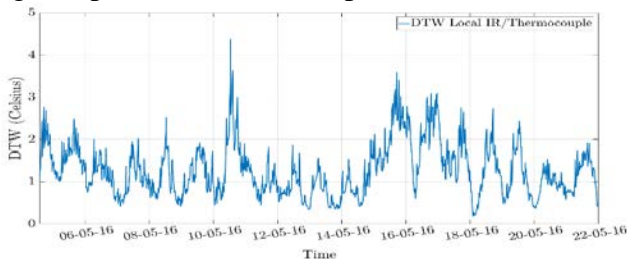


Figure 6. Comparison between the infrared thermogram and the related thermocouple signal with the DTW algorithm. Therefore, we can observe that the similitude between the two signals will be more or less important depending on the considered period (Fig. 6). The peaks that we can observe on this figure correspond to rainfall episodes for which the impact has to be considered in the correction process for outdoors infrared thermographic measurements.

Conclusion

A conversion in temperature from digital levels for infrared thermography coupled to a rectification algorithm has been presented in this study. The computed temperatures has been compared to measurements made with thermocouples on the concretes' surface. The rectification algorithm enabled us to extract thermal profiles of interest and to correct some projection errors. If differences exist between the two methods, the results are encouraging. In fact, infrared cameras can measure the temperature in multiple points on

the scene, which is difficult to reproduce with thermocouples. This study highlighted issues with long-term thermal monitoring with spatial and temporal resolutions that are different than airborne or satellite systems (due to scale difference). Some improvements are possible for the computation model we use. Indeed, our experiment enabled us to collect and synchronize numerous data, thermal, meteorological and solar. We will pursue the study of those data in order to refine our model and take into account different meteorological conditions.

References

1. Edwin K. P. Chong and Stanislaw H. Zak. An Introduction to Optimization. Wiley-Blackwell, Hoboken, New Jersey, 4th edition, February 2013.
2. K. Chrzanowski. Influence of measurement conditions and system parameters on accuracy of remote temperature measurement with dualspectral IR systems. *Infrared Physics & Technology*, (37) :295–306, 1996.
3. Jean Dumoulin and Vincent Boucher. Infrared thermography system for transport infrastructures survey with inline local atmospheric parameter measurements and offline model for radiation attenuation evaluations. *Journal of Applied Remote Sensing*, 8(1) :084978–084978, 2014.
4. Jean Dumoulin, Antoine Crinière, and Rodolphe Averty. The detection and thermal characterization of the inner structure of the 'Musmeci' bridge deck by infrared thermography monitoring. *Journal of Geophysics and Engineering*, 10(6) :064003, December 2013.
5. Richard Hartley and Andrew Zisserman. *Multiple View Geometry in Computer Vision*. Cambridge University Press, Cambridge, UK ; New York, 2 edition, April 2004.
6. J.R. Howell, R. Siegel, and M.P. Pinar. *Thermal Radiation Heat Transfer*. CRC Press, 5th edition, 2010.
7. Diego F. Silva and Gustavo EAPA Batista. Speeding up all-pairwise dynamic time warping matrix calculation. In *Proceedings of the 2016 SIAM International Conference on Data Mining*, pages 837–845. SIAM, 2016.
8. Sven Van De Vijver, Marijke Steeman, Nathan Van Den Bossche, Kim Carbonez, and Arnold Janssens. The influence of environmental parameters on the thermographic analysis of the building envelope. In *12th International Conference on Quantitative InfraRed Thermography (QIRT 2014)*, 2014.

POWER LINES INSPECTION VIA RGB, THERMAL AND INFRARED IMAGING

B. Jalil¹, D. Moroni¹, M.A. Pascali¹

¹Istituto di Scienza e Tecnologie dell'Informazione "Alessandro Faedo" CNR, Pisa, Italy

Image processing, applied to visible and infrared thermal data, is used to detect faults and anomalies in power transmission lines. Recently, Unmanned Aerial Vehicles, equipped with infrared or visible cameras, are used in urban or rural areas to acquire data, useful to comprehensively inspect the status of the infrastructure. This paper provides a concise review about vision-based algorithms used for the inspection of electric power lines, with a specific focus on methods and technologies which are suitable to be implemented in a UAV-based monitoring system of infrastructure for the transmission and distribution of the electric power.

Introduction

Power transmission lines are the means of electricity distribution and it is of extreme importance to ensure their continuous supply and high performance. At the same time, defect detection at an early stage not only can save the life of the system but also the operational cost. In addition to that, it can save the damages and can predict future anomalies too. Therefore, the continuous surveillance and inspection of power lines can play a vital role to ensure the continuous electric transmission. Much research on how to improve the power line detection methods and inspection's efficiency has been developed for a long time. In this paper, we will present different studies based on these methods using visible and thermal imaging cameras. The main focus will remain at the inspections via UAVs. We will highlight the different aspects of the methods used for the detection and inspection of power lines. We will also discuss different computer vision methods used to analyze visible and infrared image data. Before presenting these methods, we will first briefly introduce different modes of inspection.

Inspection modes

The most widely used method to inspect power lines is the foot patrolling: a team of personnel inspects the lines by or with the ground vehicle. The team is equipped with binoculars, and/or

visible and infrared cameras, however this process is relatively tedious and long. As an alternative to foot patrolling the inspection may be performed using a manned aerial vehicle, e.g. a helicopter equipped with visible or infrared cameras, hence acquiring images of conductors and insulators from high above the power lines. Then, data are either manually inspected, or automatically processed for the fault detection. This method is faster but usually more expensive. Also, when a fault is detected, skilled operators are required to climb in order to check and eventually fix the damage. In order to reduce the operational cost, climbing robots came up as an alternative solution. The climbing robot travels along the conductors, achieving similar speed as in helicopter assisted inspection. In comparison to the foot patrolling, often requiring climbing on the power lines, the climbing robot is a safer and not time consuming solution. Although having specific benefits, climbing robots are still not a practical solution to inspect the huge network of distribution lines [1].

Over the recent years UAVs are being used for a wide spectrum of applications, supporting humans in dangerous and challenging environments, including the inspection and maintenance of power equipment. Modern flight control technique and image processing allow UAVs to carry out fast inspection from some distance. Based on GPS data of both the UAV and the electric towers, the embedded algorithms are able to perform the automatic

tracking of power lines. Compared with the conventional inspection methods, UAV-based inspection is more advanced, less expensive and safer. However, UAVs and manned aerial vehicles share some common problems, occurring while monitoring the power lines: camera stabilization, pole tracking and automatic detection of defects. The acquired data, generally a sequence of images, are analysed by the operator to assess the maintenance status of the power line. In the infrastructure monitoring by UAV, the challenge is to make the inspection fully automatic and almost real-time, by using proper statistical and morphological processing techniques to highlight the hot spot in cables and insulators.

Vision-based methods

Power line inspection can be done by using visible or infrared camera. Thermal and infrared imaging has gained recognitions in the field of power systems during the last two decades. It has been used for testing and inspection of different electric parts and also for preventive maintenance work. Recently, UAV-based inspection systems are used to comprehensively inspect power transmission line in urban and rural areas. Here we focus on image processing methods used to analyse both visible and infrared images. In both cases, the acquired data is a sequence of 2D image of the scene. In this scene, the background could be green fields, water, mountains or buildings. Therefore, in order to investigate the condition of the lines, the very first step is to identify the power lines in the images. Detecting power lines from a cluttered background is one of the most important and challenging tasks. In general, all methods follow the two step process. i) Identify expected power lines and remove rest of the background. ii) Connect the expected power lines and remove unwanted straight lines. In the following sections there is a brief description of image type, along with a discussion of the methods used to identify and inspect power lines.

Processing of thermal-infrared data

Infrared thermography uses infrared sensors to capture images of thermal objects based on temperature variations. Generally, thermal imaging is considered as a robust, non-destructive and contactless methodology to inspect power lines, as the inspection can be performed by keeping some distance, hence there is no need to halt or cut down electric supply during the inspection.

Hongwei et al. [2] had presented a fusion algorithm for the infrared and visible power lines image. They extracted the SIFT features from the images and calculated the optimal homograph matrix to fuse the visible and infrared images by bicubic interpolation algorithm. Their method is invariant to large scale changes and illumination changes in the real operating environment of power equipment. Similarly, Larrauri et al. [3] identified areas of vegetation, trees and buildings close to power lines and calculated their distance from power lines. Simultaneously, the system processed the infrared images to detect hot spots in the power lines by estimating the threshold based on Otsu method and later segment the lines from the background [4]. More recently, Vega et al. presented a system based on a quadrotor helicopter for monitoring the power lines [5]. They estimated the relative temperature of the joints for qualitative inspection. The increase of the electrical resistivity at the joints is directly proportional to the temperature at the joint. Initially, the background of the thermal image was removed, and then the joints of the power lines, located in the foreground, were analyzed. They performed a thresholding-based segmentation to isolate these joints from background. On the other side, Lages et al captured video streams from both an infrared and visible cameras, simultaneously [6]. They used both statistical and morphological methods to highlight the hot spots in the lines. Their first step is to segment the image in lower and high temperature areas, by thresholding; later, the foreground is further processed

looking for hot-spots. The background is discarded. Oliveira et al. discussed in detail the generation of hot spots in the transmission lines and later they had also used the same thresholding based segmentation to highlight hot spots [7]. Several of the above mentioned and similar methods require manual operations to adjust threshold values; hence there is a risk of a high measurement error because of the influence of the background, lack of reference temperature values, and changeable emissivity or reflection of radiation from other elements surrounding power lines. For this reason, recently Wronkowicz had proposed an automated method for the hot spot detection from IR images of power transmission lines, without any reference temperature value [8]. The threshold for image segmentation is selected automatically by finding the steepest growth of successive gradients of sorted values of input image, after certain image pre-processing steps.

Processing of RGB data

In recent years, tremendous efforts have been devoted to the automation of power lines detection from aerial RGB images. Many methods, based on recent advances in aerial photogrammetry, have been proposed to detect and inspect power lines in real time. Oberweger et al. presented in [9] a method to detect the insulators in aerial images, and to automatically analyze them for possible faults. Their method is based on discriminative training of local gradient-based descriptors and a subsequent voting scheme for localization. More recently, Li et al. used the human attention mechanism model and the binocular vision system to detect and track power lines in image sequences according to their shape [10]. The binocular visual model is used to calculate the 3D coordinates of both obstacles and power lines. The proposed method uses a SURF-based matching strategy to improve the real time computation and accuracy of the system. The experimental results show that the inspection system is effective even in complex backgrounds and under different conditions.

Zhang et al. transformed the RGB image to the gradient image, and extracted the power lines by the Otsu thresholding [11]. They performed K-means in the Hough space to cluster and filter the straight lines; and Kalman filtering to predict the position of power lines in the next frame, assuming the continuous nature of video frames. Similarly, Li et al. in [12] proposed a more complex filter based on a simplified pulse coupled neural network model. This filter can simultaneously remove the background noise as well as generate edge maps. An improved Hough transform, performing knowledge-based line clustering in the Hough space, detected the power transmission lines. Song and Li in [13] first generated a line segment pool by match filtering and first-order derivative of Gaussian. Later, a graph-cut model is used to group the lines corresponding to the power lines. This method can detect not only the straight power lines but also the curve ones. Candamo detected power transmission lines from low quality videos combining the motion estimation at the pixel level with the edge detection, followed by a windowed Hough transform [14]. Yan et al. extracted straight line segments by Radon transform, followed by a Kalman filtering to connect segments into whole lines [15]. More detailed summary of some more methods were given by Kartransnik and Miralla in [16, 17].

Conclusion

In this paper, we have studied different inspection methods based on visible and infrared images designed to detect and inspect power transmission lines. Infrared imaging applied to power lines monitoring account for the differences of temperature at the joints; hence it is used for the fault diagnosis. Most of the methods performed simple thresholding to separate foreground from the scene. On the other hand, image processing applied to RGB images and videos is able to provide quite an accurate localization of the inspected power lines, by applying standard computer vision techniques (e.g. denoising, filtering, segmentation, line detection). Using more advanced techniques (e.g. Kalman filtering, 3D

photogrammetry, neural networks) it is possible to perform a detection and tracking of power lines in almost real time, during the autonomous inspection. The integration of the processing of both data (i.e., thermal infrared and visible) is a key point to have not only an accurate detection and tracking of the power lines, but also to have a reliable and robust assessment of the maintenance status of the whole infrastructure.

SCIADRO Project

This work is being carried out in the framework of the Tuscany regional project “SCIADRO” [18]. The project aims at developing the enabling technologies, which are key to accomplishing a rather rich and diverse span of missions through the use of a coordinated drone swarm within a civilian environment. In detail, the project aims at: (i) achieving computer vision techniques and algorithms able to detect complex objects and extract information on local anomalies which might affect them; (ii) developing suitable logics and algorithms to effectively organize and guide the overall swarm motion and actions during a mission; (iii) studying, developing and demonstrating network architectures and protocols allowing communication among multiple drones within a swarm, possibly increasing the communication reliability towards the ground segment.

References

1. L. Wang et al., Development of a Practical Power Transmission Line Inspection Robot Based on a Novel Line Walking Mechanism, The 2010 IEEE/RSJ International Conference on Intelligent Robots and Systems October 18-22, 2010, Taiwan.
2. H. Li et al, Research on the Infrared and Visible Power-Equipment Image Fusion for Inspection Robots, 2010 1st International Conference on Applied Robotics for the Power Industry Montréal, Canada, October 5-7, 2010.
3. J. I. Larrauri, et al. Automatic System for Overhead Power Line Inspection using an Unmanned Aerial Vehicle RELIFO Project, 2013 International Conference on Unmanned Aircraft Systems, May 28-31, 2013, Atlanta, GA.
4. N. Otsu. A Threshold Selection Method from Gray-Level Histograms, In IEEE Transactions on Systems, Man, and Cybernetics. Vol. 9, 62-66, 1979.
5. L. Vega, et al, Power Line Inspection Via an Unmanned Aerial System Based on the Quadrotor Helicopter, IEEE Mediterranean Electro technical Conference, Beirut, Lebanon, 13-16 April 2014.
6. W. F. Legas and V. Scheeren, An embedded module for robotized inspection of power lines by using thermographic and visual images, CARPI ETH Zurich, Switzerland. September 11-13, 2012.
7. J. H. Oliveira et al, Robotized Inspection of Power Lines with Infrared Vision, 2010 1st International Conference on Applied Robotics for the Power Industry, Montréal, Canada, October 5-7, 2010.
8. A. Wronkovicz A., Approach to automated hot spot detection using image processing for thermographic inspections of power transmission lines. Diagnostyka. Vol. 17, pp. 81-86, 2016.
9. M. Oberweger et al., et al. Visual Recognition and Fault Detection for Power Line Insulators, 19th Computer Vision Winter Workshop, Feb, 2014.
10. Q. Li et al., Bionic Vision-Based Intelligent Power Line Inspection System, Computational and Mathematical Methods in Medicine, Article ID 4964287, 13 pages, 2017.
11. J. Zhang et al., High speed Automatic Power Line Detection and Tracking for a UAV-Based Inspection, 2012 International Conference on Industrial Control and Electronics Engineering.
12. Z. Li et al. Towards automatic power line detection for a UAV surveillance system using pulse coupled neural filter and an improved Hough transform, Machine Vision and Applications, 2010, vol. 21:677–686
13. B. Song and X. Li, Power line detection from optical images, Neuro computing, vol. 129, 350–361, 2014.
14. J. Candamo, Detection of Thin Lines using Low-Quality Video from Low-Altitude Aircraft in Urban Settings, IEEE Transactions on Aerospace and Electronic Systems vol. 45, 2009.
15. G. Yan et al, Automatic Extraction of Power Lines from Aerial Images, IEEE geoscience and remote sensing letters, vol. 4, 2007
16. J. Katrasnik et al., A survey of mobile robots for distribution power line inspection, IEEE Transactions on Power Delivery, vol. 25, pp. 485–493, 2010.
17. F. Miralls et al, State-of-the-art review of computer vision for the management of power transmission lines. In Proceedings of the 2014 3rd International Conference on Applied Robotics for the Power Industry, pages 1–6, Oct 2014.
18. M. Bacco et al. UAVs and UAV swarms for civilian applications: communications and image processing in the SCIADRO project. Working paper, 2017. <http://puma.isti.cnr.it/dfdowload.php?ident=cnr.isti/2017-WP-001>

DETERMINATION OF ENERGETIC PARAMETERS OF BUILDING ROOFTOPS BY AERIAL INFRARED THERMOGRAPHY

F. López and X. Maldague

Dept. of Electrical and Computer Engineering, Computer Vision and Systems Laboratory, Laval University, 1065, av. de la Médecine, G1V 0A6, Quebec City, Canada

fernando@fernandol.com
xavier.maldague@gel.ulaval.ca

This paper presents a methodology to calculate energetic parameters through the measurement of the temperature field of building rooftops using aerial infrared thermography. To this aim, a thermo-numerical model based on heat transfer analysis is proposed to calculate energy losses from the thermal data collected using an unnamed aerial vehicle adapted to transport an infrared camera. An alignment algorithm based on the phase correlation method is implemented to reduce the noise produced by the vibrations of the drone. Furthermore, infrared images processing techniques based on the Fourier transform and multivariate statistical regression are applied to the 3D sequence to increase the signal to noise ratio and to reduce artifacts affecting the calculation of the energetic parameters.

Introduction

The rising attention to energy consumption problems and climate change is renewing the interest in the applications of thermal remote sensing. Precisely, one of the main factors affecting the energy consumption of buildings is related with the performance of the thermal insulation of the walls and rooftops, especially during the winter season. In this scenario, infrared thermal remote sensing has been proved to be an effective and reliable method to detect such anomalies that not only affect the energetic performance of buildings, but also affect the thermal comfort and health of their residents.

In this work – which is framed in a collaboration initiative between Torngats Technical Services and Laval University, pursuit to develop the basis for the development of a large scale thermal map that could be used by industrial enterprises. Such thermal maps will provide the enterprises with valuable information about the energy footprint of the area covered by their facilities.

Proposed Methodology

The proposed methodology consists first in developing an inspection protocol that will be used as a standard procedure to collect thermal images by means of AIT. In this context, to obtain high quality IR aerial images, several factors concerning to the environmental conditions will be taken into consideration. Currently, a wide literature that specifies the most suitable meteorological conditions for data collection using AIT exists [2] [3] [4] [5] [6]. These references will be carefully studied and an inspection protocol will be developed, considering also the characteristics of the IR camera and the UAV. The thermal IR data will be collected using a hexa-copter (model DJI S800 EVO) currently used for aerial photography surveys and adapted to transport an IR camera FLIR T620 (640 x 480-pixel array). The temperature field of the building rooftop will be monitored for 10 minutes and the data stored in the internal memory of the IR camera. The thermal sequence will then be converted into a 3D matrix from which further post-processing techniques will be applied. In this research, different techniques aimed to improve

the signal to noise ratio (SNR) of the acquired thermograms will be implemented. One of the most traditional method is ortho-rectification, which is the process of transforming an uncorrected, raw image from an arbitrary coordinate system into a map projected coordinate system [7]. Other techniques based on multivariate statistical analysis such as principal components thermography (PCT) [8] [9] [10] and partial least squares thermography (PSLT) [11] [12] will also be implemented and their performance will be analyzed based on the SNR.

For the quantitative analysis, a thermo-numerical model will be developed to compute the pixel-by-pixel heat transfer between the building rooftop and the environment. To this aim and as proposed by [13], an energy balance at the surface of the rooftop will be performed, considering conduction in the internal roofing structure, and convection and radiation between the roof the and the external environment. For the computation of the U-value, a thermal model will be implemented based on electrical analogy, considering the thermal properties and geometry of each elements of the isolation [14] [15]. Thus, from the thermal maps obtained by the AIT scanning and considering the thermophysical properties of the materials and the environmental conditions, an algorithm will be developed in Matlab language [16].

Preliminary Results

Figure 1 shows a sequence of four thermal images acquired at various times (t_1 , t_2 , t_3 and t_4). The images were obtained from the AIT inspection carried on a flat building rooftop located at 5635 Rue Rideau, Quebec City. As proposed, the acquisition window was of 10 minutes and a high sampling frequency was used (7.5 Hz). As it can be observed, the images are severely misaligned due to – among other factors – the movement caused by the wind. This situation brings incertitude when performing the pixel by pixel heat transfer analysis. To solve this drawback, it has been implemented an alignment algorithm based on the phase correlation method.

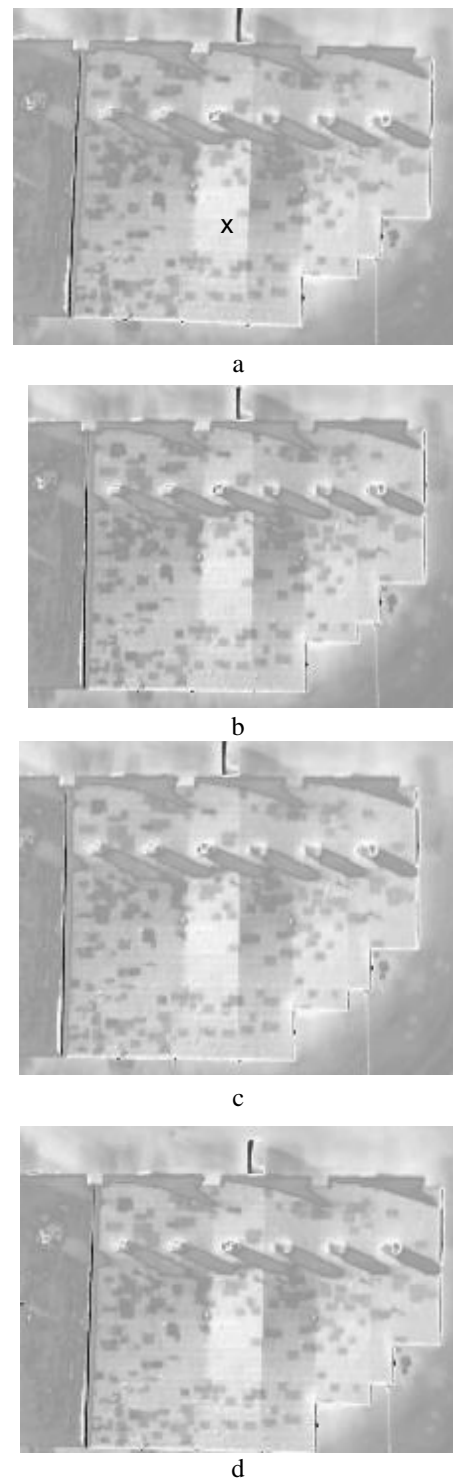


Fig. 1. Thermal sequence of non-aligned images obtained by aerial infrared thermography.

Figure 2 shows the temporal profile of a single pixel (the location of the pixel is showed in Fig. 1a) before and after the implementation of the alignment algorithm. As can be shown in Fig. 2a, the movement – which is basically due to the

translation between one frame to the other, produces peaks in the temperature behavior of the pixel. These peaks are not related to thermal phenomena nor to infrared reflection artifacts, but rather they are the result of the translation or change of the coordinates of the frames.

As depicted in Fig. 2b, a more stable and thermal profile is obtained after the implementation of the alignment algorithm, making possible the next steps of post-processing and heat transfer analysis.

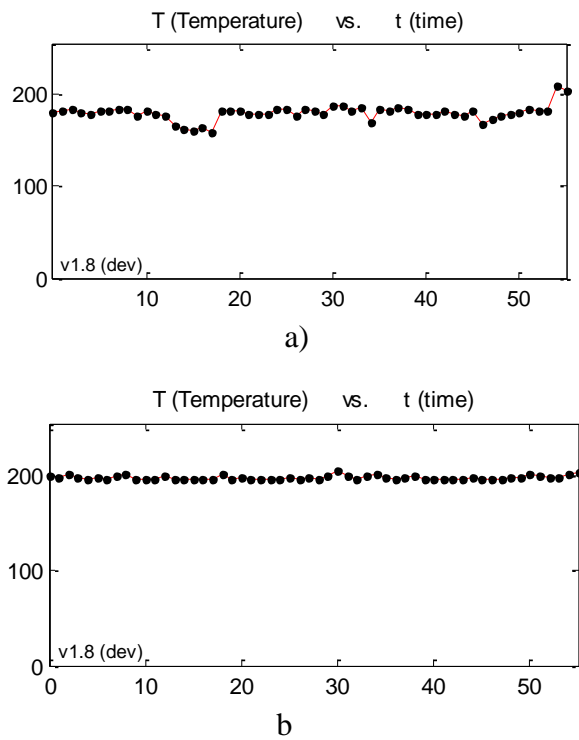


Fig. 2. Thermal sequence of non-aligned images obtained by aerial infrared thermography.

References

[1]. Campbell, D., Born, W., Beck, J., Bereska, B., Frederick, H. and Sun, H. "The airborne wildfire intelligence system: a decision support tool for wildland fire managers in Alberta", *Thermosense XXVI*, Orlando, Florida, USA, SPIE Vol. 4710, pp. 159-617. 2002.

[2]. Bowman, J. R. and Jack and R. L. "Effective Aerial thermography for energy conservation", *American Society of Photogrammetry - Thermosense II: Second National Conference on Thermal Infrared Sensing Technology for Energy Conservation Programs*, Albuquerque, New Mexico, pp. 217-225. 1979.

[3]. Brown, R. J. "Canadian experience with the use of aerial thermography", *Thermosense I: First national conference on the capabilities and limitations of thermal*

infrared sensing technology in energy conservation programs, Tennessee, USA. pp. 121-137. 1978.

[4]. Cihlar, R. J. Brown and J. Introduction to aerial thermography applications in energy conservation programs, Canada Centre for Remote Sensing. 1978

[5]. Allinson, D., Benachir, M., Robin, W. "Towards quantitative aerial thermal infrared thermography for energy conservation in the built environment", *Proceedings of SPIE Vol. 5782. Thermosense XXVII*, Bellingham, WA: pp. 133-143. 2005

[6]. Schott, W. C. and Snyder and J. R. "Combined aerial and ground technique for assessing structural heat loss", *SPIE Thermosense XVI: An International Conference on Thermal Sensing and Imaging Diagnostic Applications*, Orlando, FL, pp. 71-82. 1994

[7]. Yahyanejad, S. "PhD Thesis: Orthorectified Mosaicking of Images from Small-scale Unmanned Aerial Vehicles", Klagenfurt: Alpen-Adria Universitat Klagenfurt. 2013.

[8]. Rajic, N. "Principal component thermography for flaw contrast enhancement and flaw depth characterisation in composite structures", *Composite Structures*, Vol. 58, pp. 521-528. 2012

[9]. Omar, M.A., Parvataneni, R. and Zhou, Y. "A combined approach of self-referencing and Principle Component Thermography for transient, steady, and selective heating scenarios", *Infrared Physics & Technology*, Vol. 52, pp. 358-362. 2010.

[10]. Zhou, Y., A. Mayyas and Omar, M.A. "Principal Component Analysis-Based Image Fusion Routine with Application to Automotive Stamping Split Detection", *Research in Nondestructive Evaluation*, Vol. 22, pp. 76-91. 2001

[11]. López, F., Nicolau, V., Maldague, X., and Ibarra-Castanedo, C. "Multivariate Signal Processing Technique by Partial-Least Squares Thermography", *16th International Symposium on Applied Electromagnetics and Mechanics (ISEM16)*, Quebec City, pp. 29-34. 2013

[12]. Rosipal, R. and Kramer, N. "Overview and recent advances in partial least squares", *Proceedings of Statistical and Optimization Perspectives*, Bohinj, Slovenia. 2005.

[13]. Allinson, D. "Evaluation of aerial thermography to discriminate loft insulation in residential housing", PhD thesis, University of Nottingham. 2007.

[14]. Building components and building elements – Thermal resistance and thermal transmittance – calculation method, report: BS EN ISO 6946. 1997

[15]. D.S. Parker. "Technical support for the development of an attic simulation model for the California Energy Commission", *Florida Solar Energy Centre Report. FSEC-CR-1526-02*. 2005

[16]. Mathworks. *Matlab: The Language of Technical Computing*. 2016.

INFRARED THERMOGRAPHY APPLIED FOR ROBUST IMAGE PROCESSING TO EXAMINE HISTORICAL WOODEN BUILDINGS

K. Nakasho¹, C. Cuadra², H. Madokoro³, N. Shimoi⁴

¹ Akita Prefectural University, nakasho@akita-pu.ac.jp

² Akita Prefectural University, carlos@akita-pu.ac.jp

³ Akita Prefectural University, madokoro@akita-pu.ac.jp

⁴ Akita Prefectural University, shimoi@akita-pu.ac.jp

This study applied infrared thermography to investigate the indoor structure of historical wooden buildings, although it had been considered difficult to apply this method under such conditions as complex structures with slight temperature changes. In contrast to a uniform temperature changes that occur because of solar radiation, forced heating with heating devices tends to cause temperature unevenness of subject materials. Therefore, simple binarization and time difference methods are not always effective. As described herein, we propose an image processing method to remove temperature unevenness by calculating the difference between the original image and its Gaussian blurred image.

Introduction

Japan has many rather aged historical wooden structures. Because they sometimes deteriorate severely over time, regular inspection and renovation work are indispensable. However, in most cases, the design drawings necessary for these tasks are unavailable or nonexistent, which demands a preliminary investigation of the building structure. Moreover, historical buildings are intrinsically extremely valuable. They often strongly influence the regional economy as tourist resources. Therefore, nondestructive structural investigation techniques must be done quickly and at low cost.

X-ray imaging techniques have been used widely for nondestructive inspection of historical wooden structures. Such techniques can reveal detailed images of internal structures. However, they entail shortcomings that include large equipment, time-consuming photographic processing, use of radiation harmful to human health, and the necessity of professional technicians for photography.

Infrared thermography is used as a quick and inexpensive non-destructive inspection

technology for investigating historical structures [1][2]. In actuality, the method is most effective on wall surfaces, which can show widespread and uniform temperature changes by solar radiation. Heretofore, it has been regarded as unsuitable for structural investigation inside wooden buildings, which often have complex decorations and small temperature changes.

For this study, we applied infrared thermography using forced heating for structural investigation of indoor areas of wooden houses. Unlike solar radiation, forced heating with heating devices tends to cause temperature unevenness of subjects. Therefore, it is unsuitable to apply simple binarization method to the infrared images for extracting building structures. For this reason, we adopted an image processing algorithm that eliminates temperature unevenness by calculating the absolute difference between the original infrared image and its Gaussian blurred image [3].

Shooting with an infrared camera

The measurement target is Tsuchida house, a historical wooden structure in Akita prefecture (Fig. 1). This building was designated as a nationally important cultural property in 1973 as one of the oldest farmhouse structures dating

back to the 17th century. A thermal imager (IR-U300 M1) was used for infrared photography. Table 1 shows specifications.



Fig. 1. Exterior of Tsuchida house.

| Item | Specification |
|---|-------------------|
| Detection wavelength band | 8–12 μm |
| Number of display pixels | 320 × 240 |
| Noise equivalent temperature difference | Under 0.2 (@27°C) |

Table 1. IR-U300M1 specifications

For measurements, infrared photography of the corridor floor surface was conducted at a depression angle of 34° (Fig. 2, Fig. 3).



Fig. 2. Shooting scene with infrared camera.

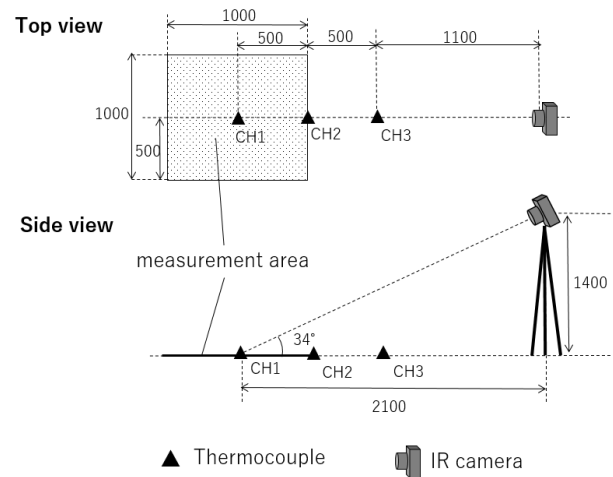


Fig. 3. Sketch of infrared shooting site.

Infrared photography was first done in a natural state. Secondly, it was performed after forced heating over the measurement area for two minutes using an electric carpet (Fig. 4). The electric carpet used for forced heating was 900 mm × 450 mm, with surface temperature of about 40 °C. The air temperature and floor temperature are shown in Table 2. The floor temperature was measured at three places using K type thermocouples (Fig. 3).



Fig. 4. Electric carpet used for forced heating.

| Measurement points | | Before heating | After heating |
|--------------------|-----|----------------|---------------|
| Air temperature | | 4.5 | 2.6 |
| Floor temperature | CH1 | 3.4 | 5.3 |
| | CH2 | 2.5 | 3.4 |
| | CH3 | 1.5 | 1.9 |

Table 2. Air temperature and floor temperature during infrared imaging (°C)

Infrared image and its image processing

Fig. 5, Fig. 6, and Fig. 7 respectively portray visible light and the infrared images before and after forced heating. The structure inside the floor was not confirmed from the visible light image (Fig. 5). However, from the infrared image taken before forced heating (Fig. 6), the floor joists were confirmed. From the infrared image after forced heating (Fig. 7), it was possible to check the nail positions from the floorboards to the floor joists.

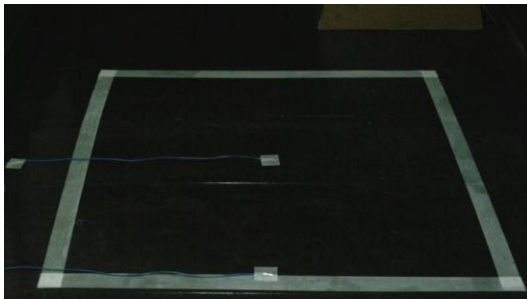


Fig. 5. Visible light image.

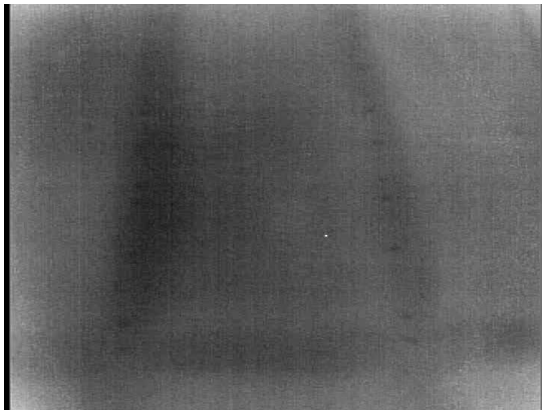


Fig. 6. Infrared image before forced heating.

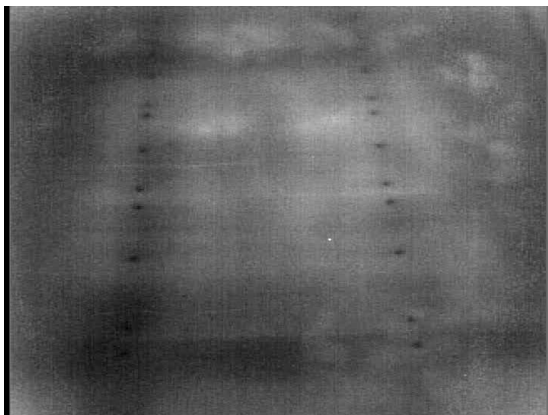


Fig. 7. Infrared image after forced heating.

The forced heating method using an electric carpet is simple, but unlike solar radiation, it tends to cause temperature unevenness. For this reason, image-processing methods such as simple binarization [4] and time difference [5] are not always effective for the automatic extraction of detection targets in infrared images. Therefore, we adopted a method to eliminate global temperature unevenness by taking the absolute difference between the infrared image and its blurred image. The algorithm used for the image processing is the following:

1. Calculate the Gaussian blurring of the original image.
2. Calculate the absolute difference between the original image and the blurred image obtained in 1.
3. Binarize the image obtained in 2.
4. Apply morphology operations (Opening, Closing) [3] and small island removal to the image obtained in 3 for noise removal.

The algorithm above is presented in Fig. 8. By changing parameters in processes 1 and 4, it is possible to adjust the detection target size.

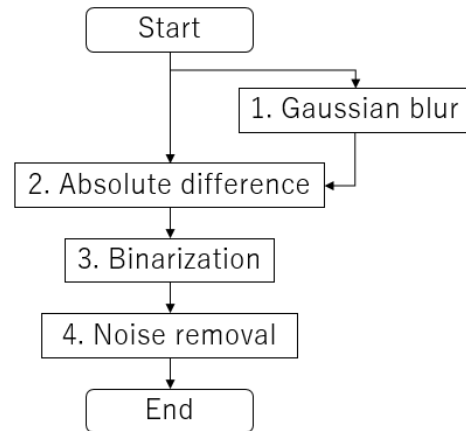


Fig. 8. Flowchart of image processing algorithm.

Table 3 shows the parameters applied to the infrared images processing.

| Target | Gaussian blur size | Morphology filter size | Small island removal area |
|--------------|--------------------|------------------------|---------------------------|
| Floor joists | 301 * 301 | 6 * 6 | < 500 |
| Nails | 61 * 61 | 3 * 3 | < 20 |

Table 3. Parameters in infrared image processing

Fig. 9 and Fig. 10 respectively depict extracted images of floor joists and nails obtained by application of this image processing algorithm to Fig. 6 and Fig. 7.



Fig. 9. Image extracting floor joists from Fig. 6.

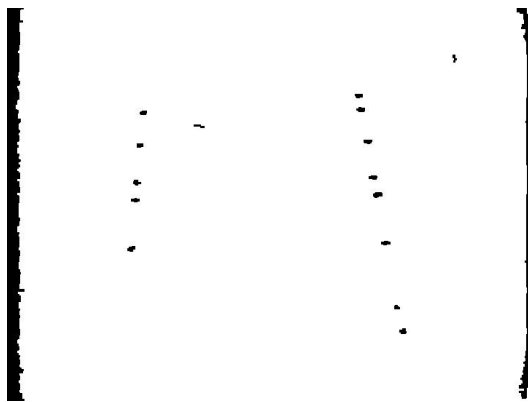


Fig. 10. Image of extracted nails from Fig. 7.

The extraction of floor joists in Fig. 9 is insufficient to remove the noise, probably because the temperature difference between the rooms and under the floor was insufficient. A clear infrared image was unobtainable. A future task is development of an image processing algorithm that appropriately extracts floor joists from such indistinct images.

Nail extraction in Fig. 10 was able to detect the nail positions reliably, but some false detection occurred. Results show that this algorithm is effective for infrared images with temperature unevenness caused by forced heating.

Conclusion

This study revealed the possibility of detecting an object with specified size automatically from the absolute difference of the original image

and the blurred image, even if the infrared image has temperature unevenness caused by forced heating. Results also show that infrared thermography is applicable to investigate indoor structures of historical wooden buildings, which was considered difficult using this method. Moreover, further system development might be done to investigate structures independent of field investigator skill and to survey structures automatically using robots.

To improve the extraction accuracy of this method, sharper infrared images must be obtained; also, the image processing algorithm must be improved. Regarding the former, photographing in the summer might be done, when a larger amount of heat is obtained. Regarding the latter, accuracy might be enhanced by adding a basic structure extraction function such as a straight line and ellipse to the image processing algorithm.

Acknowledgements

This work was supported by JSPS KAKENHI Grant Number 16K12856. We would also like to express our gratitude to Kiichiro Tsuchida, the owner of Tsuchida house.

References

1. Avdelidis, N. P., & Moropoulou, A. (2004). Applications of infrared thermography for the investigation of historic structures. *Journal of Cultural Heritage*, 5(1), 119-127.
2. Grinzato, E. (2012, April). IR thermography applied to the cultural heritage conservation. In *18th World Conference on Nondestructive Testing*.
3. Shapiro, L., & Stockman, G. C. (2001). Computer vision. 2001. ed: Prentice Hall.
4. Shimoi, N., Takita, Y., Nonami, K., & Wasaki, K. (2001). Smart sensing for mine detection studies with IR cameras. In *Computational Intelligence in Robotics and Automation, 2001. Proceedings 2001 IEEE International Symposium on* (pp. 356-361). IEEE.
5. Wasaki, K., Shimoi, N., Takita, Y., & Kawamoto, P. N. (2001). A smart sensing method for mine detection using time difference IR images. In *Multisensor Fusion and Integration for Intelligent Systems, 2001. MFI 2001. International Conference on* (pp. 133-139). IEEE.

Compressive sensing and space applications in the SWIR-FIR spectral range

D. Guzzi¹, S. Baronti¹, D. Coltuc², F. Garoi³, I. Iordache³, D. Labate⁴, C. Lastrì¹, V. Nardino¹,
M. Miranda⁵, I. Pippi¹, A. Zuccaro Marchi⁵, V. Raimondi¹

¹ CNR – IFAC, Via Madonna del Piano 10, 50019 Sesto Fiorentino, Italy
Tel.: +39 055 5226379, v.raimondi@ifac.cnr.it

² University Politehnica of Bucharest, Research Centre for Spatial
Information, Splaiul Independentei 313, 060032 Bucharest, Romania

³ National Institute for Laser, Plasma and Radiation Physics,
Strada Atomistilor 409, 077125 Magurela, Romania

⁴ Leonardo-Company S.p.A., Via Officine Galileo 1, 50013 Campi Bisenzio
(FI), Italy

⁵ ESA-ESTEC, Keplerlaan 1, NL-2200AG Noordwijk, The Netherlands

Compressive Sensing (CS) is a novel signal acquisition technique based on the sparsity of many natural signals. If prior knowledge about the signal's sparsity is available, the signal can be reconstructed using fewer samples than those envisaged by Shannon's Theorem. In particular, space applications in the SWIR-FIR spectral range are an appealing field for CS techniques due to the possibility to use of a single element detector instead of 2D arrays and to reduce requirements in terms of payload budgets and downlink requirements. Here we discuss several payload configurations that could benefit from CS approach and perform a pros and cons analysis.

Introduction

The common approach to signal sampling follows Shannon-Nyquist theorem. The theory of Compressive Sensing (CS) has provided a basis for a different approach to data acquisition, overcoming the Shannon-Nyquist sampling theorem. CS theory predicts that - if prior knowledge about the signal's sparsity is available - the signal can be recovered from far fewer measurements than those usually considered necessary [1, 2]. CS has fostered the development of several novel applications and instruments [3-5]. The single-pixel camera is probably the first implemented prototype based on this approach [6]. In the single pixel camera, a single photodetector element is used for imaging instead of an array detector. The technique used to sense images with a single detector relies on a 2-D Spatial Light Modulator (SLM), which enables use of a single photodetector. This characteristic can play a crucial role in the infrared (IR) spectral range where detection arrays/matrices either have a poor performance in comparison with single

element detectors or are very expensive or not available. Besides the possible advantage in terms of detector availability and performance, CS technique can provide other advantages in terms of payload budgets as well as memory and downlink requirements, since data are acquired intrinsically compressed and thus the compression board is not needed. In particular, Single pixel camera architecture essentially relies on the use of a SLM, which physically performs the scalar product between a random pattern and the incoming light, and on an optical assembly that concentrates the radiation on a single element detector. Recently, the European Space Agency (ESA) has funded a project - Optical CS Technologies for Space Applications (OCS-TECH) - to investigate the potential of CS-based optical instrumentation for space applications and to demonstrate the existence of substantial advantages - with respect to a traditional system - in terms of the resources required for its development. In the frame of this project, Space Science (SS), Planetary Exploration (PE) and Earth Observation (EO) applications that could benefit from CS technology were selected and

some instrumental concepts for space applications in the IR spectral range were identified. In this paper, we report a pros and cons analysis of the CS approach in the IR spectral region and a description of two instrumental concepts: the first configuration, working in the MIR-TIR region, is conceived for (PE) applications; the second one, operating in the THz region, can find application in (SS) and (EO) applications, such as atmospheric studies.

State of the art of CS system from SWIR to FIR

Cameras for IR imaging are significantly more expensive than the ones in the visible (VIS). In the last decade, CS has emerged as a potential means to produce less costly IR cameras. InView Technology Corporation presently produces and commercializes SWIR Camera based on CS technique [7]. Physical Sciences Inc. is developing a longwave infrared (LWIR) compressive sensing hyperspectral imager based on single pixel architecture [8]. High spatial and temporal resolutions have been obtained by using an array of single pixel cameras [9]. A different solution consisting in a lensless compressive imaging was proposed for VIS or IR ranges [10], while a Zeiss Axiovert 200 microscope was modified in order to have an additional single pixel camera configuration and to images simultaneously in VIS and SWIR [11]. Several imaging applications involve the use of IR radiation and for some of them the CS approach and a single pixel camera configuration can be a convenient alternative to the use of array detectors. As for the THz range, presently there are not commercial CS based imaging systems, although some prototype cameras have been developed. The major problem is represented by the SLM since DMD and LCoS do not operate at long wavelengths like THz. The first attempt to implement a THz modulator consisted in mechanical solutions [12-13]. The resolution, however, was low (up to 42x48 pixels). The main drawback of the mechanical solution is the existence of moving parts in the instrument. Recently, Si and Ge based modulators -

optically controlled through a DMD or electrically driven - were used in single pixel camera prototypes with resolution up to 32x32 pixels [14-15]. The transmissivity at THz radiation of the Si wafer is controlled by a DMD that works either in IR or VIS. The drawback of the Si or Ge based solution is the low modulation depth, which is intrinsic to the material. A more promising solution that overcomes the problem of low depth modulation is the use of metamaterials [16]. Images of 8x8 pixels have been obtained using this solution. The latest, and apparently the most efficient, solution for the THz modulators is represented by graphenes [17]. Their development is at level of proof-of-concept with resolutions of 2x2 pixels. No single pixel camera prototypes including such modulators are reported.

Instrumental concepts and applications

In general, the potential of CS-based instrumentation is better exploited in two cases: (1) multispectral/hyperspectral devices, where the sensor throughput is high and the storage and transmission of the acquired data can be challenging, so that a compression board is needed;

(2) detection arrays/matrices very expensive or not available.

In the first case, CS approach becomes very appealing in those missions with very strict limits in data downlink, such as PE missions. A first instrumental concept is a CS-based MIR-TIR hyperspectral imager housed aboard a rover for mapping emissivity and temperature in extraterrestrial environment, while a second instrumental concept is a CS-based MIR-TIR hyperspectral imager on orbiter for characterizing atmospheric compounds absorbing in the IR spectral range and mapping planetary surfaces. The use of CS technique reduces power consumption and detector throughput. The latter circumstance is particularly important in the development of rover instrumentation because it implies lower memory capacity and narrower down-link

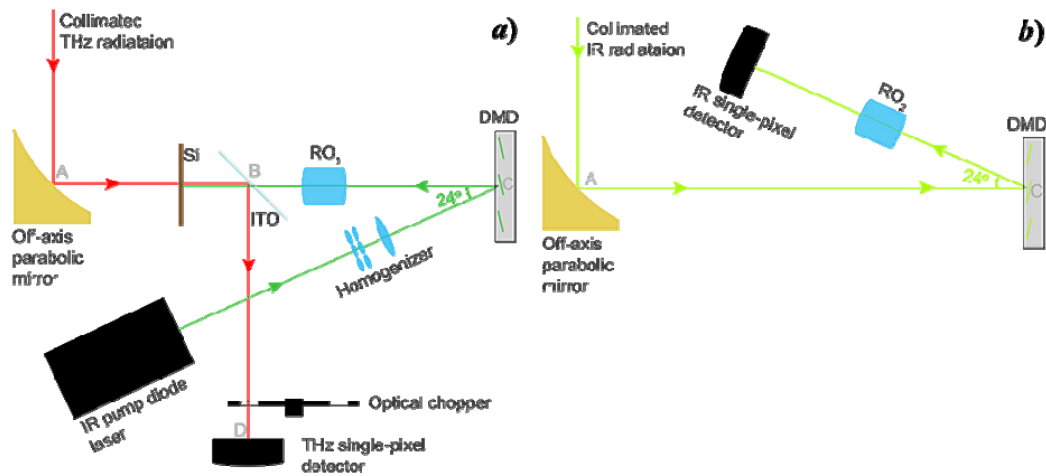


Fig.2 Single-pixel imager with the two working modes represented separately: a) THz single-pixel imaging system; b) IR single-pixel imaging system.

bandwidth. Both CS based instrument concepts can employ a low noise single pixel HgCdTe detector, instead of an array of photodetectors, reducing considerably the cost of the detection unit. HgCdTe detectors enjoy higher frame rate and are more sensitive than other cheaper competitor devices, but they have also some limitations: actually, the LWIR HgCdTe detectors need to be cooled to temperatures near that of liquid nitrogen (77°K) in order to reduce noise. This limitation does not exist for MWIR HgCdTe detectors since they can be operated at temperatures accessible to thermoelectric coolers with a small performance penalty. As far as SLM is concerned, DMD chips working in the MIR - TIR spectral range are not commercially available; however, a modified DMD with a ZnSe window was used for the implementation of a compact, TIR spectral imager for chemical-specific detection [18]. The efficiency of DMD at those wavelengths could be limited due to the dimensions of square micro-mirrors, which are comparable with the wavelengths in the considered spectral range. As far as the second application is concerned (CS-based MIR-TIR hyperspectral imager on orbiter), there are several constraints on modulator speed, detector frame rate and integration time matching the satellite speed, being the platform an orbiter.

Another promising instrumental concept is a dual use instrument working either as a THz

imager with a Si wafer based optical modulator or as an IR imager with a DMD-based modulator. Measuring THz range radiation opens the way to several SS applications, such as: the sensing of low and very low temperature gas of outer space, the detection of “protostars”, the acquisition of spectral signatures for the interstellar dust clouds. Moreover, it can give an insight of the early universe composition by observing the red shift towards THz. In Earth Observation (EO), THz radiation at atmosphere limb is useful for understanding the stratospheric ozone chemistry and the pollution existing in the upper troposphere. The proposed CS-based instrument concept is an imaging system that may be employed either in THz or IR range. It is useful in sensing low and very low temperature gas of outer space, detecting "protostars" or measuring spectral signature of the interstellar dust clouds. The imager has two working modes - THz or IR detection - accommodated within the same arrangement, as they make use of common elements. In THz working mode (Fig. 2a), the imager achieves spatial modulation on a high resistivity silicon wafer via an IR diode laser and a DMD. Photoexcitation of free carriers in the semiconductor is the physical principle used to spatially modulate THz transmission through the Si wafer. An Indium Tin Oxide (ITO) thin film deposited on glass is used as a dichroic mirror, to reflect THz radiation and transmit IR

one. Therefore, incident THz radiation passes through the semiconductor wafer (acting as a SLM at these wavelengths), is reflected on the ITO film and sent to the single-pixel pyroelectric detector. IR pump radiation is homogenized, reflected off the DMD's micro-mirrors array and then imaged on the Si wafer at the desired dimension. The IR pump radiation comes from a 980 nm wavelength diode laser with a modulation output power of 2.5W. Resulting "IR radiation masks" are projected on the Si wafer at an increased size by 1.3 times, via relay optics (RO). The system has a resolution of 32x32 pixels for an imaging area of 13 mm². When IR radiation is detected (Fig. 2b), the components Si, ITO and RO₁ must be removed from the path of the incident radiation and the DMD's micromirrors directed to reflect in the opposite direction. Relay optics RO₂ is introduced to focus the IR radiation on the IR single-pixel detector. This instrument concept could be implemented also as a pushbroom sounder for the measurement of chemical species in the Earth's upper troposphere, stratosphere and mesosphere.

Conclusions

CS-based instrumentation can provide solutions for space applications to reduce sensor throughput and payload budgets, especially when transmission and storage of all acquired data are demanding. In addition, CS single-pixel architecture can be an interesting alternative to the use of array detectors in the SWIR-FIR, which can be very expensive or even not available.

Acknowledgements

The OCS-TECH project (ITT AO/1-8235/15/NL/RA) was funded under ESA ESTEC contract n.4000116423/15/NL/BJ/gp. The view expressed in this publication can in no way be taken to reflect the official opinion of the European Space Agency.

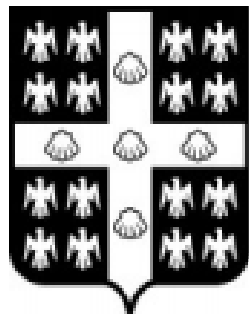
References

1. Emmanuel J. "Compressive sampling." Proceedings of the international congress of mathematicians. Vol. 3. 2006
2. M. Abolbashari, et al. High dynamic range compressive imaging: a programmable imaging system, *Opt. Eng.* 51(7), 071407, (2012).
3. L. Li, et al. Gated viewing laser imaging with compressive sensing, *Appl. Opt.* 51(14), (2012).
4. G. Howland et al. Compressive sensing LIDAR for 3D Imaging, *OSA/CLEO*, (2011).
5. R. Baraniuk. Single-pixel imaging via compressive sensing, *IEEE Trans. Signal Process.* 83-91, (2008).
6. <http://dsp.rice.edu/research/compressive-sensing>
7. <http://inviewcorp.com/products/shortwave-infrared-swir-cameras>
8. H. Chen, et al. FPA-CS: Focal plane array-based compressive imaging in short-wave infrared. In *Computer Vision and Pattern Recognition (CVPR)*, IEEE Conference on (pp. 2358-2366), 2015.
9. G. Huang, et al. Lensless imaging by compressive sensing. In *Image Processing (ICIP)*, 20th IEEE International Conference on (pp. 2101-2105). 2013.
10. J. R. Dupuis, M. Kirby, & B. R. Cosofret. Longwave infrared compressive hyperspectral imager. In *SPIE Sensing Technology+Applications* (pp. 94820Z-94820Z). 2015.
11. N. Radwell, et al. Single-pixel infrared and visible microscope. *Optica* 1.5: 285-289. (2014).
12. W. L. Chan, et al. A single-pixel terahertz imaging system based on compressed sensing. *Applied Physics Letters* 93.12 (2008): 121105.
13. O. Furxhi & E. L. Jacobs. Image plane coded aperture detectors for THz imaging. In *Microwave Symposium Digest (MTT)*, 2012 IEEE MTT-S International (pp. 1-3).
14. S. Augustin, et al. Compressed sensing in a fully non-mechanical 350 GHz imaging setting. *Journal of Infrared, Millimeter, and Terahertz Waves* 36.5: 496-512, (2015).
15. D. Shrekenhamer, C. M. Watts, & W. J. Padilla. Terahertz single pixel imaging with an optically controlled dynamic spatial light modulator. *Optics Express* 21.10:12507-12518. (2013).
16. C. M. Watts, et al. Coded and compressive THz imaging with metamaterials. *SPIE OPTO*. International Society for Optics and Photonics, 2014.
17. N. Kakenov, et al. Graphene-enabled electrically controlled terahertz spatial light modulators. *Optics letters*, 40(9), 1984-1987. (2015).
18. M.J. Fox, et al. A compact, thermal-infrared spectral imager for chemical-specific detection, *Proc. SPIE* 8870, *Imaging Spectrometry XVIII*, 887004. (2013).

Image Processing

AITA 2017

Québec City, Canada
September 27th - 29th, 2017



UNIVERSITÉ
LAVAL

ACTIVE IMAGE PROCESSING FOR WOODEN TRADITIONAL STRUCTURE USING IR CAMERAS

N. SHIMOI¹, C. CUADRA², K.NAKASHO³, H.MADOKORO⁴

¹ Akita Prefectural University, shimoi@akita-pu.ac.jp Ebinokuchi Yurihonjo, 015-0055 Japan
All authors have the same affiliation: ²carlos@akita-pu.ac.jp, ³ nakasho@akita-pu.ac.jp,
⁴ madokoro@akita-pu.ac.jp

This paper presents a proposal of an IR image camera system used for detecting nails in traditional wooden structures. Wooden structures face high risk of damage from many investigative methods. Therefore, detection must be conducted with the greatest care. Using infrared ray (IR) cameras, nails embedded in structural members can be detected safely. For embedded nails, detection can be done if the peripheral temperature difference between the nail and wooden boards is sufficiently large. Japan, as an advanced nation in terms of IR sensor technology, should promote surveys and studies that protect cultural properties.

Introduction

Japan has many historical wooden structures. To preserve its historical wooden buildings, it is first important to ascertain their value and understand their condition [1]. Elucidating the construction methods and manufacturing technology of wooden buildings is therefore crucially important for restoration work. In fact, without such knowledge, restoration of these cultural properties is not permissible. Therefore, advanced technology and detailed materials are necessary. Nevertheless, because such structures have no design drawings, understanding the structure at the time of repair presents great difficulties. When repairing historical wooden buildings, judgment of restoration is done visually as the first primary diagnosis. In many cases, the repair method is determined mainly according to this judgment. However, if detailed data of the member and joint structure are necessary, a secondary diagnosis is made. For it, such methods are applied as X-ray penetration tests, hit tests, ultrasonic imaging, and corrosion diagnostic tests, [2]. Recently, a method of visualizing and diagnosing the structure from the wood surface to a certain depth has been assessed [3][4]. This technique uses image processing with

millimeter waves or terahertz waves. In historical wooden traditional structures, it is extremely important to disassemble the tree structure safely when using nails at the joint. Therefore, to solve such problems, we propose active image processing technology and a method to detect hidden nails using IR cameras [5]. This infrared imaging camera uses a sufficiently large temperature difference between the nail and the wooden board at ambient temperatures. Furthermore, the method we propose is to expand the temperature relation forcefully between the nail and the structural plate. Figure 1 shows a model traditional wooden structure and test specimen.



(1) Model of shrine (2) Model of test specimen

Fig. 1. Traditional wooden structure and test method for detecting nails.

IR Camera image processing system theory and configuration

Fig. 2 presents a basic configuration block diagram of the experimental IR camera system. Measurement results from the IR camera and processing signals are sent simultaneously to the information processing segment. After processing information, the picture information is sent to an exclusive picture indicator. The operator can then find the nail positions [5].

Generally, even cold objects emit energy by infrared radiation. Formula (1) shows Planck's radiation law. Formula (2) shows Boltzmann's law for energy radiation [6].

$$W_{\lambda b} = \frac{2\pi hc^2}{\lambda^5 \{ \exp(hc/\lambda kt) - 1 \}} \times 10^{-5} \text{ [Watts/m}^2 \cdot \mu\text{m}] \quad (1)$$

$W_{\lambda b}$: black body radiation spectroscopy
(λ wave)

c : velocity of light ($=3 \times 10^8$ m/s)

h : Planck's constant ($=6.6 \times 10^{-34}$ J.s)

k : Boltzmann constant ($=1.4 \times 10^{-23}$ J/K)

t : absolute temperature of blackbody (K)

λ : wavelength (m)

$$W_b = \sigma t^4 \text{ [Watts/m}^2] \quad (2)$$

W_b : integral of black body radiation from
: Planck's formula from wavelength 0 to ∞
 σ : Boltzmann's constant (5.7×10^{-8} Watts/m²)
 t : absolute temperature of blackbody (K)

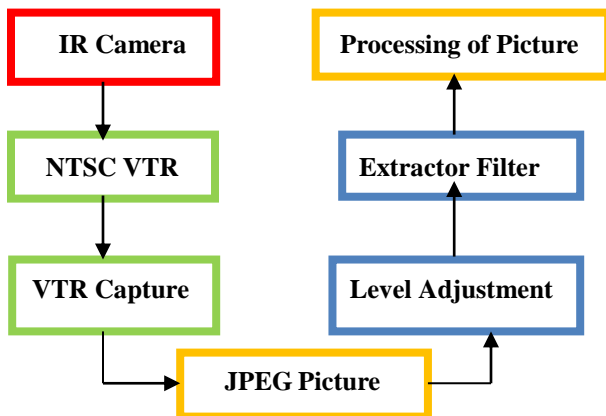


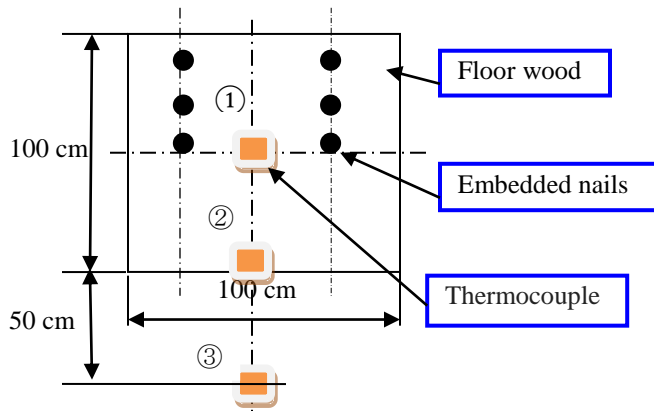
Fig.2. Configuration of the block diagram of the experimental system using an IR camera.

From these equations, it is apparent that all energies increase linearly with temperature, but the wavelength of the peak brightness value becomes shorter. The only factor deciding the temperature of radiation is the black body temperature. It exists in a very wide spectrum of frequencies and has a maximum value result. For room temperature 20 °C (ca. 300 K) the energy distribution has a peak value of approx. 10 μ m. Furthermore, when considering the penetration of energy of different wavelengths through the atmosphere, the atmosphere attenuates passing zones of 3–5 μ m and 8–12 μ m less. They can be regarded as suitable frequency zones for short-distance infrared rays [5]. However, when these two frequencies are compared, the 8–12 μ m zone is more promising for mine detecting sensors than the 3–5 μ m zone for reading measurements near the peak value at room temperature.

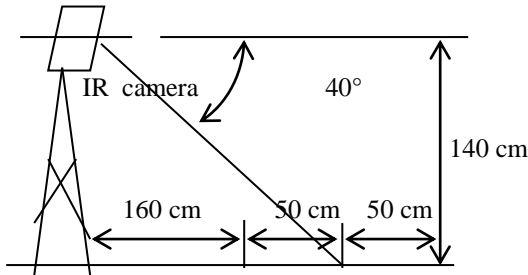
Experimentation methods

Fig. 3 portrays the experimental configuration. On the day of experimentation, room conditions were moderate with temperature of 3.1 (°C). Figure 3(a) shows that the nails were embedded in floorboards through all seasons and many years. Measurements began at 9:00 a.m. A hot carpet of 40°C was spread evenly on the floorboard surface of the area to be measured for 2 min. Immediately thereafter, measurements were taken for 4 min. Image data were recorded using an 8–12 μ m zone infrared camera (IR-U300M1; Mitsubishi ?? more information needed >) and a visual VTR camera to show the changing conditions. Figure 3(b) shows the change in the floorboard surface temperature near the nails. The embedded nails were of old steel type composition. Almost all embedded nail heads are cylindrical. Detecting this shape using IR is extremely valuable. Because of the effects of wood, it is difficult to detect embedded nails efficiently based on simple binary processing using threshold values. Moreover, because wood floor board temperatures vary by region, we must adjust the lamination level of the IR camera. We already know that it is possible to detect embedded

nails based on radiated heat when the peripheral temperature differences between the floor wood board and nail object are sufficiently large to sense. However, a problem exists for the reverse phenomenon, by which the temperature of the wood floorboard begins to rise after the wood floor board surface is heated, which occurs in an extremely short time. Therefore, when IR camera images are taken in a region outside the embedded target nails, some real time method is necessary to process pictures before and after the reverse phenomenon.



(a) Measurement area configuration

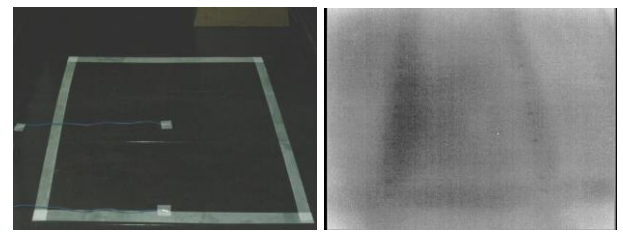


(b) IR Camera configuration

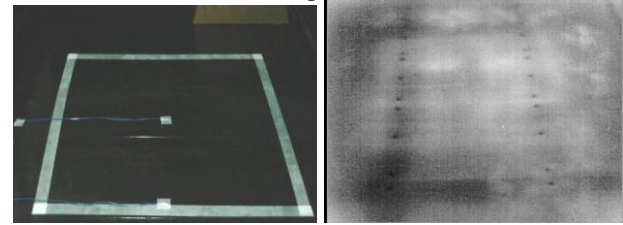
Fig. 3. Experimental configuration measurement.

Overall Evaluation of the System

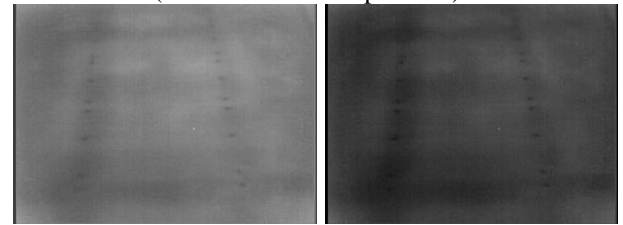
Fig. 4 portrays two-dimensional temperature images of nails taken using the infrared camera at selected intervals immediately after heating the wooden floor boards using 40°C with a hot carpet and at room temperature. Figure 4(a) shows that heating was accomplished evenly over the wooden floor board surface where the nails were embedded.



(a) Visible ray image and IR image
(Room temperature)



(b) Visible ray image and IR image by using heat
(1 minute after temperature)



(c) IR image by using heated, 3 minutes and 4 minutes
after wood board temperature

Fig.4 Images from Visible ray and IR cameras

For nails embedded near the wooden boards, images taken after the 1 min mark appeared the most clearly. Panel (b) shows that after 3 min, the image becomes indistinct. After 4 min, it is no longer impossible to distinguish the mine target images. This corresponds to measurement results portrayed in Fig. 4. This result agrees with the theory that good mine location readings can be taken when the temperature gradient of the targets and the surrounding ground is large. For panel (c) the left side shows 3 min after heating; the right side shows 4 min after heating. Then binary image processing was used. We propose image control using the following conditions. Images from the IR camera are converted to 768×600 pixel gray scaled pictures of 256 gradations using frame grabber hardware.

Fig. 5 Relation between measuring time elapsed and underground mock mine temperatures.

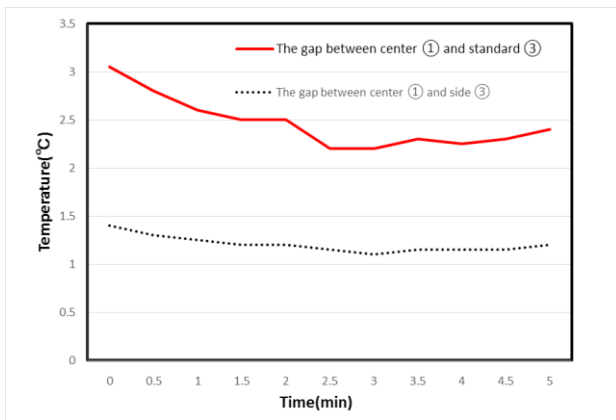


Fig. 5. Relation between woody board surface and nails embedded under the boards temperatures.

These results, which correspond to measurement results presented in Fig. 5, agree with the theory that good mine location readings can be taken when the temperature gradient of the targets and the surrounding ground is large. Additionally, we can vaguely recognize nail shapes from measurements taken after the 0–2 min mark when the temperature difference was the greatest. The result is insufficiently good compared to those of targets embedded from 1 min intervals. Sudden temperature changes of only 0–1 min produced heat areas detectable using thermometry.

Conclusion

These results emphasize the importance of enhancing nail detection information using the following image processing technology.

- (1) If difference between the radiation temperature of the wooden floor and the nail is large, the image becomes clear
- (2) To warm the wooden floor surface in winter season is effective for detecting nails.
- (3) According to the calculation, the wavelength of room temperature 20 ° C. (293 K) is about 10 μm, when the room temperature is 8 ° C and the wooden floor is 3 ° C, this difference is 5 ° C. The wavelength is expected to be about 12 μm (278 K).
- (4) Far infrared ray (8 to 12 μm) effective for measurement of low radiant heat of object.

As one means of overcoming problems related to traditional wooden structures, this work presented the development of an embedded

nail detection system and demonstrated its potential. This work serves as a stepping stone for the development of repair technology by non-destructive examination (NDE) techniques for nails embedded in traditional structures. Japan, as a nation with advanced sensor technology, should use its advanced IR sensing for imaging technologies to promote surveys and studies that will support the detection of wooden traditional structures and facilitate repair of embedded nails. Our small breakthroughs in wooden traditional house repair for preservation purposes are hoped to support many researchers seeking means of teaching detection methods that can conform to laws for protecting cultural properties.

Acknowledgements

This research was partially supported by JSPS KAKENHI Grant Number 25242033, for which we express our appreciation. We also appreciate Mr. Tsuchida's advice for producing a wooden traditional structure for outdoor experiments.

References

1. T. Itoh. Recent Advances in Studies of Wooden Cultural Properties (Aspect of wood identification and dendrochronology). The Japan wood research society Journal .Vol 51,No1.pp.67-69, 2005
2. Y.Fujii. Commentation Technical problems and future prospect for diagnosing of biodegradation in wood. Wood preservation Explanation. Vol 34,No 6, pp.256-260,2008
3. S.Tanaka,Y.Fujiwara,Y.Fujii. Effect of Diffraction on Millimeter Wave Transmission Image of Wood,Journal of the Society of Materials Science,Vol.63, No 4, pp326-330,2014
4. P.Martin, R. Collet, P. Barthelemy and G.Roussy. Evaluation of wood characteristics. Internal scanning of the material by microwave. Wood Science and Technology, Vol.21, No4, pp361-371,1987
5. N.Shimoi, Y.Takita. Remote Mine Sensing Technology by Using IR Images. American Journal of Remote Sensing issued by Science Publishing Group. Vol 2,No 4,pp.33-37, 2013
6. N. Shimoi . The Technology of Personnel Mine Detecting for Humanitarian Demining, Journal of SICE. Vol. 37, No. 6, pp. 577-583, 2001.

Quantitative evaluation of active thermography using contrast to noise ratio

M. Švantner¹, L. Muzika², T. Chmelík³, J. Skála⁴

¹ University of West Bohemia, Univerzitní 8, Plzeň, Czech Republic, msvantne@ntc.zcu.cz

² University of West Bohemia, Univerzitní 8, Plzeň, Czech Republic, muzika@ntc.zcu.cz

³ University of West Bohemia, Univerzitní 8, Plzeň, Czech Republic, chmelik3@ntc.zcu.cz

⁴ University of West Bohemia, Univerzitní 8, Plzeň, Czech Republic, jskala@ntc.zcu.cz

Active thermography is an infrared based technique for material non-destructive testing. It often uses advanced evaluation techniques based on temperature spatial and temporal changes. Results of the active thermography are contrast differences, which indicate possible defects in an inspected material. These differences cannot be quantified by temperature. This contribution is focused on active thermography results evaluation parameters and contrast to noise ratio (CNR) method, which can be used for quantitative evaluation of the results. Different results interpretation procedures are introduced. An influence of selection method for indication and reference regions and an effect of image scaling on inspection results are discussed.

Introduction

Infrared thermography [1] is a technique for analysis of objects thermal radiation, which is mostly used for measurement of temperature fields. The thermography can be sorted into passive and active and into quantitative and qualitative [2]. Active thermography [3] is the basic method for infrared non-destructive testing (IRNDT). The method can be used for inspection of inhomogeneities, delamination or other defects near the material surface. It is based on a thermal excitation of a measured object. The excitation induces a thermal process, which is influenced by defects in the object. This influence is reflected by a temperature response on an object surface. The response can be analyzed by thermographic methods and so the defects can be indicated.

A number of excitation sources, excitation methods and evaluation procedures (temperature differences evaluation, principal components thermography, TSR - thermographic signal reconstruction, pulse-phase, lock-in etc.) were developed. The theory and practice of infrared thermography used for non-destructive testing is described in detail in [4]. A methods overview of thermographic temperature measurements and

IRNDT can be found, e.g., in [5] and [6]. The most common methods of pulsed thermography, which is used in this contribution, are introduced in [7] or [8]. Active thermography is a very flexible method. It is limited to near-surface regions, however, it is usable for materials in a wide range of thermal properties [9] including for example also transparent materials [10].

The general measured quantity of thermography is mostly temperature or temperature difference. However, IRNDT results are a product of a processing of raw thermographic data and these results are mostly not in degrees. Indications of defects are demonstrated by changes of contrast or color in a thermographic testing results image (defectogram). It is sometimes useful to quantify the results with the aim to evaluate an intensity of indication or defects detectability. Contrast to Noise Ratio (CNR) evaluation is one of possible methods for results quantification.

CNR is similar to a Signal to Noise Ratio (SNR) evaluation, which is commonly used for electrical signal description. A number of equations for SNR calculations was presented [11]. In general, signal and noise are physical values (e.g. voltage) acquired from the same area or source (e.g. wire) and SNR compares a level of the signal to a level

of the background noise. SNR was also used for IRNDT [12] or magnetic resonance imaging [11], where the evaluation is based on an image analysis. In such a case, signal and noise are acquired from different regions of the same image and the designation Contrast to Noise Ratio seems to be more suitable.

IRNDT uses specific procedures for results processing. The raw thermographic sequence is processed using procedures like pulse-phase or TSR analyses. The final defectogram is then often adjusted by image processing procedures (color scale interpretation, image contrast adjustment) to enhance a contrast and highlight possible defects indications. These factors together with a missing rule for noise/reference region definition on the defectogram make a comparable quantitative evaluation of IRNDT by CNR complicated.

CNR evaluation was used for IRNDT by many authors and a comparison of raking procedures including CNR was published in [13]. However, an influence of CNR processing parameters relating to IRNDT was not summarized. In this contribution, a procedure for comparable CNR evaluation of IRNDT is suggested and some limitations of CNR evaluation for composite materials are also shown.

Methods

Influence of different post-processing procedures is demonstrated on flash-pulse thermography [7][8] results. The test sample was a carbon-epoxy composite plate with holes of different depths from one side. IRNDT inspections were performed on the side without holes, which were at the opposite side and simulated defects at different depths. The scheme of the test sample is shown in (Fig.1) and its detailed description can be found in [9]. A flash lamp with a pulse length about 3 ms and the maximum power 6 kJ with a high-speed infrared camera with 25 mm lens were used for the experiment. The IR camera framerate was 50 Hz and the acquisition duration was 20 s. The flash-pulse experimental set-up is described in more detail in [10].

The results were evaluated by TSR method based on inverse polynomial approximation and

derivation and by dynamic thermographic signal analysis (DTSA) method based on procedures described in [14] and [15].

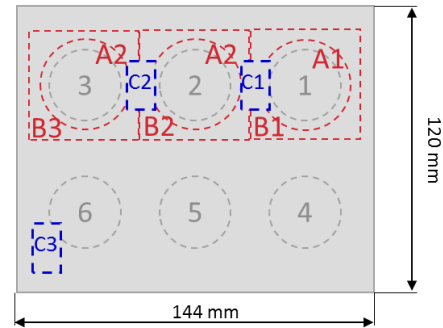


Fig. 1. Experimental carbon-epoxy composite sample scheme. Defects diameter is 30 mm and depth of defects 1-6 is 1.3, 2.3, 3.3, 1.8, 2.8 and 3.8 mm respectively.

The equation (1) was used for the CNR evaluation:

$$CNR [dB] = 20 * \log\left(\frac{|\bar{A}_S - \bar{A}_N|}{\sigma_N}\right) \quad (1)$$

It is based on ratio of difference of signal (\bar{A}_S) and noise (\bar{A}_N) mean value to standard deviation of noise (σ_N). The results are in dB and values greater than about three or five generally represents a clear indication.

The measurement was evaluated by TSR and DTSA methods. Advantages of a colored and grayscale defectogram are discussed. Influence of results image contrast adjustment is shown from the point of view of visual evaluation and evaluation by CNR. Different reference (noise) regions for CNR evaluation are selected (boundary area of different width and a region far from the selected indication) and an influence of the regions position is discussed. The results were processed by the LabIR software developed in author's laboratory.

Results and discussion

Defectograms can be interpreted as colored or grayscale images. Radiometric data (e.g. temperature) are transformed to ranges given by a corresponding color palette (e.g. 0-255 for 8 bit grayscale). Color images bring more information for a human eye, because the eye can distinguish both luminosity (brightness) and chromacity (color). They therefore seem to be more advantageous for a visual inspection.

A transformation from radiometric to image data (using a color palette) is however in general one way. A reverse transformation can be ambiguous and lossy. Thus, a radiometric data should be used for a CNR evaluation.

The raw thermographic signal and DTSA results are shown in (Fig.2). It is evident, that the experimental configuration used allows an identification of defects near the surface (1 and 4, partially 2 and 5) also on a raw thermogram. However, DTSA (Fig. 2 right) enhance the contrast as well as TSR evaluation shown in (Fig. 3) for the 1st derivative. It is also confirmed by CNR, which is 11 and -4 dB for defects 1 and 3 respectively for the thermogram and is 11 and 6 dB for defects 1 and 3 respectively for the TSA defectograms for both 1st and 2nd derivative. However, CNR for DTSA analysis is 2 and -12 dB for the defects 1 and 3 respectively, even if the defects are clearly evident. This is caused by significant small-scale noise, which takes place due to the structure of the composite and can be also found (not so significantly) on the thermogram or the TSR defectograms. Extended boundary region A1/A3 of width 6 mm was used for the noise evaluation for CNR in these analyses.

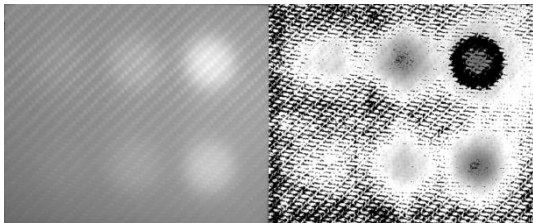


Fig. 2. Thermogram 19 s after excitation (raw signal, left) and DTSA defectogram (right).

Contrast enhancement by adjustment of limits and scale according to an area of interest is a standard procedure of IRNDT results processing. An example of such a procedure is shown in (Fig.3), where TSR 1st derivative defectograms before and after contrast enhancement are shown. Although a visual appearance changed, the CNR is the same for the tested defects 1-3 (1~11dB, 2~11dB, 3~6 dB). Based on the used CNR definition (1), the value does not change if the data in the region of interest are linearly scaled. However, if a defect or noise region data are cut to upper

(saturated) or lower intensity limit, the CNR can change significantly. Thus, such an adjustment can be used for a better visualization, but it cannot be used for a CNR evaluation.

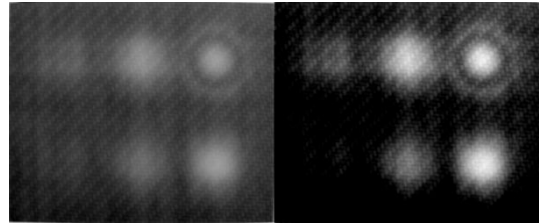


Fig. 3. 1st derivative TSR analyses without normalization (left) and normalized by B1 region (see Fig.1).

Selection of a reference region for noise data is crucial for a correct and comparable CNR evaluation. Two possible approaches can be found in literature - to extend a boundary area (e.g. defect 1 and area A1) or to use a different region far from the indication (e.g. defect 1 and region C2). Small differences of CNR evaluation are observed if an extended boundary region is used even if a different width of the region is used. For example, the CNR values for TSR 1st derivative evaluation of defect 1 are 12, 12, 12, 11 dB if the reference region width is 2, 5, 10 and 20 px respectively. The CNR values the same evaluation of defect 3 are 3, 3, 4, 6 dB respectively. This method therefore seems to be more suitable taking into account also the fact, that a contrast in a defects surrounding is important for its identification. If a region far from the defect is used, CNR evaluation can be misleading and big differences of CNR evaluation can be observed based on a reference region position. As an example, the CNR values for TSR 1st derivative evaluation of defect 1 are 12, 16 and 23 dB if the region C1, C2 or C3 respectively is selected as the reference. This approach therefore should not be preferred in the most cases.

Conclusion

Infrared non-destructive testing is mainly a visual method of defects detection, as well as other traditional non-destructive testing methods. CNR can be used for quantification of IRNDT results in some cases, as it was

demonstrated on the results of flash-pulse analyses of the carbon-epoxy composite sample. However, limitations of the CNR evaluation regarding results images processing, form of inspection results or reference region selection were shown and discussed. These parameters should be taken into account and specified properly to obtain reproducible and comparable results by the CNR evaluation.

References

The result was developed with a support of the project TE01020068 Centre of research and experimental development of reliable energy production supported by financial means of TA ČR and CENTEM PLUS (LO1402) project by financial means from the Ministry of Education, Youth and Sports under the "National Sustainability Programme I."

References

- [1] G. Gaussorgues and S. Chomet, *Infrared Thermography*. Springer Netherlands, 2012.
- [2] M. Švantner and M. Kučera, "Possibilities of IRNDT inspection of laser marked stainless steel surfaces," *NDT.net e-Journal Nondestruct. Test.*, vol. 22, no. 2, 2017.
- [3] V. Vavilov, "Thermal NDT: historical milestones, state-of-the-art and trends," *Quant. Infrared Thermogr. J.*, vol. 11, no. 1, pp. 66–83, 2014.
- [4] X. P. V. Maldague, *Theory and practice of infrared technology for nondestructive testing*. Wiley, 2001.
- [5] R. Usamentiaga, P. Venegas, J. Guerediaga, L. Vega, J. Molleda, and F. G. Bulnes, "Infrared Thermography for Temperature Measurement and Non-Destructive Testing," *Sensors*, vol. 14, no. 7, pp. 12305–12348, 2014.
- [6] C. Ibarra-Castanedo, J. R. Tarpani, and X. P. V Maldague, "Nondestructive testing with thermography," *Eur. J. Phys.*, vol. 34, no. 6, pp. S91–S109, 2013.
- [7] D. L. Balageas, "Defense and illustration of time-resolved pulsed

- thermography for NDE," *QIRT J.*, vol. 9, no. 1, pp. 3–32, 2012.
- [8] X. Maldague, F. Galmiche, and A. Ziadi, "Advances in pulsed phase thermography," *Infrared Phys. Technol.*, vol. 43, no. 3–5, pp. 175–181, 2002.
- [9] Z. Veselý and M. Švantner, "Application of IRNDT method for materials in wide range of thermal diffusivity," *NDT.net e-Journal Nondestruct. Test.*, vol. 22, no. 2, 2017.
- [10] J. Skála, M. Švantner, J. Tesař, and A. Franc, "Active thermography inspection of protective glass contamination on laser scanning heads," *Appl. Opt.*, vol. 55, no. 34, pp. D60–D66, 2016.
- [11] M. Welvaert and Y. Rosseel, "On the Definition of Signal-To-Noise Ratio and Contrast-To-Noise Ratio for fMRI Data," *PLoS One*, vol. 8, no. 11, p. e77089, Nov. 2013.
- [12] J. Gruber, K. Gresslehner, J. Sekelja, G. Mayr, and G. Hendorfer, "Signal to Noise Ratio Threshold in Active Thermography," in *Proc. 6th International symposium for NDT in Aerospace*, 2014, p. 8.
- [13] D. L. Balageas, J.-M. Roche, and F.-H. Leroy, "Comparison and ranking procedure for an objective assessment of thermographic NDE methods," in *QIRT 2016 - 13th Quantitative InfraRed Thermography Conference*, 2016, pp. 79–86.
- [14] V. P. Vavilov and S. S. Pawar, "A novel approach for one-sided thermal nondestructive testing of composites by using infrared thermography," *Polym. Test.*, vol. 44, pp. 224–233, 2015.
- [15] D. Moskal, J. Martan, V. Lang, M. Švantner, J. Skála, and J. Tesař, "Theory and verification of a method for parameter-free laser-flash diffusivity measurement of a single-side object," *Int. J. Heat Mass Transf.*, vol. 102, pp. 574–584, 2016.

Optimized setup modification for automated active thermography

J. Peeters¹, B. Ribbens¹, B. Bogaerts¹, S. Sels¹, J. Dirckx², G. Steenackers^{1,3}

¹ University of Antwerp, Op3Mech Research Group, Groenenborgerlaan 171, B-2020 Antwerp, Belgium, Jeroen.peeters2@uantwerpen.be

² University of Antwerp, Laboratory of Biomedical Physics, Groenenborgerlaan 171, B-2020 Antwerp, Belgium

³ Vrije Universiteit Brussel, Acoustics & Vibration Research Group, Pleinlaan 2, B-1050, Brussels, Belgium, gunther.steenackers@uantwerpen.be

In-line inspection of advanced components, for example a composite bicycle frame, remains a challenging task in industry. We describe a methodology which uses numerical simulations to automatically determine the best set of experimental parameters to inspect the structure on defects using active thermography. The inspection is performed using a robotic arm and advanced path planning tools to determine the optimal positions of the measurement points and excitation points. During the path planning, the directional emissivity is considered for the complex surface and a minimization of the amount of measurement points is performed. The numerical simulation optimization used a genetic algorithm and spline regression model to optimize the heat power, robot speed, camera frame rate and excitation timing to fulfil the automatic inspection. The results show that thickness evaluation of complex shaped structures is feasible.

Introduction

Active thermography is a broadly used technology to inspect large, carbon fibre reinforced plastic (CFRP) components for flaws in a fast way [1,2]. To receive accurate results on large samples, the thermal camera has to be repositioned over the structure in a way each surface is inspected with sufficient accuracy with an equal heat excitation and time resolution considering directional emissivity [3,4]. To perform these sequential experiments in a robust, repetitive way, multiple techniques are developed which mount a thermal camera and/or excitation source to a robotic arm to control the relative position and speed of the inspection unit versus the inspected structure [5–7].

Problem statement

Automatic scanning using a robotic arm is seen as an interesting way for Non-destructive Testing (NDT) of large and complex shaped components [4]. The programming of the

inspection path, speed, excitation power/duration, excitation orientation and acquisition rate is a difficult task which is highly dependent on the inspected sample geometry, material properties and interested depth resolution [3,4,8,9]. This parameter optimisation is mostly done manually by a highly qualified inspector using experience and trial and error, which is a time-consuming task for complex structures as the heat deposition and scanning speed should match the heat diffusion in the material [8].

Experimental setup

The goal is to inspect a carbon fibre reinforced plastic (CFRP) bicycle frame and estimate the tube thickness and inspect for defects like cracks and delaminations. The methodology uses a 6 degrees of freedom industrial robot arm (Kuka Kr16) calibrated in Matlab, a microbolometric thermal camera (7-14 μ m, 640x512 pixels) and an optical excitation source of 500W. The bicycle frame is painted and the tubular shapes and metallic inserts result in a challenging structure to evaluate. It is the aim

to illuminate the structure as homogeneously as possible using advanced path planning techniques. The set-up is shown in Fig. 1.



Fig. 1. Robotic thermal inspection on a CFRP bicycle frame.

Methodology

FE model updating is used to optimise the complex parameter set of the robotic thermography set-up by correlating the numerical results with NDT data. Similar methods are widely used in modal vibration inspection [10,11]. Their usage is limited in thermal optimization problems [12,13] due to the difficulties in estimating the diffusivity [3]. The numerical model is developed in Comsol Multiphysics 5.0 combining transient heat transfer with multibody dynamics and in combination with Siemens Simcenter 3D for the meshing of the composite laminates structure. The anisotropic thermal conductivity through the CFRP layers and influence on the global thermal diffusivity is considered, as further discussed in [9].

For the optimization of the experimental parameters, we use a spline-based regression technique to decrease the computational needs of the numerical simulations in combination with a genetic algorithm optimisation routine. The principle can be found in [13]. As optimisation parameters the thermal excitation power, excitation duration and thermal camera framerate are selected. Their limits are shown in Table 1.

| | Lower limit | Upper limit |
|---------------------------|-------------|-------------|
| Excitation power [W] | 100 | 500 |
| Excitation duration [sec] | 2.0 | 20 |
| Frame rate [Hz] | 5.0 | 50 |

Table 1. Optimization parameter limits

The path planning is dependent on the directional emissivity of the CFRP bicycle material. The directional emissivity is found according to [3] following formula (1).

$$\varepsilon(\theta) = \varepsilon \cdot \max(\cos(\sqrt{P_1}\theta + P_2 \cdot \pi), 0) \quad (1)$$

Where $\varepsilon(\theta)$ is the angular dependent emissivity with θ the angle tangent to the surface, P_1 and P_2 are fitting parameters which are found using a numerical model updating according to [3] as respectively 1.6 and 1.115π . The normal maximum emissivity ε is due to the paint cover equal to 0.95.

To automatically determine an efficient scanning trajectory we use a greedy ‘generate and test procedure’ similar to [14]. We first compute a set of candidate viewpoints. For every candidate viewpoint we calculate the directional emissivity in every mesh node which is dependent on the scanning angle. We select the viewpoint with the best average directional emissivity over the mesh nodes that are used in the thermal simulation. This best value is stored as current measurement state for each node. This step is then repeated until stopping criteria are met. These stopping criteria can be ‘maximum coverage reached’ or ‘maximum number of viewpoints reached’. The constraints of the articulated robot manipulator are of great importance to the final scanning trajectory. To simulate these effects we use robotic simulation software [15]. In this software we can model our complete measurement setup. This software will take care of robot specific complex path planning and collision checking.

The quality of the final path is highly dependent on the positioning of the bicycle frame because of collisions. Therefore we efficiently sample the configuration space of the bicycle frame and select the position which delivers the best scanning trajectory.

Results & discussion

As a result of the path planning and visibility study we achieved to perform sequential

measurements performing uniform automated pulsed thermography inspection. The optimized inspection path is shown in Fig.2. Using this path 85% of the full frame surface is seen in at least one measurement location. The frame was supported by placing it on a platform as seen in Fig.3. The expected emissivity on the best measurement location is rendered as a colour range on the frame. The numerical model is simplified to a uniformly distributed boundary heat source on the surface of the bicycle frame considering the emissivity map of Fig.2.

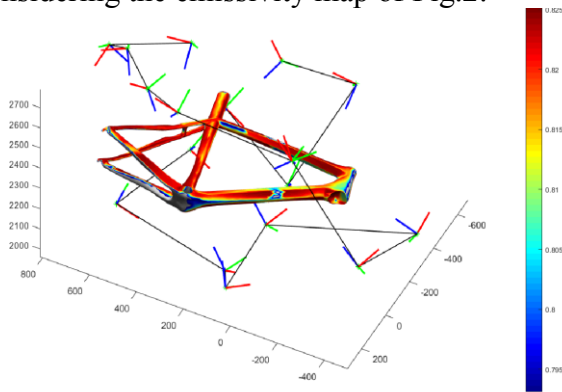


Fig. 2: Finale path covering 85% of the surface if the bicycle frame. The colorbar is the expected emissivity.

The simulated measurement setup with the field of view in one measurement location and expected radiosity is seen in Fig.3. The resulting path is optimized iteratively to a minimize path length and the amount of measurement locations.

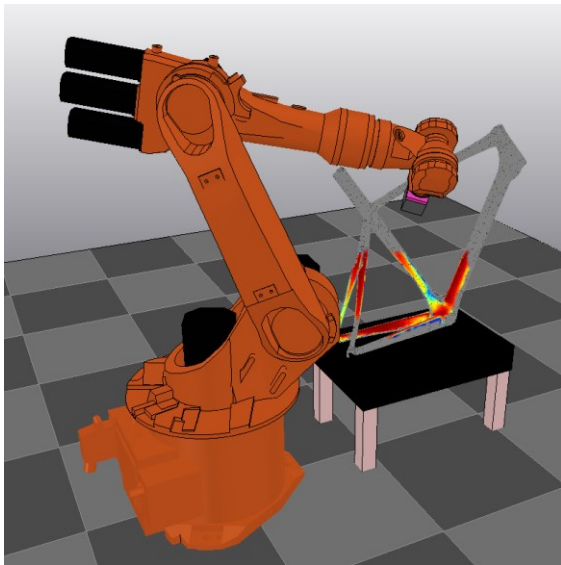


Fig. 3: Measurement setup with one example measurement pose and expected radiosity seen by the camera.

The numerical simulation model is further used to estimate the necessary excitation power and excitation pulse time needed to optimally measure the local tube thickness of the frame, considering an anisotropic fibre distribution through the laminated plies.

The numerical model which is used within the optimization routine is shown in Fig. 4. The model consists of three different material mesh collectors: one for the covering paint of 0.11 mm thick and two for the CFRP plies with a consecutive 90 degree angle between each ply and with the respective global orthotropic ply material properties. Within the initial assumption the full bicycle frame has a continuous thickness of four CFRP plies in a regular stacking: $[0,90]_s$. The material properties and heat exchange properties are defined using the numerical updating progress of [13], as described above in comparison with a preliminary static measurement.

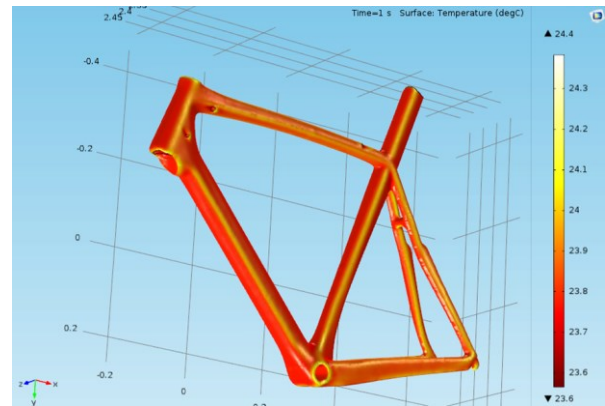


Fig. 4: Numerical finite element model result after 1 sec

The local thickness of different points is examined in comparison with some benchmark points which are possible to physical measure. The measurements are performed with an accuracy of $50\mu\text{m}$.

| | Real value | Computed value |
|--------------------------|------------|----------------|
| Saddle tube (top) [mm] | 2.64 | 2.322 |
| Head tube (top) [mm] | 4.05 | 4.052 |
| Lower tube (middle) [mm] | 2.05 | 1.95 |
| Top Tube (middle) [mm] | / | 2.21 |
| Rear Tube (middle) [mm] | / | 3.61 |

Table 2. Optimization Results

Conclusion

Within this work, it is shown that the implementation of a thermal numerical model updating routine with advanced visibility analysis and robotic path planning significantly improves the accuracy of automatic active thermography inspection without the need of excessive calibration. It is shown that thickness evaluation of complex shaped structures is feasible.



Fig. 5: Result of active thermography measurement after Principle Component post-processing.

References

- [1] X. Maldague, Theory and practice of infrared thermography for nondestructive testing, Wiley, New York, 2001.
- [2] M. Vollmer, K. Möllmann, Infrared thermal imaging: fundamentals, research and applications, Wiley-VCH, Berlin, 2010.
- [3] J. Peeters, B. Ribbens, J.J.J.J. Dirckx, G. Steenackers, Determining directional emissivity : Numerical estimation and experimental validation by using infrared thermography, *Infrared Phys. Technol.* (2016). doi:10.1016/j.infrared.2016.06.016.
- [4] C. Ibarra-Castanedo, P. Servais, A. Ziadi, M. Klein, X. Maldague, RITA - Robotized Inspection by Thermography and Advanced processing for the inspection of aeronautical components camera heating source actuator \camera heating, in: QIRT2014 Conférence, 2014: pp. 1–8.
- [5] F. Lopez, V. De Paulo Nicolau, C. Ibarra-Castanedo, X. Maldague, Thermal–numerical model and computational simulation of pulsed thermography inspection of carbon fiber-reinforced composites, *Int. J. Therm. Sci.* 86 (2014) 325–340. doi:10.1016/j.ijthermalsci.2014.07.015.
- [6] K.E. Cramer, W.P. Winfree, Thermographic detection and quantitative characterization of corrosion by application of thermal line source, *Proc. SPIE - Int. Soc. Opt. Eng.* 3361 (1998) 291–300. doi:10.1117/12.304740.
- [7] D.F. Woolard, K.E. Cramer, The thermal photocopier: a new concept for thermal NDT, in: *SPIE*, 2004: p. 366. doi:10.1117/12.541881.
- [8] O. Ley, V. Godinez-Azcuaga, Line Scanning Thermography and its Application Inspecting Aerospace Composites, in: 5th Int. Symp. NDT Aerosp., 2013: pp. 13–15.
- [9] J. Peeters, C. Ibarra-Castanedo, S. Sfarra, X. Maldague, J.J.J. Dirckx, G. Steenackers, Robust Quantitative Depth Estimation on CFRP samples using active thermography inspection & numerical simulation updating, *NDT E Int.* (2017). doi:10.1016/j.ndteint.2017.02.003.
- [10] G. Steenackers, P. Guillaume, Finite element model updating taking into account the uncertainty on the modal parameters estimates, *J. Sound Vib.* 296 (2006) 919–934. doi:10.1016/j.jsv.2006.03.023.
- [11] J.E. Mottershead, M.I. Friswell, Model Updating In Structural Dynamics: A Survey, *J. Sound Vib.* 167 (1993) 347–375. doi:10.1006/jsvi.1993.1340.
- [12] H.-C. Cheng, Y.-H. Tsai, K.-N. Chen, J. Fang, Thermal placement optimization of multichip modules using a sequential metamodeling-based optimization approach, *Appl. Therm. Eng.* 30 (2010) 2632–2642. doi:10.1016/j.applthermaleng.2010.07.004.
- [13] J. Peeters, G. Arroud, B. Ribbens, J.J.J. Dirckx, G. Steenackers, Updating a finite element model to the real experimental setup by thermographic measurements and adaptive regression optimization, *Mech. Syst. Signal Process.* 64–65 (2015) 428–440. doi:10.1016/j.ymsp.2015.04.010.
- [14] W.R. Scott, Model-based view planning, *Mach. Vis. Appl.* 20 (2009) 47–69. doi:10.1007/s00138-007-0110-2.
- [15] E. Rohmer, S.P.N. Singh, M. Freese, V-REP: A versatile and scalable robot simulation framework, in: *IEEE Int. Conf. Intell. Robot. Syst.*, 2013: pp. 1321–1326. doi:10.1109/IROS.2013.6696520.

Skeletonization and reconstruction based on graph morphological transformations

Hossein Memarzadeh Sharifipour¹, Bardia yousefi², Xavier P. V. Maldague²

¹ Department of Computer Science, Laval university, Quebec City (Quebec), Canada.
hossein.memarzadehsharifipour.1@ulaval.ca.

² Computer vision and systems laboratory, Department of Electrical and Computer Engineering,
Laval University, Quebec City (Quebec), Canada.
bardia.yousefi@ieee.org , Xavier.Maldague@gel.ulaval.ca.

Multiscale shape skeletonization on pixel adjacency graphs which corresponds to images have been proposed by Maragos et al. The interest for a graph based skeletonization that guarantees connectedness of the resulting skeleton was drawn there. We have suggested a multiscale shape skeletonization approach which extracts connected skeleton of an image. The method has been applied to skeletonization of infrared thermal images.

Introduction

Mathematical morphology is a highly used framework for binary and grayscale image processing [7,8]. The core of mathematical morphology depends upon fitting a pattern called the structuring element on an image. It extracts useful information about the geometrical structure of an image by matching small patterns into it at various locations of the image. By making use of different shapes and sizes of structuring elements, information such as connectivity, borders with regarding to the shape of different parts of the image and interrelations can be obtained.

Graph based image representations typically deal with pixel adjacency graphs, i.e, graphs whose vertices is the set of image pixels and whose edge set is determined by some adjacency relation on image pixels. In a 2D discrete grid environment the 4,6,8-connected adjacency relation applies according to the connectivity property adopted for the grid. Figure 1 indicates graph representation of 4,8-connected grids respectively. Another common graph representation of an image are Delaunay graphs which is illustrated by figure 2.

Extensive research on graph morphological transformations have led to vast applications of morphological operations for graph space in image processing and computer vision [10]. The notion of skeleton was introduced by Blum[6].

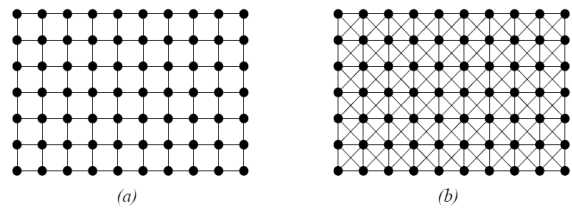


Fig.1. (a) 4, (b) 8-connected grids.

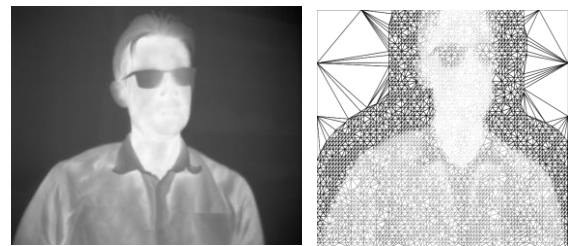


Fig.2. Delaunay graph representation.

The intuitive model suggests considering an image as a grass field. At time $t=0$ the image boundary is set to fire and the fire propagates inwards. The set of points remaining after extinguishing the fire is adopted as the skeleton of the image. Lantuéjoul employed binary morphological operations for calculating the skeleton of a binary image [15]. He has proved that the skeleton $Skel(M)$ of the image M can be extracted by:

$$skel_n(M) = (M \ominus nB) - ((M \ominus nB) \circ clB)$$

where nB denotes dilation of the structuring element B with itself iterated n times and \ominus, \circ, clB are corresponded to the binary erosion and opening and closed structuring element B respectively. This leads to an iterative approach for calculating the skeleton. The iteration

continues by n steps until $M \ominus nB \neq \emptyset$. Given the skeleton of an image, the original image can be completely or partially retrieved by,
 $M \circ clB = (\cup_{n | k \leq n \leq N : skel_n(M) \oplus nB}$
 where $q > 0$ is an integer and \oplus is the dilation operation.

By setting $q=0$, one gets a complete reconstruction of the original image. In [1], Maragos has generalized the concept of skeletonization to graphs. The binary morphological operations introduced in [7] are utilized in his approach. However, proposing a method in which the connectivity of derived skeleton is guaranteed demands a different approach since the binary morphological operations acting on graph vertices do not intuitively treat connectivity issues. We have generalized binary morphological operations with regard to graph edges introduced in [4] to structured structuring elements. Then the skeletonization procedure is formalized benefiting from these binary morphological operations. Moreover, the proposed method was employed for extracting infrared thermal samples.

Method

Given a 4,8-connected grid represented by the graph $G = (V_G, E_G)$, suppose an image is represented by $M = (V_M, E_M)$ satisfying $V_M \subseteq V_G, E_M \subseteq E_G$. The inclusion is so trivial since the image is embedded in the grid.

Inspiring from the vertex based structured graph morphology introduced in [2] and the non-structured edge based morphological operations proposed in [4], we came to the structured edge based morphological operations. We do not include any explanation on aforementioned methods for the sake of brevity but the reader can refer to indicated papers.

The idea behind the structured graph morphology based on edges is to investigate a homomorphism from the structuring graph to the source graph, find the mapping of bud edges in the source graph and adding adjacent edges to the source graph.

Given some structuring graph $S = (V_S, E_S)$, define two sets $R_S, B_S \subseteq E_S$, as the set

of roots and buds respectively. If $\theta: V_S \rightarrow V_G$ is a homomorphism and $h: E_S \rightarrow E_G$ is defined by $(u, v) \in E_S$, as $h(u, v) = (\theta(u), \theta(v))$. The reciprocal graph corresponding to S denoted by \tilde{S} is defined by $R_{\tilde{S}} = B_S$ and $B_{\tilde{S}} = R_S$. Suppose for two edges, their intersection is non empty if they share a vertex and empty otherwise. Let us define the edge adjacency function $adj: E_M \rightarrow E_G$ for an edge e in M by, $adj(e) = (\cup e_i | e_i \in E_G: e \cap e_i \neq \emptyset)$. The neighborhood function can now be defined by,

$$N_S(e|G) = (\cup h | h \text{ maps an edge in } R_S \text{ to } e: adj(h(B_S))).$$

homomorphism that maps a root edge of the structuring element to it, the neighborhood function, computes adjacent edges to the mapping of bud edges of the structuring element through that homomorphism. Now the dilation of graph G by S as the structuring element is defined as follows:

$\delta_S(M|G) = (\cup e | e \in M : N_S(e|G))$. Erosion can be calculated making use of its Galois connection with the dilation.

Definition: Let P, Q be sets. A pair of functions

$$f: \rho(P) \rightarrow \rho(Q), g: \rho(Q) \rightarrow \rho(P)$$

is called a Galois connection if for each $X \in \rho(P)$ and $Y \in \rho(Q)$ we have:

$$X \subseteq f(Y) \Leftrightarrow Y \subseteq g(X)$$

It is pretty known that dilation and erosion engage in a Galois connection. This allows to extract the axiomatization of erosion from dilation.

According to the Galois connection between dilation and erosion we can write: $\delta_S(M|G) \subseteq P \Leftrightarrow M \subseteq \epsilon_S(P|G)$.

$$\begin{aligned} \delta_S(M|G) &\subseteq P \\ \Leftrightarrow &\langle \text{Definition of dilation} \rangle \\ (\cup e | E_M \in E_M: N_S(e|G)) &\subseteq P \\ \Leftrightarrow &\langle \text{Properties of } \cup \rangle \\ (\forall e | e \in E_M: N_S(e|G) &\subseteq P) \\ \Leftrightarrow &\langle E_M \subseteq E_G \rangle \\ G \subseteq (\forall e | e \in E_G: N_S(e|G) &\subseteq P) \\ \Leftrightarrow &\langle \text{Properties of } \forall \rangle \\ G \subseteq (\cap e | e \in E_G: N_S(e|G) &\subseteq P) \end{aligned}$$

Thus the erosion can be defined by:

$$\epsilon_S(P|G) = (\cap e | e \in E_G: N_S(e|G) \subseteq P).$$

With dilation and erosion in hand, one can simply express the opening and closing. However, there is another way of specifying opening and closing called structural opening [2].

One can also define the opening transform for structured morphological graph transformations based on edges as follows:

$$\alpha_S(M|G) = \left(\begin{array}{l} \cup h|h \text{ corresponds to a homomorphism and} \\ \text{adj}(h(B_S)) \subseteq M: \text{adj}(h(B_S)) \end{array} \right).$$

This definition of opening does not deal with roots of the structuring element. It is not hard to prove that this formula is indeed an opening. To prove that we need to prove that $\alpha_S(M|G)$ is anti-extensive, idempotent and increasing.

Definition. Let $O: X \rightarrow X$ be a function acting on complete lattice X . We can say that:

- I. O is idempotent if $O^2 = O$.
- II. O is anti-extensive if for every $u \in X$, $O(u) \leq u$.
- III. O is increasing if for every, $u, v \in X, u \leq v \Rightarrow O(u) \leq O(v)$.

Proving having the anti-extensive property is straightforward since $\text{adj}(h(B_S)) \subseteq M \Rightarrow \alpha_S(M|G) \subseteq M$. The proof for increasing property is that $M_1 \subseteq M_2 \Rightarrow \alpha_S(M_1|G) \subseteq \alpha_S(M_2|G)$ because for if $\text{adj}(h(B_S)) \subseteq M_1$ for a homomorphism h , we have also $\text{adj}(h(B_S)) \subseteq M_2$. For proving idempotency we have $\alpha_S(\alpha_S(M|G)) \subseteq \alpha_S(M|G)$ by the anti-extensive property. For any edge $e \in \alpha_S(M|G)$ we have $e \in \alpha_S(\alpha_S(M|G))$. Thus $\alpha_S(\alpha_S(M|G)) = \alpha_S(M|G)$.

The primary definition of skeleton requires dilating the structuring element by itself n times. However, this concludes a complicated structuring graph. Maragos attacks this problem by first calculating erosion of the source graph by the structuring graph and repeating this n times. We also adopt this pathway. Regarding this issue, the skeleton of a picture represented by a graph can be obtained by,

$$\text{skel}_n(M) = \epsilon_S(M|G)^n - (\epsilon_S(M|G) \circ X) = \epsilon_S(M|G)^n - \delta_S(\epsilon_S(M|G)^{n+1}).$$

Where $\epsilon_S(M|G)^n$ denotes eroding the picture represented by graph M with the structuring graph S and $\delta_S(\epsilon_S(M|G)^{n+1})$ stands for opening graph M by S after performing n Intuitively for any edge e in M , if there exist an operation, by skeleton of a graph M we can reconstruct it by the following formula:

$$\delta_S^k \epsilon_S^k = \left(\cup_n |k \leq n \leq N : \delta_S^n(\text{skel}_n(M)) \right).$$

Specifying $k=0$ yields almost the exact reconstruction of the source image. The advantage of skeletonization and reconstruction built on the graph morphological transformations which rely on graph edges instead of vertices is preservation of connectivity after acquiring final results. The binary skeleton approach using graphs can be generalized to grayscale and color images. This area of research has been mentioned by Maragos. For skeletonizing a grayscale image, we assumed the edge weight of e_{ij} coinciding between nodes i, j in the graph as $|l_i - l_j|$ where l_n is the gray level of the node n . However, the method will be explained in the coming full paper since the lack of space here. For colored images it might be possible to assign vectors representing R, G, B difference of two vertices to the edge connecting them and formalize the solution.

Results

We have applied the aforementioned approach so as to obtain the skeleton of infrared thermal images. Since the implementation of the method for grayscale images remains for future research, the sample infrared images were transformed to binary counterparts and then their skeleton was calculated. Figure (3a) illustrates the sample. Its skeleton using the structuring graph isomorphic to 3*3 grid is depicted in (3d). Figure (3e) represents the skeleton of (3b) by the same structuring graph. Figure (3f) illustrates the result of reconstruction of the source image using the skeleton (3e).

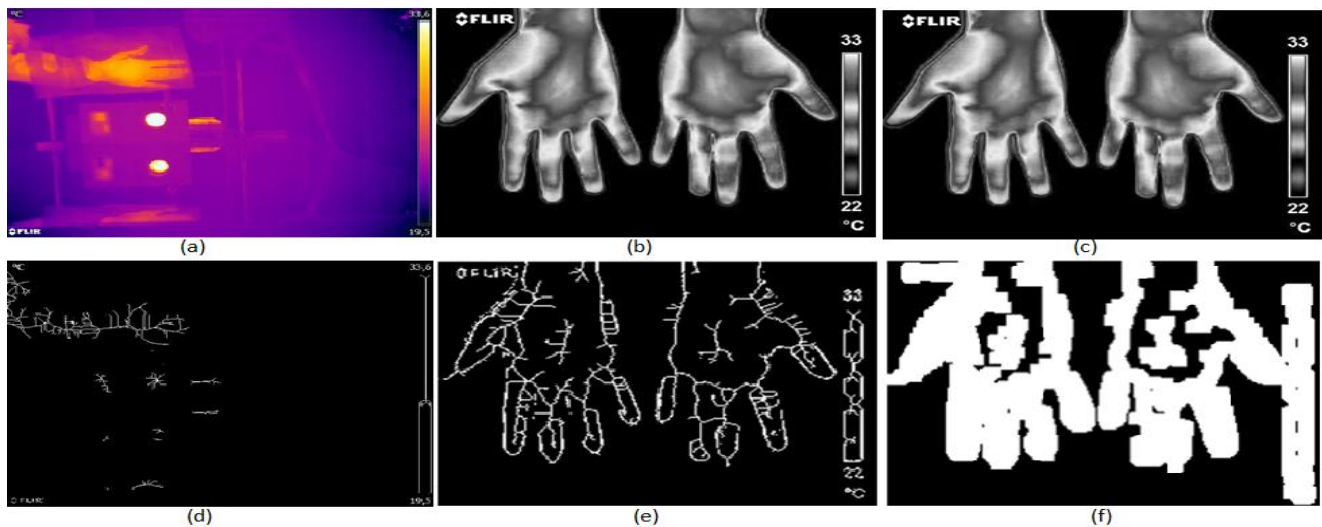


Fig.3. (d) skeleton of (a), (e) skeleton of (b), (f) reconstruction

Conclusion

A new method for extracting skeleton of a binary image using graph morphological operations based on edges. Some experiments have been issued. The reformulation of the method for grayscale images will be included in the full paper. Implementing the new method for grayscale images and generalizing the proposed method and implementing it for color images can be pursued along with the future research.

References

1. Maragos, Petros, and Kimon Drakopoulos. "Segmentation and Skeletonization on Arbitrary Graphs Using Multiscale Morphology and Active Contours." *Innovations for Shape Analysis*. Springer Berlin Heidelberg, 2013. 53-75.
2. Heumans, H. J. A. M., et al. "Graph morphology." *Journal of visual communication and image representation* 3.1 (1992): 24-38.
3. Vincent, Luc. "Graphs and mathematical morphology." *Signal Processing* 16.4 (1989): 365-388.
4. Najman, Laurent, and Fernand Meyer. "A short tour of mathematical morphology on edge and vertex weighted graphs." (2012): 141-174.
5. Maragos, Petros, and Ronald W. Schafer. "Morphological systems for multidimensional signal processing." *Proceedings of the IEEE* 78.4 (1990): 690-710.
6. H. Blum. A transformation for extracting new descriptors of shape. In W. Wathen-Dunn, 2004.
7. Heijmans, Henk JAM, and Christian Ronse. "The algebraic basis of mathematical morphology I.
8. Dilations and erosions." *Computer Vision, Graphics, and Image Processing* 50.3 (1990): 245-295.
9. Heijmans, Henk JAM. "Mathematical morphology: A modern approach in image processing based on algebra and geometry." *SIAM review* 37.1 (1995): 1-36.
10. Vollmer, Michael, and Möllmann Klaus-Peter. *Infrared thermal imaging: fundamentals, research and applications*. John Wiley & Sons, 2010.
11. Najman, Laurent, and Jean Cousty. "A graph-based mathematical morphology reader." *Pattern Recognition Letters* 47 (2014): 3-17.
12. Cousty, Jean, et al. "Morphological filtering on graphs." *Computer Vision and Image Understanding* 117.4 (2013): 370-385.
13. Maragos, Petros, and R. Schafer. "Morphological skeleton representation and coding of binary images." *IEEE Transactions on Acoustics, Speech, and Signal Processing* 34.5 (1986): 1228-1244.
14. Kresh Renato, David Malah. "Morphological reduction of skeleton redundancy." *Signal Processing* 38.1 (1994): 143-151.
15. Yousefi B. and Mirhassani S.M and Ahmadifard A. and Hosseini M. "Hierarchical segmentation of urban satellite imagery." *International Journal of Applied Earth Observation and Geoinformation* 30 (2014): 158-166.
16. Lantuejoul Christian. "La squelettisation et son application aux mesures topologiques des mosaïques polycristallines." PhD thesis, École nationale supérieure des mines de Paris, 1978.
17. Beucher, Serge. "Digital skeletons in Euclidean and geodesic spaces." *Signal Processing* 38.1 (1994): 127-141.

DEEPSIRF – SUPER-RESOLUTION INFRARED FACE IMAGES USING DEEP CONVOLUTIONAL GENERATIVE ADVERSARIAL NETWORKS

M. A. Akhloufi¹, A-C. Gueï¹

¹ Computer Science Department, University of Moncton, Moncton, NB, Canada,
{moulay.akhloufi, eag4439}@umoncton.ca

This work presents a deep learning framework based on the use of Deep Convolutional Generative Adversarial Networks (DCGAN) for infrared face image super-resolution. We use DCGAN for upscaling the images by a factor of 4x4, starting at a size of 16x16 and obtaining a 64x64 face image. Tests are conducted using two infrared face datasets operating in the near infrared (NIR) and the long wave infrared (LWIR) spectrum. We can see that the proposed framework performs well and preserves important details of the face. This kind of approach can be very useful in security applications where we can scan faces in the crowd or detect faces at a distance and upscale them for further recognition through an infrared or multispectral face recognition system.

Introduction

Upscaling the images to get a higher resolution image from its lower resolution counterpart is a complex and challenging task. This process is called super-resolution and has been widely studied by computer vision and image processing researchers [1-3]. Super-resolution can be obtained using a single image [2, 4] or multiple images [5, 6]. In this work, we are interested in the single image super-resolution.

Many classical techniques based on filtering were proposed in the past and are largely used in different applications today. They use interpolation techniques to produce new pixels based on the neighboring pixels, among them, nearest-neighbors, bilinear, bicubic, lanczos, etc. [7, 8]. These techniques tend to smooth the edges. Other techniques were developed to preserve the edges during the interpolation process [9-11].

Super-resolution using a large factor tend to reduce the texture details present in the image. In recent years, Deep learning techniques were proposed in order to upscale the image by large factors while preserving the edges and texture details. These techniques are mainly based on Convolutional Neural Networks (CNN). CNN

have known a tremendous success after the spectacular results obtained by AlexNet in the ImageNet challenge [12]. Many state of the art techniques in computer vision today are based on Deep Neural Networks. For super-resolution, deep neural networks have shown a very interesting performance in preserving the image details for large upscaling factors [13-18]. In [18], the authors propose a new approach called SRGAN (Super-Resolution Generative Adversarial Networks) to generate a photo-realistic single image super-resolution.

In this work, we propose the use of a **Deep Convolutional Generative Adversarial Networks (DCGAN)** for **Super-resolution InfraRed Faces (DeepSIRF)**. The objective is to upscale small sized image of 16x16 pixels by a factor of 4x4 to a 64x64 image. We will use thermal long-wave (LWIR) and near-infrared (NIR) images to test the proposed approach. The proposed framework can be used in a security system where facial biometrics can be used to recognize faces at a distance even if they appear at a smaller resolution in the image. The infrared or a multispectral face biometrics system [19, 20] can then be used for recognizing the upscaled version of the face image.

Deep Convolutional Generative Adversarial Networks (DCGAN) for super-resolution

The Deep Convolutional Generative Adversarial Networks (DCGAN) are a newly developed convolutional deep learning networks [21, 22], that use two types of networks (generative and discriminative) in order to train the deep network. The generative network (generator), generate images during the training and the discriminative network (discriminator) tries to classify the images as generated or real. We feed, for example, N generated images and N real images into the discriminative network and train it to classify them as real or generated. During training, errors are backpropagated through both the discriminator and the generator so that the generator can learn how to change its parameters to make the images more confusing to the discriminator. The two networks are interdependent in a way that the discriminator tries to distinguish real images from generated ones and the generator tries to create images that look real to the discriminator. This way, the generator learns the parameters that lead him to create images to fool the discriminator in considering them as real.

For super-resolution, this property of generating realistic images is used, and we train the network to generate new images by feeding lower resolution images and their higher resolution counterparts during the training phase. This way, the generator learns how to create high resolution images from the lower resolution ones.

Figure 1 gives the architecture of the DCGAN used in this work. We can see the different layers used in the generator and the discriminator networks. Also, are given the parameters of the convolution and the fractionally-strided convolution layers (or transposed convolution), where k is the convolutional filter size, n is the number of filters used, and s is the stride value.

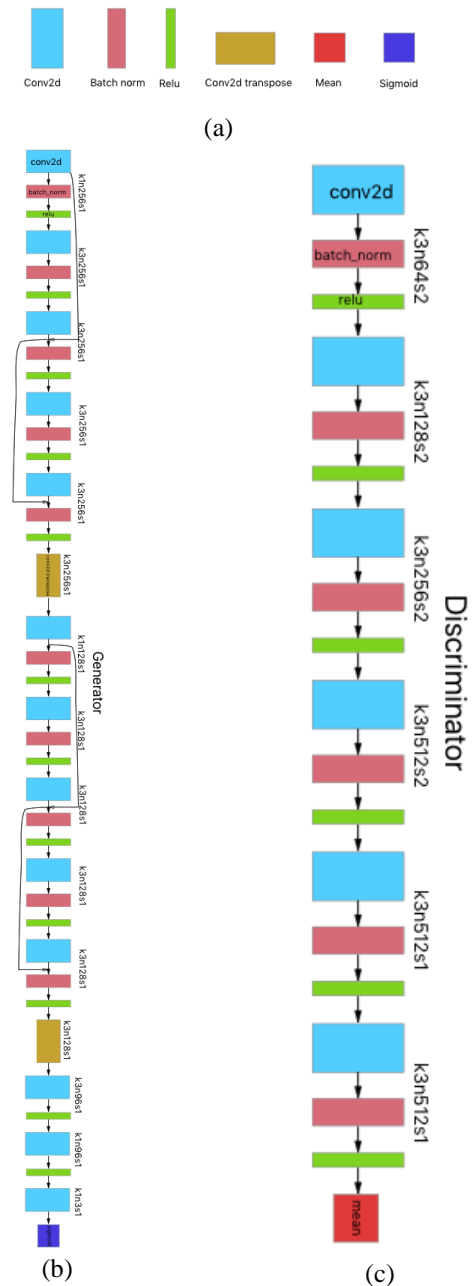


Fig. 1. Architecture of the DCGAN for DeepSIRF: (a) labels (as colors) of each block; (b) deep generator network; (c) deep discriminator network

DeepSIRF results

In this work, we used 2 infrared image datasets:

1. Terravic Facial IR Database [23]: this database contains 20 thermal LWIR sequences captured in different conditions: front, left, right; indoor/outdoor; glasses, hat. The total number of images is 18,066, in an 8-bit grayscale JPEG format and an image size of 320x240 pixels.

2. CBSR NIR Face Dataset [24, 25]: this dataset contains images captured by a near infrared (NIR) camera using an active NIR lighting (850nm). 3,940 NIR face images of 197 people were collected. The image is an uncompressed 8-bit grayscale 480x640 pixels. The dataset contains variations such as change in lighting conditions, facial expressions, eyeglasses, etc.

To test the performance of the deep super-resolution image generation, we downsampled the images to two sets of 16x16 pixels and 64x64 pixels. The 64x64 pixels resolution is our super-resolution target from the 16x16 starting size, thus the resize factor tested in this approach is 4x4 factor (16 times the starting size). 32 images were kept for test and the remaining images were used in the training of the Deep Convolutional Generative Adversarial Networks (3,908 training images for NIR and 18,034 training images for LWIR). DCGAN was implemented using Tensorflow [26]. Different learning rates and epochs were tested. The best results were obtained using a learning rate $\alpha = 0.000025$ and 8 hours fixed-time training. We use the adaptive moment estimation (Adam) [27] for optimisation during the learning phase.

Some results are shown in figure 2. We can see that the proposed approach (3rd column) gives interesting results that preserve some edge/texture details. Table 1, gives the NIR images mean quality metrics over the test set obtained for bicubic and DeepSIRF super-resolution. We can see that DeepSIRF has better signal to noise ratio (PSNR and SNR). SSIM is also better for DeepSIRF, the structural similarity (SSIM) measures the quality of reconstruction and takes into account the similarity of the edges (high frequency content). Finally, DeepSIRF has a small mean-squared error (MSE) distance from the ground truth image. The proposed approach can be further improved using a larger dataset and more training images. The performance of the proposed approach is promising and show that we can use this kind of framework for infrared super-resolution.



Fig. 2. DeepSIRF results, from left to right: low resolution image; bicubic; DeepSIRF; high resolution image (first 3 rows: LWIR; last 3 rows: NIR)

| | Bicubic | DeepSIRF |
|------------------|----------------|-----------------|
| PSNR (dB) | 25.56 | 29.59 |
| SNR (dB) | 13.18 | 17.21 |
| SSIM | 0.71 | 0.84 |
| MSE | 191.56 | 77.36 |

Table 1. Mean image quality metrics for NIR images

Conclusion

In this paper, we introduced the use of a Deep Convolutional Generative Adversarial Networks (DCGAN) for super-resolution infrared facial image generation. The face images were upsampled by a factor of 4x4. The tests were conducted in two datasets containing images in the near infrared (NIR) and the long wave infrared (LWIR) spectrum.

The analysis of the images show that the proposed framework is promising and can help improve the performance of image super-

resolution generation in the infrared spectrum. The small number and quality of infrared face images available for training was the main limiting factor. Future work includes adding higher quality infrared images and testing the performance of the proposed approach with other deep learning super-resolution approaches.

References

1. J. Yang, J. Wright, T. Huang, Y. Ma. Image super-resolution as sparse representation of raw image patches. In *IEEE Conference on Computer Vision and Pattern Recognition (CVPR)*, pp. 1–8, 2008.
2. K. Nasrollahi, T.B. Moeslund. Super-resolution: A comprehensive survey. In *Machine Vision and Applications*, volume 25, pp. 1423–1468. 2014.
3. W. Zou, P.C. Yuen. Very Low Resolution Face Recognition in Parallel Environment. *IEEE Transactions on Image Processing*, 21:327–340, 2012.
4. D. Glasner, S. Bagon, M. Irani. Super-resolution from a single image. *2009 IEEE 12th International Conference on Computer Vision, Kyoto*, pp. 349–356, 2009.
5. S. Farsiu, M.D. Robinson, M. Elad, P. Milanfar. Fast and robust multiframe super resolution. *IEEE Transactions on Image Processing*, 13(10):1327–1344, 2004.
6. S. Borman, R.L. Stevenson. Super-Resolution from Image Sequences - A Review. *Midwest Symposium on Circuits and Systems*, pp. 374–378, 1998.
7. R.C. Gonzalez, R.E. Woods. *Digital Image Processing (3rd Edition)*. 976 pages, Pearson, ISBN-13: 978-0131687288, August 2007.
8. K. Turkowski, S. Gabriel. Filters for Common Resampling Tasks. In *Andrew S. Glassner. Graphics Gems I*. Academic Press. pp. 147–165, 1990.
9. J. Allebach, P.W. Wong. Edge-directed interpolation. In *Proceedings of International Conference on Image Processing*, volume 3, pp. 707–710, 1996.
10. X. Li, M.T. Orchard. New edge-directed interpolation. *IEEE Transactions on Image Processing*, 10(10):1521–1527, 2001.
11. R. Fattal. Image upsampling via imposed edge statistics. *ACM Trans. Graphics (Proc. SIGGRAPH 2007)*, 26(3):95–102, 2007.
12. A. Krizhevsky, I. Sutskever, G. E. Hinton. Imagenet classification with deep convolutional neural networks. In *Advances in Neural Information Processing Systems (NIPS)*, pp. 1097–1105, 2012.
13. Z. Wang, D. Liu, J. Yang, W. Han, T. Huang. Deep networks for image super-resolution with sparse prior. In *IEEE International Conference on Computer Vision (ICCV)*, pp. 370–378, 2015.
14. C. Dong, C. C. Loy, K. He, X. Tang. Learning a deep convolutional network for image super-resolution. In *European Conference on Computer Vision (ECCV)*, pp. 184–199, 2014.
15. C. Dong, C. C. Loy, K. He, X. Tang. Image super-resolution using deep convolutional networks. *IEEE Transactions on Pattern Analysis and Machine Intelligence*, 38(2):295–307, 2016.
16. C. Dong, C. C. Loy, X. Tang. Accelerating the super-resolution convolutional neural network. In *European Conference on Computer Vision (ECCV)*, pp. 391–407, 2016.
17. Y. Wang, L. Wang, H. Wang, P. Li. End-to-End Image Super-Resolution via Deep and Shallow Convolutional Networks. *CoRR. arXiv preprint arXiv:1607.07680*, 2016.
18. C. Ledig, L. Theis, F. Huszar, J. Caballero, A. Cunningham, A. Acosta, A. Aitken, A. Tejani, J. Totz, Z. Wang, W. Shi. Photo-Realistic Single Image Super-Resolution Using a Generative Adversarial Network. (accepted for CVPR 2017), *CoRR. arXiv preprint arXiv:1609.04802*, 2017.
19. M.A. Akhloufi, A. Bendada. Locally adaptive texture features for multispectral face recognition. *IEEE International Conference on Systems, Man and Cybernetics, Istanbul*, pp. 3308–3314, 2010.
20. M.A. Akhloufi, A. Bendada. Fusion of active and passive infrared images for face recognition *Proc. SPIE 8705, Thermosense: Thermal Infrared Applications XXXV, 87050B (May 29, 2013)*.
21. I. Goodfellow, J. Pouget-Abadie, M. Mirza, B. Xu, D. Warde-Farley, S. Ozair, A. Courville, Y. Bengio. Generative adversarial nets. In *Advances in Neural Information Processing Systems (NIPS)*, pp. 2672–2680, 2014.
22. A. Radford, L. Metz, S. Chintala. Unsupervised representation learning with deep convolutional generative adversarial networks. In *International Conference on Learning Representations (ICLR)*, *CoRR. arXiv preprint arXiv:1511.06434*, 2016.
23. R. Mieziako. *IEEE OTCBVS WS Series Bench: Terravic Research Infrared Database*. <http://vcipl-okstate.org/pbvs/bench/>, visited May 2017.
24. *IEEE OTCBVS WS Series Bench; Center for Biometrics and Security Research (CBSR)* [www.cbsr.ia.ac.cn. AuthenMetric Co. Ltd \(Beijing\)](http://vcipl-okstate.org/pbvs/bench/), <http://vcipl-okstate.org/pbvs/bench/>, visited May 2017.
25. S.Z. Li, R.F. Chu, S.C. Liao, L. Zhang. Illumination Invariant Face Recognition Using Near-infrared Images. *IEEE Transactions on Pattern Analysis and Machine Intelligence (Special issue on Biometrics: Progress and Directions)*, Vol.29, No.4, pp. 627–639, April 2007.
26. TensorFlow. Software available from tensorflow.org, visited May 2017.
27. D.P. Kingma, J.L. Ba. Adam: a Method for Stochastic Optimization. *3rd International Conference for Learning Representations, San Diego*, 2015, 1–13, 2015.

An Improved Algorithm for Detection and Segmentation of Defects.

J. FLEURET^{1,2}, L. LEI^{1,2}, C. SHUI^{1,2}, H. ZHANG^{1,2}, C. IBARRA-CASTANEDO^{1,2}, X. MALDAGUE^{1,2}

¹Faculty of Sciences and Engineering, University Laval, Quebec City, Quebec, Canada.

²Laboratory of Computer Vision and Numerical Systems, Multipolar Infrared Vision team, Quebec City, Quebec, Canada.

In this paper we introduce an approach in order to refine and improve the detection of defects using far infrared thermography by using a two step algorithm. During the first step the phase congruency of the signal is processed. Because the phase congruency is based on the processing of a monogenic signal this step enhances the information contained in the image. However the image also contains a lot of artifacts that make it unprocessable as is. In the second step, in order to maximize the removal of the artifacts while minimizing the loss of information, we use an optimization based on the minimization of the weighted nuclear norm. This approach has been evaluated with other state of the art algorithms and several materials and seems to outperform most of them or give comparable results depending on the materials.

Introduction

The main goal in any Non Destructive Testing is to detect and segment the Regions Of Interest (ROIs) that represent a defect or an anomaly by analyzing either an image or a sequence of images. Another obvious goal is to detect such ROIs as early, accurately and condition invariantly as possible. In order to achieve this goal Infrared (or Thermal) NDT use among others, the Pulsed Phase Thermography (PPT) [4], Principal Component Thermography (PCT) [6], Difference of Absolute Contrast (DAC) [5], and Thermographic Signal Reconstruction (TSR) [7, 8]. More recently approaches such as Partial Least Squares Thermography (PLST) [3] as well as Candid Covariance Free Incremental Principal Component Thermography (CCIPCT) [10] have given noticeable results. These algorithms constitute the state of the art and have been the object of numerous publications.

The aim of the work described in this paper is to propose another approach and to evaluate it comparatively to the state of the art. This work is divided into three steps. In a first step a feature image is processed by using

monogenic signal and phase congruency approaches. Because the feature image has a very high signal over noise ratio an optimization algorithm is applied in order to reduce the noise while preserving information contained in the feature image. At last an adaptive approach is use in order to locate and segment the defects.

The comparison with the state of the art methods has been conducted over several datasets acquired under different contexts.

Conclusion

This work proposed a new method to detect defects in infrared images. It can be divided into three steps. During the first step a monogenic signal and its phase are processed from the thermal image. From these images several oriented and multiscale filters are processed in order to extract a feature image. That feature image contains most of the defects that have be detected but the signal over noise ratio is high. In order to reduce the noise while retaining the information the image is sent to the second step. The second step consists in applying a denoising algorithm using an optimization algorithm ba-

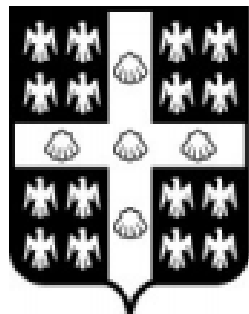
the weighted nuclear norm [9] that reduces the noise but is also able to reconstruct some of the information. At last the regions of interest are located and segmented using an adaptative approach. That method is then compared to other state of the art [2, 3, 10] methods and the results are discussed. Depending on the context of acquisition this work outperforms or gives similar results in comparison to the state of the art algorithms.

- [1] Shuhang Gu, Lei Zhang, Wangmeng Zuo, and Xiangchu Feng. Weighted nuclear norm minimization with application to image denoising. In *Proceedings of the IEEE Conference on Computer Vision and Pattern Recognition*, pages 2862–2869, 2014.
- [2] Clemente Ibarra-Castanedo, Daniel Gonzalez, Matthieu Klein, Mariacristina Pilla, Steve Vallerand, and Xavier Maldague. Infrared image processing and data analysis. *Infrared physics & technology*, 46(1) :75–83, 2004.
- [3] Fernando Lopez, Vicente Nicolau, Xavier Maldague, and Clemente Ibarra-Castanedo. Multivariate infrared signal processing by partial least-squares thermography. In *international symposium on applied electromagnetics and mechanics. Québec City, Canada*, volume 31, pages 661–666, 2013.
- [4] Xavier P Maldague. *Theory and practice of infrared vision (wiley series in microwave and optical engineering)*. Wiley, 2014.
- [5] Mariacristina Pilla, Matthieu Klein, Xavier Maldague, and Antonio Salerno. New absolute contrast for pulsed thermography. In *Proc. QIRT*, volume 5, 2002.
- [6] Nikolas Rajic. Principal component thermography for flaw contrast enhancement and flaw depth characterisation in composite structures. *Composite Structures*, 58(4) :521–528, 2002.
- [7] Steven M Shepard and Maria Frendberg Beemer. Advances in thermographic signal reconstruction. In *SPIE Sensing Technology+ Applications*, pages 94850R–94850R. International Society for Optics and Photonics, 2015.
- [8] Steven M Shepard, James R Lhota, Bruce A Rubadeux, Tasdiq Ahmed, and D Wang. Enhancement and reconstruction of thermographic ndt data. In *Proc. SPIE*, volume 4710, pages 531–535, 2002.
- [9] Jun Xu, Lei Zhang, David Zhang, and Xiangchu Feng. Multi-channel weighted nuclear norm minimization for real color image denoising. *arXiv preprint arXiv :1705.09912*, 2017.
- [10] Bardia Yousefi, Stefano Sfarra, Clemente Ibarra Castanedo, and Xavier PV Maldague. Thermal NDT applying Candid Covariance-Free Incremental Principal Component Thermography (CCIPCT). In *SPIE Commercial+ Scientific Sensing and Imaging*, pages 102141I–102141I. International Society for Optics and Photonics, 2017.

Medical

AITA 2017

Québec City, Canada
September 27th - 29th, 2017



UNIVERSITÉ
LAVAL

NEAR IR BIOLOGICAL TRANSPARENCY WINDOW AND THERANOSTICS STRATEGIES

M. D'Acunto

CNR-IBF, via Moruzzi 1, 56124, Pisa, Italy, mario.dacunto@cnr.it

The term theranostics denotes in nanomedicine the combined and simultaneous effects of diagnostic and therapy for many diseases, in a special way, in oncology. Theranostic agents take advantage of the high capacity of nano-platforms to ferry cargo and loads onto them both imaging and therapeutic functions. The resulting nanosystems, capable of diagnosis, drug delivery and monitoring of therapeutic response, are expected to play a significant role for early diagnosis of many cancers. One theranostic agent is composed by gold nanoshells (AuNSs) (a nanoparticle (NP) made of a dielectric core and an external gold layer) able to absorb light in the NIR range. The near infrared transparency window defines a range of wavelengths from 650 to 1350 nm where light has its maximum depth of penetration (some centimeters) in biological tissues. The combination of such characteristic with AuNSs could improve both diagnosis or cancer treatments. This paper critically reviews the theranostic role of AuNSs taking advantage of NIR tissue transparency.

Introduction

Theranostics denotes in nanomedicine the combined and simultaneous effects of diagnostic and therapy for many diseases, in a special way, in oncology. Theranostic agents take advantage of the high capacity of nano-platforms to ferry cargo and loads onto them both imaging and therapeutic functions. In this paper, we will focus on the application of AuNSs, for theranostic approach, i.e, the combination of early diagnosis and cancer therapy, with particular emphasis on their use *in vivo* and their potential to be translated into clinical settings. During the past decade, it has been demonstrated that NPs of 4-150nm, which are more and more smaller than normal human cells, exhibit strong interactions with biomolecules such as enzymes, receptors and antibodies, both on the surface and inside the cell [1]. By surface chemical modification, nanoparticles can be coated, functionalized, and integrated with a variety of bioconjugated moieties for selective detection and treatment.

New theranostic functionalities can be gained combining the optical properties of AuNSs with NIR transparency window. Basically, the cells are transparent to NIR light so the cellular uptake of AuNSs gives the possibility to control targeted delivery of drugs to tumor sites, controlling release of specific drugs at different locations, i.e., improving diagnosis and cancer treatments.

Materials and Methods

One specific material in this study is represented by AuNSs. AuNSs is a NP composed by a dielectric core and a layer of gold, fig. 1. When the dimensions of core and layer are approximately 100nm (core) and 20-40nm (layer), the AuNSs shows a localized plasmon resonance falling in the NIR range.

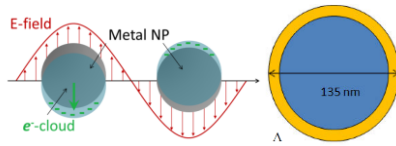


Fig. 1. Example of plasmonic effect (left) showing the displacement of the conduction electron charge cloud relative to the core in an oscillating electric field; representation of a AuNS (right, the yellow denotes the gold layer).

The methods considered in this study are based on the photothermal activation of AuNSs via NIR light, fig. 2. This activation can be used for diagnosis or (photo-)therapy. Both diagnosis and therapy are made with the same NPs eventually functionalized with biomolecular components demonstrating the capacity of theranostics as a common tool for cancer detection and treatment, fig. 3.

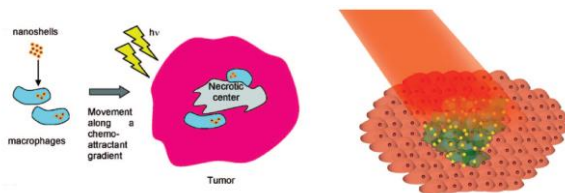


Fig. 2. Schematic sketch on the usage of AuNSs as photothermal agents for in vivo therapy for cancer treatments. The photothermal therapy combines two key components: (i) light source, such as lasers with a spectral range of 650–900nm for deep tissue penetration and (ii) optical absorbing AuNSs which efficiently transforms the optical irradiation into heat on a picosecond time scale, thus inducing photothermal ablation of the tumor cells where previously AuNSs were embedded.

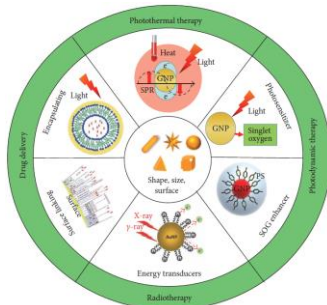


Fig. 3. Schematic example of different cancer treatments using AuNSs.

Results and Discussion

AuNSs with controlled geometrical and optical properties are the subject of intensive studies in theranostics, including laser phototherapy for cancer cells and tumors genomics, and diagnostics tools, biosensing, immunoassays, targeted delivery of drugs, DNA and antigens, optical bioimaging and the monitoring of cells and tissues.

As case study of a theranostic application, here, we consider a combination of AuNSs, NIR transparency window and near-field optics addressed to the problem of identification of AuNSs inside a cell. The ability to identify AuNSs inside cells is of vital importance for medical treatments of cancers, as well as for the investigation of inner cell organs and components. Recently, we have demonstrated the possibility to identify 100-150nm diameter AuNSs inside mouse cells using an aperture Scanning Near-Optical Microscope (SNOM) [2]

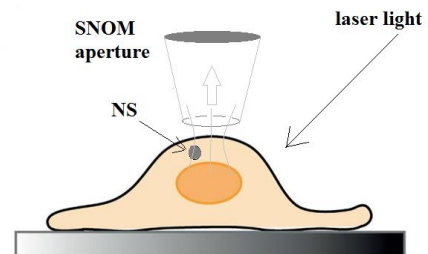


Fig. 4. Schematic sketch representing the cell+AuNS sample with the aperture SNOM.



Fig. 5. 20µm×20µm image representing an overlapping of topography of a h9c2 mouse cell recorded with a home-made aperture SNOM; with the correspondent optical map, the arrows denote the AuNSs identified within the cell. Strong-absorption points marked by

arrows in the overlapping image represent the AuNSs uptaken by the mouse cell [2].

This result shown in fig. 5 denotes the possibility to detect single AuNSs inside cells exploiting NIR transparency window. This result is particularly significant because it gives an accurate knowledge of the depth distance localization of AuNSs inside the cells. This feature is due to a combination of two properties: the NIR transparency of biological systems and the strong absorption capability of appropriate size gold nanoshells in the near-infrared range. Our results can stimulate further developments in the field of thermal treatments of cancers or near-field plasmonics investigation of biological systems.

In turn, the processes of cellular uptake of AuNSs can be now studied when the NPs are functionalized with biomolecules such as enzymes, receptors and antibodies, both on the surface and inside the cell and integrated with a variety of bioconjugated moieties for selective detection and treatments. At the lights of such results, our talk discusses the possibility of improved roles of AuNSs in theranostics applications.

Conclusion

Most biological soft tissues have a relatively low light absorption coefficient in the NIR regions, characteristic known as the tissue optical window. Over such window, near infrared light transmits through the tissues with the scattering-limited attenuation and minimal heating preventing the healthy tissues to be damaged. In this conference, starting from some experimental results previously obtained by our group on the identification of AuNSs inside mouse cells, we review the possible role of such results within the theranostics challenges improving early diagnosis and cancer treatments.

References

1. S.T. Selvan, T.T.Y. Tan, D.K. Yi, N.R. Jana, Functional and multifunctional nanoparticles for bioimaging and biosensing, *Langmuir*, Vol. 26, pp. 11631-11641, 2010.
2. M. D'Acunto, A. Cricenti, S. Danti, S. Dinarelli, M. Luce, D. Moroni, O. Salvetti, Detection and localization of gold nanoshells inside cells: near-field approximation, *Applied Optics* Vol. 55, pp. D11-D16, 2016.

Incremental Low Rank Noise Reduction for Thermal Monitoring of Human Body Using Infrared Imagery

Bardia Yousefi¹, Hossein Memarzadeh Sharifipour², Mana Eskandari¹, Clemente Ibarra Castanedo¹,
Xavier P V Maldague¹, Denis Laurendeau¹

¹Computer vision and systems laboratory, Department of Electrical and Computer Engineering,
Laval University, Quebec City (Quebec), Canada.

{bardia.yousefi.1, mana.eskandari.1}@ulaval.ca, {clemente.ibarra-castanedo, Xavier.Maldague, laurend}@gel.ulaval.ca.

²Department of Computer Science, Laval University, Quebec City (Quebec), Canada
hossein.memarzadehsharifipour.1@ulaval.ca

Thermal imagery for monitoring of body temperature provides a powerful tool to decrease the risk (e.g. of infection) for intensive care patients. It is created by traditional thermal measurement and involves many relevant researches in the field of thermography. The presented approach addresses an experiment to simulate the hospital's condition for the patients along with an automatic monitoring system for patient's temperature. The monitoring system uses an incremental low-rank noise reduction applying Incremental Singular Value Decomposition (SVD) and applies color based clustering for initialization of the Region of Interest (ROI) boundary. Then a particle filter tracks the ROI(s) for entire thermal stream (video sequence). The conducted thermal database contains 15 subjects in sitting and lying positions in front of camera and it is created to verify the robustness of our method facing motion-artifacts and in the presence of noise (2%-20% - Salt and pepper noise). The proposed approach has been tested and could track the ROI continuously and correctly, and provided considerable robustness against noise and motions, which shows the promising performance and demonstrated a confirmation for the outlined properties.

Keywords: Infrared and thermal image analysis, Incremental low rank noise reduction, Incremental Singular value decomposition, segmentation, monitoring of body temperature, particle filter tracking.

Introduction

The thermographic applications in the medicine increasingly grew [1] and there are many researches have been accomplished in different fields of medicine such as pain diagnosing and treatment monitoring [2], breast cancer [3], psychology[4], dermatology [5], dentistry [6], avian flu [7], and many other medical applications. Here the applications of thermography focus on medical prevention and monitoring. There are some similar approaches for tracking of body temperature using Kalman filter [8] and Particle filter [9]. The proposed approach creates a thermal dataset from several volunteers in lying position in front of thermal camera. For every frame, a color based segmentation performed to Region of Interest (ROI) in the thermal image. Then, this region gives the information to a particle filter to track it throughout the stream. In the next section, the methodology of the approach will be briefly

described and the proposed algorithm will be presented. The experimental and computational results, as well as the discussion and conclusions Sections are presented afterward, respectively.

Method

The necessity of employing the thermal infrared system to monitor thermal changes for medical applications is discussed in previous section. Here, the proposed method for monitoring the thermal variations is presented. The process begins with lower rank noise reduction and then an automatic detection of the ROI.

Low rank noise reduction

Due to the nature of process in thermal cameras, having noise in the thermal images seems inevitable. The sensitivity of the acquisition also depends on the acquisition's condition which might decrease the Signal to Noise Ratio (SNR) in the system.

Let X is an input matrix which has $p \times q$ dimension where p is number of frames and q is the vector correspond to each image ($q = \text{image's height } (m) \times \text{image's wide } (n)$). The Singular Value Decomposition (SVD) [10] gives a bilinear factoring of input matrix X , ($X = U\Sigma V^T$) which can be shown by r to decrease the rank and ultimately reducing the noise level as the noise's eigenvectors correspond to the lower eigenvalues in Σ . The mentioned process can be shown as below:

$$X'_{p \times q} \xrightarrow{\text{SVD}_r} U_{p \times r} \Sigma_{r \times r} V_{r \times q}^T, r \leq \min(p, q) \quad (1)$$

Once we have low-rank, $r_{\text{true}} \ll \min(p, q)$, the data represents in more explanatory form due to noise reduction (X').

Incremental SVD

Performing the low rank noise reduction by SVD eq. (1) for the purpose of video processing and possible online performing system enforces the SVD to function incrementally. Incremental SVD [11] can handle randomly missing, and incomplete or uncertain data. It is potentially showed an efficient robust subspace tracker. For the additional matrix C to the previous data, $U^T C$ is eigen-coding.

$$\begin{aligned} [X' \ C] &= [U\Sigma V^T \ C] \\ &= [U(I - UU^T)C/M] \begin{bmatrix} \Sigma & Y \\ 0 & M \end{bmatrix} \begin{bmatrix} V & 0 \\ 0 & I \end{bmatrix}^T \\ &= [U \ \Psi] \begin{bmatrix} \Sigma & Y \\ 0 & M \end{bmatrix} \begin{bmatrix} V & 0 \\ 0 & I \end{bmatrix}^T \end{aligned} \quad (2)$$

where $\doteq (I - UU^T)C = C - UL$, $Y = U^T C$ and $M \doteq \Psi^T T$ that Ψ is an orthogonal basis of T . Applying QR-decomposition, there will be $T \xrightarrow{QR} \Psi M$. The middle matrix denotes as Q and must be updated and diagonalized to lead to the answer for the whole process. In the case of adding a single vector $c = C$ the computation speed increases by calculating the vector $\psi = \Psi = (c - UU^T c)/m$ and scalar $c^T c - 2Y^T Y + (UY)^T (UY) \rightarrow m$. First $m \in M$, $\|m\| \rightarrow \Sigma$, $m/\|m\| \rightarrow U$, and $V \rightarrow \mathbf{1}$ and then updates by iteration for above mentioned calculations with truncation [12]. In the proposed approach, the initial data matrix constructs using initial frames and after noise reduction, the additional frame (c) adds to current data (X') to complete the process.

Clustering and tracking

After noise reduction for initialization of particle filter, a color based K-means clustering [9,13] is used. Here, a brief review of the kernelled K-means [14] is presented. Suppose $S = \{X_1, \dots, X_n\} \subset \mathbb{R}^p$ is our observation set (p) and dissimilarities are calculated by $\|X_i - X_j\|_2^2$ for $X_i \in \mathbb{R}^p$ and K is the number of clusters. Clustering of the data X is nothing more than a function C assigning every observation X_i to a set of $k \in \{1, \dots, K\}$. The minimization of the following formula is required:

$$J_k = \sum_{k=1}^K \sum_{C(i)=k} \|X_i - X_j\|_2^2 \quad (3)$$

Let $X = \frac{1}{n} \sum_{i=1}^n X_i$ and $C(i) = k$ means that X_i is assigned to group k . Different observation here is closely related to different color base X . The color based clustering determines the ROI and labelled used the reference temperature provided by blackbody during the experiment or in the calibration process (one time for all). Tracking these labels is done using a particle filter which is considerably similar to the previously presented approaches [9]. The function updates the ROI and concentrates the particles within the video stream.

Results

Experimental Setup and Thermal Image Database

The experiments were conducted in the room temperature using A65 FLIR camera for the infrared images acquisition at the wavelength ($7.5\mu\text{m} < \lambda < 13\mu\text{m}$). The resolution of the IR-camera was 640×512 pixels with the Field of View (FOV) of 45° (H) $\times 37^\circ$ (V) where the focal length were 13mm. This provides 1.31mrad Spatial resolution (IFOV). Image frequency of the camera capable to reach 9Hz but it set to have 1 second interval time between the frames to avoid high computational complexity. The object temperature range can be varied from -40°C to $+160^\circ\text{C}$. During the experiment the subjects were sitting in 1.2m and lying at 3m distance in front of the camera. The camera located at 1.7m from the ground having 36.5° from the vertical axe. Figure 1 shows the schematic experimental setup along with two examples from thermal images.

The thermal image database¹ created by 15 subjects for two minutes acquisition while the

¹. The mentioned dataset is available for research uses. A sample set of this database is provided at the following link: <http://vision.gel.ulaval.ca/~bardia/web%20page/ThermalDatabase.html>

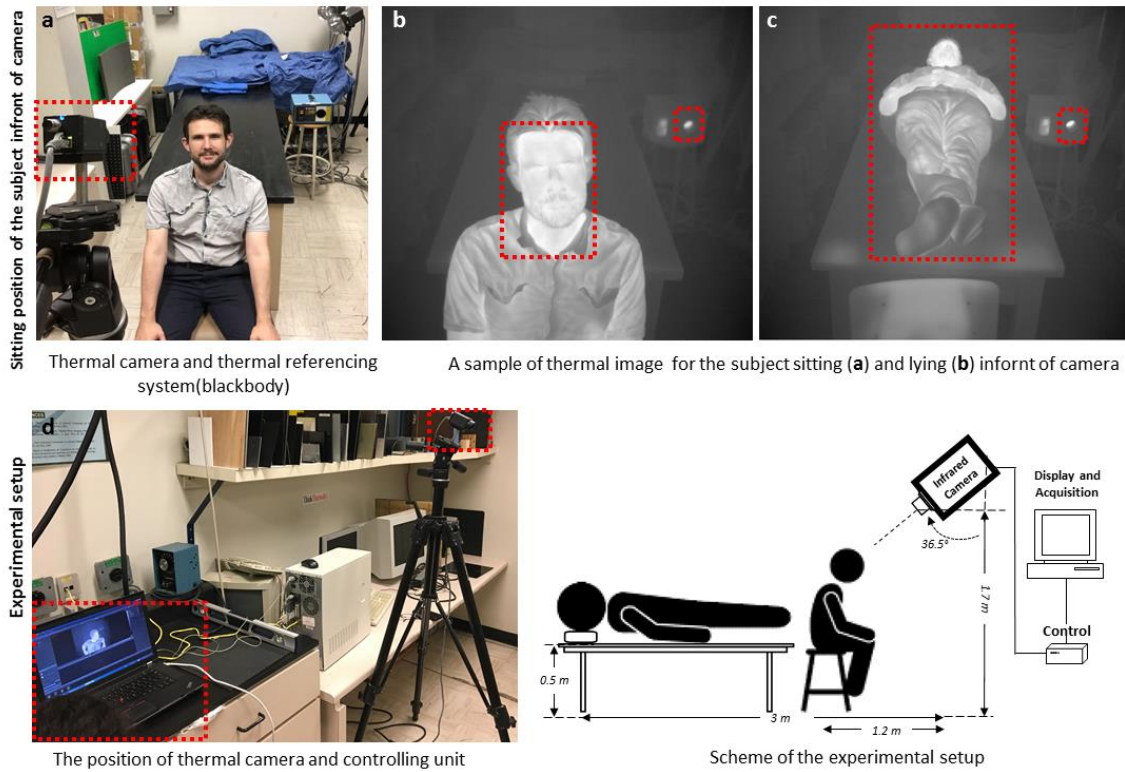


Figure1. The experimental setup of the approach is shown along with schematic design of the experiment. (a) shows an example of a subject sitting in the field of view of the IR-camera. (b,c) are the two thermal image samples of sitting and lying in front of the camera. The position of the blackbody and subject as our ROI are highlighted.

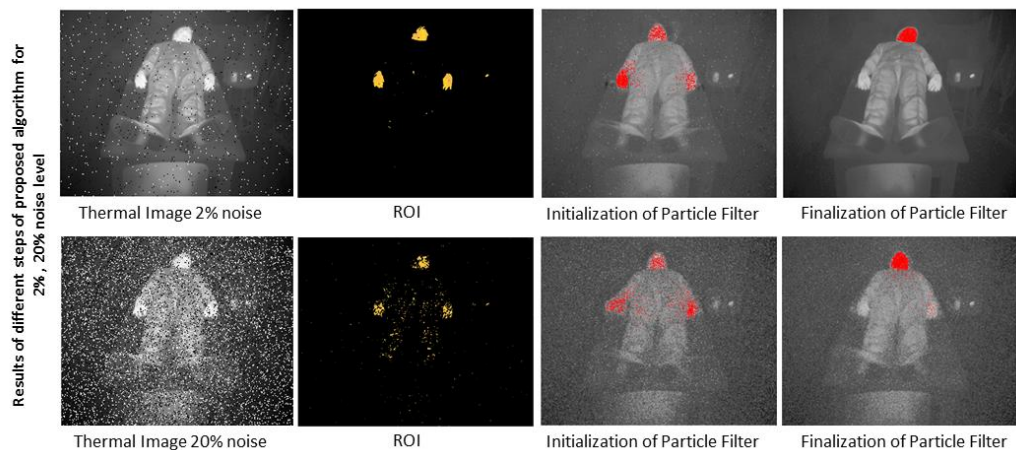


Figure2. The results of the proposed approach are shown for two levels of noise (2% and 20%).

subjects are sitting or lying in front of the camera. The subjects were free to have arbitrary movements during the acquisition to not only simulate the actual condition but also to verify the ability of the system against motion artifact. The process has been done with a PC (Intel(R) Core(TM) i7 CPU, 930, 2.80GHz, RAM 24.00GB,

64 bit Operating System) and processing of thermal data has been conducted using MATLAB computer program.

System Evaluation

To verify the performance of the system in the presence of noise, we added seven levels of

| Noise level (%) | Computational load (<i>per frame</i>) | | | Tracking ability (O,V) |
|-----------------|---|----------------|------------------------------|------------------------|
| | Noise reduction (s) | Clustering (s) | Particle Filter tracking (s) | |
| 2 | 1.059 | 1.656 | 0.126 | √ |
| 4 | 1.001 | 2.271 | 0.117 | √ |
| 6 | 1.175 | 1.708 | 0.119 | √ |
| 8 | 1.073 | 1.535 | 0.118 | √ |
| 10 | 1.045 | 1.579 | 0.117 | √ |
| 12 | 1.284 | 1.414 | 0.117 | √ |
| 15 | 1.068 | 2.401 | 0.118 | √ |
| 20 | 1.049 | 1.748 | 0.118 | √ |

Table 1. The computational load and performance of the system are shown.

additive Salt and pepper noise into the input stream. The system showed considerable robustness against noise due to the incremental low-rank noise reduction stage in the process. Table 1 represents the performance of the system in front of additive noise and computational complexity of the proposed approach. Figure 2 also shows two examples of system performance for 2% and 20% noise.

Conclusions

The approach presented an automatic monitoring system for patient's temperature used incremental low-rank noise reduction applying Incremental SVD and applied color based K-means clustering for finding ROI and particle filter to track the ROI(s) within the sequence. The system tested by an experiment conducted to simulate the hospital's condition which contained 15 subjects in sitting and lying positions. The robustness of the method verified in the presence of subject's arbitrary movements and additive noise. The system was able to function even in the presence of 20% (salt & pepper) noise with reasonable computational load. As future work, the low ranking noise reduction process can be modified to avoid the vulnerability of the system facing higher level of noise. This objective can be done having the additional penalty term in computing of the low rank data representation or adding a possible relaxation coefficient into the calculation.

ACKNOWLEDGMENT

This research was conducted under Canada Research Chair in Multipolar Infrared Vision at

Computer Vision and Systems Laboratory (CVSL), Laval University.

References

1. Jones, B. F. (1998). A reappraisal of the use of infrared thermal image analysis in medicine. *IEEE transactions on medical imaging*, 17(6), 1019-1027.
2. Etehadtavakol, M., & Ng, E. Y. (2017). Potential of Thermography in Pain Diagnosing and Treatment Monitoring. In *Application of Infrared to Biomedical Sciences* (pp. 19-32). Springer Singapore.
3. Amalu, W.: Nondestructive testing of the human breast: the validity of dynamic stress testing in medical infrared breast imaging. In: *Engineering in Medicine and Biology Society, 2004. IEMBS '04. 26th Annual International Conference of the IEEE*, vol. 2, pp. 1174-1177 (2004)
4. Shastri, D., Merla, A., Tsiamyrtzis, P., Pavlidis, I.: Imaging facial signs of neurophysiological responses. *Biomedical Engineering, IEEE Transactions on* 56(2), 477-484 (2009)
5. Parsi, K., Kossard, F.: Thermosensitive lichen amyloidosis. *International Journal of Dermatology* 43(12), 925-928 (2004)
6. Tabatabaei, N., A. Mandelis, et al. (2011). "Thermophotonic lock-in imaging of early demineralized and carious lesions in human teeth." *Journal of biomedical optics* 16(7): 071402-071402-071410.
7. Chiang, M., Lin, P., Lin, L., Chiou, H., Chien, C., Chu, S., Chiu, W.: Mass screening of suspected febrile patients with remote-sensing infrared thermography: Alarm temperature and optimal distance. *Journal of the Formosan Medical Association* 107(12), 937-944 (2008)
8. Bilodeau, G. A., Torabi, A., Lévesque, M., Ouellet, C., Langlois, J. P., Lema, P., & Carmant, L. (2012). Body temperature estimation of a moving subject from thermographic images. *Machine Vision and Applications*, 23(2), 299-311.
9. Yousefi, B., Fleuret, J., Zhang, H., Maldague, X. P., Watt, R., & Klein, M. (2016). Automated assessment and tracking of human body thermal variations using unsupervised clustering. *Applied optics*, 55(34), D162-D172.
10. Gene Golub and Arthur van Loan. *Matrix Computations*. Johns Hopkins U. Press, 1996.
11. Bunch, J. R., & Nielsen, C. P. (1978). Updating the singular value decomposition. *Numerische Mathematik*, 31(2), 111-129.
12. Brand, M. (2002). Incremental singular value decomposition of uncertain data with missing values. *Computer Vision—ECCV 2002*, 707-720.
13. Jain, A. K. (2010). Data clustering: 50 years beyond K-means. *Pattern recognition letters*, 31(8), 651-666.
14. Yousefi, P., Jalab, H. A., Ibrahim, R. W., Mohd Noor, N. F., Ayub, M. N., & Gani, A. (2016). River segmentation using satellite image contextual information and Bayesian classifier. *The Imaging Science Journal*, 64(8), 453-459.

NEAR INFRARED AND THERMAL IMAGING OF NORMAL AND OBESE WOMEN DURING ORAL GLUCOSE TOLERANCE TEST (OGTT)

B. Jalil^a, V. Hartwig^b, D. Moroni^a, O. Salvetti^a, A. Benassi^a, Z. Jalil^e, L. Guiducci^b, L. Pistoia^c, T. Minutoli Tegrini^c, A. Quinones-Galvan^c, G. Iervasi^b, A. L'Abbate^{b,d}

^aIstituto di Scienza e Tecnologie dell'Informazione "Alessandro Faedo" CNR, Pisa, Italy

^bIstituto di Fisiologia Clinica CNR, Pisa, Italy

^cFondazione G. Monasterio CNR - Regione Toscana, Pisa, Italy

^dScuola Superiore Sant'Anna, Institute of Life Sciences, Pisa, Italy

^eDepartment of Computer science, Iqra University, Islamabad, Pakistan

Originally considered as an imbalance between energy intake and expenditure, obesity is studied in this paper by comparing body temperature of abdomen, neck and hand in obese subjects to lean ones with oral glucose tolerance test during thermos neutral and cold conditions. We studied obese and normal weight females with infrared thermal imaging (IRT) and near infrared spectroscopy (NIRS). We observed that a significantly reduced temperature was much more prevalent in the obese subjects around abdominal area and relatively higher temperature on the hand of obese subjects as compared to lean ones. However, we observe the higher oxygen saturation in obese females in both hand and abdomen.

Introduction

Obesity, now recognized as a major public health issue, is a condition associated with high body heat content. Several physiological changes that accompany the development of obesity tend to increase heat production. Obesity increasing with an alarming rate worldwide with the particular concern is the increase in health risk evidenced in younger persons and ultimately increases the risk of many serious conditions including hypertension, diabetics, coronary heart disease and many more. People with a body mass index (BMI) of 30 or higher are considered obese as it describe the health condition of significantly above ideal healthy weight [1, 2]. These negative health consequences of obesity attracted many researchers to study further and explore its effects on human health. Infrared thermography (IRT) has been used in the past few decades to study diseases in which skin temperature is an indicator of inflammation or blood flow changes. The use of IRT in the measurement of human skin temperature has the advantage to be completely noninvasive. A thermal camera makes use of infrared imaging to visualize and measure the thermal energy

emitted from objects in the environment. Thermal cameras are capable of discriminating temperature differences and used to assess the absolute temperature of specific points on the body, or alternatively to calculate average temperature of a specific region of the body as specified [3]. Savastano et al had studied human obesity in relation to the heat production using such cameras. They examined heat production and dissipation in obese adults as compared to normal weight adults [2]. Analysis of data indicated that obese participants demonstrated significantly lower abdominal thermal patterns than those of their normal weight counterparts. Similarly, Ludwing et al had studied maximal skin temperature at different region of interests [4]. Chudecks et al had drawn a thermal map of obese women and highlighted the body area where heat transfer is particularly impeded [5]. More recently, Gatidis et al had presented their extensive research on skin temperature using infrared thermography [6].

Assessment of oxygen saturation (StO₂) is important to study clinical condition and in monitoring several pathological changes. During the past few years, near infrared spectroscopy (NIRS) has been used to study

human adipose tissues to investigate obesity effects. NIRS is a method to non-invasively measure tissue oxygenation in vivo [7]. NIR spectroscopy has been largely used for measurement of changes in intravascular hemoglobin (Hb) and intramuscular myoglobin (Mb) for many applications *e.g.* Nirengi et al had evaluated the oxygenation in brown adipose tissues using near infrared spectroscopy in thermos neutral and cold conditions [8].

The aim of this study was to achieve a better understanding of the body temperature and oxygenation conditions on neck, hand and abdomen of normal and obese females during oral glucose tolerance tests. In the coming sections, we will first explain the methods, subjects and designed experimental protocols and then we will present our findings with discussion.

Subjects and Methods

We had performed 3-hours Oral Glucose Tolerance Test (OGTT) to find the difference of temperature and oxygenation in lean and obese subjects. The glucose tolerance test is a medical test in which glucose is given and blood samples are taken afterwards to determine how quickly it is cleared from the blood.

All the thermal images were acquired with Ti9Thermal Imagers (Fluke Corporation, Everett, WA) camera. The technique is based on the principle that the amount of energy radiated depends on the surface temperature of the object and the emissivity of the object's surface. The camera detects the infrared energy from an object and uses this information to estimate its temperature. Additionally, we acquired NIRS 2D images at the same time. The Kent imaging camera, used to take the NIRS images, is a non-invasive system for tissue oxygenation measurement based on near infrared light. The camera reports and approximates value of Hb + Mb StO₂ in superficial tissue. We have selected neck, abdomen and hand regions to study temperature and microcirculatory features in obese and lean subjects. Five healthy women (age 34.4±10.5)

with low body mass index (BMI= 19.6±2.3 kg/m²) and five overweight healthy women (age 39.8±11.0) (BMI= 27.5±1.8 kg/m²) were studied. Table 1 shows the characteristics of all subjects. The study was authorized by the local Ethical Committee. Each subject gave written informed consent.

Experimental Design

All subjects were selected from the Metabolic Unit of Fondazione G. Monasterio CNR – Regione Toscana, Pisa, Italy. Firstly, height and weight were measured and then BMI was calculated. Moreover, NIRS and thermographic baseline images were collected (after a 15-min acclimatization period).

| | Sex | Age (years) | BMI (Kg/m ²) |
|-------------------------------|----------|-------------|--------------------------|
| <i>Subject 1</i> | <i>F</i> | 27 | 20,4 |
| <i>Subject 2</i> | <i>F</i> | 33 | 19,0 |
| Lean <i>Subject 3</i> | <i>F</i> | 22 | 17,9 |
| <i>Subject 4</i> | <i>F</i> | 44 | 18,0 |
| <i>Subject 5</i> | <i>F</i> | 46 | 19,8 |
| <i>Subject 6</i> | <i>F</i> | 50 | 30,1 |
| <i>Subject 7</i> | <i>F</i> | 48 | 24,9 |
| Obese <i>Subject 8</i> | <i>F</i> | 43 | 33,4 |
| <i>Subject 9</i> | <i>F</i> | 23 | 27,2 |
| <i>Subject 10</i> | <i>F</i> | 35 | 25,0 |

Table 1. Participant characteristics.

A 3-h oral glucose tolerance test (OGTT) with the ingestion of 75 g of oral glucose was performed. NIRS and IRT images were taken every hour during 180 minutes. At the end of OGTT, a cold stimulation was performed by immersing the subject's left hand in ice-water for one minute. Finally, NIRS and IRT images were acquired immediately after the cold stimulus.

Results

Figure 1 (a) and (b) show respectively the thermal and StO₂ images of hand. Similarly, Figure 2 (a) and (b) represent abdomen temperature and StO₂ respectively and Figure 3 (a) and (b) show thermal and StO₂ images of the neck area.

Figures 4, 5 and 6 show the temperature averaged on five lean subjects and on five

overweight subjects for hand, neck and abdomen area during the entire experimental paradigm (3-h OGTT test and post ice stimulation). Figure 7, 8 and 9 show the mean StO_2 for both groups in hand, neck and abdomen respectively.

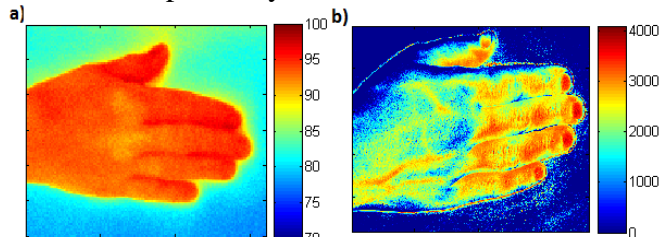


Fig1. a) Thermogram of hand. b) NIRS image of hand.

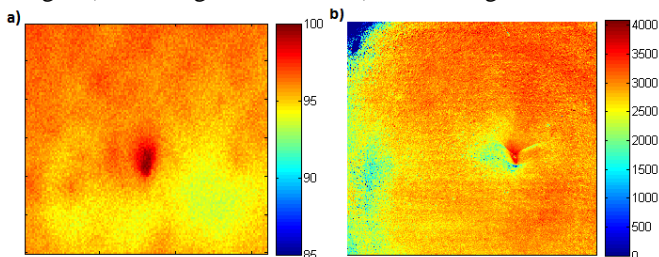


Fig2. a) Thermogram of abdomen. b) NIRS image of abdomen.

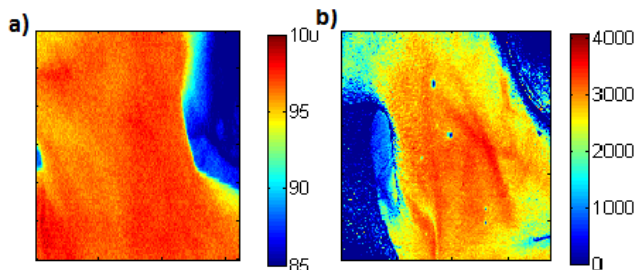


Fig3. a) Thermogram of neck. b) NIRS image of neck.

Discussion

The major finding of the present study is that we detected, both in lean and overweight subjects, a consistent, and highly localized, increase in local temperature of hand, neck and abdomen area induced by a glucose ingestion. We also observed that obese participants had lower abdominal skin temperature and higher in hand as compared to the lean subjects. This result, relative only to the baseline condition, is the same that is reported in [4]. It is even more interesting to note that the hand temperature in lean subjects continues to increase during the OGTT test while in the obese subjects the hand temperature remains more or less constant. Interestingly, abdomen temperature in obese

subject changes more during the first 2 hours of OGTT protocol respect to the temperature of the same area in lean subjects.

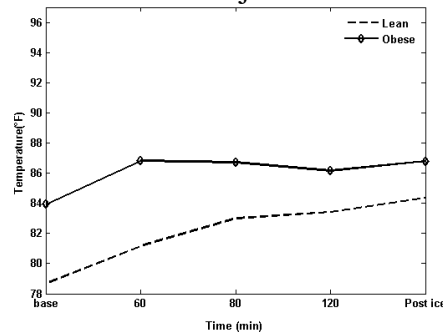


Fig 4. Mean hand temperatures in all subjects measured by infrared thermography.

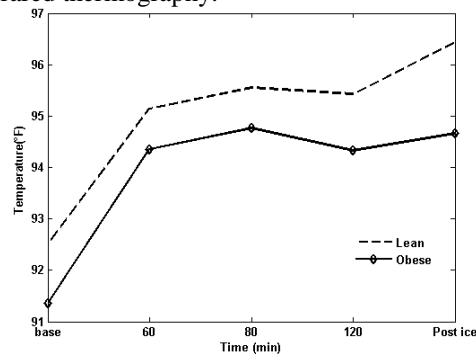


Fig 5. Mean neck temperatures in all subjects measured by infrared thermography.

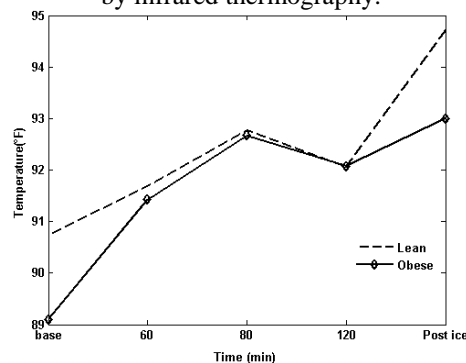


Fig 6. Mean abdominal temperatures in all subjects measured by infrared thermography.

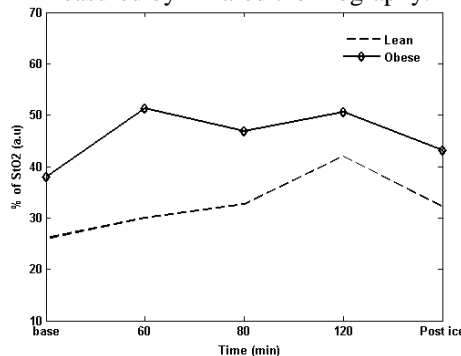


Fig 7. Mean hand StO_2 in all subjects measured by near infrared camera.

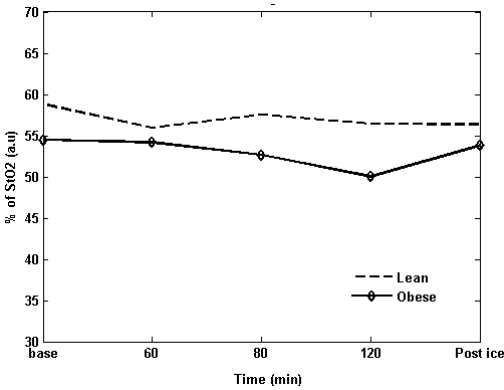


Fig 8. Mean neck StO₂ in all subjects measured by near infrared camera.

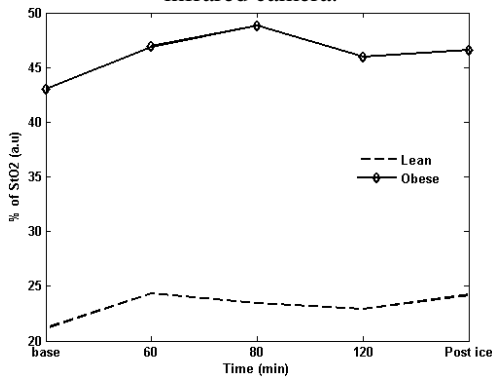


Fig 9. Mean abdominal StO₂ in all subjects measured by near infrared camera.

Temperature of the neck area have similar trends during the entire experimental paradigm for the both two groups.

We had also evaluated the differences in the oxygenation saturation of both lean and obese subjects in order to obtain information about the tissue perfusion. StO₂ has significant differences between lean and obese group only for hand and abdomen area but not for the neck. This difference is more pronounced in the abdomen area: oxygen saturation is higher in the abdomen area of obese subjects during the entire experimental paradigm. This could indicate a different distribution of vessel in superficial tissue of the abdomen. Otherwise this could be due to a very different depth of subcutaneous fat.

Conclusion

In this paper, we have applied non-invasive multimodal imaging techniques to monitor thermogenesis conditions in lean and obese females with different body mass index. We

observed relatively lower abdominal skin temperature and relatively higher temperature in hand in obese females as compared to the lean ones measured in both thermos neutral and cold conditions. As body core temperature represents a marker of energy expenditure, results from this study suggest that reduction of body core temperature plays a crucial role in favoring weight gain in obese subjects. At the same time, we observed higher oxygenation level in obese females. The difference is much higher in abdominal area as compared to the hand in obese females. In conclusion, IRT and NIRS methods are non-invasive, inexpensive and simple methods to investigate fatty tissues in human body. It is important to validate these finding further on large data set in different physical conditions and with obesity related diseases.

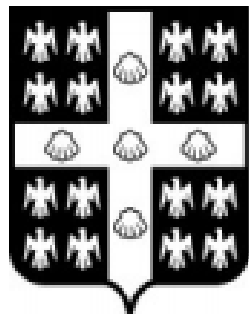
References

1. Martorell R et al, Obesity in women from developing countries. *European Journal of Clinical Nutrition* (2000) 54, 247-252.
2. Heubergerlet al, The relationship between thermal imaging and waist circumference in young adults, *Health*, Vol.4, No.12A, 1485-1491 (2012)
3. Chudecka M et al, Body surface temperature distribution in relation to body composition in obese women. *Journal of Thermal Biology*, 2014 Jul.
4. Savastano DM et al, Adiposity and human regional body temperature, *American Journal of Clinical Nutrition* 90(5):1124-31 · September 2009.
5. N. Ludwig et al, Skin temperature evaluation by infrared thermography: Comparison of image analysis methods, *Infrared Physics & Technology* Volume 62, January 2014, Pages 1–6.
6. Nirengi S et al, Human brown adipose tissue assessed by simple, noninvasive near-infrared time-resolved spectroscopy, *Obesity (Silver Spring)*. 2015 May 23(5):973-80. doi: 10.1002/oby.21012. Epub 2015 Apr 10.
7. Sergios Gatidis, Is It Possible to Detect Activated Brown Adipose Tissue in Humans Using Single-Time-Point Infrared Thermography under Thermoneutral Conditions? Impact of BMI and Subcutaneous Adipose Tissue Thickness, *PLoS One*. 2016; 11(3): e0151152.
8. Jalil et al, Near Infrared Image Processing to Quantitate and Visualize oxygen saturation during Vascular Occlusion, *Computer methods and programs in biomedicine*, Jan 2016.

NDT

AITA 2017

Québec City, Canada
September 27th - 29th, 2017



UNIVERSITÉ
LAVAL

INDUCTION THERMOGRAPHY OF STEEL COUPONS WITH CRACK

M. Genest¹, G. Li²

NRC Aerospace, 1200 Montreal Rd, Bldg M14, Ottawa, ON, K1A 0R6,

¹Marc.Genest@nrc-cnrc.gc.ca

²Gang.Li@nrc-cnrc.gc.ca

Induction thermography technique was assessed experimentally and numerically on notched steel coupons using two coil configurations: straight line and loop conditions. The coupons had different fatigue crack lengths varying from zero to 3 mm. The numerical predictions showed that the peak temperature was always located at the crack tip or the notch tip position. The loop coil resulted in higher temperatures than that of the straight line coil. Results showed that the numerical methods effectively supported the application assessment of this non-destructive evaluation (NDE) technique for the steel material, but crack geometry remains a challenge as the exact shape of a natural crack is typically unknown. It is shown that induction thermography can detect crack as small as 1 mm in the notched steel coupons.

Introduction

Induction heating is the process of heating an electrically conductive object by electromagnetic induction, where induced currents are generated within the test piece and electrical resistance leads to heating of the test piece. Induction thermography is a non-destructive evaluation (NDE) technique that uses induction heating for detection of flaws in conductive materials and has been used since the 1980s. This technique has potentials to improve the inspection speed and eases the visualization of flaw detection in complex geometries with the aid of infrared cameras. Infrared cameras can accurately detect real-time temperature profile and small temperature gradient caused by the presence of flaws. Over the last decade, this NDE technique has gained more and more interest and has been used on both metallic and carbon or boron fiber reinforced composite materials.

Finite element (FE) methods have been widely applied to this area to support testing investigations. Due to the model limitation, a

two-dimensional (2D) model cannot study the temperature profile generated in a 3D test piece containing a complex shaped crack or flaw [1-3]. To this end, a 3D modelling capability was developed to support the assessment of induction thermography for metallic panels [4]. In the present study, the relevant 3D FE models were created using COMSOL Multiphysics software version 5.1 to support the induction thermography of notched steel coupons with different crack lengths. Through comparing the temperature profiles and temperature distributions obtained, the capability of induction thermography on the steel coupons is discussed.

Theory and Experimental Details

According to Ampere's law, an alternating current flowing through a wire or coil will produce an alternating magnetic field of the same frequency as the source current. The electromagnetic field's strength will depend on the coil current, coil geometry, and distance from the coil. The alternating magnetic field induces current that leads to the induction heating of the conductive test piece.

A commercial induction heating system, the Easyheat 2.4 from Ambrell, was employed in the experiments. The system supplies up to 2.4 kW of power to the work head. A copper coil excited by the work head is placed in proximity of the test piece surface to create induction heating of the test piece. Water is circulated through the coil using a water-to-air heat exchanger to maintain the coil element cool during the test. Thus, the heat transfer is mainly inductive and there is minimal radiation transfer from the coil to the test piece. The temperature distributions on the test piece were captured by an infrared camera (FLIR SC3000), which has a 320x240 pixels array, a maximum full frame rate of 60Hz, and noise equivalent temperature difference of ~20 mK.

The test pieces investigated in this study were notched 2.7 mm thick AISI type O1 steel coupon made according to ASTM E399-05 standard. Each specimen has a length and width of 143 and 137 mm, respectively. The samples were fatigued to generate controlled nominal crack length of 0.1, 1, 2, and 3 mm using a tension-tension sinusoidal fatigue load at frequency of 10 Hz and a load ratio of 0.1 with a maximum load of 15.5kN. One sample was kept as manufactured without crack as a reference coupon. The samples were painted black with high emissivity coefficient paint (~0.95) to avoid reflection issue typical with low emissivity surfaces such as bare metal.

Experiments were carried out using two different coil configurations, a straight coil and three-loop coil made of a hollow copper tube with a 6.35 mm outer diameter and 1.2 mm wall thickness. The steel coupon geometry with the coil setups is shown in Figs. 1 and 2, in which the distance between the coil and the sample face was approximately 10 mm. In the straight coil configuration, the coil was placed perpendicular to the notch and the crack, with its side aligned with the notch tip. Induction heating was carried out for duration of 500 ms using three different current intensities: 100 A, 150 A, and 200 A. In the three-loop coil configuration, the loops were centered over the

notch tip. Since this coil configuration generates significantly more electromagnetic fields than the straight line coil, the current intensities were reduced to 25A, 50A and 100A.

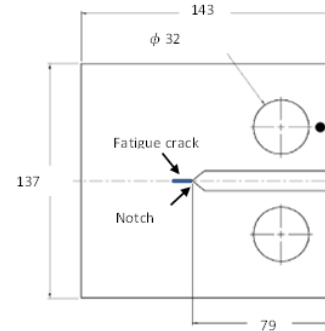


Fig. 1. A schematic drawing of the notched coupon (dimension in mm)

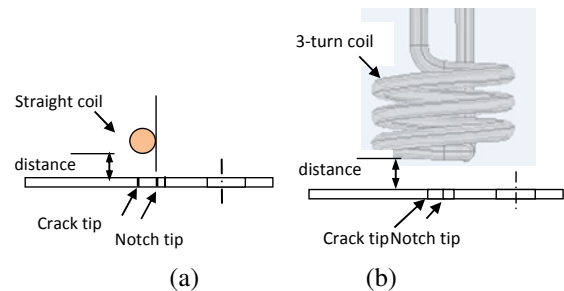


Fig. 2. Side view showing the (a) straight coil and (b) three-loop coil setups and positions

Multiphysics Finite Element Modelling

COMSOL Multiphysics software version 5.1 was used to create the relevant 3D FE models that included four domains: air, steel sample, coil, and water. Two coupling multiphysics: (i) magnetic field (MF) and (ii) heat transfer in solids (HT) were used in the induction heating simulation.

A model for the steel sample with a straight line coil is shown in Fig. 3. The path, highlighted by a red line in Fig. 3b on the sample coil side (front) surface, was used to study the temperature profiles. To lower computational time, only a section of the steel sample was modelled covering the area of interest around the notch and the crack. The dimension of the steel coupon modelled was 80x60x2.7 mm.

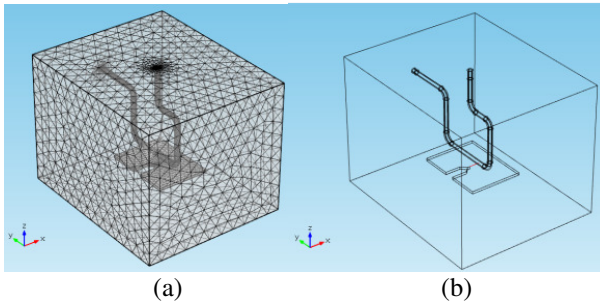


Fig. 3. A 3D FE model of the notched steel coupon induced by a straight coil for (a) meshed condition and (b) a surface path along the crack direction for temperature assessment.

Table 1 gives the material properties used in the numerical analyses. Since the exact material properties of the steel (relative permeability and thermal conductivity) were not known, two values for each of the two properties were selected based on value scatter found in the literature.

| Material properties | Copper | Steel |
|---|---------|------------|
| Relative permeability, μ_r | 1 | 100 & 1000 |
| Relative permittivity, ϵ_r | 1 | 1 |
| Electrical conductivity, σ (S/m) | 5.998E7 | 4.E+6 |
| Specific heat, C_p (J/kg K) | 385 | 435 |
| Density, ρ (kg/m ³) | 8700 | 7850 |
| Thermal conductivity, k (W/(m K)) | 400 | 15 & 45 |

Table 1. Material properties used in the numerical models.

Experimental Results

Experimental results obtained with the straight line coil showed a high temperature increase at the notch tip, regardless of the presence of a crack. This is due to the geometry of the samples which results in a concentration of electromagnetic field and results in no distinctive detection of crack at the notch tip. Fig. 4 shows normalized temperature distributions on the cracked sample front faces. Further signal processing consisting of subtracting normalized temperature obtained

for reference coupon from that of the crack coupons, was performed using a processing technique called differential thermography [5-7]. Using this technique it is possible to clearly detect the 2 and 3mm long cracks. It can be noticed in the experimental results that the temperature peaks are not located exactly at the crack tip position. Plausible causes for this include the crack shape and width varying through its length that could result in higher electromagnetic field concentration as a location other than the crack tip. For comparison purpose, the temperature distributions obtained numerically at the 500 ms heating time using a 100 A current intensity for the reference coupon and the 3 mm crack are shown in Fig. 5. Unlike the experimental results, numerical results show that the peak temperatures are always located at the notch tip or crack tip location, with significant higher temperature for the cracked samples.

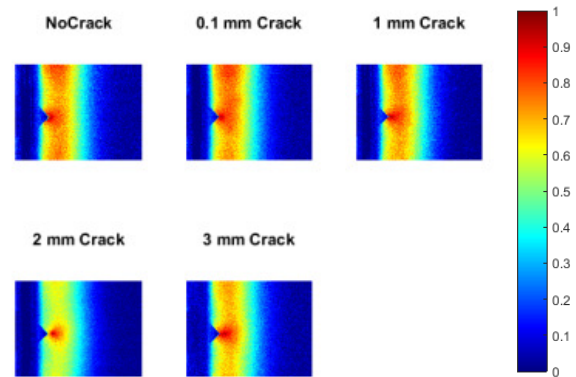


Fig. 4. Line coil normalized temperature increase with the 100 A at the 500 ms heating time

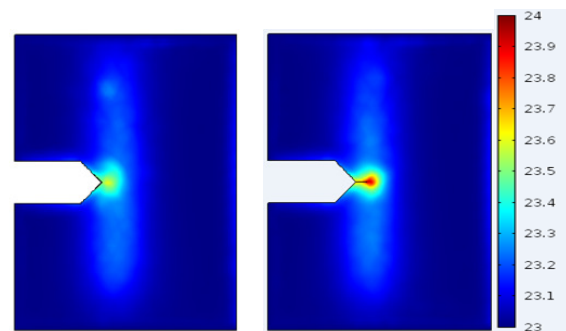


Fig. 5. Predicted surface temperature distributions induced by the straight line coil with the 100 A at the 500ms heating time (a) no crack, and (b) 3 mm cracks at the notch tip conditions.

Inspections were repeated for the 3-turn coil configuration and a high temperature increase was generated at the notch tip, regardless of the presence of a crack, as shown in Fig. 6. By performing the differential thermography technique it was possible to detect cracks as small as 1 mm as can be seen in Fig. 7. The numerical simulations also confirmed the detection capability, while the 0.1 mm crack remained undetected in both experimental and numerical methods. Earlier observation times such as 100 ms or 250 ms as oppose to 500 ms yielded stronger contrast, and the contrast also increased with the current intensity used for the induction.

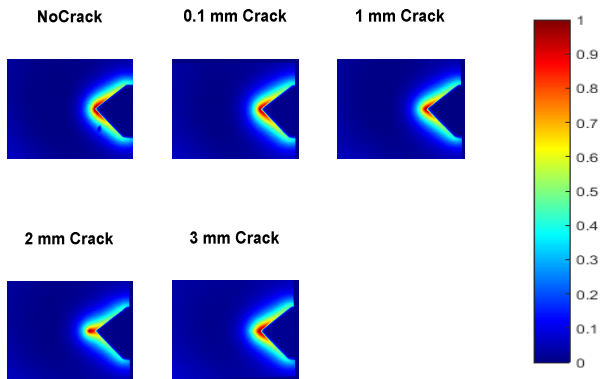


Fig. 6. Three-loop coil normalized temperature from reference coupon with the 50 A current at time 250 ms.

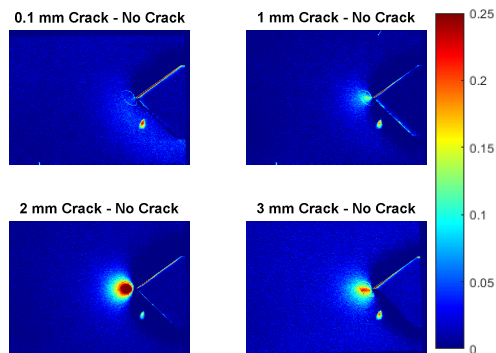


Fig. 7. Three-loop coil temperature difference from reference coupon with the 50 A current at time 250 ms.

Conclusion

Both experimental and numerical assessments of the induction thermography technique were conducted for detecting cracks in notched steel coupons based on the temperature gradients.

The straight line coil detection capability was limited to 2 mm and longer cracks, while the three-loop configuration was able to detect cracks as small as 1 mm. Higher current intensity and earlier observation time resulted in higher signal to noise ratio and eased the flaw detection. Based on the findings it is recommended that induction thermography inspection of steel parts be performed using a multiple-loop coil system, using at least 100 A current intensity and looking at a short heating time such as 100 ms or 250 ms. Moreover, an additional signal processing using differential thermography can significantly improve the flaw detection sensitivity, especially in the case of complex geometry that inherently creates electromagnetic field concentration such as in notched coupons.

References

1. M. Omar, M. I. Hassan, K. Satio, R. Alloo, IR self-referencing thermography for detection of in-depth defects, *Infrared Phys. Technol*, 46, 283-289, 2005.
2. J. Wilson, G. Y. Tian, I. Z. Abidin, S. Yang, D. P. Almond, Pulsed eddy current thermography: system development and evaluation, *Insight-Non-Destructive Testing and Condition Monitoring*, 52, 87-90, 2010.
3. R. Yang, Y. He, Eddy current pulsed phase thermography considering volumetric induction heating for delamination evaluation in carbon fiber reinforced polymers, *Applied Physics Letters*, 106 2015.
4. G. Li, M. Genest, Three-dimensional numerical modelling of induction thermography on metallic panels, *Proceedings of the NDT in Canada 2016 November 15-17, 2016*
5. M. Genest, M. Martinez, N. Mrad, G. Renaud, A. Fahr, Pulsed thermography for non-destructive evaluation and damage growth monitoring of bonded repairs, *Composite Structures*, 88, 1, 112-120, 2009
6. J. N. Zalameda, W. P. Winfree, J. P. Seebo, and P. H. Johnston, Thermography Inspection for Detection and Tracking of Composite Cylinder Damage During Load Testing, *Review of Progress in Quantitative Nondestructive Evaluation: Volume 30A; AIP Conf. Proc. Vol 1335, 450-457, 2011.*
7. W. P. Winfree, J. N. Zalameda, and P. A. Howell, Improved flaw detection and characterization with difference thermography, *Proc. SPIE 8013, 80130U, 2011.*

QUANTITATIVE NONDESTRUCTIVE TESTING USING INFRARED THERMOGRAPHY: AN INVERSE GEOMETRY PROBLEM

F. B. Djupkep Dizeu¹, D. Laurendeau², A. Bendada³

Computer Vision and Systems Laboratory, Laval University
 1065, avenue de la Médecine, Québec City (QC), G1V 0A6, Canada

¹ dizeubilly@yahoo.fr; ² denis.laurendeau@gel.ulaval.ca; ³ hakim.bendada@gel.ulaval.ca

We formulate the quantitative nondestructive testing using infrared thermography as an inverse geometry problem whose solution, i.e., the volume geometry of the inspected object, is determined using a new approach combining the temporal tracking of thermal front and the method of steepest descent. The proposed algorithm takes three inputs: the temperature history recorded on the external surface of the inspected object by an infrared camera, the 3D point cloud of that surface captured by a 3D scanner and the irradiation heat flux density resulting from the external thermal stimulus. While the thermal front propagates inside the inspected object, the method of steepest descent is used to accurately reconstruct its volume geometry by minimizing the difference between the theoretical temperature provided by an accurate 3D solver and the measured temperature.

Introduction

In the recent three decades, active infrared thermography (IRT) has been widely used for nondestructive testing (NDT) of objects. In the conventional approach, the object being inspected is thermally excited by an external thermal stimulus while its surface temperature is recorded by an infrared (IR) camera [1]. Image processing techniques allow detecting regions of the inspected object where defects may exist; the qualitative inspection results are then obtained. For providing quantitative inspection results, the existing methods use a one dimensional (1D) thermal model for estimating defects depth. Depending on the thermal stimulus used (pulsed, step-unit or modulated), specific strategies are used [2,3,4,5]. In the 1D model, it is assumed that the irradiation heat flux is uniform and no connection exists between the pixels. For these reasons, the reliability of existing methods used for quantitative NDT is guaranteed only for planar or almost planar objects having defects

with simple geometry [6].

A three-dimensional (3D) formulation of the problem contributes to improve the quantitative results whatever the shape (planar, cylindrical, or more complex) of the inspected object, its thermal diffusivity (Plexiglas, metal, etc.) and the geometry of defects (flat-bottom, spherical, corrosion) without the constraint of a uniform thermal stimulus. Recently a new paradigm, the temporal tracking of thermal front, has been introduced and a demonstration has been made to show the reliability and the generality of the 3D thermal model for quantitative NDT of objects [7]. Thanks to the use of a 3D scanner, the visible surface of the inspected object can be captured as a 3D point cloud. Using an acquisition system including a 3D scanner and an IR camera, it is possible to fuse the thermographic data and the 3D point cloud [8] and build an accurate 3D numerical solver [9]. The purpose of the method presented in this paper is to reconstruct the volume geometry of the inspected object by using the method of steepest descent (MSD) and the temporal tracking of thermal front to solve an inverse

geometry problem formulated for the quantitative NDT of objects using IRT. While the thermal front propagates inside the inspected object, the difference between the theoretical temperature provided by the 3D solver and the measured temperature is minimized by updating the volume geometry of the object using the MSD.

In the next section we present the theoretical fundamentals of the proposed method. In section 3 the algorithm sustaining the method is presented. In section 4 some preliminary experimental results are given for a cylindrical object with flat-bottom defects.

Theoretical fundamentals

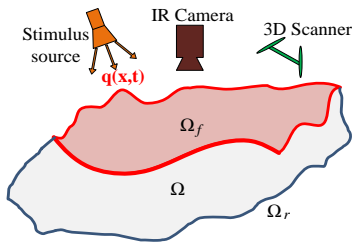


Figure 1. Adopted experimental setup.

Figure 1 shows the experimental setup adopted. The acquisition system consists of a 3D scanner and an IR camera. A calibration is performed to determine the rigid transformation between their coordinate systems [8]. The inspected object is constituted by the internal domain Ω surrounded by the rear surface Ω_r and the frontal surface Ω_f which is observed by the acquisition system while it is submitted to the thermal stimulus. For isotropic objects, the temperature recorded on frontal surface Ω_f is theoretically found as the solution of equations (1-4) where $T(X, t)$ is the temperature at time t at point X with coordinates $[x, y, z]$. α is the thermal diffusivity of the material, \vec{n} with coordinates $[n_x, n_y, n_z]$ is the inward-pointing normal vector at point X on the boundary. $q(X, t)$ is the spatiotemporal irradiation heat flux density on frontal surface [10]. h is the convective heat transfer coefficient, ε is the emissivity, λ is the thermal conductivity, T_{amb} is the ambient temperature, T_{rad} is the mean

radiant temperature and T_0 is the initial temperature.

$$\frac{\partial T}{\partial t} = \alpha \left(\frac{\partial^2 T}{\partial x^2} + \frac{\partial^2 T}{\partial y^2} + \frac{\partial^2 T}{\partial z^2} \right), X \in \Omega \quad (1)$$

$$\vec{n} \cdot \lambda \nabla T = q(X, t) + h_f(T_{amb} - T) + \sigma \varepsilon_f (T_{rad}^4 - T^4), X \in \Omega_f \quad (2)$$

$$\vec{n} \cdot \lambda \nabla T = h_r(T_{amb} - T) + \sigma \varepsilon_r (T_{rad}^4 - T^4), X \in \Omega_r \quad (3)$$

$$T(X, t = 0) = T_0, X \in \Omega \cup \Omega_f \cup \Omega_r \quad (4)$$

We parametrize the volume geometry of the inspected object by a set of depths measured from the frontal surface to the rear surface along the normal directions. We represent the frontal surface Ω_f by N_f nodes $F_i, i = 1, 2, \dots, N_f$ with corresponding normal vectors $\vec{n}_i, i = 1, 2, \dots, N_f$ and rear nodes $R_i, i = 1, 2, \dots, N_f$.

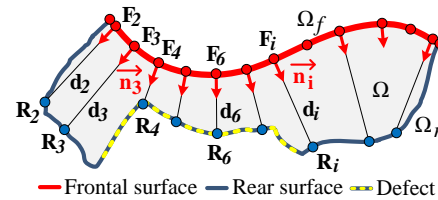


Figure 2. Parametrization of the rear surface

Therefore, as presented in Figure 2, the reconstruction of the volume geometry of the inspected object is reduced to the determination of depths $d_i, i = 1, 2, \dots, N_f$ which are such that:

$$\vec{F}_i \vec{R}_i = d_i \vec{n}_i \quad (5)$$

Internal nodes are generated between nodes F_i and R_i with a step size Δd . These nodes (frontal, rear and internal) form the discretized version of the inspected object which is used to numerically solve equations (1-4). A 3D numerical solver based on a meshless approach has been implemented to solve these equations [9]. This solver achieves the same level of accuracy as the available mesh-based commercial solvers but with a low computational cost and a high flexibility. Thus, it can easily be used when solving inverse geometry problems since in such procedures, the solving domain (volume geometry of the object) is iteratively updated and equations (1-4) are solved for each update.

Each iteration, the method of steepest descent is used (see algorithm) to update the volume geometry of the object. For that, the sensitivity coefficients must be determined. Let us define $\vec{d} = [d_1, d_2, d_3, \dots, d_{N_f}]$ as the vector of unknowns. The sensitivity coefficient $\psi_{\vec{d}^i}$ is defined as the derivative of the temperature of frontal surface with respect to the i^{th} component \vec{d}^i of vector \vec{d} . We have:

$$\begin{aligned} \psi_{\vec{d}^i} &= \frac{\partial T}{\partial \vec{d}^i} = \frac{\partial T}{\partial d_i} \\ &= \frac{[T(X, t)]_{d_i + \Delta d} - [T(X, t)]_{d_i}}{\Delta d} \end{aligned} \quad (6)$$

$[T(X, t)]_{d_i}$ is the frontal surface temperature obtained after solving equations (1-4) in the domain $\Omega_f \cup \Omega \cup \Omega_r$ and $[T(X, t)]_{d_i + \Delta d}$ is the frontal surface temperature obtained after solving equations (1-4) in the domain $\Omega_f \cup \Omega \cup \Omega_r^*$ which is obtained from $\Omega_f \cup \Omega \cup \Omega_r$ by increasing only the value d_i by Δd .

Algorithm for solving the inverse geometry problem

The following steps are used to reconstruct the volume geometry of the inspected object using only the temperature history recorded as a set of N_t images $\{T_{mes}(p, t_j)\}_{p=1,2,\dots,N_L \cdot N_C}^{j=1,2,\dots,N_t}$ of size $N_L \times N_C$ and the 3D point cloud X_f of frontal surface Ω_f :

- (a) Determine the irradiation heat flux $\{q(p, t_j)\}_{p=1,2,\dots,N_L \cdot N_C}^{j=1,2,\dots,N_t}$ [10].
- (b) Initialize the $N_L \cdot N_C$ -vector of unknowns \vec{d} to a small value and error $E \rightarrow \infty$. Define the set $\{D\}$ of pixels with known depths.
- (c) Solve equations (1-4) to find the theoretical temperature $\{T_{theo}(p, t_j)\}_{p=1,2,\dots,N_L \cdot N_C}^{j=1,2,\dots,N_t}$.
- (d) Find pixel $P \notin \{D\}$ such that $\|T_{theo}(P, t_j) - T_{mes}(P, t_j)\| > E$. If P exists, take $w = 1$; $er^0 \rightarrow \infty$ and go to step (e), otherwise do $E = \|T_{theo} - T_{mes}\|$ and $\vec{d}^p = \vec{d}^p + \Delta d, p \notin \{D\}$ and go to step (c).
- (e) Build vector $Nbor^w$. It is constituted by all the pixels in the windows of width w

centered at pixel P .

- (f) Use the MSD to find the depths \vec{d}^w associated to $Nbor^w$, the other depths being constant. The obtained error is er^w . If $er^w \leq er^{w-1}$, do $w = w + 1$ and go to step (e), otherwise the obtained depths \vec{d}^{w-1} for $Nbor^{w-1}$ are stored in $\{D\}$. Update \vec{d} .
- (g) If the size of $\{D\}$ is $N_L \cdot N_C$, exit. Otherwise go to (c)

Preliminary experimental results

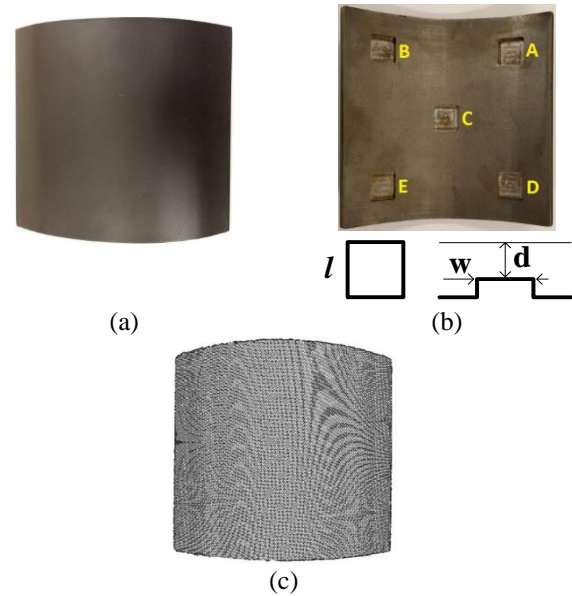


Figure 3. Cylindrical objects used. (a) Frontal surface. (b) Rear surface. (c) 3D point cloud. Size in mm: radius (r), height (H), arc length (a_l), thickness (e), depth (d), width (w), length (l). $r = 114$; $H = 152$; $a_l = 165$; $e = 6$; $w = 20$; $l = 20$; $d_A = 1.5$; $d_B = 2$; $d_C = 2.5$; $d_D = 3$; $d_E = 4$.

We consider the cylindrical object presented in Figure 3. It contains five square flat-bottom defects whose depths are between 1.5mm and 4mm. Figure 4 shows the experimental setup used. As presented in Figure 4a, the 3D point cloud of the frontal surface is captured first with a handheld 3D scanner [11]. Afterward, a pulsed thermal stimulus is applied on this frontal surface while its temperature is recorded with the IR camera (Figure 4b). As only open defects are present here, the volume geometry reconstruction consists in reconstructing the rear surface of the object. The algorithm presented above has been used and the results

obtained are summarized in Figure 5. The relative error obtained is around 6%.

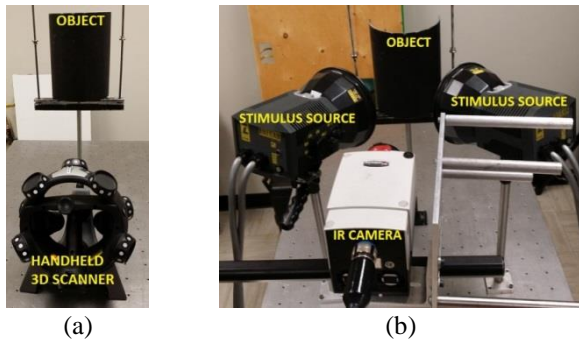


Figure 4. Experimental setup. (a) Capture of the 3D point cloud of frontal surface. (b) Record of the frontal surface temperature.

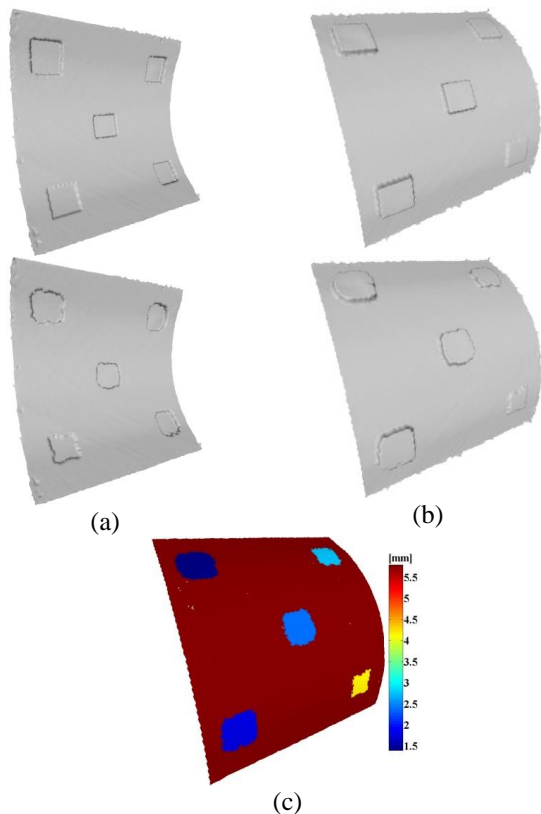


Figure 5. Results. (a-b) Top: real rear surface. Bottom: reconstructed rear surface. Rear surface viewed from outside (a) and from inside (b). (c) Depth map.

Conclusion

We formulated the quantitative nondestructive testing as an inverse geometry problem having a forward problem described by the three-dimensional heat equation. In order to solve this inverse problem, we proposed a method combining the method of steepest descent and the temporal tracking of thermal front. The

preliminary experimental results have shown the reliability of the method for reconstructing a rear surface with square flat-bottom defects. We are expecting satisfying results also for rear surfaces of more complex geometry.

References

1. X. Maldague, Theory and Practice of Infrared Technology for Non Destructive Testing, John-Wiley & Sons, 2001.
2. C. Ibarra-Castanedo, X. Maldague, Pulsed phase thermography reviewed, *QIRT Journal* 1, 47-70, 2004.
3. S. M. Shepard, J. R. Lhota, B. A. Rubadeux, D. Wang, T. Ahmed, Reconstruction and enhancement of active thermographic image sequences, *Optical Engineering* 42, 1337-1342, 2003.
4. Z. Zeng, J. Zhou, N. Tao, L. Feng, C. Zhang, Absolute peak slope time based thickness measurement using pulsed thermography, *Infrared Physics & Technology* 55 200-204, 2012.
5. C. Maierhofer, P. Myrach, R. Krankenhagen, M. Röllig, H. Steinfurth, Detection and characterization of defects in isotropic and anisotropic structures using lockin thermography, *Journal of Imaging* 1 220-248, 2015.
6. Y. Liu, X. Guo, G. Guo, A comparison between 3D and 1D numerical simulation models for infrared thermographic NDT, *Proc. 10th European Conference on Non-Destructive Testing*, Moscow, Russia, 2: 1484-89, 2010.
7. F. B. Djupkep Dizeu, D. Laurendeau, A. Bendada, Non-destructive testing of objects of complex shape using infrared thermography: rear surface reconstruction by temporal tracking of the thermal front, *Inverse Problems* 32: 125007 (20pp), 2016.
8. S. Hesabi, 3D Modeling of Large Elongated Structures for Non-Destructive Testing and Inspection, Thesis, Laval University, 2016.
9. F.B. Djupkep Dizeu, D. Laurendeau, A. Bendada, A localized radial basis function meshless method for modeling the nondestructive testing of complex shape objects using infrared thermography, *Internal report*, Computer Vision and Systems Laboratory, Laval University, 2016.
10. F. B. Djupkep Dizeu, D. Laurendeau, A. Bendada, Nondestructive testing of objects of complex shape using infrared thermography: Determination of the spatiotemporal distribution of the irradiation heat flux, *Infrared Physics & Technology* 83, pp. 164-176, 2017.
11. <http://www.creaform3d.com/fr/solutions-demetrologie/scanners-sur-mmt-optique-metrascan-3d>.

PRACTICAL APPLICATION OF ACOUSTIC AND THERMOGRAPHIC METHODS FOR ANALYSIS OF IMPACT DAMAGE TO COMPOSITE AVIONIC PARTS

M. Bondy¹, D. Gavrilov², I. Seviaryna³, R. Maev⁴

- ¹ Department of Mechanical Engineering, 401 Sunset Avenue, University of Windsor, Windsor, Ontario, N9B 3P4, Canada, bondy1z@uwindsor.ca
² Institute for Diagnostic Imaging Research, 688 University Avenue West, Windsor, Ontario, N9A 5R5, Canada, gavrilov@uwindsor.ca
³ Institute for Diagnostic Imaging Research, 688 University Avenue West, Windsor, Ontario, N9A 5R5, Canada, seviary@uwindsor.ca
⁴ Institute for Diagnostic Imaging Research, 688 University Avenue West, Windsor, Ontario, N9A 5R5, Canada, maev@uwindsor.ca

The work addresses the problem of impact damage diagnostics in samples of composite materials used for aerospace industry. In particular, materials used for Bombardier C-series wing were studied. The defects were produced by quasi-static loading with various energies, and the samples were visualized by means of principal component thermography and scanning acoustic microscopy. The differences in methods and their results are discussed.

Introduction

Composite materials are particularly attractive for the aerospace industry given their high specific stiffness and strength and the multiplier effect of the associated decrease in structural mass on fuel and engine mass savings. In contrast to negligible use in the 1970s, composites now constitute 50% of the Boeing 787 Dreamliner's structural components and Airbus has pushed this envelope even further with the A350XWB continuous fibre laminates. Barely visible impact damage (BVID) detection is an active field of research for laminates; delamination resulting from low energy impact may not be visible by traditional inspection methods and may propagate to cause catastrophic failure. Non-destructive evaluation (NDE) techniques, including thermography and acoustic microscopy, allow such damage to be

characterized such that any necessary precautionary measures can be taken.

Methodology

Eight specimens (140 mm x 140 mm) extracted from a carbon fibre Bombardier C-Series wing skin by water jet (pressure of 345 MPa, nozzle diameter of 0.076 mm) were subjected to quasi-static loading on an MTS electromechanical load frame (150 kN load cell, loading rate of 2.6 mm/min) to energies of approximately 20, 50, 130, and 420 J. The fixture, based upon the apparatus in standard ISO 6603-2, consisted of a 20 mm hemispherical indenter and two plates, between which the specimen was clamped (preload of approximately 3 kN), with 100 mm diameter circular cut-outs as shown in Figure 1. A Correlated Solutions digital image correlation (DIC) system acquired the

displacement and strain fields on the inner surface of the wing skin (opposite the surface loaded directly by the hemispherical indenter). Images were acquired with two Point Grey Research Grasshopper GRAS-50S5M-C 5 megapixel (MP) monochrome cameras with Schneider Kreuznach Cinegon 1.4/12 lenses at 5 frames per second (fps). The acquisition of images was synchronized to the load-deflection data by connecting the user defined output of the MTS load frame to a National Instruments (NI) USB-6221 data acquisition device and through the use of transistor to transistor logic (TTL) triggering in Correlated Solutions VIC-Snap software.

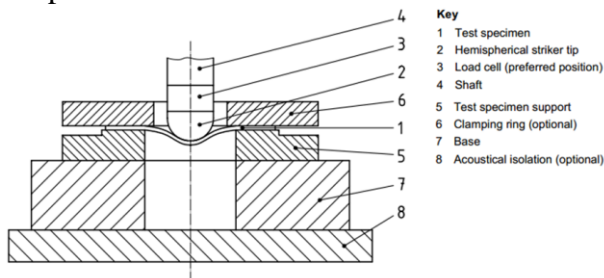


Fig. 1. Apparatus for mechanical characterization [1].

DIC data allowed for constructing distributions for von Mises strains, which are calculated from principal stresses in material and used for prediction of failures.

Digital image correlation (DIC)

DIC represents an optical approach for finding small deformations of material specimens caused by external influence. For performing DIC measurements, the specimen's surface is painted with a distinct pattern (typically, randomly dotted). Displacements in this pattern as the sample is loaded are detected by optical camera and provide clues to deformations and stresses in material [2].

Acoustic microscopy

Acoustic imaging techniques are widely used nondestructive techniques in automotive and aerospace industries as they allow not only detection of the presence of defects but to measure their size, shape, and location [3, 4].

The ultrasonic inspection is based on the propagation of an ultrasound pulse through the specimen and its interaction with structural components. As a sound pulse emitted from a transducer travels through the material, it partially transmits and reflects at each acoustic interface (flaw, damage, or discontinuity). The amplitude of the reflected signal is determined by reflection R coefficients of the two media:

$$R = \frac{Z_2 - Z_1}{Z_2 + Z_1}, \quad (1)$$

where Z is characteristic acoustic impedance of the media $Z = C\rho$; C is sound velocity and ρ is mass density. Thus, the greater difference between acoustic impedances in two media, the greater reflection coefficient and the more acoustic energy is reflected back to the transducer. The acoustic impedances of composite materials typically vary within $20\text{-}40 \cdot 10^6 \text{ kg m}^{-2}\text{s}^{-1}$, and the acoustic impedance of air is $40 \text{ kg m}^{-2}\text{s}^{-1}$. This drastic difference provides a basis for visualization of internal defects and adhesive presence at the interface.

Observation of the BVID was performed using a KSI V8 scanning acoustic microscope at 3.5 MHz frequency. The scanning area was set as 14 cm by 12 cm.

Thermography

Thermographic inspection is based on analysis of temperature distributions across the surface of the sample of interest – either produced naturally (e.g., as the result of some internal heat generation) or deposited externally. The latter approach is known as active thermography, and is of interest for inspection of wide range materials used in science and industry [5]. Active thermography generally assumes heat deposition on the surface of the sample under analysis with the aid of a flash or fan heater.

For this research, Principal Component Thermography method was utilized [6]. It allows for relatively fast extraction of qualitative information related to defective

areas – namely, their shapes and locations. The method consists of processing of a stack of thermal images represented as points in multidimensional space (number of dimensions is equal to the number of pixels in each image) and finding patterns (principal components) which represent common patterns in the entire image stack processed. In general, the most common pattern (PC1) corresponds to the non-uniformity of surface heating, a few higher PCs bear the information related to subsurface defects while most of PCs of higher orders correspond to uncorrelated noise. In this research, the temperature monitoring was performed by a FLIR SC4000 thermal imager (320x256, InSb FPA, 3-5 μm wavelength) at 80 frames per second.

Results and discussion: Acoustic microscopy

Acoustic microscopy has demonstrated the ability to visualize internal composite structure and detect damage in each ply of the composite. The impact damage dimensions and damage depth profile were visualized (Fig. 2b) and compared to von Mises strain distributions (Fig. 2a). Acoustic images show complex, layered structure of the impact damage. The delamination in each ply layer has a typical 2 lobe-shape with some regularity; the major axis of the delamination corresponds to the fibers direction. The total damaged area has a circular shape with the diameter increasing towards the back side of the specimen, which is typical for the impact damage of laminates. The B-scan images indicate position, length and depth of the damage at each ply. Vertical inter-laminar fractures were not detected. It is to be noted that due to the acoustic shadow effect, it is not possible to evaluate and visualize the area beneath the delamination in the upper plies.

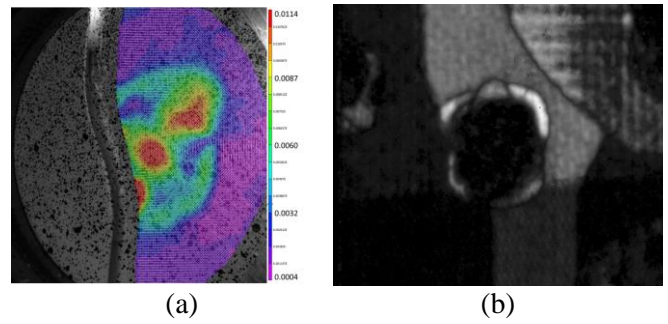


Fig.2. Specimen S2 (2.5 mm deflection): (a) Von Mises engineering strain field at maximum deflection, (b) Acoustic microscopy C-scan.

Results and discussion: Thermography

Thermographic inspection allowed for visualization of some of the defects present in the composite plates. The images presented below represent the principal component images extracted from a series of thermal images collected by thermal imager (Fig 3 – for sample S2). Collection of images was performed at 80 fps for 15-25 s after a deposition of a xenon flash excitation. The images presented should only be treated as a qualitative result due to unknown thermal properties of these materials. The thermal properties of materials as well as the depths of defects have drastic effect on appearance of defects on thermal images. Although thermography may not provide as sharp images as acoustic microscopy can provide, it is highly suitable for a quick inspection of relatively large samples.

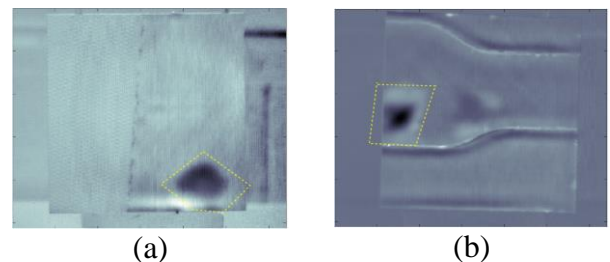


Fig.3. Specimen S2, results of thermographic inspection: (a) Face side (PC3), (b) Reverse side (PC3).

Conclusions and future work

An initial investigation of barely visible impact damage (BVID) in composites was completed by quasi-static loading of samples extracted from a Bombardier C-Series wing skin. Thermography was found to be the simplest effective method for capturing subsurface damage but with some limitations. Comparison of the acoustic and thermographic images indicates that the qualitative thermographic method selected was unable to evaluate full extent of the damage in the composite especially for low applied energies. Only delaminations at the upper plies were successfully detected with the thermography method employed. More significant damage was effectively detected by both acoustic microscopy and thermography. Using digital image correlation, the von Mises strain field captures highly localized surface strains associated with damage at the surface but consistency between surface strains and subsurface damage identified through acoustic microscopy was not observed at most energy levels. Some consistency between DIC and thermography for subsurface damage detection was observed for most energy levels but thermography was the superior inspection method. However, the true value of DIC lies in model validation where the model has predictive capabilities for failure. Visual inspection performed poorly for all but the highest energy level. Further mechanical characterization will be completed to assess any strain rate sensitivity (with a focus on damage mechanisms).

References

1. ISO, 6603-2: 2000 Determination of puncture impact behaviour of rigid plastics. 2000, ISO. p.1-28.
2. N. McCormick and J. Lord. Digital Image Correlation Materials Today, Vol.13, N.12, 2010, p.52-54.
3. F. Severin, I. Seviaryna, E. Maeva. Industrial Applications of Scanning Acoustic Microscopy. Materials Evaluation, Vol.71, N.7, 2013.
4. F. Severin, A. Denisov, R. Maev. Analysis of Laminated Composites with Portable Ultrasonic Imaging. Materials Evaluation, Vol.71, N.7, 2013.

5. X. Maldague, Theory and practice of infrared technology for nondestructive testing. 2001.
6. N. Rajic. Principal component thermography for flaw contrast enhancement and flaw depth characterisation in composite structures. Composite Structures, Vol.58, N.4, pp. 521-528, 2002.

Using numerical experimental design for crack detection by active thermography

Abdoulahad THIAM^{1*}, Jean-Christophe KNEIP¹, Eugen CICALA¹, Jean-Marie JOUVARD¹, Yannick CAULIER²,

¹ : Laboratoire Interdisciplinaire Carnot de Bourgogne (ICB - UMR6303 CNRS-UB), Université de Bourgogne-Franche-Comté, IUT de Chalon/Saône, 1 rue des granges forestiers, 71100, Chalon/Saône, France

² : AREVA/INTERCONTRÔLE / Reactors & Services –Installed Base BU, 4 rue Thomas Dumorey, 71100 Chalon Sur Saône, France

*: abdoulahad.thiam@u-bourgogne.fr

The aim of this work is the using of numerical experimental design method to improve open and subjacent cracks detection on metallic materials by active thermography. This process is a possible alternative for magnetic particles testing and dye penetrant testing in the field of non-destructive testing. In this context, a numerical simulation has been developed with COMSOL Multiphysics coupled with a virtual thermal camera in order to reproduce the exact process. We based on this model to do the numerical experimental design works. This study has been done for different materials with different kind of defects. We present here the most influence parameters in an open and a subjacent crack.

Introduction

Since several years, companies have in search of alternative methods for penetrate testing and magnetic particles testing [1]. Among several techniques, active thermography [2] appears as an interesting possibility. Generally the methods used on metallic materials are based on the “flying spot” [3]–[7]. In our studies we do a back and worth scanning, the reason of this choice is developed in [8].

The process of active thermography to detect defect has been summarized in Fig. 1. The laser is moving with a velocity v following x direction. Temperature is measured on laser irradiated surface in the place where is located laser line thanks to a pin of thermographic detectors (in y direction).

Several parameters are taken into account during inspection. We used numerical experimental design to optimize some of them. We divided this work into three main parts: in a first part, we expose a various methodologies implemented to obtain experimental data using for our numerical simulation model and numerical experimental

design methods. We also present the methodology adopted for the numerical model and the numerical experimental design method developed.

In a second part we focus on the influence of thermophysical properties on crack detection.

In a last part, we present the approach followed for the numerical experimental design [9], [10] by using model developed in [8] and [11] which present equation solved (1) and boundary conditions used and the validation step also.

$$\frac{\partial^2 T}{\partial x^2} + \frac{\partial^2 T}{\partial y^2} + \frac{\partial^2 T}{\partial z^2} - \frac{\rho C_p}{k} \frac{\partial T}{\partial t} = 0 \quad (1)$$

Two types of defects have been expected: open cracks and subjacent cracks. In the particular case of subjacent cracks, we studied the effect of work distance and defect shape on the capability of detection.

For the open cracks, we identified and studied, thanks to numerical experimental design, the most influential parameters on the signal, and how these parameters could be optimized.

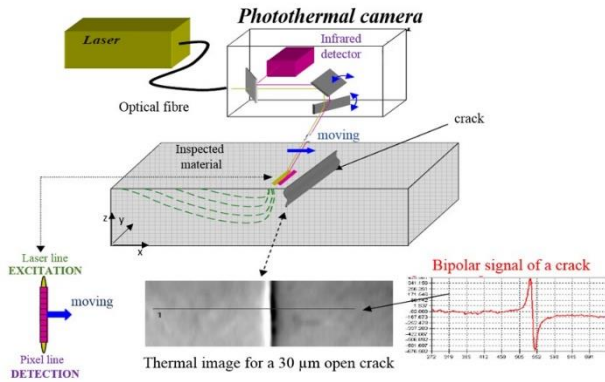


Fig. 1: active thermography process: “flying spot process”

Fig. 2 gives the temperature fields given by COMSOL (a) and by the virtual camera. In the last one, the working distance is equal to 500 mm. We can see a difference between these two images in particular on pixel size. It also shows the necessity to take into account the parameters of the camera.

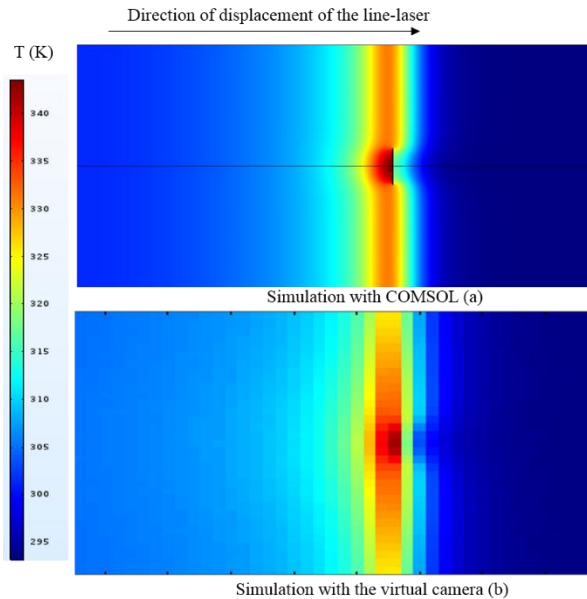


Fig. 2: Temperature field given by COMSOL (a) and the virtual camera (b)

Thermal properties influence on open crack detection

Tab. 1 gives different calculations computed for the thermophysical study. This table is named “matrix program”. We have defined four main parameters: the thermal conductivity (K), the heat capacity (C_p), the density (ρ) and the absorptivity (α), each of them have a domain of variation in which the results we obtain are valid.

Tab. 1: matrix program for calculation

| | X1 | X2 | X3 | X4 |
|----|------------------------|-----------------------------|-----------------------|----------|
| | K $W.m^{-2}.K^{-1}$ | C_p $J.Kg^{-1}.K^{-1}$ | ρ $Kg.m^{-3}$ | α |
| 1 | 13.5 | 450 | 7000 | 0.3 |
| 2 | 13.5 | 500 | 7500 | 0.45 |
| 3 | 13.5 | 450 | 8000 | 0.6 |
| 4 | 15 | 500 | 7500 | 0.6 |
| 5 | 15 | 450 | 8000 | 0.3 |
| 6 | 15 | 500 | 7000 | 0.45 |
| 7 | 16.5 | 450 | 8000 | 0.45 |
| 8 | 16.5 | 500 | 7000 | 0.6 |
| 9 | 16.5 | 450 | 7500 | 0.3 |
| 10 | 15 | 500 | 7500 | 0.45 |

The effect diagram for an open crack in a stainless steel is given by Fig. 3. The most important parameters governed the detection is the absorptivity follow up to the thermal conductivity. This study allows us to make a selection on the most important parameters to characterize for the numerical model.

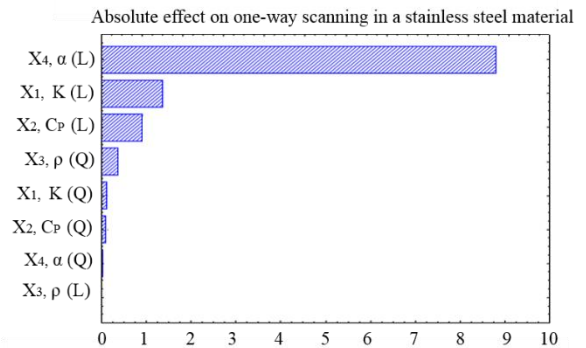


Fig. 3: Diagram of absolute effects on one-way scanning

Influence of parameter on subjacent defect

The evolution of the signal on one-way scanning in subjacent defect is represented in Fig. 4. We identify an exponential decrease of the signal when the ligament increase.

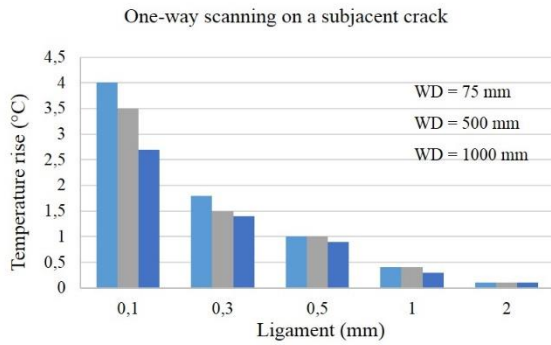


Fig. 4: Evolution of the signal amplitude according to the ligament for various working distances.

During inspection in industrial field, we identified that, some subjacent defect have been showed better than others, because of their length. This parameter is taken into account in our model, in order to find how it modifies the signal. Fig. 5 presents the evolution of the signal according to the defect length and opening. We can notice that the most important parameters governing the signal is the size of the ligament for a subjacent crack. The influence of length is very small compared to the ligament. As regards the opening, its influence is unimportant. This is due to the thermal resistance, which is mostly in vertical axis.

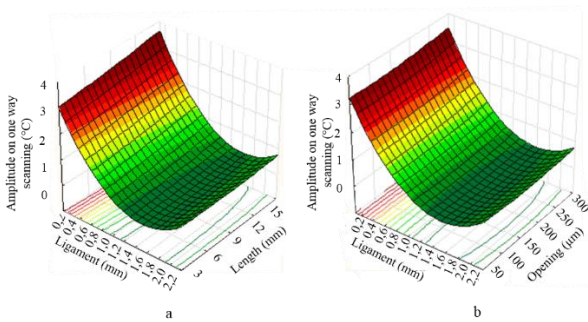


Fig. 5: Signal according to the defect, for ligament and length (a), for ligament and opening (b).

The signal obtained with a thermal camera depends on the pixel size. In our study we used defect made by electrical discharge machining. These defect have rectangular or round forms in their top. Unfortunately the real crack haven't the same form. Then we have decided to evaluate the influence of the form in subjacent crack detection. Figure 6 presents various defects that we expected. Three forms have been studied: rectangular, round and triangular with the same ligament (0.1 mm).

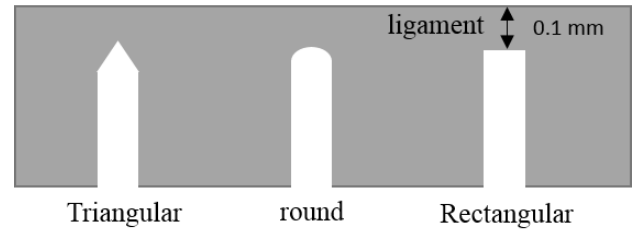


Figure 6: different forms of considered defects

Notable differences can be noticed between signal defects according to their form. Fig. 7 a and b shows the signal we have obtained on each form of defects for various working distance. We can show that we will have more difficulties to detect subjacent crack (triangular form) than subjacent defect done by electrical discharge machining (round and rectangular form). The signal magnitude decrease by 20% from the round to the real triangular form, and 30% from the rectangular to the triangular form.

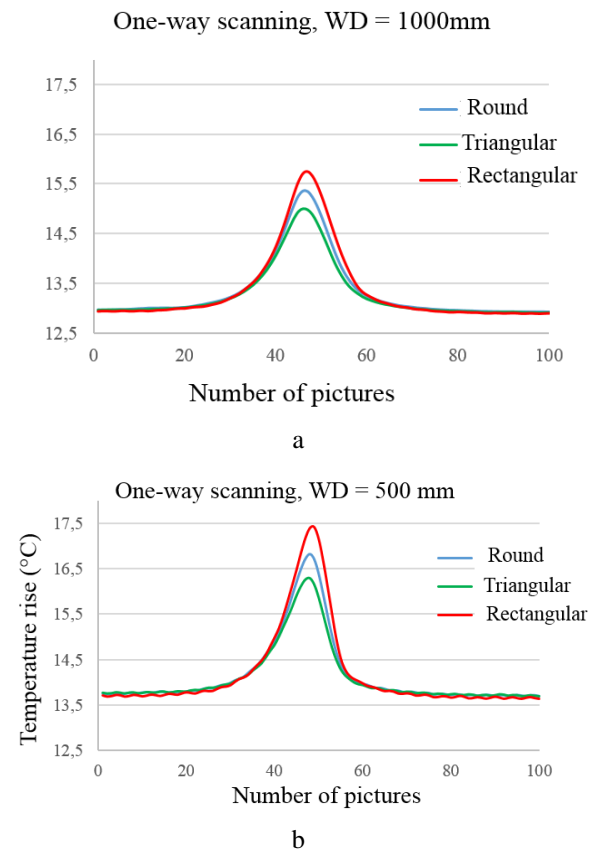


Fig. 7: influence of the defect form

Influence of some parameter on open crack detection

A previous study showed that the influence on velocity and opening in the signal are presented in [8]. In this study height parameters have been used. Thanks to numerical experimental design their influence on crack detection has been evaluated. We used a laser with 50W power, the wavelength is equal to 1064nm. Fig. 8 gives influences of the most important parameters studied. In the studied domain for each parameter, we can see that the laser power in the most important parameter which governed the detection. We can also observe the detection is better when the line laser in parallel (laser orientation = 0°) to the defect. Also the gap between the line laser and line pixel is very important, and the detection is improved when the line pixel is slightly in front of the line laser. Several parameters have linear effect on the signal. However the defect orientation, the gap between line laser and line pixel have quadratic effect.

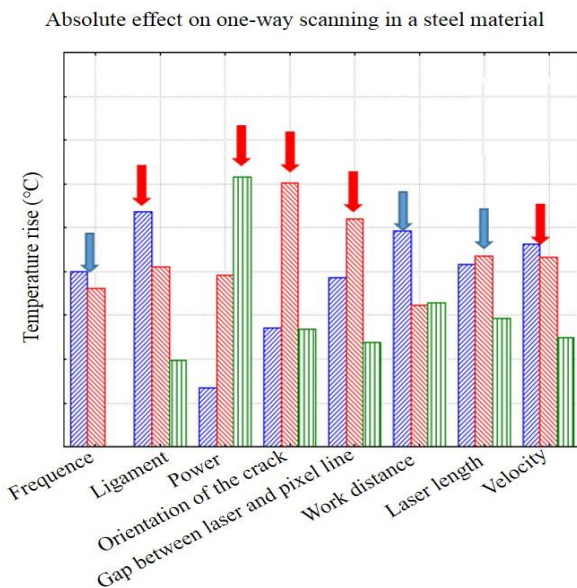


Fig. 8: effects diagram on a steel material

Conclusions

The developed numerical model, combining finite elements and virtual thermal camera allows us to take into account all parameters in the process, which is essential to carry out by numerical experimental designs (NED). The NED enables us to have an idea on several

parameters influence, and how these parameters act on the signal.

Subjacent defect can be detected until a certain ligament. The quality of detection for this type of defect depends on its forms and essentially on its ligament dimension. The signal decrease exponentially according to the ligament. The work distance also could be optimized in order to increase the quality of detection.

References

- [1] R. Singh, "Penetrant Testing," in *Applied Welding Engineering*, Elsevier, 2016, pp. 335–342.
- [2] G. Gaussorgues and S. Chomet, *Infrared Thermography*. Springer Science & Business Media, 1993.
- [3] E. J. Kubiak, "Infrared Detection of Fatigue Cracks and Other Near-Surface Defects," *Appl. Opt.*, vol. 7, no. 9, p. 1743, Sep. 1968.
- [4] I. Kaufman, P.-T. Chang, H.-S. Hsu, W.-Y. Huang, and D.-Y. Shyong, "Photothermal radiometric detection and imaging of surface cracks," *J. Nondestruct. Eval.*, vol. 6, no. 2, pp. 87–100, Jun. 1987.
- [5] C. Gruss, "Caméra photothermique etude théorique et réalisation pratique d'une caméra infrarouge active avec excitation laser," Université de Poitiers, 1992.
- [6] J.-C. Krapez, "Résolution spatiale de la caméra thermique à source volante," *Int. J. Therm. Sci.*, vol. 38, no. 9, pp. 769–779, Oct. 1999.
- [7] J. L. Bodnar and M. Egée, "Wear crack characterization by photothermal radiometry," *Wear*, vol. 196, no. 1–2, pp. 54–59, Aug. 1996.
- [8] A. Thiam, J.-C. Kneip, E. Cicala, Y. Caulier, J.-M. Jouvard, and S. Mattei, "Modeling and optimization of open crack detection by flying spot thermography," *NDT E Int.*, vol. 89, pp. 67–73, Jul. 2017.
- [9] E. Cicală, G. Duffet, H. Andrzejewski, D. Grevey, and S. Ignat, "Hot cracking in Al–Mg–Si alloy laser welding – operating parameters and their effects," *Mater. Sci. Eng. A*, vol. 395, no. 1–2, pp. 1–9, Mar. 2005.
- [10] J. Goupy, "Plans d'expériences." Techniques de l'ingénieur, Nov-2015.
- [11] A. Thiam, J. C. Kneip, S. Mattei, and E. Cicala, "Modélisation et optimisation de la détection de défauts débouchants par thermographie active." Congrès SFT, Juin-2016.

Acknowledgments

We would like to thanks BPI France and the Burgundy region for ATHENA project funding. We also thanks PNB for labeling the project.

Using Active Infrared Thermography for Characterizing Types of Ballistic Impacts

A. Huot¹, F. Marcotte¹, K. Mouhoubi², J.L. Bodnar²

¹ Telops, 100-2600, St-Jean-Baptiste Ave, Quebec City, Qc, Canada, G2E 6J5,
alexandrine.huot@telops.com

² UFR Sciences Exactes et Naturelles, GRESPI, BP 1039, 51687 Reims Cedex 2, France

Active infrared imaging has been used to analyze the thermal signature of different types of impacts on a ballistic plate, such as impacts from a bouncing projectile or impacts causing partial or complete perforation. The results of that study shown that the plot of the mean signal as a function of speed or kinetic energy seems to be a good tool to determine the type of impact even without knowing the speed of the projectile during the shot.

Introduction

Ballistic impact testing allows to better understand the interaction between projectiles and their target, and to analyze the properties of different materials in order to improve their resistance. Researchers evaluate amongst other properties, the amount of energy that can be absorbed by a given material and how efficiently the material can spread this energy.

A ballistic impact can be understood as a transfer of energy that generates huge amounts of heat, and that thus can easily be monitored using passive thermography. High-end infrared cameras combining high speed and high spatial resolution represent powerful tools for directly measuring the energy absorbed by the impacted area.

High-end scientific infrared cameras can also be used to quantify damage following the ballistic impact experiment. As there is no thermal contrast after the impact, it is possible to use an external source in order to generate a thermal contrast; this technique is known as active thermography.

In this study, active infrared imaging has been used to observe the infrared signature of the defects created by bouncing projectiles and defects resulting from partial perforation and complete perforation (Fig. 1). The plot of the mean signal as a function of speed or kinetic

energy proves to be enough to determine type of impact when the speed of the projectile during the shot is unknown.

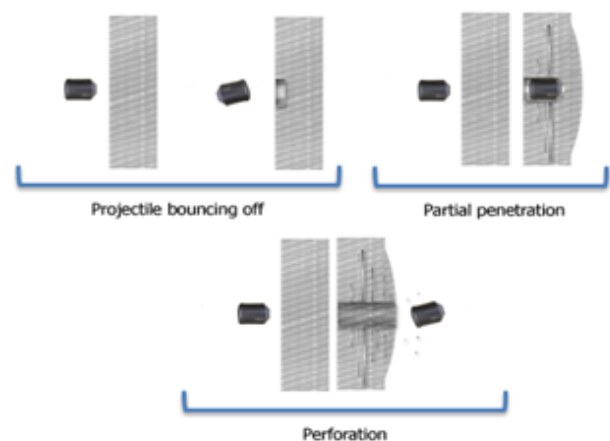


Fig. 1. Types of impacts.

Experimental Information

The FAST M2k from Telops (Fig. 2) is a cooled high-performance infrared camera using a 320×256-pixel indium antimonide (InSb) focal plane array (FPA) detector covering the 3 – 5.4 μm spectral range. This high-performance camera has been used with a fixed exposure time of 100 μs, allowing a frame rate of 1000 Hz at full resolution. For the experiment, a 50-mm Janos lens was used. The excitation source chosen for warming up the sample was a flash lamp of 3000 J.



Fig. 2. The Telops M2k high-speed infrared camera.

The ballistic plate that has been analyzed is shown in the Fig. 3. The projectile's speed has been recorded for 13 of the 16 shots that were fired. Table 1 shows the types of impacts for each shot as well as the projectile's speed. Kinetic energy has also been calculated assuming a projectile's weight of 10 g.

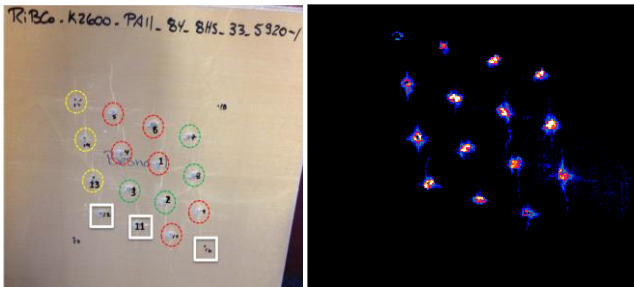


Fig. 3. Visible image of the composite ballistic plate (left) and the associated infrared image after the flash excitation (right).

Results

The infrared image obtained after the flash excitation is shown in Figure 3 (right). From this image, taken with the ImageJ software, it was possible to determine the active zones as well as parameters such as area size (in pixels), mean signal, standard deviation, minimum temperature value, maximum temperature value and perimeter.

From this data shown in Table 1, correlations between speed and some of these parameters such as active area, mean signal and perimeter can be noted (shown in the Fig. 4). The most conclusive correlation is obtained by plotting the mean value as a function of speed (Fig. 4B). A weak thermal signature is associated with a superficial impact while higher mean thermal signals are related to stronger impacts generating partial or complete perforation.

Active area and perimeter plotted as a function of speed give similar results independently of the type of impact (Fig. 4A and 4C respectively).

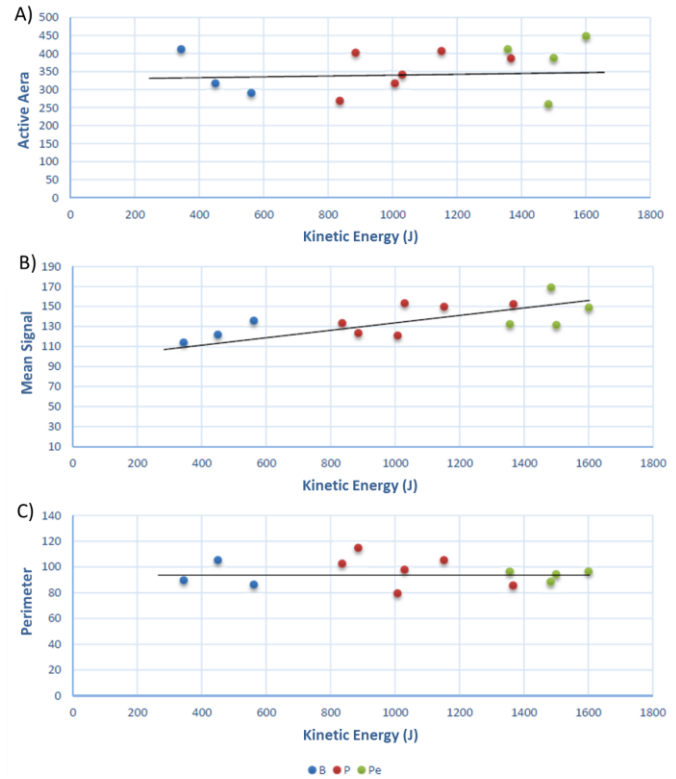


Fig. 4. Correlation between kinetic energy and active area (A), mean signal (B), perimeter (C).

From these results, it is possible to extrapolate and estimate the speed of a projectile by characterizing the thermal signature using active infrared imaging. For the three shots for which the speed of the projectile has not been recorded, the kinetic energy has been estimated using the mean signal (Fig. 5).

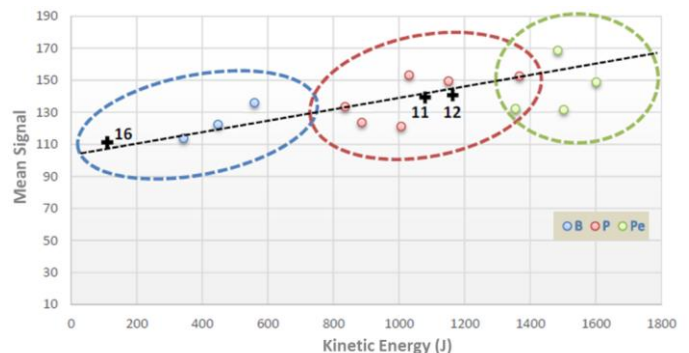


Fig. 5. Estimation of the kinetic energy for shot 11, 12 and 16.

| Shot | Type | Projectile's Speed | Kinetic Energy | Area | Mean | Standard Deviation | Min | Max | Perimeter |
|------|--------|--------------------|----------------|------|--------|--------------------|-----|-----|-----------|
| | B/P/Pe | m/s | J | | | | | | |
| 13 | B | 335 | 561.1 | 289 | 135.92 | 25.41 | 108 | 225 | 85.98 |
| 14 | B | 300 | 450.0 | 316 | 122.05 | 15.11 | 107 | 183 | 104.81 |
| 15 | B | 262 | 343.2 | 412 | 113.54 | 3.17 | 106 | 118 | 89.36 |
| 1 | P | 454 | 1030.6 | 340 | 153.1 | 46.5 | 107 | 255 | 97.42 |
| 4 | P | 480 | 1152.0 | 406 | 149.22 | 40.78 | 107 | 255 | 105.1 |
| 5 | P | 449 | 1008.0 | 316 | 120.84 | 11.59 | 107 | 152 | 79.29 |
| 6 | P | 523 | 1367.6 | 387 | 152.36 | 44.85 | 107 | 255 | 85.41 |
| 9 | P | 421 | 886.2 | 401 | 123.77 | 12.27 | 108 | 148 | 114.38 |
| 10 | P | 409 | 836.4 | 268 | 133.51 | 25.91 | 107 | 223 | 102.24 |
| 2 | Pe | 521 | 1357.2 | 412 | 132.08 | 20.74 | 107 | 221 | 95.94 |
| 3 | Pe | 545 | 1485.1 | 258 | 168.67 | 50.04 | 108 | 255 | 88.35 |
| 7 | Pe | 548 | 1501.5 | 387 | 131.32 | 24.3 | 107 | 211 | 93.98 |
| 8 | Pe | 566 | 1601.8 | 448 | 149.02 | 46.25 | 107 | 255 | 96.55 |
| 11 | ? | ? | 1083.2 | 302 | 138.33 | 39.3 | 107 | 251 | 73.12 |
| 12 | ? | ? | 1174.4 | 479 | 140.61 | 44.76 | 107 | 255 | 130.18 |
| 16 | ? | ? | 97.2 | 196 | 113.68 | 3.64 | 107 | 118 | 94.95 |

Table 1. Characterization of the impacts (B= bouncing projectile, P= partial perforation, Pe= complete perforation).

For shot 11, the kinetic energy estimated is 1083 J, which gives a projectile speed of 465 m/s. For shot 12, estimated kinetic energy is 1174 J, giving a speed of 485 m/s. Those two results in terms of mean signal are typical of partial perforation. As for the shot 16, its thermal signature is representative of a bouncing projectile of 139 m/s (97 J).

In order to corroborate the results above, active infrared imaging measurement has been done, not only on the front side, but also on the back side of the sample. Infrared images recorded by looking at the back side of the panel allow noting the complete perforations. Indeed, shots 11, 12 and 16 were not classified as complete perforations.

Conclusion

This work aimed to analyze the thermal signature of defects created by ballistics impact and to find

some correlation between the projectiles' speed and their thermal signature. The correlation between the active surface and the perimeter of the thermal signature cannot be used as the results seem to be similar for all kinds of impact. However, it was possible to note a correlation between the mean thermal signal and speed; this correlation proved to be helpful in the classification of different types of impacts.

DETECTION OF FATIGUE DAMAGE IN SHORT CARBON FIBER REINFORCED PLASTICS USING THERMOELASTICITY

T. Sakagami¹, D. Shiozawa², Y. Nakamura², S. Nonaka³, K. Hamada³

¹ Dept. of Mechanical Engineering, Kobe University
1-1 Rokkodai, Nada, Kobe 657-8501 Japan
sakagami@mech.kobe-u.ac.jp

² Dept. of Mechanical Engineering, Kobe University

³ DIC Corporation, 3-7-20 Nihonbashi, Chuo-ku, Tokyo 103-8233 Japan

Short carbon fiber reinforced plastics are receiving a lot of attentions because of their excellent moldability and productivity, however they show complicated behaviors in fatigue fracture due to the random fibers orientation. In this study, the thermoelastic stress analysis (TSA) was applied to the detection of fatigue damage in short carbon fiber composites. Evolution of fatigue damages was detected from distributions of the thermoelastic temperature change as well as the phase delay of the thermoelastic temperature change from the applied loading signal. It was found that damaged area was emphasized in differential phase delay images utilizing the property that carbon fiber showed opposite phase in thermoelastic temperature change.

Introduction

Carbon fiber reinforced plastic (CFRP) has been widely employed for structural members of transportation vehicles utilizing its excellent specific strength and specific rigidity in contrast with those of the metal. Short carbon fiber reinforced plastics are receiving a lot of attentions because of their excellent moldability and productivity. However they show complicated behaviors in fatigue fracture due to their random fibers orientation. Damage evaluation technique based on the thermoelastic stress analysis (TSA) using an infrared thermography has been examined for composite materials. Uenoya et al. [1] developed the thermoelastic damage analysis (TDA) for the early damage detection in plain-woven CFRP. Yoshida et al. [2] applied the TSA technique for characterizing impact damages in cross-ply carbon fiber/thermoplastic composites. The present authors [3] investigated the relationship between the fiber orientation angles and the phase delay of the thermoelastic temperature change from the applied loading signal to develop a new approach for fatigue damage identification for the short carbon fiber

reinforced plastics. In this study distributions of the thermoelastic temperature change were measured for the short carbon fiber reinforced plastics during fatigue test. Fatigue damages were detected by the conventional TDA procedure as well as the newly developed phase-delay based damage characterizing technique; thermoelastic phase damage analysis (TPDA).

TSA using infrared thermography

Dynamic stress change causes a very small temperature change under adiabatic conditions in a solid. This phenomenon is known as the thermoelastic effect and is described by Lord Kelvin's equation, which relates the temperature change (ΔT_E) to the sum of the changes in the principal stresses ($\Delta\sigma$) under cyclic variable loading as follows.

$$\Delta T_E = -\frac{\alpha}{\rho C_p} T \Delta\sigma = -k T \Delta\sigma \quad (1)$$

Here, α is the coefficient of thermal expansion, ρ is the mass density, C_p is the specific heat at constant pressure and T is the absolute

temperature. The coefficient k is called thermoelastic constant. The sum of the changes in the principal stresses ($\Delta\sigma$) is obtained by measuring the temperature change (ΔT_E) using an infrared thermography.

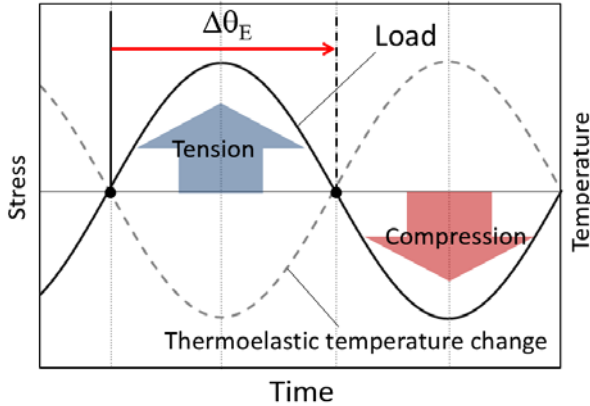


Fig. 1 Phase of thermoelastic temperature change.

When a tension and compression loading in sinusoidal waveform as shown in Fig. 1 is applied to materials with positive value of the thermoelastic constant k , the thermoelastic temperature change shows opposite phase waveform against the loading waveform. In this study the value of phase delay $\Delta\theta_E$ was defined as the difference in phase between the thermoelastic temperature change and the loading signal as shown in the figure. For the materials with positive thermoelastic constant k , the phase delay $\Delta\theta_E$ is 180 deg. In this study, thermoelastic temperature measurement was conducted for the short carbon fiber reinforced plastics, and the thermoelastic temperature change ΔT_E and the phase delay $\Delta\theta_E$ was obtained from experimental data.

Experimental setup

Configurations of the CFRP specimen employed in this study are shown in Fig. 2. The specimens were cut from laminated short carbon fiber composite sheet with vinyl ester resin and 25.4 mm long carbon fiber bundles. Each bundle was composed of 12000 short carbon fibers. The mass content [wt%] of resin and fiber was 67 and 33, respectively. The specimen has circular notches with the radius of 2 mm.

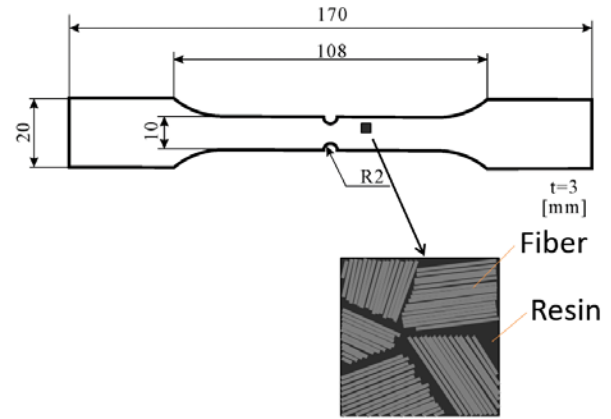


Fig. 2 Configurations of employed CFRP specimen.

Sinusoidal waveform cyclic loading with a frequency of 7 Hz and a stress ratio $R = 0.1$ was applied to the specimen by an electrohydraulic fatigue testing machine. Microscopic visible images on the specimen surface and side surface were taken by optical microscope. The thermoelastic temperature change on the specimen surface was measured by the infrared thermography (CEDIP Titanium530L, QVGA MCT array detector, NETD 25mK). The thermoelastic temperature change ΔT_E and the phase delay $\Delta\theta_E$ was obtained from experimental data.

Experimental results

The present authors [3] investigated the relationship between the fiber orientation angle from the loading axis ϕ_f and the thermoelastic temperature change ΔT_E as well as its phase delay $\Delta\theta_E$. It was found that ΔT_E measured in the area where ϕ_f is around 90° takes higher values compared with those measured in the area where ϕ_f is around 0° . It was also found that the phase delay $\Delta\theta_E$ takes the value of 180° where the fiber orientation angles are around 90° . On the other hand, $\Delta\theta_E$ takes 0° where ϕ_f is around 0° . This phenomenon can be interpreted by the property that carbon fiber showed opposite phase in thermoelastic temperature change. Sugimoto et al. [4] reported that the thermoelastic constant k of unidirectional CFRP had negative value since the thermal expansion coefficient α of the carbon fiber in longitudinal direction had negative value. It was supposed that carbon

fibers mainly shared the applied axial load in the region where the orientation angles of the carbon fiber bundles are 0° (parallel with the loading axis). Therefore the thermoelastic temperature change showed a coordinate-phase waveform with that of applied loading.

Fatigue test was conducted for the short carbon fiber composite specimens with circular notches under the applied maximum stress $\sigma_{max} = 180$ MPa.

The TDA technique was applied to detect fatigue damage in short carbon fiber composite first. In the TDA technique, a differential thermoelastic temperature distribution image was generated by subtracting an image of thermoelastic temperature change obtained at certain loading cycle from a reference initial image of thermoelastic temperature change. Fatigue damage evolution causes local stress change, and this is emphasized in the differential thermoelastic temperature distribution image.

The reference initial image of the thermoelastic temperature change was set at 200 cycles. Obtained TDA images at 10000, 30000, 40000 and 44000 cycles are shown in Fig. 3, with the infrared image obtained after failure of the CFRP specimen at 40168 cycles.

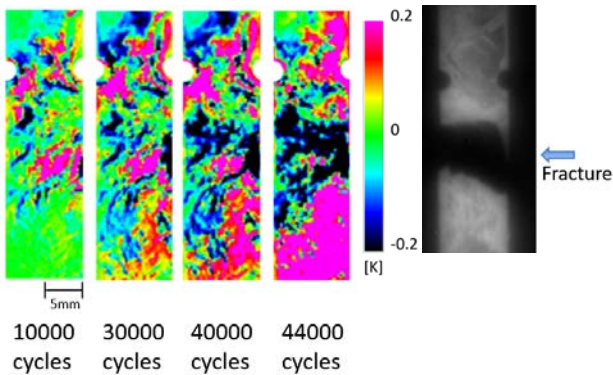


Fig. 3 Obtained TDA images in fatigue test.

It is found from the obtained TDA images that the thermoelastic temperature change ΔT_E on the fracture part was decreasing with the increasing loading cycles. The decreasing area of ΔT_E was expanded in the transverse direction of the specimen. The fatigue damage can be detected from the local stress change caused by the change in load sharing condition due to the damage evolution.

Secondly fatigue damage was detected by the newly developed thermoelastic phase damage analysis (TPDA) utilizing the change in phase delay $\Delta\theta_E$. In TPDA a differential phase delay distribution image was generated by subtracting a phase delay data obtained at certain loading cycle from a reference initial phase delay data. In this experiment the reference initial phase delay data was set at 200 cycles. The obtained TPDA images at 10000, 35000, 40000 and 44000 cycles are shown in Fig. 4. Microscopic visible images of the specimen side surface taken at 35000 and 40000 cycles are shown in Fig. 5 comparing with TPDA results.

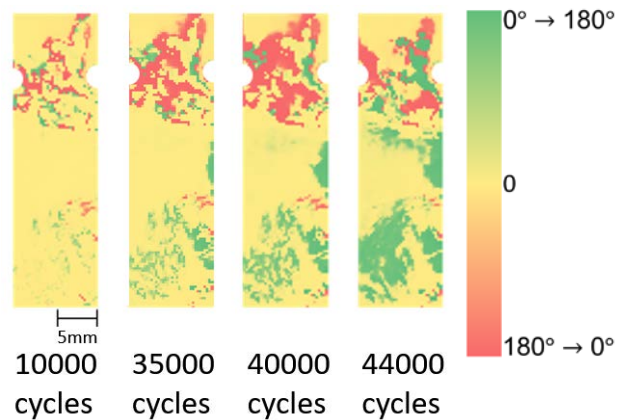


Fig. 4 TPDA images indicating fatigue damage evolution.

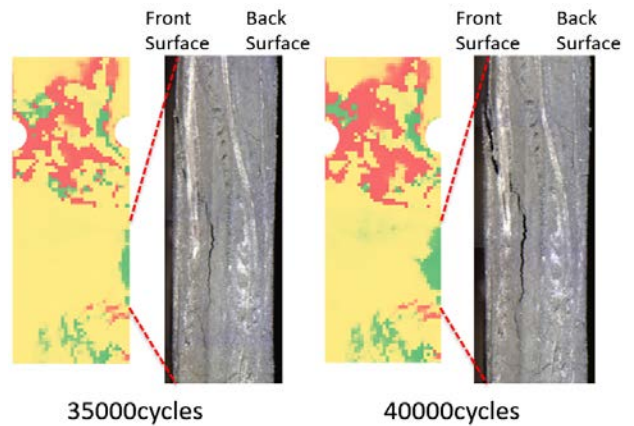


Fig. 5 Microscopic visible images of specimen side surface indicating delamination damage evolution.

It is found from Fig. 5 that delamination damage was initiated at 35000 cycles and it grew and reached the front surface of the specimen (infrared observation side). It can be seen from Figs. 4 and 5 that the change in phase values were clearly detected in the region where the

delamination fracture was detected. The phase values were changed from 0° to 180° , and the phase change region was expanded with the increasing loading cycles. As described in the foregoing paragraph, $\Delta\theta_E = 0^\circ$ means that the thermoelastic effect of carbon fiber bundles is predominant, on the other hand $\Delta\theta_E = 180^\circ$ means that the thermoelastic effect of matrix resin is predominant. The change in phase values indicates the change of load sharing condition between resin and carbon fiber bundles due to the evolution of delamination damage.

Conclusions

The thermoelastic stress analysis using infrared thermography was applied to the evaluation of fatigue damage in short carbon fiber reinforced plastics. The conventional thermoelastic damage analysis TDA was employed for fatigue damage detection. A phase-delay based fatigue damage detection technique TPDA was newly developed, in which the phase delay of the thermoelastic temperature change from the applied loading signal was measured. Feasibility of the TPDA was investigated for damage detection in short carbon fiber composite. Fatigue damages were evaluated by the conventional TDA procedure as well as the TPDA technique. It was found from the TPDA images that the significant change of phase values from 0° to 180° (indicating the change in load sharing condition between resin and carbon fibers due to fatigue damage evolution) was found in the region where the structural fracture was detected.

Acknowledgement

The authors would like to acknowledge that this research was partly supported by a Grant-in-Aid for Scientific Research from the Japan Society for the Promotion of Science (B: 26289009).

References

1. T. Uenoya, T. Fujii. Damage characterization of woven fabric composite materials by thermoelastic analysis, *Journal of the Society of Materials Science, Japan*, Vol. 49, No. 8, pp.941– 947, 2000.
2. T. Yoshida, T. Uenoya, H. Miyamoto. Impact damage characterization in cross-plyed carbon fiber/thermoplastic composites using thermoelastic stress analysis, *Proceedings of SPIE*, Vol. 8347, pp. 83470P-1 – 83470P-8, 2012, doi:10.1117/12.915144.
3. T. Sakagami, D. Shiozawa, Y. Nakamura, S. Nonaka, K. Hamada. Fatigue damage evaluation of short fiber CFRP based on phase information of thermoelastic temperature change, *Proceedings of SPIE*, Vol. 10214, pp. 102140M-1 – 102140M-6, 2017, doi:10.1117/12.2262972.
4. S. Sugimoto, T. Ishikawa. Examination of quantitative infrared stress measurement of CFRP laminates and its application to non-destructive evaluation, *Technical Report of National Aerospace Laboratory*, 1396, pp.1–23, 1999.

Practical simulation of delamination in composites for thermography NDT

L.-D. Thérroux¹, J. Lewandowski², B. Masson³, J.-F. Vandenrijt⁴, M. Georges⁴

^{1,2} Centre Technologique en Aérospatiale, 5555 place de la Savane, St-Hubert, Québec, Canada

¹louis-daniel.theroux@cegepmontpetit.ca, ²jacques.lewandowski@cegepmontpetit.ca

³Bombardier Aerospace, 1800 Boul. Marcel Laurin, Saint-Laurent, Québec, Canada

³benoit.masson@aero.bombardier.com

^{4,5} Centre Spatial de Liège, Avenue du Pré Aily, 4031 Angleur, Liège, Belgium

⁴jfvandenrijt@ulg.ac.be, ⁵mgeorges@ulg.ac.be

This paper tackles the issue of simulating delaminations in reference standards made of CFRP (carbon fiber reinforced polymer) used for non-destructive testing by thermography. Thermography results of a real delamination are compared with flat bottom holes with similar size and depth. Results show a notable difference of the thermal contrast between the real delaminations and the FBH. To replicate the thermal behavior of a real delamination, a solution is proposed by plugging the flat-bottom hole. Thermography tests were conducted with plugs using various materials with thermal properties similar to CFRP.

Introduction

In NDT (Non Destructive Testing), a RS (Reference Standard) is a manufactured sample containing artificial discontinuities. RS are used to optimize techniques, calibrate systems, validate procedures or determine probabilities of detection. Thus, a RS must be as similar as possible to the real structures in all aspects: its geometry, its materials, fabrication process, etc. The RS must also contain defects according to the acceptance criteria determined during the engineering design process [1]. Inducing real defects of precise size and depth can be problematic, this is why most RS use artificial defects. It is crucial that those artificial defects contained in the RS are representative of the real defects. In composites materials, it has been shown that for ultrasound testing (UT), a flat bottom hole (FBH) and a delamination results in the same signal (except using immersion or through transmission). Both are regarded as an interface between the CFRP and the air that reflect most of the ultrasound beam back to the probe. In other words, if a UT procedure can detect a FBH, it can effectively detect a real

delamination that is similar in depth, size and shape. The same can be said about Teflon inserts that are also widely used in composite RS.

Thermography is a NDT method used to inspect composites structures [2]. However, thermography is based on the thermal properties while ultrasound is based on the acoustic properties. Since both methods are fundamentally different, can we assume that FBH are a valid way to simulate delaminations for thermography? A review of the scientific literature shows that some studies on thermography have been conducted on composite RS with FBH [3,4,5] but none compare the results with a real delamination. In this study, tests were conducted on a RS containing FBH and a real delamination to expose the difference of their thermal response. To make the FBH thermal behavior more concordant with an actual delamination, plugs were fabricated to fill the FBH. These plugs are made with various materials and tests are conducted to evaluate the optimal material to reduce the difference in thermal conduction between the FBH and the real delamination. The

idea of using a plug to modify the heat propagation in a FBH was mentioned in a previous study [6] but was applied to coating disbands on metallic structures and the solution wasn't tested on a real defect.

Reference Standard

To validate the simulated defects, they must be compared to real delaminations. Real delamination appears for different reasons, some are induced during the curing process but it is difficult to adjust the fabrication parameters to create a local delamination. For this project, it was decided to induce a delamination using low velocity impact since it is easier and does not require the manufacturing of a new sample.

The RS used is a 3.0 mm thick monolithic plate of prepreg UD cured in autoclave. The layup configuration is $[45/0/45/90]_{2s}$. Impact tests were conducted on the RS to create a delamination that is large enough to be detected by thermography. The impact tests were done on the tool side. The norm D7136 was referenced to determine the impact parameters. Various impact energies were tested. An impact energy of 30 J induced two delaminations that spread sideways. No visual indications or surface damage suggested the presence of the delamination or affected the thermography inspection.

The plate was inspected by ultrasounds confirming that the delaminations are located between two plies. To verify this, the RS is inspected in UT from both sides and the defect's depths from both sides add up to the plate thickness. From the tool side, the depths of the two delaminations are 2.0 and 2.1 mm and from the bagside, they were located at 1.0 and 0.9 mm (see Fig.1). The UT inspection also allowed to measure the size of the defects which is roughly 20 mm at its widest point. With those results, two FBH were machined on each side of the sample, each with radius of 19 mm and located at the same depth as the delaminations.

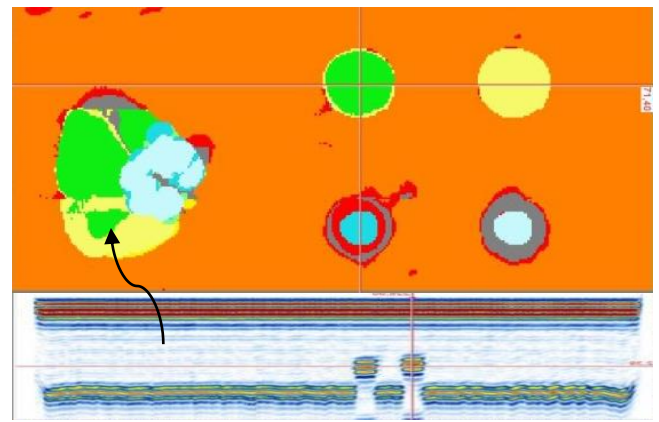


Fig. 1. C-Scan and B-Scan position from the UT inspection on the tool side. The C-Scan shows that both flat-bottom holes (upper left, and upper right circle) are at the same depth as the delamination on the left side, i.e. 2.1 and 2.0 mm. The bottom left and right circle are the open side of the FBH machined for inspection from the other side of the RS.

Comparing FBH with a Delamination

Step thermography with a duration of 5 sec was done with two halogen lamps of 1 kW each, placed symmetrically at 30 cm from the RS and oriented in order to have a uniform heating. The infrared camera used is a TEL-1000 MW from Telops and was placed also at 30 cm facing the sample. Initial results show a notable difference in thermal contrast between the FBH and the real delamination (see Fig. 2). No images processing was used in Fig.2 and Fig. 4.

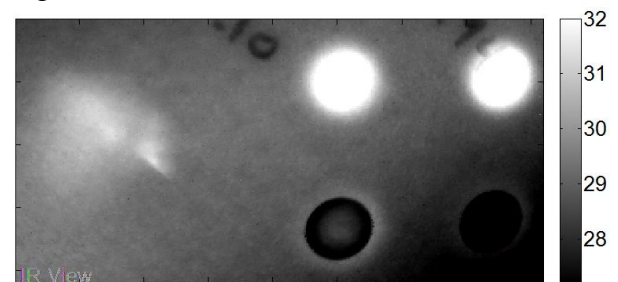


Fig. 2. Thermogram of the RS with the real delamination on the left and the two flat bottom holes on the right with step heating of 5 sec.

To improve the thermal behavior of the artificial defects, the solution is to fill the FBH with plugs. These plugs were made from various materials: wood, gypsum plaster, nylon and spackling paste (Polyfilla®). These materials were chosen because their thermal properties were similar to CFRP (see Fig.3 and [7]). No plugs were made from CFRP because

if they must be fabricated for each depth and size of the defects, in the long run it will be easier and less expensive to use common materials.



Fig. 3. Picture of the reference standard from the backside with flat bottom holes and the corresponding plug.

Thermography NDT result presented in Fig.4 clearly show that the use of plugs allows the FBH to behave more like a real delamination.

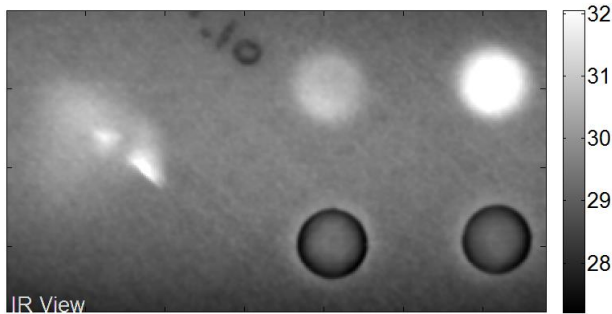


Fig. 4. Thermogram of the reference standard. On the left, the delamination and on the right the FBH. The FBH on the left was filled with a plug made of wood.

To validate the representation of the plugged FBH compared to a real delamination, their absolute thermal contrast [7] is compared:

$$Ca(t) = T_{def}(t) - T_s(t) \quad (1)$$

Where $T_{def}(t)$ represent the temperature over an area with a defect and $T_s(t)$ the temperature over a sound area.

The absolute contrast was calculated for each defects, real and artificial, located at 0,9 mm and in function of the plug material.

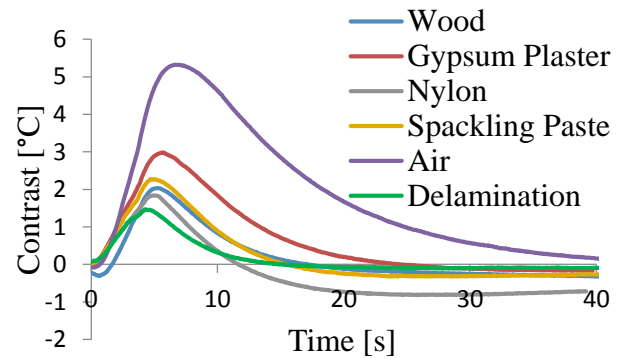


Fig. 5. Plot of the absolute contrast for the delamination and the FBH of 0.9 mm depth.

The tests were also conducted on the 1.0, 2.0 and 2.1 mm deep defects. All show that an empty FBH has a greater thermal contrast than a real delamination. Even though the difference diminishes for deeper defect, at 2.1 mm the absolute contrast of air (no plug) is still twice the contrast of the real delamination. To determine the best material to make the plug, the difference in contrast between the delamination and the plugged FBH is calculated. The mean and maximum value of this difference in contrast is presented in Fig.6. The graph also show the difference in contrast at time $t(C_{max}) = 4\text{sec}$, the time where the contrast of the delamination is at its peak.

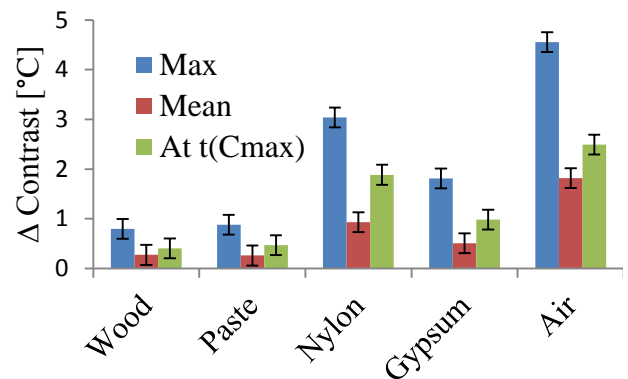


Fig. 6. Bar graph of the difference between the contrast of the FBH with plugs and the delamination for a depth of 0.9mm for an observation duration of 40sec. The graph show the maximum, the mean and the value at time of maximum contrast (4 sec. after end of heating).

The uncertainty of the measure is based on multiple measurements made in the same conditions. This uncertainty is calculated using the standard deviation of the temperature of the delamination. It can be explained by the

variation of the ambient temperature and the NETD of the infrared camera.

Results shows that for all the material tested, those that caused the FBH to behave the most like a real delamination is the wood and the spackling paste. Results from the delamination at 1.0 mm lead to the same conclusion. For the delamination at 2,0 and 2.1 mm deep, the thermal contrast is too small compared to the uncertainty of the measurements to make a conclusion.

Even with the plug, the visibility of the artificial defect is still slightly overestimated. We believe that a plug made of CFRP would be the best solution to simulate a defect. However, machining CFRP can be challenging and spare materials are not always easily and cheaply available. Perhaps making a plug out of resin only, such as the phenolic resin, could be a valid alternative.

Conclusion

This study has compared artificial defects with real delaminations. Results show that FBH are not representative of real delaminations caused by low velocity impacts in CFRP. This issue can be partially resolved by using a plug in the FBH. It seems the gap in a delamination is small enough to let a significant portion of the heat conduct through it. An empty FBH induce a thermal contrast that can reach up to twice the contrast of the delamination, more than 4°C. Using a plug of wood or spackling paste, the difference in contrast is reduced to less than 1°C for a delamination at 0.9 mm deep. These conclusions were validated using step thermography. The results of this study should be validated with a RS made of fiber-glass instead of carbon fiber and with other types of defects, such as disbonds in monolithic structures. It would also be interesting to investigate other types of defects representation, for example Teflon inserts and occlusions.

In the light of the results, it seems pertinent to verify how accurate are the artificial defects

for other emerging NDT methods, such as shearography and bondtesting. To improve the analysis of the thermal behavior of the artificial defects, it would help to have a finite element model to simulate the inspection. The model could help in optimizing the plug material and thickness. It could also be used to determine the thermal resistance value for a real delamination. For artificial defects, the thermal contact resistance depends on various factors, like the roughness of both the FBH and the plug. Finally, it would be interesting to see the differences between a real and an artificial defect when using an image processing analysis, such as the Fourier Transform.

References

1. W.D. Rummel, G.A. Matzkanin, *Nondestructive Evaluation (NDE) Capabilities Data Book*, Nondestructive Testing Information Analysis Center, Austin, Texas, 1997.
2. I. Jorge, P. Venegas, L. Vega, I. Lopez, B. Vollheim, L. Krausz, M. Georges, Review of thermal imaging systems in composite defect detection, *Infrared Physics & Technology*, Vol. 61, 167-175, 2013.
3. M. Freundberg Beemer, S. Shepard, Aspect Ratio Considerations for Flat Bottom Hole Defects in active Thermography, *QIRT 2016*.
4. B. Oswald-Tranta, R. Schmidt, T. Grandl, Comparaison of samples with flat bottom holes and with hidden occlusions using flash thermography, *QIRT 2016*
5. M.Reischel, P.Myrach, C.Maeierhofer, Development of Reference Test CFRP Specimens for the Standardization of Active Thermography with Flash Excitation, 4th International Symposium on NDT in Aerospace, 2012.
6. G. Ptaszek, P. Cawley, D. Almond, S. Pickering, Artificial disbonds for calibration of transient thermography inspection of thermal barrier coating systems, *QNDE*, 2011.
7. X. Maldague, *Theory and Practice of Infrared Technology for Nondestructive Testing*, Wiley Series in Microwave and Optical Engineering, 2001.

Eddy Current Pulsed Thermography for Basalt-Carbon Hybrid Composites Subjected to Ballistic Impacts: A Numerical and Experimental Study

H. Zhang¹, S. Sfarra^{2,3}, A. Osman^{4,5}, U. Netzelmann⁴, C. Ibarra-Castanedo¹, S. Perilli², F. Sarasini⁶, X. Maldague¹

¹Computer Vision and Systems Laboratory, Department of Electrical and Computer Engineering, Université Laval, 1065, av. de la Médecine, Québec, QC G1V 0A6, Canada

²Las.E.R. Laboratory, Dept. of Industrial and Information Engineering and Economics (DIIE), University of L'Aquila, Piazzale E. Pontieri no. 1, Monteluco di Roio – L'Aquila, I-67100, Italy

³Tomsk Polytechnic University, Thermal Control Methods Lab. N° 34, Tomsk 634050, Russia

⁴Dept. Inspection of Components and Assemblies, Fraunhofer-Institute for Nondestructive Testing IZFP, Saarbrücken, Germany

⁵University of Applied Sciences, Saarland, htw saar, Goebenstraße 40, 66117 Saarbuecken, Germany

⁶Department of Chemical Engineering Materials Environment, Sapienza-Università di Roma, Via Eudossiana 18, 00184 Rome, Italy

In this paper, eddy current pulsed thermography (ECPT) was used to detect the damages caused by ballistic impacts in basalt-carbon hybrid fiber-reinforced polymer laminates. In particular, different hybrid structures including intercalated stacking and sandwich-like structures were used. Numerical simulations were performed to predict the damages due to the impact loading. X-ray computed tomography (CT) was used for validation. Finally, a comparative study based on the experiments and simulations was conducted.

Introduction

Infrared thermography (IRT) techniques have been widely used for the composite materials due to the fast inspection rate, contactless nature, spatial resolution and acquisition rate improvement of infrared cameras. Among the IRT techniques, eddy current pulsed thermography (ECPT) is gaining increasing attention, especially for conductive materials, such as carbon fiber-reinforced polymer composites (CFRP).

Problem statement

Due to the high specific strength and stiffness, CFRPs are often used in the aerospace industry. However, their toughness is considerably low, therefore, the impact damage resistance is not very high. A solution is represented by fiber-hybridization

usually with high strain to failure fibers. In this regard, basalt fiber is attracting increasing attention because it is inexpensive and eco-friendly. An in-depth study of post ballistic impacts in basalt-carbon fiber hybrid fiber-reinforced polymer composites has not been documented yet in the open literature centred on ECPT.

Approach and techniques

In this paper, ECPT in transmission mode was used to detect the damages caused by ballistic impacts in six basalt-carbon hybrid fiber-reinforced polymer laminates. In particular, different hybrid structures including intercalated stacking and sandwich-like structures were used. Numerical simulations were performed to predict the damages from the mechanical aspect. X-ray computed tomography (CT) was used for the validation of thermographic results. Finally, a

comparative study based on the experiments and simulations was conducted.

Results

ECPT is able to show the damages in detail. The numerical and experimental results are in good agreement between them. In addition, CT validated the thermographic results.

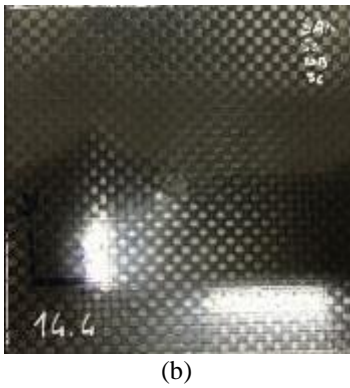
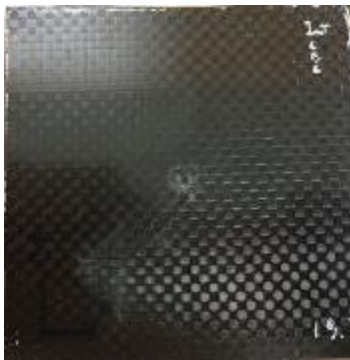


Fig. 1. Photographs of the impacted specimens at ballistic level: (a) intercalated stacking, (b) sandwich-like structure.

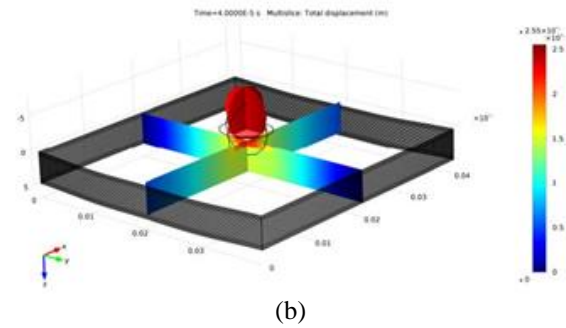
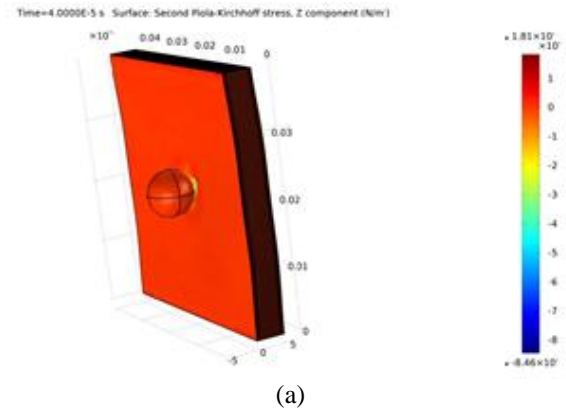


Fig. 2. Finite Element Analysis (FEA) simulations of the sandwich-like structures: (a) side view, (b) top view.

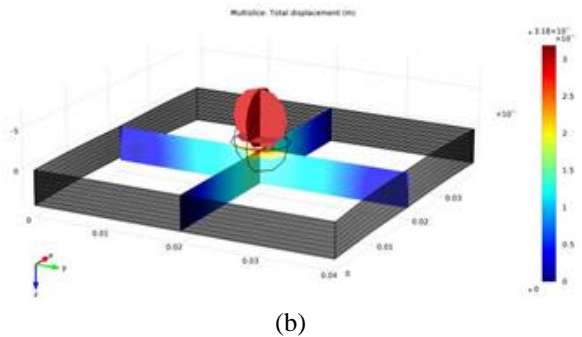
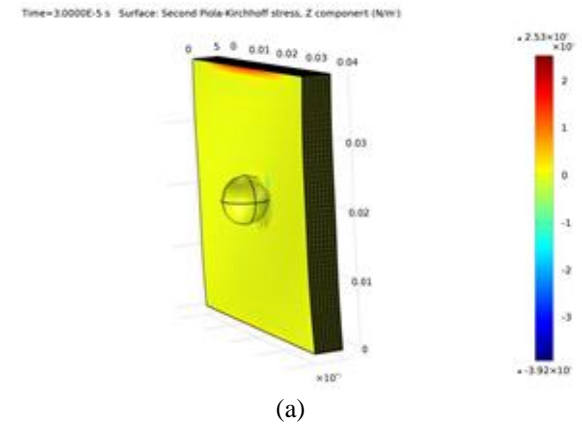


Fig. 3. FEA simulations of the intercalated stacking structures: (a) side view, (b) top view.

Conclusions

The results indicate that ECPT technique is able to retrieve defects linked to basalt-carbon hybrid fiber-reinforced polymer composites even if basalt fiber is not a conductive material. FEA shows the behavior of the impacts from a mechanical point of view, while CT validated the thermographic results.

References

1. Zhang, H., et al. "Numerical and experimental analyses for natural and non-natural impacted composites via thermographic inspection, ultrasonic C-scan and terahertz imaging." SPIE Commercial+ Scientific Sensing and Imaging. International Society for Optics and Photonics, 2017.
2. Sfarra, S., et al. "Analysis of damage in hybrid composites subjected to ballistic impacts: an integrated non-destructive approach." Handbook of Composites from Renewable Materials, Physico-Chemical and Mechanical Characterization (2017): 175.

Detection of back-surface crack based on temperature gap measurement using infrared thermography

Y. Izumi¹, Y. Mizokami², A. Moriyama³, T. Sakagami⁴

¹ The University of Shiga Prefecture, 2500 Hassaka, Hikone, Shiga 522-8533 Japan,
izumi.yu@mech.usp.ac.jp

² Honshu-Shikoku Bridge Expressway Co., Ltd., 4-1-22 Onoe-dori, Chuo, Kobe 651-0088 Japan,
yoshiaki-mizokami@jb-honshi.co.jp

³ Honshu-Shikoku Bridge Expressway Co., Ltd., 18 Tosadomari Ura Aza-Oge, Naruto,
Tokushima 772-0053 Japan, akira-moriyama@jb-honshi.co.jp

⁴ Kobe University, 1-1 Rokkodai, Nada, Kobe 657-8501 Japan, sakagami@mech.kobe-u.ac.jp

For large-scale steel structures such as orthotropic steel decks in bridges, nondestructive inspection of fatigue damages are indispensable for securing their safety. As conventional NDT techniques for steel bridges, visual testing, magnetic particle testing and ultrasonic testing have been commonly employed. However, these techniques are time- and labor-consuming techniques. The present authors developed a new thermography NDT technique for crack detection, which was based on temperature gap appeared on the surface of structural members due to thermal insulation effect of the crack. The practicability of the developed technique to through crack was demonstrated by the field experiments for steel bridges in service. In this paper, the applicability of the inspection technique based on temperature gap measurement to back-surface crack is investigated by the laboratory testing.

Introduction

In recent years, fatigue crack initiations and propagations in aged steel bridge which may lead to catastrophic structural failures have become a serious problem. For large-scale steel structures such as orthotropic steel decks in highway bridges, nondestructive inspection of fatigue damages are indispensable for securing their safety and for estimating their remaining strength. As conventional NDT techniques for steel bridges, visual testing, magnetic particle testing and ultrasonic testing have been commonly employed. However, these techniques are time- and labor-consuming techniques, because special equipment is required for inspection, such as scaffolding or a truck mount aerial work platform. The present authors developed self-reference lock-in thermography, as a remote NDT

technique based on thermoelastic temperature measurement by infrared thermography [1-2]. In this technique, fatigue cracks were detected and evaluated from localized high thermoelastic temperature change around crack tips due to stress singularity under variable loading from traffics on the bridge. Self-reference lock-in data processing technique for infrared thermography data was developed for the improvement of signal/noise ratio in the crack detection process. The practicability of the technique was demonstrated for weld-bead-penetrant-type fatigue cracks as well as through-deck-type fatigue cracks in steel bridges in service [1-2]. The present authors developed another thermography NDT technique for crack detection, which was based on temperature gap appeared on the surface of structural members due to thermal insulation effect of the crack. The practicability of the developed technique to through crack was

demonstrated by the field experiments for highway steel bridges in service [3]. This technique provides time and cost saving NDT scheme.

In this paper, the applicability of the inspection technique based on temperature gap measurement to back-surface crack detection is investigated considering the crack shape. The experimental studies were conducted for several specimens with semi-elliptical slit introduced by wire electrical discharge machining (EDM).

NDT technique based on temperature gap detection

Basic principle of the NDT technique based on temperature gap detection for weld-bead-penetrant-type fatigue crack in the orthotropic steel deck is shown in Fig. 1. Asphalt pavement on the surface of steel bridge is heated by sun shine. Heat conduction occurs from the pavement to trough rib through deck plate and this makes temperature gradient in the trough rib. The temperature change is continuous when there is no crack in weld bead, on the other hand temperature gap is observed between deck plate and trough rib due to thermal insulation effect of the crack in weld bead. The temperature gap can be detected by the continuous temperature monitoring along the weld bead using traveling infrared thermography equipment. In this study, this technique is applied for back-surface crack detection.

Experimental setup

The applicability of the inspection technique based on temperature gap measurement to back-surface crack detection was investigated. A schematic illustration of the experimental setup is shown in Fig. 2. The experiments were conducted for several specimens. A semi-elliptical slit of 1.0 mm width was introduced in a back surface of each specimen by wire electrical discharge machining (EDM). The specimen material was carbon steel, JIS SS400. The dimensions of the specimen were shown in

Fig. 3. Table 1 shows the slit size of each specimen. As shown in Fig. 2, a temperature gradient of the specimen longitudinal direction was given to the specimen using a refrigerant and a halogen lamp. The temperature gradient was set to 0.04 °C/mm based on the field temperature condition of steel bridge [3].

For thermal image measurement, the high performance infrared camera (FLIR systems, phoenix infrared camera) with an InSb array sensors (temperature resolution: 25 mK, spectral range: 3.0 - 5.0 μm, number of pixels: 320×256) was employed. Space resolution was set to 1 mm/Pixel. Flat black paint for emissivity improvement was applied on the temperature measurement surface of the specimen.

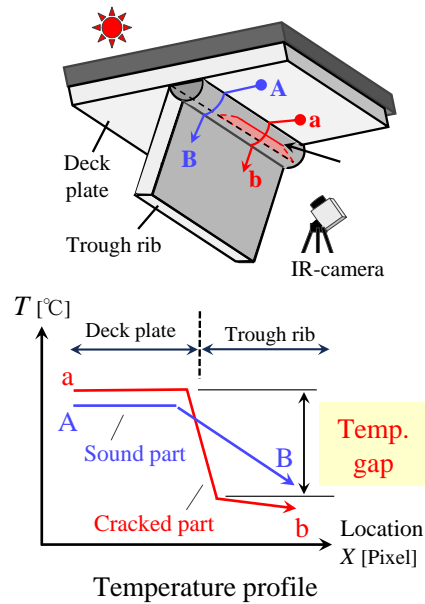


Fig. 1. Schematic illustration of principle of NDT technique based on temperature gap detection.

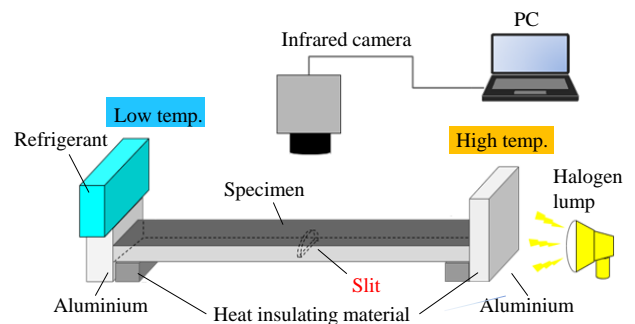


Fig. 2. Schematic illustration of the experimental setup.

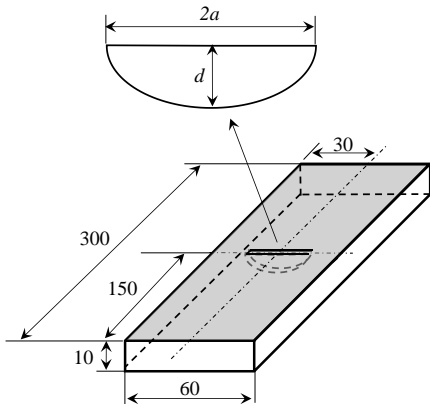


Fig. 3. Specimen shape (mm).

| Specimen | Slit length $2a$ [mm] | Slit depth d [mm] |
|----------|-----------------------|---------------------|
| No.1 | 30.1 | 9.0 |
| No.2 | 30.0 | 8.0 |
| No.3 | 30.1 | 7.0 |
| No.4 | 30.1 | 6.0 |
| No.5 | 15.2 | 9.0 |
| No.6 | 45.0 | 9.0 |

Table 1. Slit size of each specimen.

Experimental results

Fig. 4 shows the temperature evaluation area. Experimental results obtained for specimen No.1 is shown in Fig. 5. Fig. 5(a) and (b) is the temperature distribution and the distribution of the x -direction temperature differential, respectively. In the distribution of the temperature differential as shown in Fig. 5(b), temperature gap appears at the slit. However, it is difficult to clearly identify the temperature gap in the raw temperature differential.

Fig. 6 shows the results of noise reduction processing by spatial smoothing (3×3) to the raw temperature data of specimen No.1 as shown in Fig. 5. For the distribution of smoothed temperature differential as shown in Fig. 6(b), it can be seen that temperature gap clearly appears around the back-surface slit indicating thermal insulation effect by the slit.

Fig. 7 shows the x -direction temperature differential distributions of each specimen after

spatial smoothing (9×9). From these figures, it is found that temperature gap clearly appears at the slit in all specimens. Furthermore, the peak of the temperature gradient becomes larger with increasing the crack depth. When the crack length is large, the temperature gradient distribution has a spread in the crack length direction. It is considered that this technique may be applied for qualitative evaluation of the crack shape.

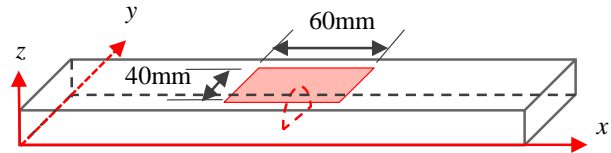
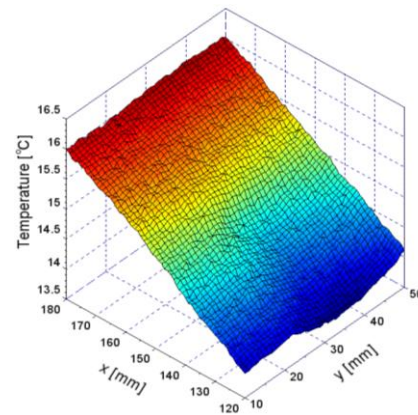
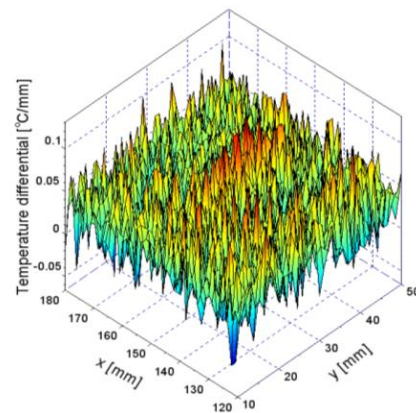


Fig. 4. Temperature evaluation area.

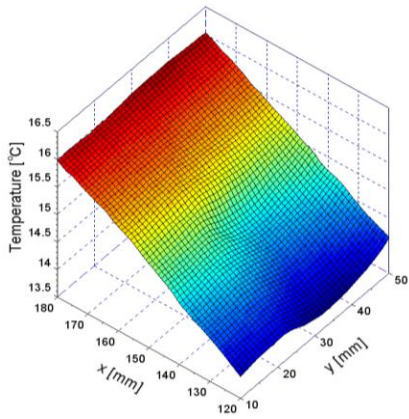


(a) Temperature distribution.

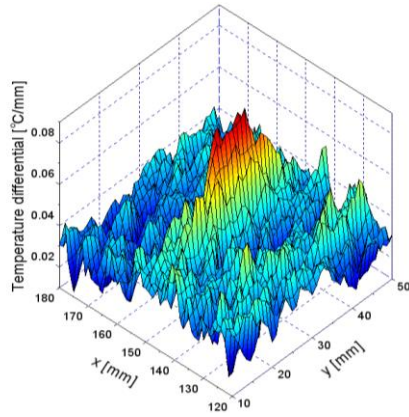


(b) Distribution of x -way temperature differential.

Fig. 5. Results of temperature gap measurement in specimen No.1 (raw temperature data).



(a) Temperature distribution.



(b) Distribution of x-way temperature differential.

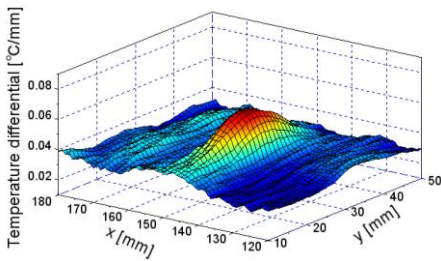
Fig. 6. Results of temperature gap measurement in specimen No.1 (smoothed temperature data (3×3)).

Conclusions

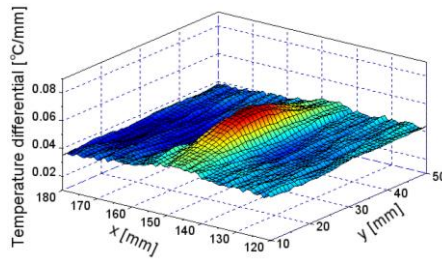
In this paper, the applicability of the developed technique to back-surface crack was investigated by the laboratory testing using slit specimen. In the results, it was found that back-surface crack can be detected by the proposed technique. Furthermore, it was considered that this technique may be applied for qualitative evaluation of the crack shape.

References

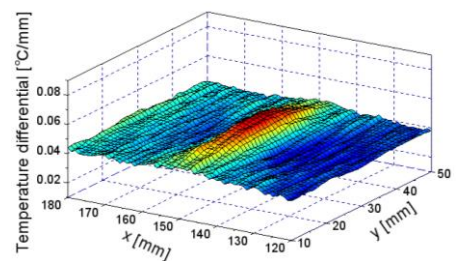
1. T. Sakagami, Y. Izumi, S. Kubo, Application of Infrared Thermography to Structural Integrity Evaluation of Steel Bridges, Journal of Modern Optics, Special Issue on Advanced Infrared Technology and Applications, Vol. 57, Issue 18, pp. 1738-1746, 2010.
2. T. Sakagami, Y. Izumi, T. Konishi, Y. Matsuoka, Detection of Through-Deck-Type Fatigue Cracks in Highway Steel bridges by Self-reference Lock-in Thermography, Proc. of ASCE 2013 International Orthotropic Bridge Conference, pp. 279-286, 2013.
3. Y. Mizokami, Y. Kobayashi, Y. Izumi, T. Sakagami, Remote NDT technique for through-weld crack in orthotropic steel deck by temperature gap measurement using infrared thermography, Steel Construction Engineering, Vol. 22, No. 87, pp. 47-56, 2015.



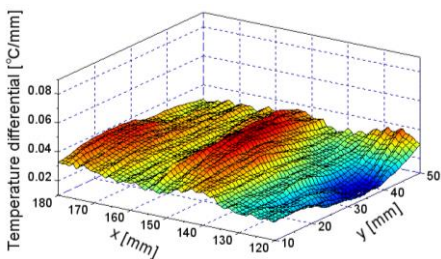
(a) Specimen No.1
($2a=30.1$ mm, $d=9.0$ mm)



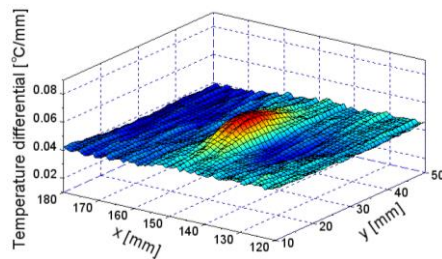
(b) Specimen No.2
($2a=30.0$ mm, $d=8.0$ mm)



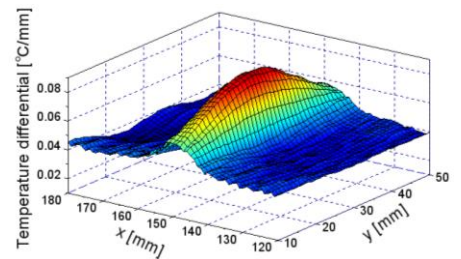
(c) Specimen No.3
($2a=30.1$ mm, $d=7.0$ mm)



(d) Specimen No.4
($2a=30.1$ mm, $d=6.0$ mm)



(e) Specimen No.5
($2a=15.2$ mm, $d=9.0$ mm)



(f) Specimen No.6
($2a=45.0$ mm, $d=9.0$ mm)

Fig. 7. Temperature differential distributions for each specimen (smoothed temperature data (9×9)).

Effect of mean stress on phase difference of dissipated energy

D. Shiozawa¹, T. Inagawa¹, T. Washio¹, T. Sakagami²

¹ Dept. of Mechanical Engineering, Kobe University, 657-8501,
shiozawa@mech.kobe-u.ac.jp

² Dept. of Mechanical Engineering, Kobe University,
sakagami@mech.kobe-u.ac.jp

The dissipated energy can be used to estimate the fatigue limit and to predict the fatigue life for steels. The temperature change due to the energy dissipation has a specific phase difference for the thermoelastic temperature change. The phase information of dissipated energy is useful for the accuracy improvement of dissipated energy measurement. In this paper, to discuss about the mechanism of the phase information of the dissipated energy, the effect of mean stress of a cyclic loading on the phase difference of the dissipated energy was investigated. It was found that the phase difference of dissipated energy decreases with increasing in tensile mean stress. The stress for the timing of heat generation due to the energy dissipation was evaluated based on the phase difference of dissipated energy. The stress for the timing of irreversible heat generation was nearly constant with increasing in tensile mean stress. It was considered that phase difference of dissipated energy indicated the beginning to plastic deformation during loading cycles.

1. Introduction

The dissipated energy, which was measured under cyclic loading, can be used to estimate the fatigue limit and to predict the fatigue life of steels ⁽¹⁾⁻⁽⁷⁾. The dissipated energy can be obtained as the component having a double frequency of the reference loading signal. This measurement method is called the $2f$ lock-in infrared method, which uses the reference signal of the double frequencies. From a phase analysis of the double frequency component, the phase difference between the thermoelastic temperature change and the double frequency component is a specific value ⁽⁸⁾. This specific phase of the dissipated energy can be utilized for removing the noise component such as the thermoelastic temperature change due to the harmonic vibration of fatigue testing machine. To study the mechanisms of the phase information of the dissipated energy, the effect of the mean stress of cyclic loading on the phase difference of the dissipated energy was investigated in this work.

2. Measurement of dissipated energy and phase analysis for dissipated energy

A reversible temperature change is observed for a specimen subjected to cyclic loading. This phenomenon is called the thermoelastic effect, and the thermoelastic temperature change ΔT_E can be expressed by the thermoelastic coefficient k , the absolute temperature T , and the sum of the principal stresses $\Delta\sigma$ as follows:

$$\Delta T_E = -kT\Delta\sigma \quad (1)$$

In reality, the increase in the temperature due to irreversible energy dissipation ΔT_D occurs at

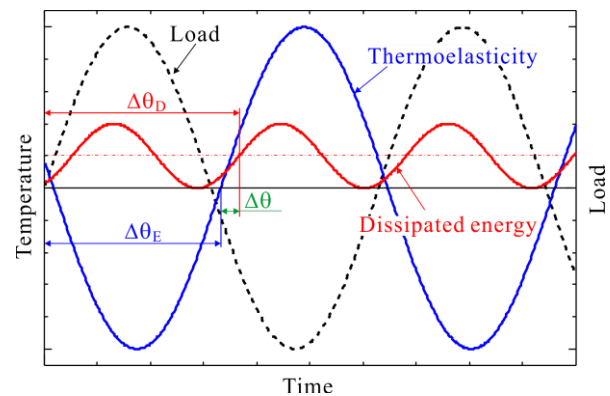


Fig. 1 Schematic of the temperature changes due to thermoelasticity and energy dissipation and the load signal.

the maximum tensile stress and maximum compressive stress. Thus, the measured temperature change $T(t)$ on the surface includes ΔT_E and ΔT_D , as shown in Fig. 1. The phase lag between the thermoelastic temperature change and the cyclic load θ_E is caused by thermal diffusion.

ΔT_D can be obtained as the component having a double frequency of the reference signal by a lock-in algorithm. ΔT_D is presented as a range of temperature changes. The dissipated energy q is calculated from ΔT_D , the density ρ , and the specific heat c of the material as follows:

$$q = \rho c \Delta T_D \quad (2)$$

The phase lag θ_D between the temperature change due to the energy dissipation and the double frequency reference signal. θ_D includes the influence of thermal diffusion. To remove this influence on the phase information of the energy dissipation, the phase difference $\Delta\theta$ is defined as follows:

$$\Delta\theta = \frac{1}{2}\theta_D - \theta_E \quad (3)$$

$\Delta\theta$ is based on the phase space of the reference signal frequency f ; thus, it has value from 0° to 180° . Further, $\Delta\theta$ also indicates the phase lag between the temperature change due to the energy dissipation and the double frequency reference signal based on the thermoelastic temperature change, as shown in Fig. 1.

3. Experimental setup

The material under test is JIS type 316L austenitic stainless steel. The cyclic axis loading with a frequency of 5 Hz was applied to the specimen by an electrohydraulic fatigue testing machine. In the staircase-like stress level test ⁽¹⁾, the applied stress amplitude was increased from 200MPa to 280MPa step by step. The temperature change on the specimen surface was measured by infrared

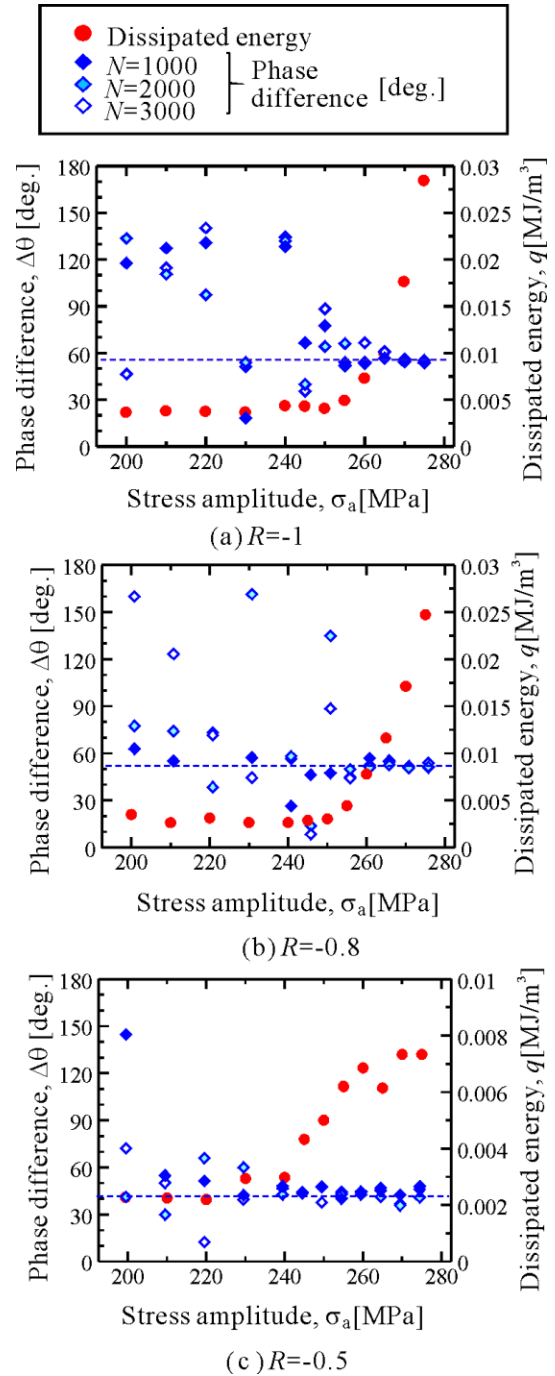


Fig. 2 Change in the dissipated energy and the phase difference of the dissipated energy for stress ratio $R = -1, -0.8, \text{ and } -0.5$

thermography with a MCT array detector. The number of cycles for each step is 3100cycles, and each temperature measurement is performed by 1000 cycle loadings.

To investigate the effect of mean stress on the phase difference of dissipated energy, the stress

ratio was changed, such as $R=-0.5$, -0.8 , and -1.0 .

4. Results and discussion

The changes in the dissipated energy and the phase difference in the staircase-like stress level test for $R=-1$, -0.8 and -0.5 are shown in Fig. 2.

From Fig. 2, it is found that q significantly increases for all stress ratio. In addition, the phase difference $\Delta\theta$ is unstable at low stress levels from 200 to 250 MPa. On the other hand, $\Delta\theta$ is constant at high stress levels, where the change in the dissipated energy is increasing. The phase difference change according to the stress ratio. The relationship between the phase difference and stress ratio is shown in Table 1. The phase difference for $R= -0.8$ and -0.5 where the mean stress is tensile, decrease with increasing in the mean stress. When the compressive mean stress is applied, the phase difference decreases, as is the case in tensile mean stress.

The phase difference of dissipated energy $\Delta\theta$ is assumed to be related to the timing of heat generation due to the energy dissipation. The stress for the timing of heat generation due to the energy dissipation σ_D is evaluated as shown in Fig. 3. The timing of heat generation due to the energy dissipation appears twice per a cycle. When the tensile mean stress is applied, the σ_D is obtained based on $\Delta\theta$, as follows;

$$\sigma_D = \sigma_a \sin\left(\Delta\theta - \frac{\pi}{4}\right) + \sigma_m \quad (4)$$

σ_D is plotted against the maximum stress, as shown in Fig. 4. σ_D shows approximately same value, and slightly increases.

The dissipated energy is related to the local plasticity in the material under the cyclic loadings. It is considered that the phase difference means the beginning of the local plastic deformation, such as slip movement. σ_D is thought to be a mechanical property in the

Table 1 Relationship between stress ratio and phase difference.

| Stress ratio, R | -1.0 | -0.8 | -0.5 |
|---|------|------|------|
| Phase difference, $\Delta\theta$ [deg.] | 57 | 51 | 43 |

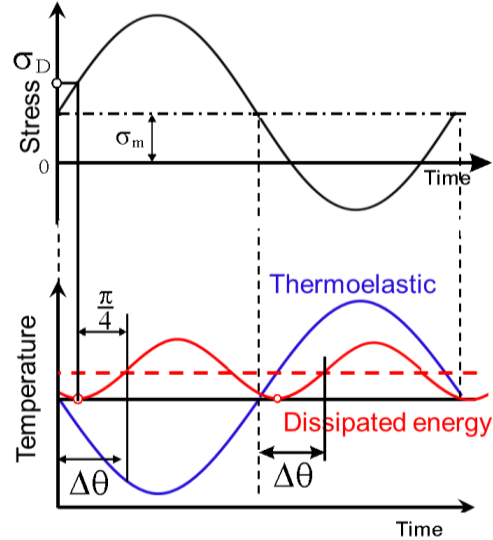


Fig. 3 Schematic illustration of the phase difference of dissipated energy and stress at the phase difference σ_D .

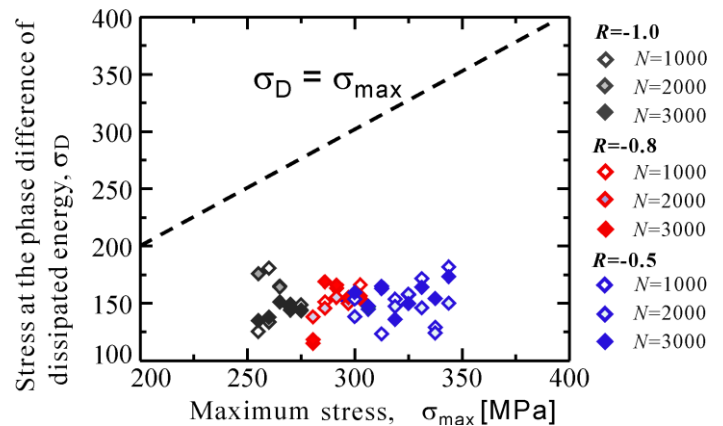


Fig. 4 Relationship between stress at initiation of energy dissipation of tensile side and maximum stress ($R=-1.0$, -0.8 and -0.5)

microscopic behavior under a cyclic loading, such as yield stress in macroscopic behavior under a monotonic loading. The cyclic work hardening may appear in change of σ_D . The time before the applied stress reaches σ_D

becomes shorter with increasing in the tensile mean stress.

The temperature change due to the energy dissipation would represent the timing and amount of dislocation movement.

5. Conclusion

To study the mechanism of phase information of dissipated energy, the effect of the mean stress in cyclic loading on the phase difference of dissipated energy was investigated. The phase difference of dissipated energy decreases with increasing in the tensile mean stress. The stress for the timing of heat generation due to the energy dissipation shows the nearly constant with increasing in the tensile mean stress. It is considered that the phase difference means the beginning of the local plastic deformation, such as slip movement.

References

1. G. La Rosa and A. Risitano, Thermographic methodology for rapid determination of the fatigue limit of materials and mechanical components, *International Journal of Fatigue*, Vol.22, 65-73, 2000.
2. J. -C. Krapez and D. Pacou, Thermography Detection of Damage Initiation during Fatigue Tests, *Proceedings of SPIE*, Vol.4710, 435-449. 2002.
3. Y. Irie, H. Inoue, T. Mori and M. Takao, Evaluation of Fatigue Limit of Notched Specimen by Measurement of Dissipated Energy, *Transactions of the Japanese Society of Mechanical Engineers, Series A*, Vol.76, No. 764, 410-412 2010.
4. M. P. Luong, Infrared thermography of fatigue in metals, *Proceedings of SPIE*, Vol.1682, 222-233, 1992.
5. D. Shiozawa, K. Inaba, A. Akai and T. Sakagami, Experimental Study of Relationship Between Energy Dissipation and Fatigue Damage From Observation of Slip Band by Atomic Force Microscope, *Advance Materials research*, Vol. 891-892, pp.606-611, 2014.
6. A. Akai, D. Shiozawa. and T. Sakagami, Fatigue Limit Evaluation for Austenitic Stainless Steel, *Journal of the Society of Materials Science Japan*, Vol. 61, No. 12, pp. 953-959, 2012.
7. D. Palumbo. and U. Galietti, Characterisation of Steel Welded Joints by Infrared Thermographic Methods,

Quantitative InfraRed Thermography Journal, Vol. 11, No. 1, pp. 29-42, 2012.

8. D. Shiozawa, T. Inagawa, T. Washio, T. Sakagami, Accuracy improvement in dissipated energy measurement by using phase information, *Measurement Science and Technology*, Vol. 28, 2017

FIBER ORIENTATION DETECTION ON FIBER REINFORCED POLYMERS MOULDED WITH RANDOMLY-ORIENTED STRANDS

H. Fernandes¹, S. Sfarra², H. Zhang³, C. Ibarra-Castanedo³, X. Maldague³

¹ School of Computer Science, Federal University of Uberlandia, Uberlandia, Brazil

² Department of Industrial and Information Engineering and Economics, Las.E.R. Laboratory,
 University of L'Aquila, Roio Poggio, Italy

³ Department of Electrical and Computer Engineering, Computer Vision and Systems
 Laboratory (CVSL), Laval University, Quebec City, Canada

Composite materials (CM) are been used more and more every day in several applications, especially in aeronautic structures where complex shaped parts are highly demanded. The arrangement or orientation of the fibers relative to one another, the fiber concentration, and the distribution all have a significant influence on the strength and other properties of fiber reinforced composites. Thus, one needs to develop testing methods to assess the material's fiber content. Non-Destructive Evaluation (NDE) methods must be employed in some cases to assess the material's fiber content in order to presser the samples integrity. In this paper, InfraRed Thermography (IRT), is used in order to assess fiber orientation on Randomly-Oriented Unidirectional Strand (ROS) samples. More specifically, Pulsed Thermal Ellipsometry (PTE) using a static laser spot heating source is employed in order to create a fiber orientation map of the fiber distribution on the surface of ROS panels.

Introduction

Infrared Thermography (IRT) popularity has grown in the recent years due to spatial resolution and acquisition rate improvements of infrared (IR) cameras while they became more affordable. Other facts include: it is a fast inspection method, which provides noncontact, noninteraction, real-time measurements over a large detection area with a long range; it does not offer any danger to the personnel; and the results are relatively easy to interpret. Additionally, the development of advanced image processing techniques focused on this kind of image have enabled the assessment of more and more detailed information of these material's structures. In active IRT, an external heat source is used to stimulate the material being inspected in order to generate a thermal contrast between the feature of interest and the background. The active approach is adopted in

many cases given that the inspected parts are usually in equilibrium with the surroundings [1].

IRT has been used for several applications involving composite materials. In the case of fiber reinforced composites, the arrangement or orientation of the fibers relative to one another, the fiber concentration, and the distribution all have a significant influence on the strength and other properties of fiber reinforced composites. In fact, several studies have been done in the recent years involving this subject [2,3,4]. Thus, effective testing techniques are needed to assess fiber content. Destructive methods can be employed to evaluate a composite fiber content, e.g. cutting a section of the material, polishing the area and evaluating it by microscopy. However, the destructive approach is not always an option since the sample will be "damaged" after the inspection and probably unfit for use. Thus, Non-Destructive (NDE)

techniques must be employed in some cases to assess the material's fiber content.

In this paper we present an active IRT approach to quantitatively assess the fiber orientation on carbon fiber reinforced polymers (CRP) moulded with randomly-oriented strands (ROS). The samples inspected in this project were manufactured via compression moulding of Carbon/PEEK material. Fiber orientation measurement using IRT on flat laminates with continuous fibers is a well-studied topic. However, to the best knowledge of the authors our work is the first in the literature addressing this problem for ROS samples. Therefore, the goal of this paper is to validate and developed those known techniques to the ROS case so that they can be applied on in-line quality assurance within the industry. In the end, we compare our results with some 3D micro-CT scanning performed with the ROS samples

Pulsed Thermal Ellipsometry - PTE

PTE is an inspection technique that enables the assessment of fiber orientation on CM. It is already been used in the literature for years [5]. It involves the spot heating of the sample's surface and following the observation of the heated pattern in the IR spectrum. A short pulse is used to spot heat the sample. If the material has an oriented structure, such as CFRP, an elliptical thermal pattern is observed, with the ratio between the two principal axes (b/a) being related to the square root of the thermal diffusivities in the longitudinal and transverse directions. A test on an isotropic material would give a circle instead of an ellipse. Fig. 1 shows a typical PTE experimental set-up.

The ellipse's major axis, b , has the same orientation than the fibers on that region. This "elliptical" behavior occurs due to the difference in the thermal conductivities values on the surface of the sample. The thermal conductivity value parallel to the fibers is greater than the value perpendicular to them, i.e. material is thermally anisotropic. Thus, heat

will travel faster on the direction parallel to the fibers and consequently the thermal pattern observed on the surface will be larger on the direction parallel to the fibers, which results in an elliptical pattern. The heat diffusion process is recorded with an IR camera and stored in a 3D matrix (or an array of images). In order to extract the elliptical pattern from the IR images, i.e. thermograms, some image processing techniques must be applied.

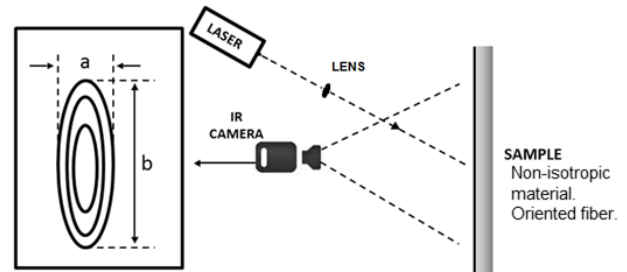


Fig. 1. Pulsed Thermal Ellipsometry (PTE) set-up.

Infrared Image Processing

Fig. 2 summarizes the processing steps involved on the extraction of the fiber orientation based on the data provided by a PTE experiment. The process is fully detailed and discussed in our previous work [6]. Nonetheless, their major points are going to be outlined here.

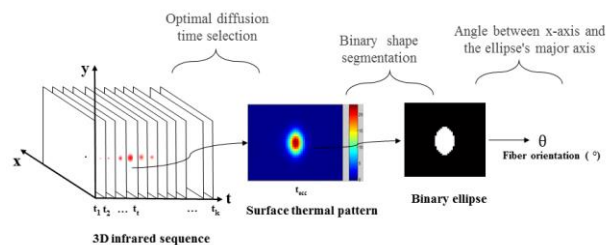


Fig. 2. Infrared image processing steps for PTE. Adapted from [6].

Optimal diffusion time selection

As stated before, a heating-spot, produced by a laser beam, is used to stimulate the surface of the sample producing the thermal behavior that will lead to the fiber orientation assessment. After the spot is heated, the heat diffusion

process is recorded with an IR camera and stored in a 3D matrix M , i.e., an array of images, for post-processing. The size of M is $m \times n \times k$ which means that it is composed of k images of size $m \times n$. The number of images, or thermograms, depends on the duration of the acquisition as well as the camera's acquisition frame rate.

This sequence of images contains: the plate before heating, the moment when the beam heated the plate, the rise of the temperature profile and finally the temperature profile decrease. In the case of our ROS samples, which are thermally anisotropic, the heat pulse will produce an elliptical pattern on the surface of the sample. However, this pattern would be closer to a circle on the very beginning of the experiment and in later times where the thermal behavior of deeper layers would be much more present. Thus, our assumption is that, sometime between this two moments an image would contain the best pattern that reflects the fiber orientation on the surface, i.e., the direction which the thermal conductivity is higher. This optimal moment is selected by calculating the eccentricity (ϵ) of each elliptical thermal pattern on the thermograms on M and choosing the image which contains the ellipse with the largest ϵ . Eccentricity (ϵ) is a quantity defined for a conic section which can be given in terms of major and minor axes. In the case of a circle $\epsilon = 0$ while in the case of an ellipse $0 < \epsilon < 1$. Based on this idea the thermal pattern that would better express the fiber orientation is the one with the largest ϵ . During our experiments, it always occurred before 0.5s after the beam has been stopped.

Binary shape segmentation

After the image with the optimal diffusion time was selected, the next step is to segment, or binarize, the ellipse on the image. This is a simple task that can be accomplished by using automatic clustering based image thresholding method. There is a wide range of classical histogram based algorithms for automatic threshold selection for bimodal and multimodal

images available in the literature. In this work, Otsu's method [7], a well-established method, is used.

After the selection of the threshold level the binary image is created by applying the following characteristic function in the infrared image selected based on the optimal diffusion time calculated in the previous step:

$$f_{be}(P_{Ti}) = \begin{cases} 1, & \text{if } T_i \geq Th \\ 0, & \text{otherwise} \end{cases} \quad (1)$$

Calculation of angle between x-axis and binary ellipse's major axis

With the resulting binary image obtained via Equation 1, which is represented by a binary matrix, a simple MATLAB native function was used to calculate the ellipse orientation. The orientation of the image, here the binary ellipse, is the angle (in degrees ranging from -90° to 90°) between the x-axis and the major axis of the ellipse that has the same second-moments as the region.

Results and Discussion

In order to evaluate the effectiveness of the PTE approach for ROS samples, individual strands were first inspected separately. The results obtained for two different strands chosen on the surface of a ROS sample will be presented in the final version of the paper. A first PTE inspection was performed. Next, the plate was rotated 90° clockwise and a second PTE inspection was then performed. Inspections were expected to be also rotated 90° from each other. Results obtained presented an estimation error as low as 1.5° . Details are going to be presented in the paper's final version.

Therefore, one can conclude from these first experimental results presented that, similarly to the laminate case, where the fiber orientation on each layer of the laminate is uniform, fiber

orientation can also be assessed for ROS material using PTE.

For the ROS case, only the local inspection of a single strand is not enough to meaningfully assess the fiber orientation on the surface of this kind of sample. In order to have an assessment about how random and how strands (fiber orientation) are distributed, several points, systematically distributed on the surface of the ROS sample, should be inspected. The outcome of such inspection is going to be called "Orientation Map".

A section of each surface of a ROS sample was inspected with a point-by-point approach in order to create the so called "Orientation Map". The dimension of each section was 50 x 50 mm². A total of 121 points was inspected for each section. Details of the experimental set-up images with results are going to be provided in the final version of the manuscript.

The results were also statistically analyzed. First, the mean orientation angle was calculated for each section as well as the correspondent standard deviation (STD) value. Table 1 shows these values. Second, orientation values for each section were sorted then the values were plotted and analyzed. These images are going to be presented in the final version of the manuscript.

| | Front section | Back section |
|------|---------------|--------------|
| Mean | 93° | 82° |
| STD | 58.1° | 59.3° |

Table 1. Statistical results from ROS point-by-point inspection.

Conclusion

Primarily, inspections were performed on single strands since each strand has its own fiber orientation. Ultimately, a matrix of several points on the surface of a flat ROS sample was inspected in order to estimate "how random" fiber orientation is on the sample's surface. An "Orientation Map" was created and statistical analysis of the results showed that the fiber orientation on a ROS sample is well distributed,

which confirms the quasi-isotropic behavior of ROS samples. Additionally, results will be compared in the final version of the paper with 3D micro-CT scans.

However, an inspection approach based on a matrix of several points obtained with PTE of a ROS sample is very time consuming. The inspection of 121 points in this paper took about 2 hours. Thus, we proposed in one of our works [8] to use a line-heating source combined with an Artificial Neural Network (ANN) to inspect a broader region at once. In the experiments reported in [8] a region that would take 25 minutes to be inspected with the point-by-point approach would take about 30 seconds to be inspected with the line-heating approach.

References

1. X. Maldague, Theory and practice of infrared technology for nondestructive testing, 1st Edition, Wiley-Interscience, New York, 2001.
2. Y. Zhu, J. Liu, D. Liu, H. Xu, C. Yan, B. Huang, D. Hui, Fiber path optimization based on a family of curves in composite laminate with a center hole, *Composites Part B: Engineering* 111, 91–102, 2017.
3. C. Barile, C. Casavola, C. Pappalettere, The influence of stitching and unconventional fibres orientation on the tensile properties of CFRP laminates, *Composites Part B: Engineering* 110, 248-254 2017.
4. H. Rolland, N. Saintier, P. Wilson, J. Merzeau, G. Robert, In situ x-ray tomography investigation on damage mechanisms in short glass-fibre reinforced thermoplastics: Effects of fibre orientation and relative humidity, *Composites Part B: Engineering* 109, 170-186, 2017.
5. J.-C. Krapez, Thermal ellipsometry applied to the evaluation of fibre orientation in composite, *Tiré à part-Office national d'études et de recherches aérospatiales* 171, 26, 1994.
6. H. Fernandes, H. Zhang, X. Maldague, An active infrared thermography method for fiber orientation assessment of fiber-reinforced composite materials, *Infrared Physics & Technology* 72, 286-292, 2015.
7. N. Otsu, A threshold selection method from gray-level histograms, in: *International Conference on Systems, Man, and Cybernetics (SMC)*, 9, 62-66, 1979.
8. H. Fernandes, H. Zhang, C. Ibarra-Castanedo, X. Maldague, Fiber orientation assessment on randomly-oriented strand composites by means of infrared thermography, *Composites Science and Technology* 121, 25-33, 2015.

Optimal Design of Chirp Excitations for Pulse Compression Thermography

G.Silipigni¹, S.Laureti¹, L.Senni¹, R.Tomasello¹, P.Burrascano¹ and M.Ricci²

¹Department of Engineering, University of Perugia, Strada di Pentima 4, Terni, Italy

²Department of Computer Science, Modelling, Electronics and System Science, University of Calabria, Via P. Bucci I-87036, Rende (CS), Italy

Pulse Compression Thermography is an emerging Non-Destructive technique, whose effectiveness strictly depends on the choice of the coded excitations used to modulate the heating stimulus. In this paper, the features of frequency-modulated coded signals, *i.e.* chirps, have been tested for imaging thin Teflon defects embedded within a carbon fiber composite specimen. With the aim to maximize the heat transferred within the sample, the use of several optimized non-linear chirp signals has been also investigated and their features compared in terms of maximum achievable Signal-to-Noise ratio.

Introduction

Active Thermography (AT) is a Non-Destructive Testing (NDT) technique widely used for research activities and quality control in several industrial environments [1]. Commonly, two main approaches have been followed in performing AT: Pulsed Thermography (PT) and Lock-In Thermography (LIT). A precise time-domain analysis can be performed by exploiting PT scheme. This is because a short time duration heating stimulus excites the sample under test within a continuous bandwidth. On the other hand, LIT provides a higher Signal-to-Noise Ratio (SNR) by concentrating the signal energy within a narrow frequency range, at the cost of a less amount of information with respect to PT [2-3]. In recent years, efforts have been made to combine the advantages of both the above-mentioned techniques, leading to Pulsed-Phase Thermography, Multi-Frequency Lock-In Thermography and Pulse-Compression Thermography (PuCT). In PuCT, the heating stimulus is in the form of a coded excitation, which has a unique characteristic: the bandwidth B and the time duration T are uncorrelated. Both the time and frequency domain analysis can be performed by exploiting PuCT. The time domain analysis can be performed on the

impulse response estimate, which is obtained by implementing the Pulse Compression (PuC) algorithm. The frequency domain analysis is achieved by analyzing directly the acquired data. It is worth to note that the quality of the time domain analysis achievable by using PuCT with respect to PT is strictly related to (i) the optimal choice of the coded excitation, *i.e.* time-frequency signal characteristics, and (ii) the effectiveness of the employed PuC algorithm. For this reason, several efforts have been made to optimize the quality of the retrieved impulse response estimate, both in terms of PuC algorithm and in the choice of the coded heating stimulus [4-5]. In this work is proposed the combined use of a specific class of coded excitation, *i.e.* chirps, to both optimize the quality of the impulse response estimate and to enhance the detection capability of flaws embedded within a composite specimen, here in the form of artificial thin inclusion of Teflon tapes in a Carbon Fiber Reinforced Plastic (CFRP) sample. Chirps signals have been here exploited in their Linear (LChirp) and Non-Linear versions (NLChirp) and their features compared. Finally, an ad-hoc designed non-linear chirp has been here proposed and its advantages studied. It is shown that the use of Non-linear chirps helps in maximizing the heat energy transferred to the sample, thus the

detection capability of defects at deeper depth. This is demonstrated by showing the SNR values obtained with the various coded excitations used.

Background

A brief introduction about the PuC technique and chirp signals is here reported. The reader is suggested to refer for example to *Hutchins et al.* [6] for further details.

- Pulse compression

PuC is a powerful measurement technique widely used to estimate the impulse response of a Linear-Time Invariant (LTI) system in noisy environment. Given a coded excitation $s(t)$ and another signal $\Psi(t)$, the so-called matched-filter, such that their convolution (denoted by $*$) approximates the Dirac's Delta function $\delta(t)$, $s(t) * \Psi(t) = \tilde{\delta}(t) \sim \delta(t)$, the impulse response $h(t)$ can be estimated by exciting the LTI system with the signal $s(t)$ and then by convolving the system output $y(t)$ with $\Psi(t)$. The main pros of the combined use of PuC and coded signals is that an SNR enhancement is achieved by simply increasing the time duration of the excitation. If T and B are respectively the time duration and the bandwidth of the coded signal, it can be demonstrated that the SNR gain achieved by using PuC with respect to a pulse excitation is $\sim T \cdot B$. However, the limited B into which a chirp signal spectrum can be considered flat and the short T employed in PuCT result in the onset of the so-called impulse response sidelobes. Hence, only an estimate $h_{es}(t)$ of the real impulse response $h(t)$ is always obtained, whose quality depends strictly on the coded signal time/frequency characteristics. It is known that for a fixed B and T , a LChirp signal gives the best $h_{es}(t)$ with respect to a NLchirp one. On the other hand, NLChirp can be designed for concentrating the sent energy at the frequencies of interest at the cost of a broader time duration of $h_{es}(t)$ with respect to LChirp. A tradeoff between these two aspects is here proposed. This is in the form of a Weighted Non-Linear Chirp (WNLChirp), which can help in achieving a PuC output like LChirp one, with the advantage of concentrating the sent energy at lower

frequencies normally provided by using NLChirps.

- Linear Chirp

A LChirp signal is a frequency modulated coded signal whose frequency increases linearly within a chosen range. A general mathematical definition of a chirp is here given:

$$s(t) = \cos(\Phi(t)) \quad (1)$$

The design of a chirp strictly depends from the definition of the instantaneous frequency $f_{ist}(t)$:

$$f_{ist}(t) = \frac{1}{2\pi} \frac{d\Phi(t)}{dt} \quad (2)$$

with $\Phi(t)$ the accumulated signal phase, i.e. the difference between the higher chirp frequency and lower one. For a LChirp signal, the phase is quadratic $\Phi(t) = f_0 t + \frac{B}{2T} t^2 - \frac{B}{2} t$ and the respective instantaneous frequency is linear:

$$f_{ist}(t) = f_0 + \frac{B}{T} t \quad (3)$$

with the bandwidth $B = f_1 - f_0$.

- Non-Linear Chirp

When $f_{ist}(t)$ varies non-linearly with time the signal is a non-linear chirp (NLChirp). NLChirps can be defined so that its $f_{ist}(t)$ follows a specific trajectory in the time-frequency plane. This can be done to cope with a prescribed smooth shape of the power spectrum or for other aims. For instance, a NLChirp can be defined so that its instantaneous thermal diffusion length $\mu_{ist}(t) = \sqrt{\frac{\alpha}{\pi f_{ist}(t)}}$ varies linearly with time to span all the sample depth at different time intervals, where α is the thermal diffusivity.

If Z is the thickness of the sample and Z_{min} the minimum depth to inspect, we can define $\mu_{ist}(t) = Z - \frac{\Delta z}{T} t$, with $\Delta z = Z - Z_{min}$. From these quantities, the instantaneous frequency has been derived by using the following expression:

$$f_{ist}(t) = \frac{1}{\mu_{ist}(t)^2} \frac{\alpha}{\pi} = \frac{1}{(Z - \frac{\Delta z}{T} t)^2} \frac{\alpha}{\pi} \quad (4)$$

Note that for the CFRP sample, the thermal diffusivity α has been estimated to be $\alpha = 0.125 \left[\frac{mm^2}{s} \right]$, as described in [4].

- *Weighted non-linear chirp*

Starting from the definition of $f_{ist}(t)$ for both the LChirp and NLChirp signals, three Weighted Non-linear chirps (WNLChirp) excitations have been proposed. Values of the weight parameter close to a hundred percent refers to an instantaneous frequency handling of the WNLChirp close to its LChirp counterpart, see Fig. 1:

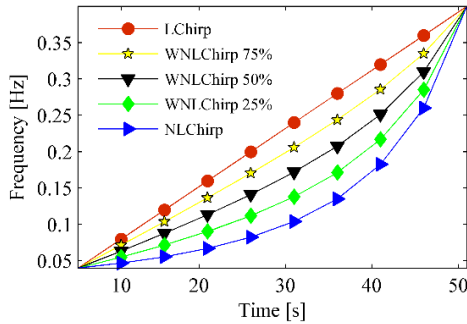


Fig. 1. Instantaneous frequency trend for the proposed coded excitations.

- *Optimal coded excitation design*

For the LChirp and NLChirp cases, the starting excitation frequency f_0 has been retrieved exploiting Eq.(4) for $d_{ist}(t)|_{t=0} = Z_{min}$, whilst f_1 considering $d_{ist}(t)|_{t=T} = Z$, leading to $f_0 = 0.04$ Hz and $f_1 = 0.4$ Hz. These boundary frequency values have been exploited to obtain both the desired linear LChirp $f_{ist}(t)$, as for Eq.(3), and the NLchirp $f_{ist}(t)$ by exploiting both Eq.(4) and the constrains imposed by the linearized frequency-depth swept. Finally, WNLChirp excitations have been designed to stay at longer time at the frequencies of interest (see Fig. 1 for more details).

Experimental Setup

A detailed sketch of the experimental setup is depicted in Fig. 2.:

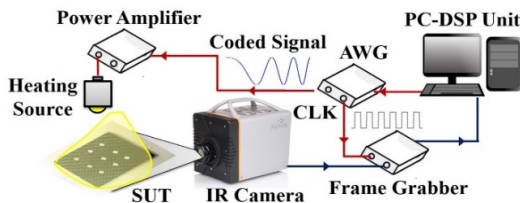


Fig. 2. Sketch of the experimental setup. The heating source consisting of eight 50 W LED chips placed at ~30 cm from the SUT and the Xenics Onca-MWIR-InSb IR

camera are synchronously driven by the signals provided by an AWG board. The data generation and acquisition was controlled using Labview™ Software.

A quoted sketch of the twelve plies CFRP sample containing 75 μm thick Teflon tape defects is depicted in Fig. 3:

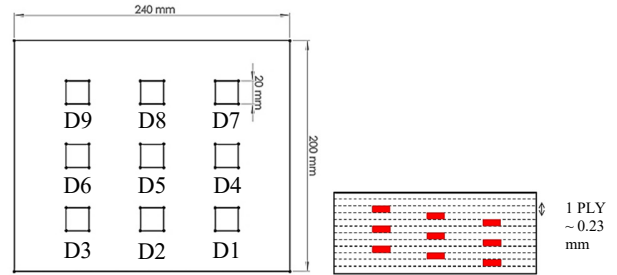


Fig. 3. Quoted sketch of the sample.

Results

Figure 4 depicts a series of thermograms obtained by using PuCT corresponding to the time instant at which the maximum SNR value for D6 is achieved. Those are shown for each coded excitation used, *i.e.* LChirp, NLChirp, WNLChirp 25%, WNLChirp 50%, WNLChirp 75%. Fig. 5 shows the impulse responses $h(t)$ retrieved for the considered defect location (D1-D8)) for the said signals – D9 was far below the noise level for the current setup. All the exploited coded excitations provided a good reconstruction of the defect impulse responses (see Silipigni et al. for further details). By introducing the definition of SNR, a qualitative analysis of the features provided using NLChirp and WNLChirp with respect to their LChirp counterpart is given. The SNR for the k^{th} -Defect SNR_{D_k} is defined as follows:

$$SNR_{D_k} = \frac{h_{D_k}(t) - \bar{h}(t)}{\sigma_h(t)} \quad (6)$$

where $h_{D_k}(t)$ is the impulse response of the k -th defect averaged over the 3x3 pixel region, $\bar{h}(t)$ is the impulse response averaged over all the UT area and $\sigma_h(t)$ is its standard deviation. The maximum SNR values achieved at the investigated locations are showed in Fig.6.

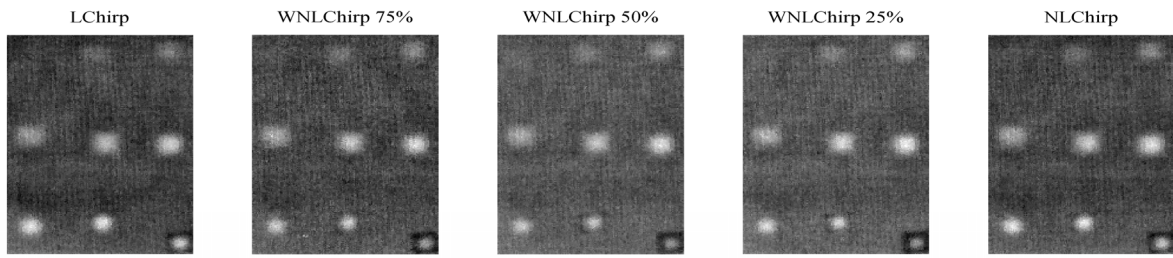


Fig. 4. Obtained thermograms for the exploited signals (labelled), for the time instant at which the maximum SNR value for D6 is achieved.

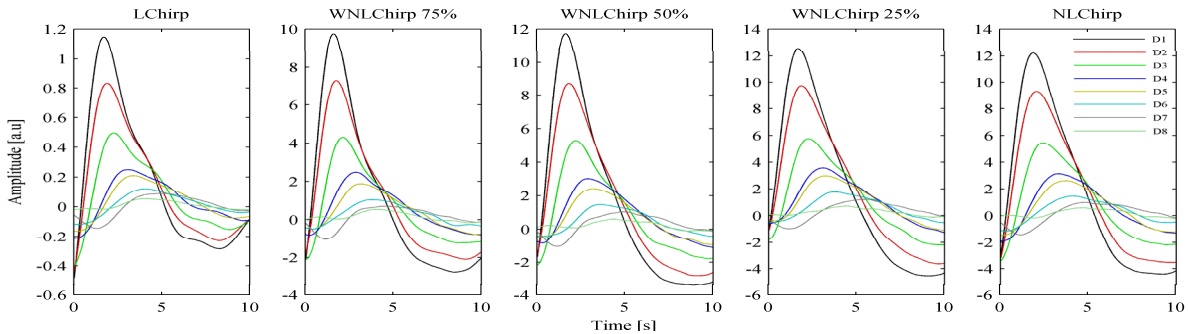


Fig. 5. Defects impulse responses obtained for the signals used (labelled), for defects at increasing depth (D1 to D8).

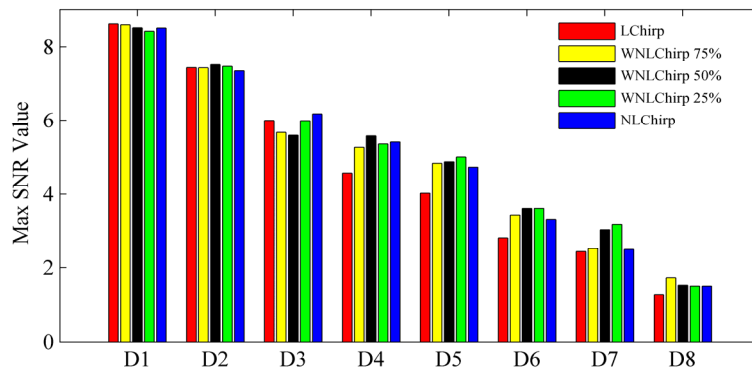


Fig. 6. Maximum SNR value achieved at the defects locations.

Conclusions

Different chirp signals have been used to modulate the heating stimulus in PuCT. Their peculiarities have been tested for detecting thin Teflon defects embedded in a CFRP benchmark sample. For the investigated B and T , it has been found that the use of NLChirps excitation provided higher values of the SNR with respect to LChirp counterpart for deeper defects. In addition, a linearized version of NLChirp, *i.e.* WNLChirp, further improved the achieved SNR values for above-said defects.

References

1. C. Meola, G.M. Carlomagno. Recent advances in the use of infrared thermography, *Meas. Sci. Technol.* 15 R27–R58, 2004.
2. X.P. V Maldague. Introduction to NDT by active infrared thermography, *Mater. Eval.* 60, 1060–1073, 2002.
3. N.P. Avdelidis, B.C. Hawtin, D.P. Almond, Transient thermography in the assessment of defects of aircraft composites, *NDT E Int.* 36 (2003) 433–439.
4. G. Silipigni, P. Burrascano, D. A. Hutchins, S. Laureti, R. Petrucci, L. Senni, L. Torre, M. Ricci. Optimization of the pulse-compression technique applied to the infrared thermography nondestructive evaluation, *NDT & E International*, 87, 100-110, 2017.
5. R. Mulaveesala, S. Venkata Ghali. Coded excitation for infrared non-destructive testing of carbon fiber reinforced plastics, *Review of Scientific Instruments* 82.5: 054902, 2011.
6. D.A. Hutchins, P. Burrascano, L. Davis, S. Laureti, M. Ricci. Coded waveforms for optimised air-coupled ultrasonic nondestructive evaluation. *Ultrasonics*, 54(7), 1745-1759, 2014.

AN EMPIRICAL MATHEMATICAL MODEL DEVELOPED FOR PULSED THERMOGRAPHY ANALYSIS ON MARBLE SURFACES

E.T. Delegou¹, M. Krokida², N.P. Avdelidis³, A. Moropoulou⁴

¹National Technical University of Athens, School of Chemical Engineering, Iroon Polytechniou 9, 15780 Athens, Greece, edelegou@central.ntua.gr

²National Technical University of Athens, School of Chemical Engineering, Iroon Polytechniou 9, 15780 Athens, Greece, mkrok@chemeng.ntua.gr

³National Technical University of Athens, School of Chemical Engineering, Iroon Polytechniou 9, 15780 Athens, Greece, nico.avdel@gmail.com

⁴National Technical University of Athens, School of Chemical Engineering, Iroon Polytechniou 9, 15780 Athens, Greece, amoropul@central.ntua.gr

Pulsed thermography was applied on marble specimens differently treated in lab and on marble samples collected in situ before and after pilot cleaning interventions as an evaluation tool. Quantitative analysis using temperature-time plots from the acquired images was completed and the temperature falling rate for the investigated samples was studied. Consequently the cooling rate of the samples can be described by a first order kinetic model, whereas the time constant of the cooling rate is an exponential function of marble surface fracturing and luminosity (luminosity recorded using colorimetry, whilst fracturing values attained by digital image processing of microscopy images).

Introduction

Pulsed thermography (PT) is the thermographic technique where the sample surface is pulse heated by a flash lamp and the thermal transient at the surface is monitored by an infrared camera [1]. Up to now many experimental approaches using PT can be found in bibliography for the non destructive evaluation of near surface structures concerning the investigation of the depth or the diameter of different type of defaults [2, 3].

Marble surfaces are of high priority regarding strategic planning of periodical conservation interventions, since even partially reconstruction is out of question and sampling is rather limited not to say restricted. Cleaning is one of the first conservation interventions that take place for the protection of marble architectural surfaces. It is defined as: “The removal of every substance which is hurtful for the stone: soluble salts, crusts insoluble or not very soluble, stratification of different materials intentionally applied and not stable, animals secretions, developed flora, etc”

[4]. Cleaning is an irreversible but necessary step of conservation interventions, due to (a) physical and physicochemical reasons; (b) aesthetical reasons; and (c) promotion of monument artistic value. Moreover, compatibility assessment of cleaning interventions incorporates the study of physical-chemical properties modification, as well as aesthetics alterations that took place on the surface because of the applied treatment [5, 6]. Therefore, the investigation of the modifications of marble properties employing PT is very important for the strategic approach of marble surfaces protection and their durability assessment. In this work, PT was applied on quarry marble specimens and marble samples collected on site before and after pilot cleaning interventions, in order to record temperature variations in the transient phase. It is demonstrated that temperature falling rate follows a first order kinetic model. Moreover, several surface morphology parameters were investigated in order to result in a power model that describes the effect of luminosity and fracturing on the

cooling rate for marble samples treated by different methods.

Experimental

12 quarry specimens of Pentelic marble were cut into the following size (cm): 6x6x1 (LxWxH). Sandpapers of different grit sizes (grit designation according to European FEPA – “P” grade), using SiC as abrading particle, were applied on the marble quarry specimens, to accomplish different finishes of surface texture. For further differentiation of the surface texture of the quarry specimens chemical treatment using poultice AB57 for 20 minutes was applied on six of them after the sandpapers processing. Poultice AB57 is one of the most commonly used poultices for marble cleaning, mainly due to the chelate action of bisodium EDTA which sequesters metal ions like Ca^{2+} and Fe^{3+} .

Furthermore, marble samples were collected by the architectural surfaces of the historic buildings of the National Library of Greece (NLG) and the National Archaeological Museum (NAM); both consisted of Pentelic marble, both located in the Athens centre, Greece, and constructed at the beginning of 20th century.

Samples were collected from four investigated architectural marble surfaces during the study of decay diagnosis and after the pilot cleaning interventions, during the study of cleaning assessment.

Decay diagnosis results indicated the presence of three characteristic decay patterns on the four investigated architectural marble surfaces: black-grey crusts, washed out surfaces and inter-granular fissuring (Figures 1, 2 and 3). The pilot conservation interventions that were applied consisted of different cleaning methods. Pulsed thermography, digital image processing of Scanning Electron Microscopy (SEM) images, and colorimetry were among the techniques used for decay diagnosis and cleaning interventions assessment.



Fig. 1. The investigated marble surface of NLG, that presented black-grey crust (upper part) and inter-granular fissuring (lower part).

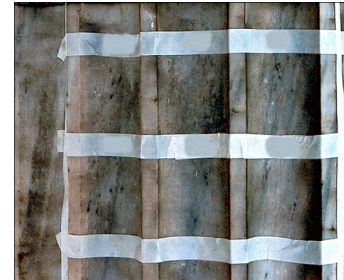


Fig. 2. The investigated marble surface of NAM, that presented black-grey crust.



Fig. 3. The investigated marble surface of NAM that presented washing out.

An integrated pulsed thermographic system employing a medium wave infrared camera (3-5 μm) that uses a cooled indium antimonide detector with a frame rate of 60 Hz, a focal plane array pixel format of 320 (H) x 256 (V) and an optical lens of 13 mm focal length was utilised for the pulsed thermographic analysis. The system has an integrated power flash heating system with a power output of 2KJ in 2-5 ms.

All investigated quarry specimens and onsite collected samples were measured in lab by this pulsed thermographic system under identical conditions. Thermal contrast plots, displaying the intensity of pixels against time were plotted from the acquired 16-bit thermal images.

As for the fracturing estimation, Scanning Electron Microscopy (SEM) was applied on the quarry specimens, as well as on the collected monument samples, in order to evaluate morphology and surface microstructure of the differently treated, decayed and cleaned marble surfaces.

The core samples analyses in the presented work, that is stone specimens cut in cross-section, were carried out using JEOL JSM-5600, OXFORD LINK™ ISISTM 300, Accelerating Voltage 20 KV, Beam current: 0.5nA, Livetime: 50 sec, Beam diameter <2µm. All the collected images were back-scattered electron-micrograph images.

Digital Image Processing (DIP) of SEM images was carried out, using the EDGE program, which was developed by the US Geological Survey [7]. EDGE program was developed for the analysis of back-scattered electron-micrograph images stored in a binary file format that represents images with lateral resolution of 1.7µm/pixel. However, the images presented in this work had a lateral resolution of 2µm/pixel. EDGE measurements have to be made by computer analysis of 100x SEM images of core cross sections, consisting of 512 rows with 512 pixels per row, where each pixel is encoded with 8 bits on a 256-shade gray-scale palette. The fractal dimension of the exposed surfaces of stone specimens cut in cross-section was measured.

Three indexes of the marble micro-structure can be assessed, based on the fractal dimension determination and the special image calibration procedure. One of these marble micro-structural indexes is the near-surface fracture density (FD) of the stone, which is a measure of the fraction of the stone volume filled by fractures, crevices, and pore space. The FD results are reported as the percentage of pixels identified as components of the fractures calculated until 100µm under the surface area. FD value was used as evaluation index of the marble fracturing on the treated quarry specimens, as well as on the onsite collected samples before and after cleaning.

For the luminosity estimation, the Dr Lange spectro-color colorimeter was applied on the

investigated marble surfaces for measuring the luminosity as expressed by lightness variable L^* according to CIE $L^*a^*b^*$ Color Space. Lightness variable L^* varies from zero, for black, to 100 for white and could be considered as an indicator of material surface reflectance. Using this portable spectrophotometer ($d/8^\circ$ geometry, standard illuminant D65, standard observer 10°), an average of 10 values of lightness variable L^* was calculated for each marble quarry specimen in lab (1 measurement per 1.2 cm^2). Furthermore, an average of twenty five values of L^* was calculated per investigating area in NLG, both before and after cleaning, at exact points (that is 1 measurement per 20 cm^2 per investigation area, before and after cleaning). Correspondingly, an average of fifteen values of L^* was calculated per investigating area in NAM, both before and after cleaning, at exact points (that is 1 measurement per 10 cm^2 before and after cleaning). The variation of the L^* readings' number among lab specimens, NLG investigation areas and NAM investigation areas was inevitable due to the area differences (cm^2) of the investigated marble surfaces. Investigation areas of cleaning treatments in monuments scale are selected according to several parameters like the presence of representative decay patterns and their extent on architectural surfaces, surface orientation, accessibility, possibility of scaffolding raise, etc, that vary at each case. Nevertheless, each onsite collected sample from the investigated marble surfaces corresponded to the calculated L^* values average of each respective area. Luminosity, as expressed by lightness variable L^* , was used as an evaluation index of the reflectance modifications that the marble surfaces present after different kind of treatments.

PT experimental data demonstrated that intensity (temperature) of investigated marble samples is correlated to time in the transient phase by a first order kinetic model:

$$\frac{dI}{dt} = -\frac{1}{t_c} (I - I_e) \quad (1)$$

where dl/dt is the intensity rate, corresponding to the temperature rate; I is the intensity at time t ; I_e is the intensity in equilibrium that is for infinity time; t_c is the time constant for $I=0,666 I_e$ and its value has physical meaning, as defined by 1st order kinetics, denoting the required time for the intensity (temperature) to fall at 2/3 of its equilibrium value. Equation (1) is integrated to the following one:

$$\frac{I - I_e}{I_o - I_e} = \exp\left(-\frac{t}{t_c}\right) \quad (2)$$

where I_o is the intensity for $t=0$. Several surface morphology parameters were investigated in order to conclude in the effect of luminosity and fracturing on the time constant t_c of intensity falling rate for the differently treated marble samples. A power model is suggested to describe the relationship of time constant t_c with fracture density and luminosity as follows:

$$t_c = \frac{1}{c_o} \left(\frac{FD}{FD_o}\right)^{c_1} \left(\frac{L}{L_o}\right)^{c_2} \quad (3)$$

where c_o is an adjustable empirical constant of the material; c_1 is an adjustable empirical constant depending on fracture density; c_2 is an adjustable empirical constant depending on luminosity; FD is the fracture density; L is the luminosity. The model parameters are estimated by:

$$S = \left[\sum_{i=1}^N \frac{(I - I^*)^2}{(N - p)} \right]^{1/2} \quad (4)$$

where, I and I^* are the experimental and predicted values of intensity, N is the number of experimental points and p is the number of estimated parameters.

It was shown that the cooling rate of the samples could be described by a first order kinetic model, where the time constant of the cooling rate is an exponential function of marble surface fracturing and its luminosity. Increase of surface fracturing results in decrease of cooling rate; while increase of luminosity leads to faster cooling. Moreover, the suggested model can also be used as a prediction tool of marble surface fracturing, knowing luminosity and intensity falling rate; parameters that easily can be measured using

the corresponding NDE techniques on monuments scale and in lab.

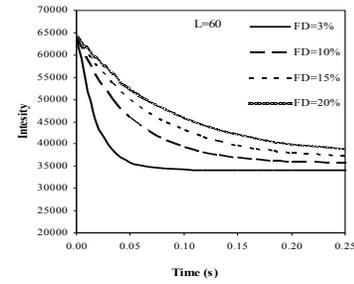


Figure 4: Cooling rate prediction for marble surfaces presenting luminosity $L=60$ and four different fracture density values ($FD = 3, 10, 15, 20\%$).

Conclusions

It is concluded that pulsed thermography can be a skilful means of inspecting marble surfaces, (differently treated, decayed, cleaned etc), using the suggested empirical mathematical model.

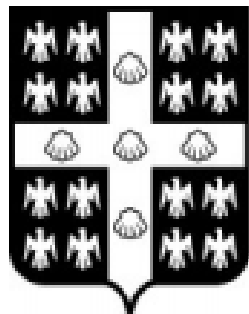
References

1. Avdelidis NP, Almond D. Transient thermography as a through skin imaging technique for aircraft assembly: modeling and experimental results. *Infrared Phys. Technol.* 2004; 45: 103-14.
2. Vallerand S, Maldague X. Defect characterization in pulsed thermography: a statistical method compared with Kohonen and Perceptron neural networks. *NDT&E Int.* 2000; 33: 307-15.
3. Bison PG, Cernuschi F, Grinzato E, Marinetti S, Robba D. Ageing evaluation of thermal barrier coatings by thermal diffusivity. *Infrared Phys. Technol.* 2007; 49: 286-91.
4. Normal document 20/85. Interventi Conservativi Progettazione Esecuzione e Valutazione Preventiva, 1985, ICR-CNR.
5. Moropoulou A, Delegou ET, Konstadinidou M, Kiranoudis C. Decision making about cleaning interventions on marble surfaces using a fuzzy logic approach. *Proc. 11th Int. Conf. Durab. Build. Mater. Compon.* Istanbul. 2008; 3: 1275-85.
6. Delegou ET, Avdelidis NP, Karaviti E, Moropoulou A. NDT&E techniques and SEM-EDS for the assessment of cleaning intervention on pentelic marble surfaces. *J. X-Ray Spectrom.* 2008; 37: 435-43.
7. Mossotti VG, Eldeeb AR. MORPH-2, A software package for the analysis of scanning electron micrograph (binary formatted) images for the assessment of the fractal dimension of exposed stone surfaces. Open file rep.: 00-013, 2000; U.S. Geol. Surv. Va. USA.

Techniques

AITA 2017

Québec City, Canada
September 27th - 29th, 2017



UNIVERSITÉ
LAVAL

METRIC MEASUREMENTS ON A PLANE WITH AN INFRARED CAMERA

R. Usamentiaga¹, D.F. Garcia¹, C. Ibarra-Castanedo², X. Maldague²

¹ Department of Computer Science and Engineering, University of Oviedo, Spain,
rusamentiaga@uniovi.es, dfgarcia@uniovi.es

² Computer Vision and Systems Laboratory, Laval University, Quebec, QC, Canada,
Clemente.Ibarra-Castanedo@gel.ulaval.ca, maldagx@gel.ulaval.ca

Geometric information from infrared images can complement the information about the measured infrared radiation. However, this requires geometric camera calibration. In this work, three calibration methods for infrared cameras are compared: a direct and an iterative estimation of the transformation between image and world coordinates, and a standard camera calibration method using a specifically designed calibration target. The three methods are compared and the obtained performance for metric measurements on a plane is evaluated. The results indicate acceptable performance in the three cases, with the standard method clearly outperforming the others two.

Introduction

Infrared cameras are not normally used to perform metric measurements on a plane. The main reason is that visible cameras can perform this task much more accurately due to the increased resolution [1], and at a reduced price. Therefore, geometric calibration for infrared cameras has not been a major research field. However, performing metric measurements with an infrared camera greatly enhances the information provided about the measured infrared radiation. For example, in non-destructive testing applications the size and the shape of the detected subsurface defects provide important information that can be used to characterize the defects. In building inspection applications, infrared thermography is generally combined with other signals, such as visible images and 3D point clouds. The geometric calibration of the infrared cameras in this case enables accurate aligning and fusion of all the signals. Therefore, geometric calibration for infrared cameras provides major advantages in a wide variety of applications.

Infrared camera calibration can be performed following the same procedures used for visible cameras. However, infrared cameras cannot capture the calibration targets used for visible cameras. Thus, they require calibration targets with distinguishing features in terms of infrared radiation. Several recent research works have

proposed different calibration targets suitable for infrared cameras. The most popular approaches are based on calibration targets with burning lamps and calibration targets that combine materials with different emissivity.

In this work three calibration methods for infrared cameras are compared. The first method is based on a direct homography estimation. The homography transformation requires four point correspondences between image and world points. When inspecting a rectangular object these correspondences can be easily obtained from the four corners of the object. The calculated homography transformation provides a mapping between image points and world coordinates and vice versa, which enables metric measurements on a plane with a single camera. This first method considered, with a specially designed calibration target is used in [2]. The accuracy of this method largely depends on the accuracy of the extracted coordinates of the four corners of the object in the image. An alternative approach is to use the whole contour of the object to estimate the homography iteratively [3]. This is the second calibration method considered in this work. The third method is based on a standard complete calibration approach, where observations of a calibration target at different orientations provide the necessary information to fit the pinhole camera model [4]. This third

method includes lens distortions, providing much more accurate results. However, it also requires a specific calibration target with features that can be distinguished in the images.

The three methods compared in this work, direct, iterative and complete, go from simple to more complex. In the direct method the detection of four points in a single image is sufficient. In the complete method, between 7 and 15 images of a specially built calibration target, acquired at different orientations are required. The increased complexity is compensated by an improved accuracy.

Infrared camera calibration

Direct method

The transformation of a 3D point in the scene into a 2D point in the image is generally described using the pinhole camera model. This transformation consists of a combination of a 3D rigid transformation, from world coordinates to camera coordinates; a perspective projection from 3D to 2D that depends on the focal length; and an affine transformation that depends on the size of the pixels and the position of the central pixel. The result is a transformation 3×4 matrix that can be used to transform a point in world coordinates to a pixel in image coordinates. When all the points lie on the same plane of the scene, called the measurement plane, the transformation matrix can be simplified to a 3×3 matrix. This is the homography that provides an invertible mapping between points and lines on the measurement plane and in the image.

The homography that describes the invertible transformation from the world to the image has only 8 degrees of freedom even though it contains 9 elements. This is because it can be changed by multiplying by an arbitrary non-zero constant without altering the projective transformation. Therefore, the homography has 8 unknown coefficients that must be estimated in order to perform measurements with the images. A point correspondence between the image and the world provides 2 equations, one for x and one for y . Therefore, only 4 point correspondences, 3 non-collinear, are required to estimate the coefficients of the homography. The most straightforward approach is to detect the corners of a rectangular

object in the image with known dimensions in the world. The four detected points in the image, and the correspondences in the world can be used to estimate the homography.

Iterative method

The direct method largely depends on the accuracy of the detection of only four points in the image. On the contrary, the iterative method uses the whole contour of a known object in the image, which can contain hundreds of points. Then, the method approximates the extracted contour to the real shape of the object in world coordinates using a variant of the iterative close point algorithm. This method requires an initial coarse approximation of the projection parameters. Part of the required parameters can be obtained from the camera manufacturer specifications, including the focal length, detector pitch, and sensor resolution. The parameters that depend on the position of the camera relative to the measurement plane must be estimated manually. Another possible approach is to estimate the initial approximation using the direct method.

The iterative method calculates the correct homography even when the extracted contour of the object is affected by noise and includes outliers. Robust statistics are used for outlier detection based on the calculated residual vectors. Combining the increased number of points with noise filtering, the iterative method can calculate an invertible homography mapping between the image and the world with enhanced accuracy. Neither this method nor the direct method consider lens distortions, which reduces the obtained accuracy.

Complete method

The standard method for camera calibration is based on the procedure proposed in [5]. Different image observations of a known flat target at different orientations are required. Feature extraction from the images provides the position of known points in the calibration pattern, which are used to estimate the camera parameters. This method is more complete than the two previous methods, as it includes the calibration of the internal and external camera parameters, but also the lens distortion parameters. The resulting

calibration is also much more accurate because the calibration target used is specially designed for the extraction of the required features easily and with extreme precision.

The drawback of this method is that it requires a specially built calibration target with features that can be detected in terms of infrared radiation. One possible solution is a calibration target made of Dibond® where the calibration pattern is printed with a different emissivity using an industrial flatbed printer used for advertising boards.

Results and discussion

In order to compare the performance of the three considered calibration methods, a measurement experiment based on the calibration target used in the complete method has been designed. The calibration target contains a grid of 9x9 circles. The diameter of each circle is 6.25mm and the distance between them is 25 mm. The experiment measures the distances between each of the circles in the grid using the calibration obtained by the considered methods.

The camera used for the experiments is a Flir T450sc, which includes a long-wave infrared sensor of 320x240 resolution and an 18mm focal length lens. The infrared camera is configured to perform measurements in the [-20, 120°C] temperature range. The manufacturer reports measurement accuracy of $\pm 1K$ and sensitivity lower than 30mK at 30°C. Using this camera, five images of the calibration target are acquired on the same plane relative to the camera. The images can be seen in Fig. 1. One image is used to perform the calibration and the other four to test the calibration. In order to create thermal contrast in the calibration marks, the calibration target is heated using an electric fan heater before the image acquisition.

The three calibration methods are coded in Matlab. The complete calibration method uses the camera calibration toolbox.

The direct method requires the detection of four points in the image with known correspondences in world coordinates. In the experiment, the corners of the calibration target are used. The coordinates of these points in the images used for calibration are detected using a well-known sub-

pixel corner detection algorithm [6]. The results can be seen in Fig. 2.

The iterative method requires the extraction of the contour of a known object in the image. In the calibration experiment, the contour of the calibration target is extracted using edge detection. Fig. 2 shows the results of the contour extraction, the first and last iterations of the homography estimation, and the rectified image with no perspective distortion.

The complete method requires the calibration of the internal camera parameters using a set of images of the calibration target at different orientations. Fig. 3 shows the images acquired using the sky reflection. Then, the first image of the test set is used to calibrate the external parameters.

The centers of the circles in the four test images are extracted from the images and transformed into world coordinates using the three calibrations. Then, the distances from each point to all the others in all the images are calculated and compared with the real distances in the calibration target. The results can be seen in Fig. 4, where a histogram of the absolute errors are shown for each calibration method. Errors are calculated as the difference between the actual distance and measured distance. As can be seen, the complete method produces much better accuracy than the two others, obtaining an average error of only 0.060mm. The average error of the iterative method, 0.443mm, is greater than the complete method, whereas the direct method produces an average measurement accuracy of 1.118mm.

The results indicate acceptable performance with the three methods, with the complete method outperforming the other two by a large margin. Moreover, the iterative method reduces the error by more than half compared with the direct method because more points are used to estimate the homography.

Conclusion

In this work three calibration methods for infrared cameras are compared. The results indicate that a standard calibration using a specific calibration target produces much better accuracy than a direct or an iterative calibration, where the

iterative method is the second best. However, this increased accuracy is obtained at the expense of increased complexity in the calibration and the requirement of a properly designed calibration target for infrared images. Future work will focus on extending this calibration methods for other type of surfaces, such as spheres or cylinders.

Acknowledgements

This work has been partially funded by the project TIN2014-56047-P of the Spanish National Plan for Research, Development and Innovation, and the Spanish National Program for Mobility of Professors and Researchers at an International Level.

References

1. R. Hartley and A. Zisserman, Multiple view geometry in computer vision. Cambridge university press, 2003.
2. H. González-Jorge, S. Lagüela, P. Krelling, J. Armesto, and J. Martínez-Sánchez, "Single image rectification of thermal images for geometric studies in façade inspections," *Infrared Physics & Technology*, vol. 55, no. 5, pp. 421–426, 2012.
3. R. Usamentiaga, "Easy rectification for infrared images," *Infrared Physics & Technology*, vol. 76, pp. 328–337, 2016.
4. D. Rzeszotarski and B. Wiecek, "Calibration for 3d reconstruction of thermal images," in *Conf. on QIRT*, 2008, pp. 563–566.
5. Z. Zhang, "A flexible new technique for camera calibration," *Pattern Analysis and Machine Intelligence, IEEE Transactions on*, vol. 22, no. 11, pp. 1330–1334, 2000.
6. C. Harris and M. Stephens, "A combined corner and edge detector," in *Fourth Alvey vision conference*, vol. 15, 1988, pp. 147–151.

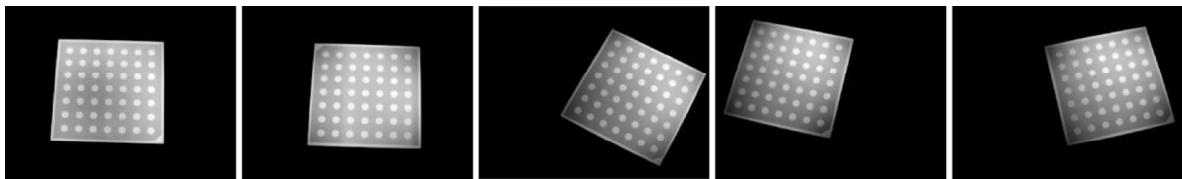


Fig. 1. Images used for tests

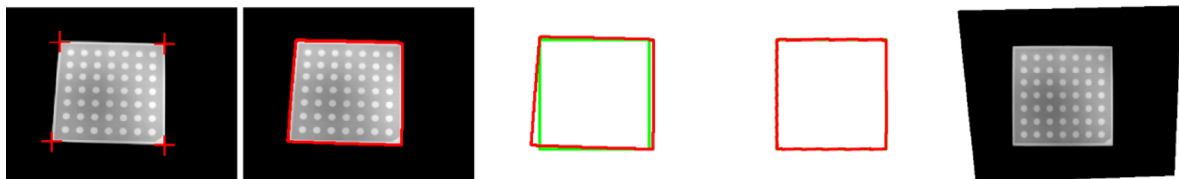


Fig. 2. Calibration of the direct and iterative methods. Corners, contour, iterations and rectified image

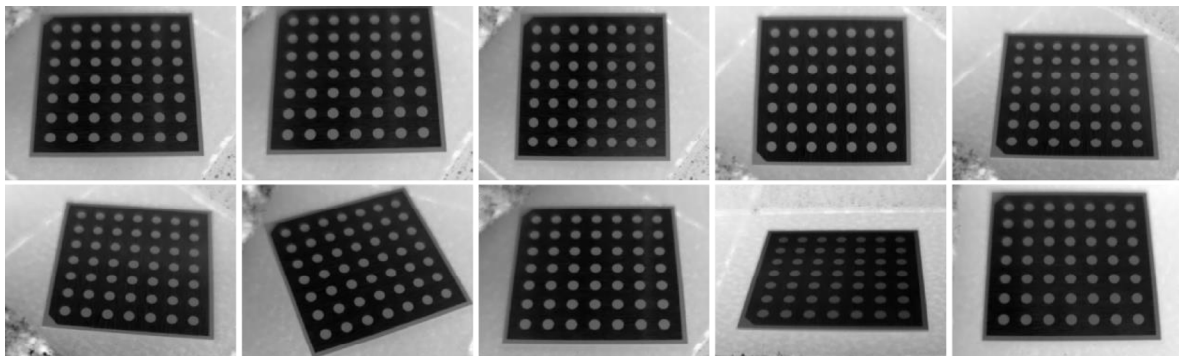


Fig. 3. Images used for the calibration of the complete method

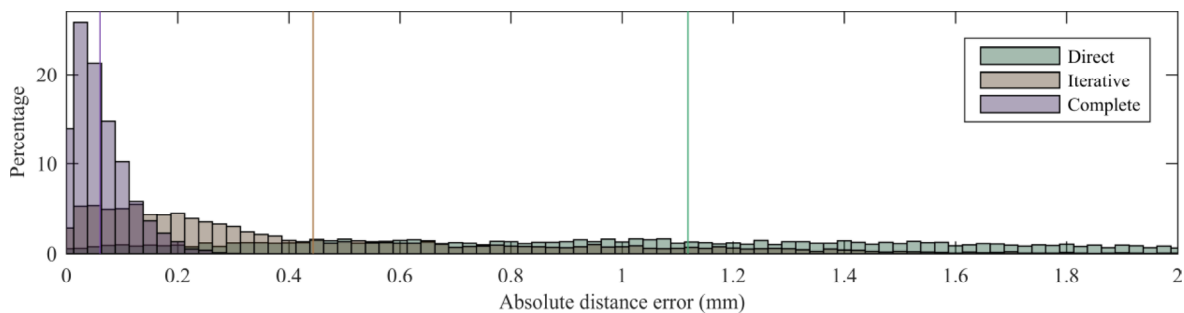


Fig. 4. Histogram of the absolute errors for the compared calibration methods

MEASUREMENT OF THREE DIMENSIONAL SURFACE TEMPERATURE DISTRIBUTION BY HYBRID DIGITAL HOLOGRAPHIC IMAGING SYSTEM

S.-H. Yi¹, I.-H. Kwon², H.-C. Jung^{3,*}, K.-S. Kim⁴, C.-K. Hong⁵

¹ School of Mechanical System Engineering, Chosun University, snow773558@gmail.com

² Department of Physics, Pohang University of science and technology, imperial@postech.ac.kr

^{3,*} School of Mechanical System Engineering, Chosun University, hyunchul.jung@chosun.ac.kr

⁴ School of Mechanical System & Automotive Engineering, Chosun University, gsckim@chosun.ac.kr

⁵ Department of Physics, Pohang University of science and technology, ckhong@postech.ac.kr

This paper introduced a hybrid digital holography which combined a Nd:YAG phase shifting digital holography with a thermal image obtained from IR camera. For achieving the combined hybrid digital holography, the numerically reconstructed digital holography has 3.25 μm spatial resolution with preserving the temperature accuracy of the IR camera. This combined high resolution hybrid digital holography can improve the capabilities of digital holography in three dimensional thermal imaging and microscopy.

Introduction

Digital holography allows the reconstruction of the images of three-dimensional objects by numerical processing techniques [1,2]. It has a significant advantage to acquire both the amplitude and the phase information of the objects. This significant advantage of digital holography can be applied to many fields such as three-dimensional imaging, phase-contrast imaging, surface profile measurement and others [3,4]. IR (infrared) digital holography is one of technique to achieve the thermal information of the object surface in reconstructed wave field [5-7].

However, the resolution of digital holography is influenced by the wavelength of a laser source. IR digital holography has lower resolution than the general digital holography that is used with a visible laser. Because the typical IR digital holography acquire the interference pattern in the mid-range of IR coherent source like CO₂ laser with 10.6 μm wavelength.

So, we developed a novel digital holography which combined a phase shifting digital holography with a thermal image from IR camera. IR camera could take a high sensitivity thermal image. Otherwise, in-line phase shifting digital holography can acquire a precise phase contrast image. Our novel digital holography takes most of benefits of both measurement systems.

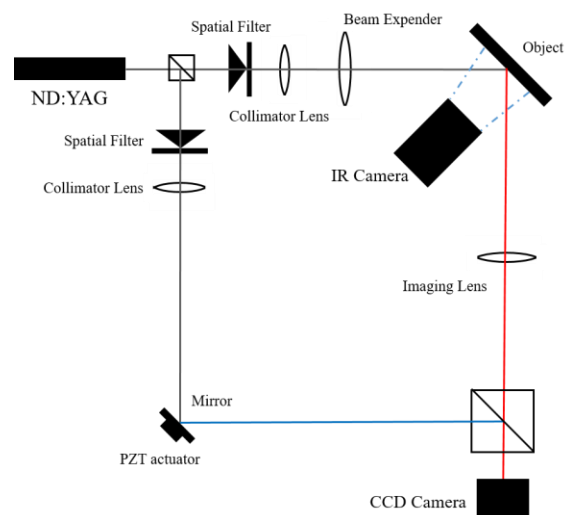


Fig. 1. Schematic of hybrid digital holography interferometer.

Principle & method

Our goal is reconstructed the thermal information of the object surface from IR image and digital holography in 3D. First of all, we should acquire the digital holography. The intensity of interference pattern of phase shifting digital holography could express as Eq. (1)

$$I_N = I_R + I_O + 2\sqrt{I_R I_O} \cos(\theta_N) \quad (1)$$

where I_R and I_O represent the intensities of the reference and object wave, the phase $\theta_N = \theta_R - \theta_O$ is the difference of phases of the reference and object wave.

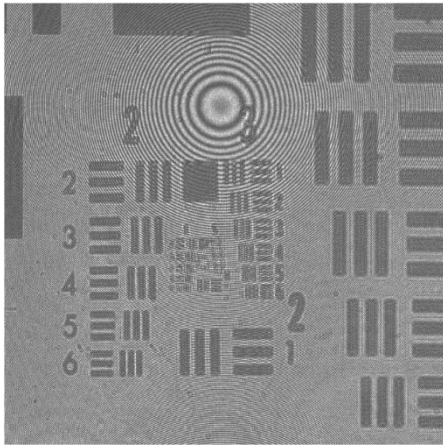


Fig. 2. Interference pattern image of negative USAF resolution target using off-axis digital holography.

For estimating the complex amplitude of the wavefront on a CCD camera, we used 8-steps phase shifted reference field which called interframe intensity correlation (IIC) methods [10]. Estimated wavefront is called the digital holography function $h(x, y)$ which is proportional to the interfered intensity distribution. It could express that the digital holography function $h(x, y)$ calculated through a coherent superposition of two fields. In the digital holographic reconstruction process, the reference beam is illuminated onto the hologram, that is also can be described

mathematically through multiplying the corresponding complex field. The diffraction of a light wave at an aperture (in this case a hologram) which is mounted perpendicular to the incoming beam is described by the Fresnel-Kirchhoff integral as Eq. (2)

$$\Gamma(\xi', \eta') = \frac{i}{\lambda} \int_{-\infty}^{\infty} \int_{-\infty}^{\infty} h(x, y) E_R(x, y) \frac{\exp(-i \frac{2\pi}{\lambda} \rho')}{\rho'} dx dy \quad (2)$$

where $\Gamma(\xi', \eta')$ is the reconstructed wave field, and $\rho' = \sqrt{(x - \xi')^2 + (y - \eta')^2 + d^2}$ is the distance between a point in the hologram plane and a point in the reconstruction plane. ρ' determines the image-plane of reconstructed digital holography. The reconstruction of the wave-field can be numerically achieved by the angular spectrum method, also known as plane wave expansion method [11]. This reconstructed wave-field contains the amplitude and phase information of the object surface.

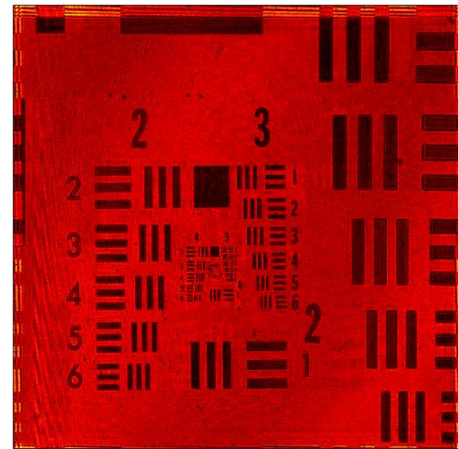


Fig. 3. Reconstructed digital holography of negative USAF resolution target from Fig. 2.

As mentioned above, our goal is to combine the thermal image and the digital holography. Before combining these two images, we should geometrically match the reconstructed image and the thermal image obtained from IR camera. These images could be represented in a 3D image using texturing function *surf* as Eq. (3).

$$\begin{aligned}
 H &= A_H \exp(-i\theta_H) \\
 T &= \text{surf} \{U[\exp(-i\theta_H)], A_{Th}\}
 \end{aligned}
 \quad (3)$$

H is the reconstructed object plane wave-field from digital holography which measured by CCD. H includes the amplitude of object A_H and wrapped phase of object θ_H . The reconstructed object phase can be unwrapped by 2D least square phase unwrapping function U . This unwrapped phase contains the object surface deformation. A_{Th} is the thermal amplitude of an image focused on the surface by IR camera. Because U and A_{Th} are geometrically matched by using surf function. This 3D textured image simultaneously represents the object surface deformation and the temperature distribution.

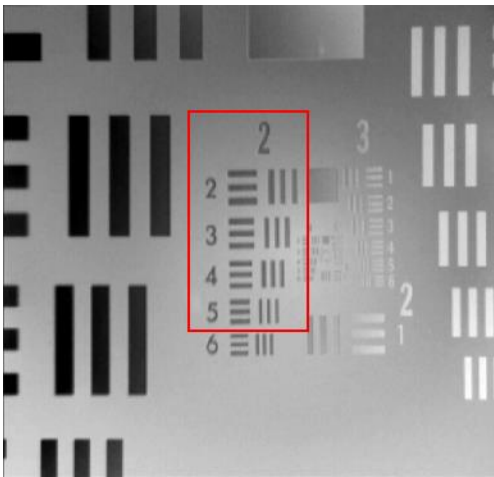


Fig. 4. USAF resolution target of thermal image from IR camera (FLIR SC5500).

Experimental result

The Newport negative USAF resolution target was measured by the 2048 X 2048 pixels CCD (PointGrey Grasshopper 3), 5.5 μm pixel size. We acquired 8 steps phase shifted interference pattern by a piezo actuator and reconstructed amplitude shown as Fig. 3. The resolution of group 2 was verified by using the intensity line profile on group 2, elementary 2 to 5 in red box. The average lateral resolution is 14 μm . and the axial resolution is 0.75 μm . During the resolution target

is measuring, it is also heated simultaneously by a halogen lamp and a thermal image was acquired by IR camera (FLIR SC5500, 320 X 256, mid Infrared waveband 2.5 μm ~ 5.1 μm , temperature accuracy ± 1 %). An obtained image is shown as Fig. 4. This thermal image is superposed thermal image with unwrapped phase which shown as Fig. 5. This image could simultaneously show the surface deformation and the temperature of resolution target.

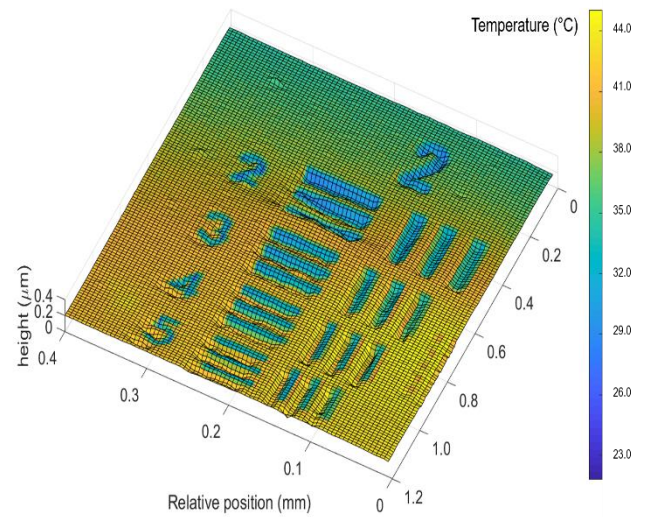


Fig. 5. Experiment result of ~~our~~ superposed thermal image with ~~phasesurface~~ deformation-method.

Conclusion

We acquired surface information which include amplitude, phase and temperature by our hybrid digital holography. The superposed thermal image with reconstructed digital holography image could simultaneously express the surface deformation and thermal information. Our method has advantage that it preserves the lateral and axial resolution of visible digital holography and thermal sensitivity of IR camera. This hybrid digital holography could suggest a novel micro thermography which can be applied to measure 3D surface deformation like the hidden damage inspection, dynamics surface thermal changing and etc. The suggested method is also used to investigate the effect of exothermic phenomena on cracking of the target surface. We currently

configure the phase shifting digital holography microscopy with IR camera. Beside, we also achieve the dynamics digital holography with a thermal image using the suggested method. This experiment results would be presented in AITA 2017.

Acknowledge

This research was financially supported by the National Research Foundation of Korea (NRF) as a grant funded by the Korean government (NRF-2013M2A2A9046502) and was supported by Basic Science Research Program through the Nation Research Foundation of Korea (NRF) funded by the Ministry of Education (2017R1D1A1B03034347).

References

1. U. Schnars, W. Jüptner. Direct recording of holograms by a CCD target and numerical reconstruction, *Applied Optics*, Vol.33(2), pp.179-181, 1994.
2. J.W. Goodman, R.W. Lawrence. Digital image formation from electronically detected holograms, *Appl. Phys. Lett*, Vol.11, pp.77-79, 1967.
3. Z. Johan, S. Staffan, A. Magnus. Cell shape identification using digital holographic microscopy, *Applied Optics*, Vol.54(24), pp.7442-7448, 2015.
4. V.P. Prabhu, R. John. Optofluidic bioimaging platform for quantitative phase imaging of lab on a chip devices using digital holographic microscopy, *Applied Optics*, Vol.55(3), pp.A54-A59, 2016.
5. T. Konishi, A. Ito, Y. Kudo, A. Narumi, K. Saito, J. Baker, P.M. Struk. Simultaneous measurement of temperature and chemicalspecies concentrations with a holographic interferometer and infrared absorption, *Applied Optics*, Vol.45(22), pp.5725-5732, 2006.
6. M. Locatelli, E. Pugliese, M. Paturzo, V. Bianco, A. Finizio, A. Pelagotti, P. Poggi, L. Miccio, R. Meucci, P. Ferraro. Imaging live humans through smoke and flames using far-infrared digital holography, *Optics Express*, Vol.21(5), pp.5379-5390, 2013.
7. P. Ferraro, L. Miccio, S. Grilli, R. Meucci, S.D. Nicola, P.B. Bassuah. Infrared digital holographic imaging, *SPIE Newsroom*, 10.1117/2.1200802.0991.
8. N. Miyamoto, S. Nisiyama, S. Tomioka, and T. Enoto. Application of the nitroanisole as an infrared detector used in middle infrared interferometer, *Opt. Commun*, Vol.260, pp.25-29, 2006.
9. M.P. Georges, J.F. Vandenrijt, C. Thizy, I. Alexeenko, G. Pedrini, B. Vollheim, I. Lopez, I. Jorge, J. Rochet, W. Osten. Combined holography and thermography in a single sensor through image-plane holography at thermal infrared wavelengths, *Optics Express*, Vol.22(21), pp.25517-25529, 2014.
10. H.Y. Yun, C.K. Hong. Interframe intensity correlation matrix for self-calibration in phase-shifting interferometry, *Applied Optics*, Vol.44(23), pp.4860-4869, 2005.
11. H.Y. Yun, S.J. Jeong, J.W. Kang, C.K. Hong. 3-dimensional micro-structure inspection by phase-shifting digital holography, *Key. Eng. Mater.* Vol.270-273, 756-761, 2004.

THERMAL CHAMBER FOR DNA AMPLIFICATION AT GIVEN TEMPERATURE (T = 62 C): PRELIMINARY TEST RESULTS

Hector Torres-Ortega¹, Marija Strojnik², Guillermo Garcia-Torales¹, Michelle K. Scholl³

¹ Universidad de Guadalajara, Departamento de Electronica Av. Revolucion 1500, Guadalajara, Jalisco, Mexico, CP 44840, hector.hhto@gmail.com, gmogt13@gmail.com

² Centro de Investigaciones en Optica A.C. Loma del Bosque 115, León Guanajuato, CP 37000, Leon, Gto., Mexico, mstrojnik@gmail.com

³ Alenka Associates, P. O. Box 27488, Tempe, AZ 85285 USA

The successful implementation of the μ -LAMP lab on chip technology requires design of a reliable thermal chamber, maintained at a constant temperature, and capable of temperature cycling. We describe design, fabrication and preliminary thermal tests of a sample chamber that fosters amplification of minute amounts of DNA (at the test temperature of 62 C).

Introduction

The loop-mediated isothermal amplification (LAMP) method is a highly popular technique for nucleic acid amplification. It can synthesize large amounts of DNA in a short time with high specificity and sensitivity. The potential of lab-on-chip (LOC) to detect pathogens, bacterial and viral infestation, disease diagnosis, biological safety, food analysis has started to be explored¹.

Its successful implementation could change samples processing in forensics for police work, including reduce time to process rape kits. Microfluidic chip technology can integrate those operations that once were performed in the laboratory with cm³ samples on a small scale of a microfluidic chip.

The molecular biological method of LAMP has been combined with miniaturized microfluidic chip to evolve into a new technology, known as to as micro-LAMP (μ -LAMP).

Many researchers consider μ -LAMP the future of diagnostics in the field of health, medicine, and sanitation monitoring due to its high sensitivity to the target sample, 10⁻¹⁵ g, and small volume requirements². Its disadvantages are that the small sizes make temperature control more difficult to implement³. Likewise, process-monitoring sensors must also be miniaturized.

We propose a sample chamber built up of layers, with the amount of heating current controlled by a microprocessor. We describe the chamber design, fabrication, and preliminary tests.

DNA amplification at temperature, T=62 C

The process of DNA amplification in LOC requires that the original DNA sample be placed inside a small sample chamber that is kept at constant temperature: we chose a process temperature of 62 C. We use resistive heating of the base card⁴. The primary function of the sample chamber is to hold an adequate amount of the fluid sample. Additionally, it allows its rapid initial heating of the sample with relatively low power consumption, and maintains the sample at the requisite temperature for the duration of the process (1 hour for the test case). The volume of the sample chambers is preferably small, but sufficiently large enough to contain 0.3 cm³ of the sample in a liquid form.

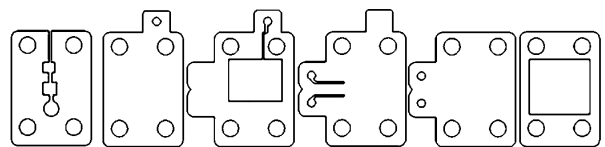


Fig. 1. Computer-aided design (CAD) of the thermal chamber and its implementation in acrylic. The left-most layer is in contact with the thermal bed. The four circles in the corners serve as the alignment guides.

With CAD, we design the thermal chamber mechanically. We illustrate the chosen design incorporating 6 layers in Fig. 1. The left-most layer is in contact with the thermal bed employing resistance heating. The primary consideration in the design of the first layer (left) is the selection of location of temperature and color sensors. The color sensors are used for determination whether the sample has achieved the degree of DNA amplification required for further processing. The remaining part is in thermal contact with the thermal bed.

The function of the second stage is to maintain the wall continuity and serves as the chamber bottom. The third layer determines the volume of the chamber. Additionally, it has an output channel. The fourth layer has two input channels: the first one is for the DNA sample; the second one is for the primer. The function of the fifth layer is to cover the inlet channels. The function of the sixth layer is to make room for the RGB (red, green, blue) LEDs of the illumination board and their sensors. They are temperature and color sensors.

Furthermore, any probe introduced inside the sample chamber would modify the temperature distribution established upon the heat transfer from the heating PCB board. Three temperature regions are indicated on the inset of Fig. 2.

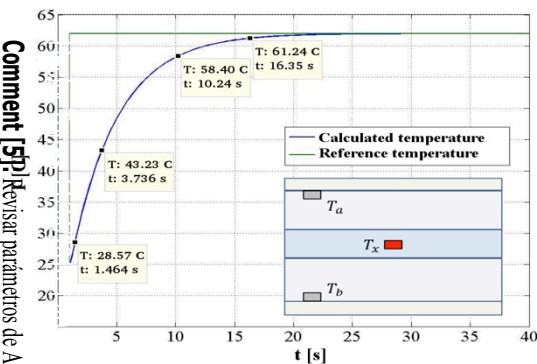


Fig. 2. Temperature increase inside the sample chamber (red) as a function of time. Time constant is 5 s.

Figure 3 illustrates the solid model of the thermal chamber. We import the model of the 3-D object into the finite element program ANSYS™. The advantage of finite element technique is that the mesh size may be adjusted according to the

complexity of the mechanical object. We calculate the 3-D heat distribution as a function of time⁵ upon resistive heating.

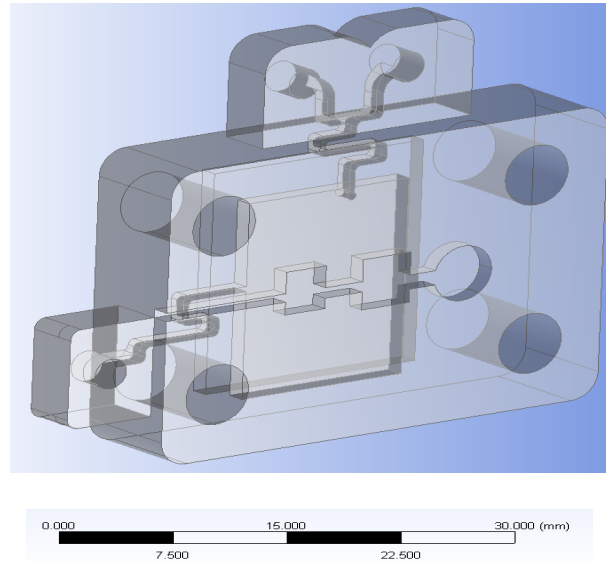


Fig. 3. Geometry of the thermal chamber used as the input to the finite element program to determine temperature distribution.

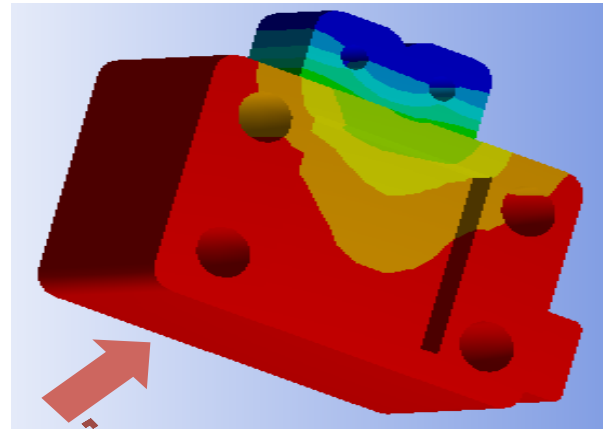


Fig 4. Temperature distribution throughout the thermal chamber is calculated by the finite element heat transfer program, shown here for one specific time of observation (red is hot, blue is cold).

The results of simulation shown for temperature in Fig. 4 for one point in time. The simulation also provides the power consumption, and thermal heating and cooling temporal constants. We only perform the actual temperature measurement at three points to anchor the results of the heat transfer simulation program. The points T_a and T_b correspond to the actual physical position of the temperature sensors on the printed circuit board (PCB).

Temperature T_a corresponds to the temperature of the sensor welded onto the control board. Temperature T_b is that of the illumination source board (ISB).

T_x is the proposed virtual test point at the internal base of the fluid chamber. It is presumed that T_x represents the temperature of the sample. In the actual, physical system, there will not exist a sensor for T_x , because its presence would interfere with the thermalization and separation process that takes place inside the chamber.

Figure 2 presents the calculated temperature (increase) inside the sample chamber (red in the inset) as a function of time. The green line denotes the process reference temperature, in this case 62 C. The reference may be changed to a more complicated function when thermal cycling is implemented. From the graph we can read the thermal time constant τ (5 s) for the heating process and the time delay, Δt (15 s). The time delay is the time it takes the incremental sample volume at T_x to reach the required process temperature (62 C), at which the amplification process initiates. Time constant τ and delay time Δt are used as input parameters for the temperature controller.

Prototype fabrication

We fabricated the chamber modules from acrylic sheeting material employing laser cutting. The photo in Figs. 5 and 6 show the cut layers and the layers stacked up in a vertical arrangement, respectively. The entrance and the exit channel are marked with red and blue. Their width is 1 mm. The fluid container is marked in green. The volume of the thermal chamber within which the sample DNA is to be amplified depends on size of green area. The thickness of the material used in this particular case is 3 mm. The acrylic layers are welded with chloroform to form the thermal chamber.

This would first be modeled in a thermal program to obtain alternate values for time delay and time constant to input into controller. In the present case, the reference curve is a constant.

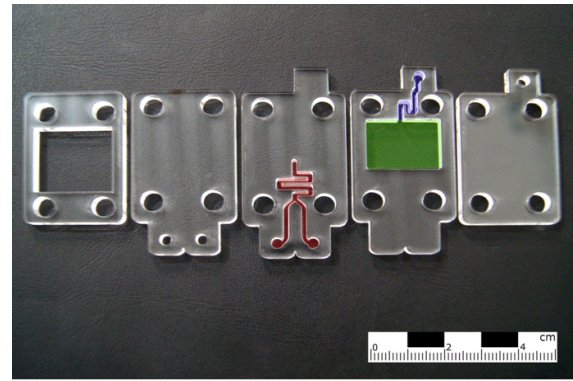


Fig. 5. Layers of the thermal chamber are fabricated from acrylic, using laser cutters

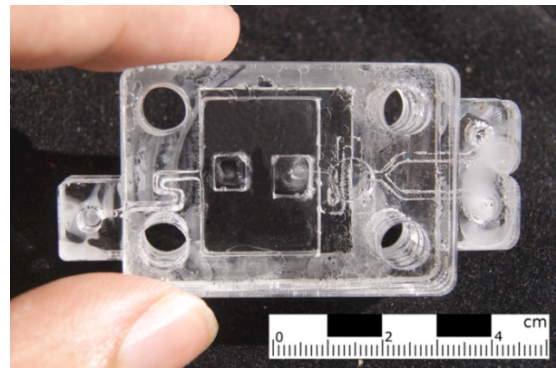


Fig. 6. We use chloroform to weld together individual layers of the thermal chamber.

Thermal tests on the Prototype

We show the measured performance on Figs. 7 and 8. On the left side of Fig. 7, the PCB board was stable, in the steady state at the reference temperature of 62 C. On the right side, the PCB board was in the state of the temperature overshoot, at the highest temperature value to which the board has been exposed.

Summary and future work

We designed a sample chamber to maintain the DNA sample at 62 degrees C for an hour in an micro-LAMP lab on chip LOC. It is used for DNA amplification of a small fluid sample volume that is microprocessor-controlled. Preliminary results confirm its thermal performance.

References

1. L. George, A. Ali y N. Homyoun, "Microfluidics Integrated Biosensors: A Leading Technology

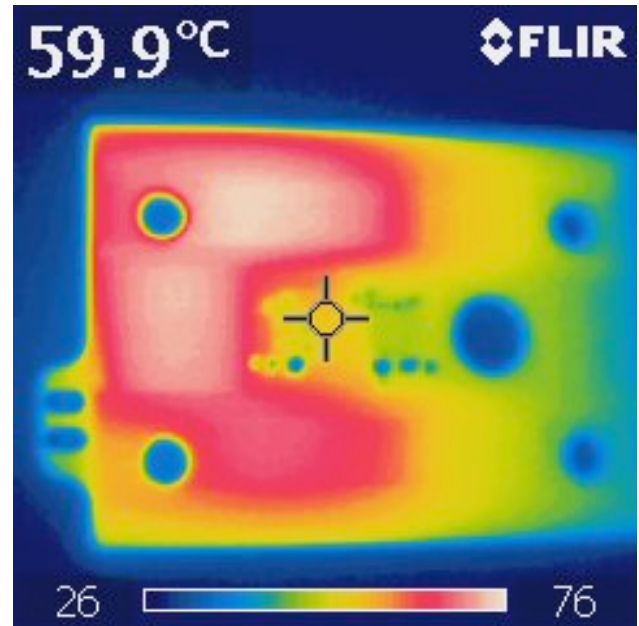
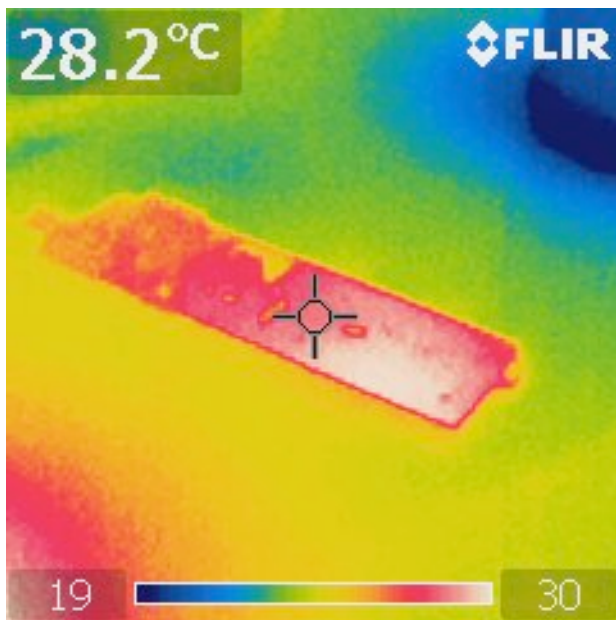
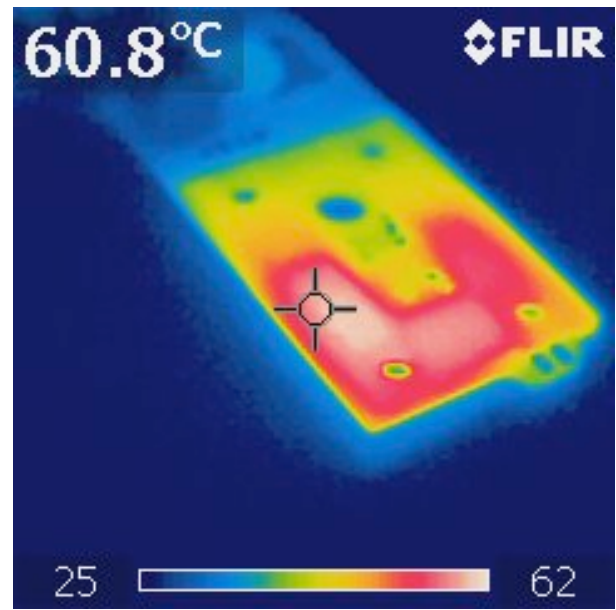
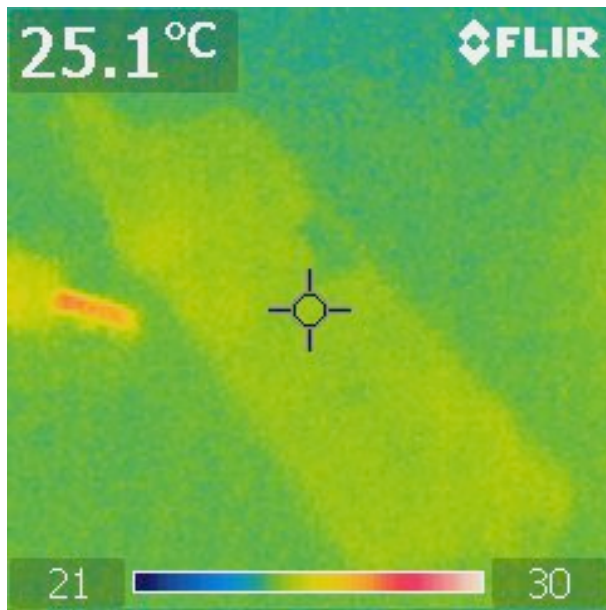


Fig. 7. The photographs were taken at the beginning of the thermal control cycle. The PCB board was still not powered on top. On the bottom, the thermalization process was ready to initiate.

Fig. 8. The thermographs were obtained at the end of thermal control cycle with a FLIR (thermal) camera. On the top, the PCB board has achieved the steady state at the reference temperature of 62 C. On the bottom, the PCB board is in the state of the temperature overshoot.

towards Lab-on-a-Chip and Sensing Applications,” *Sensors (Basel)* **12**, 30011–30031 (2015)

- B. Charles, V. Iwijn, K. Jad, W. Jianbin, G. Charles y Q. S. R., “A Quantitative Comparison of Single-Cell Whole Genome Amplification Methods,” *PLOS ONE* **9** (8) (2014).
- S. Andrea, T. Michele, P. Pisana y Z. Stefano, “Thermal Modeling and Characterization of a Thin-Film Heater on Glass Substrate for Lab-on-Chip Applications,” *Transactions On Instrumentation and Measurement* **64** (5) 1215-1222 (2015).

- M.-Q. Jose, C.-G. Saul, R. Matthew y S. David, “Deterministic Design of Thin-Film Heaters for Precise Spatial Temperature Control in Lab-on-Chip Systems,” *Journal of Microelectromechanical Systems* **25** (3), 508-516 (2016).
- M. S. Scholl, “Thermal Considerations in the Design of a Dynamic IR source,” *Appl. Opt.* **21**(4), 660-667 (1982).

Thermal Bed for DNA Amplification at given Temperature (test case $T = 62\text{ C}$)

Hector Torres-Ortega¹, Marija Strojnik², Guillermo Garcia-Torales¹, and Michelle K. Scholl³

¹Departamento de Electronica, Universidad de Guadalajara, Av. Revolucion 1500, C. P. 44840
Guadalajara, Jalisco, Mexico

²Optics Research Center, AP 1-948, CP 37000, Leon, Gto., Mexico

³Alenka Associates, P. O. Box 27488 Tempe, AZ 85285, USA

mstrojnik@gmail.com, hector.hhto@gmail.com

The successful implementation of the μ -LAMP lab-on-chip technology requires implementation of a reliable thermal heating and temperature control system. It has to perform within strict tolerances to enable the evolution of the requisite biological processes. We describe design and fabrication of a thermoelectric system to heat the thermal chamber at a requisite heating rate and, consequently, maintain it at a required temperature. This is accomplished within tolerances that allow optimum survival and then amplification of the DNA (for test case of 62 C) and electro-optical components.

1. Introduction

Recently there is a great deal of interest in the implementation of biological processes, monitoring of chemical evaluation, and in-situ analyses for different applications. Areas such as biology, chemistry, and medicine have required technologies that perform processes that used to be performed during lengthy trials in the laboratory. The processes may rapidly take place within a miniaturized intelligent device [1].

In this paper we describe a model of the thermal control and the implementation system for a DNA amplification device. The specific objectives are to evaluate the thermoelectric parameters of a copper trace and to model and simulate the copper trace as a thermal bed for the sample chamber.

In the thermoelectric stage, we develop a system that generates heat to elevate the temperature of the sample chamber and another subsystem that measures and controls this temperature. We propose to implement it with a trace of copper that is part of a printed circuit board (PCB). In the case presented here, the process is the amplification of DNA incorporating the LAMP process. This isothermal process takes place at 62 C. The temperature control system may be applied to many other processes, at different temperatures upon some parameter changes.

Providing a suitable temperature for a wide range of processes will facilitate the deployment of devices for the application in diverse areas, such as biology, medicine, chemistry, forensics, and more [2, 3]. In the last few years a number of proposals for devices or methodologies that focus on the thermal part where we can find silicon arrays for temperature control for PCR amplification processes [4], micro-coils with temperature-control for the Lab-On-Chip platforms [5], thermal generator with thermistors for biological processes [[7]], manufacture of thin films for the PCR, characterization of PCR heaters, and more.

2. Thermoelectric system

The development of the requisite environment for the Lab-On-Chip devices focuses on the thermal subsystem. The biological processes usually require temperature control with tight tolerances.

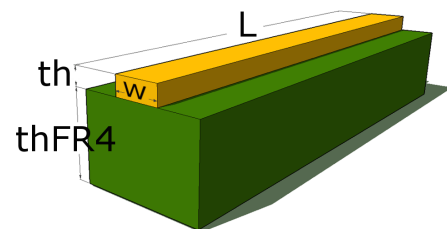


Fig. 1. A cross-section of a copper trace on a (standard) dielectric material type FR-4.

First we need to raise the temperature of the sample to a recommended operating point. We maintain this temperature for the required period of time. We first refine the mechanical parameters of the trace of the PCB to be designed as the heating coil.

Figure 1 shows a PCB segment with a single trace, and its cross section. It illustrates the mechanical parts to be considered in this thermal analysis. The thickness of the copper is fixed for the entire PCB layer and is selected according to the copper foil to be used. We chose 1 ounce per square foot (1 oz/ft²). The width of a copper trace, determined in the design program, is measured in thousandths of an inch (1 mil). The desired rate of temperature increase and the process temperature determine the required maximum electrical current.

The design and manufacturing standard for the PCBs, IPC-2221A ((D-31b), 1998), proposes an approximation to the temperature of a trace as a function of the current flowing through it. This basically defines the physical geometry of the width of the trace as a function of the necessary current.

Initially, we assume a nominal power of 1 W. Then we evaluate the system with specific parameters. A copper trace with the width of 10 mils, and the thickness of 1 oz/ft² yields the thickness of 34.79 μm. Initially, the current is set to 1 A, later raised to 2 A. For our system, the temperature increase depends primarily on the electric current. The temperature increase is considered uniform within the short length of the incremental volume of the copper trace.

Theoretical development, leading to the increase in temperature for a short segment of the copper trace, has been developed in Ref. [8]. Here we summarize the result.

$$\frac{dT}{dt} = \frac{I^2 R_e - h((w + th) * L)(T - T_\infty) + \varepsilon \sigma ((w + th) * L)(T^4 - T_{sur}^4)}{\rho c (w * th)} \quad (\text{K/s})$$

Next we define the quantities and their units.

T is the temperature increase in [K] or [C];

t is time in [s];

I is the current in amperes, [A];

R_e is the electrical resistance of the copper

trace per unit length;

h is the convection heat transfer coefficient in W/(m²K);

w is the width of the copper trace in m;

th is the thickness of the copper trace in m;

L is the total length of the trace in m;

T and T_∞ are the temperature of the outer layer of the copper volume and the environment, respectively;

ε is the emissivity of the copper trace, between 0.03 and 0.04;

σ is the Stefan-Boltzmann constant, with the value of 5.67 x 10⁻⁸ W/(m²K⁴);

ρ is the mass density of the copper trace, 8933 kg/m³;

c is the specific heat capacity of the copper trace, 385 J/(kgK); and

the star (*) denotes a product.

This approach works well for the panel PCBs with a dielectric separation of 0.8 mm for the FR-4 material and for copper conductor with a width of 4.252 mil or greater. We numerically evaluated our system for a 10-mil wide and 1-oz/ft² thick copper trace, as proposed in the design. We find that the temperature depends on the current through the copper trace as roughly a quadratic function. The initial condition for temperature is its background value, 27 C. Less than 1 A is required in order to raise the temperature to the process temperature of 62 C (actually, 0.3 A).

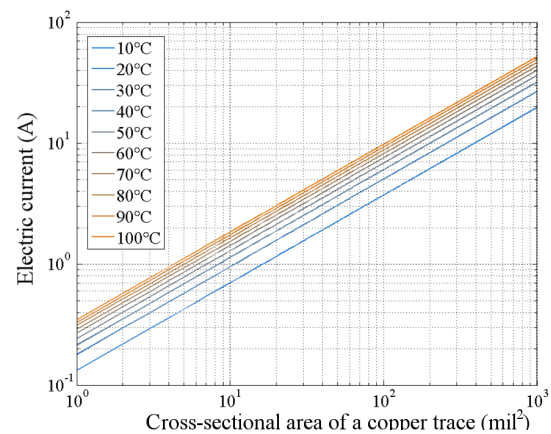


Fig. 2. Electrical current as a function of the cross-section of the copper trace with a 1-W source. The temperature increase is a parameter that varies from 10 C to 100 C in increments of 10 C.

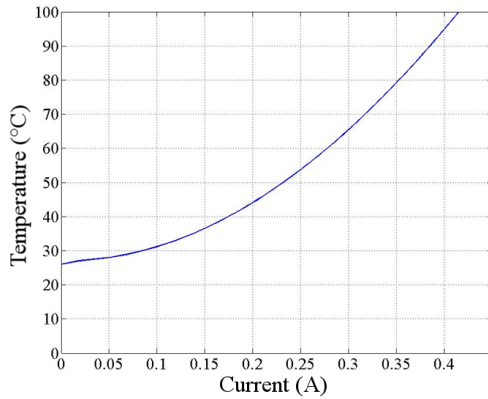


Fig. 3. Numerical evaluation of temperature vs current through the copper trace in the PCB.

To increase the temporal response of the system, we are increasing the heating power from 1 to 2 W. This design power was easily implemented in our device. Using larger power may damage the system because the temperature rise exceeds the recommended operating parameters for the electrical components. If using a lesser power source, the thermo-mechanical system may never reach the requisite temperature.

3. Simulations of the thermoelectric stage

A section of the copper trace, drawn in the ANSYS™ program, is shown in Fig. 4. The model was exported from an Eagle™ CAD PCB design tool and imported into the ANSYS™ simulation tool. This simulation program uses finite element theory for structures to predict their behavior and specifically, to determine the temperature distribution. With the calculated current density and with the parameters and materials already described, we find the temperature distribution in the copper trace versus time.

Figure 5 presents the temperature distribution on the copper trace for two specific times. The copper trace starts at a reference temperature (25 C) in the top part of the figure and remain relatively cold for 0.5 s. After a certain heating time, 2.5 s, the target temperature is achieved, which in this case is 62 C. At this temperature the DNA amplification takes place, and can be verified with process monitoring sensors.

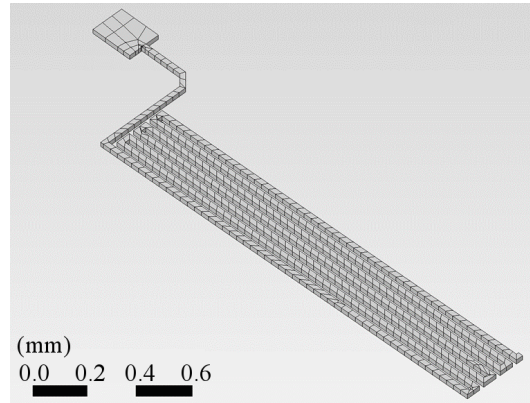


Fig. 4. Dynamic mesh of nodes of the copper trace. The mesh density increases in areas of interest.

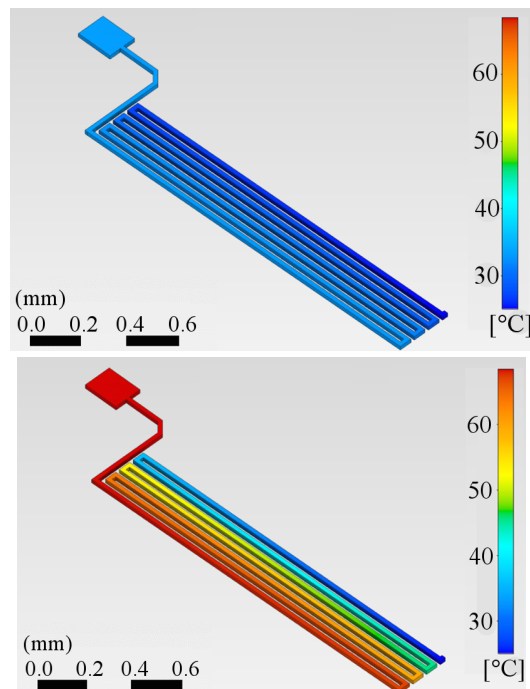


Fig. 5. The temperature distribution over the outside surface the copper trace for the heating current of 0.5 A at two times: upper, $t=0.5$ s; lower, $t=2.5$ s.

4. Design of thermal bed

The choice of the parameters obtained is passed to the PCB design program. The proposed design of the upper and lower layers can be seen in Fig. 6.

The thermal stage of the PCB has an effective area of 39.7 by 28.45 mm² where the thermal traces satisfy the design rule of 10-mil width, and 10-mil separation between traces.

The ground contacts outside the thermal stage provide the return path for electrical signals, serve as a conduit to dissipate the

generated heat, and to keep the temperature of the electronics within the nominal operating range. We designed the wider traces that control this stage to decrease the localized heat generation.

The central opening in the thermal bed is used in the cases where an external light source is required. The four holes near the perimeter of the card are position guides for the fluid

chamber, placed above it during the device use. The green pads on the right side are for a connector. It changes between alternate modes of temperature control.

The electronics and the associated control systems that govern the thermoelectric stage will be discussed in a separate publication. The photo of the temperature sensor mounted over the PCB is presented in Fig. 7.

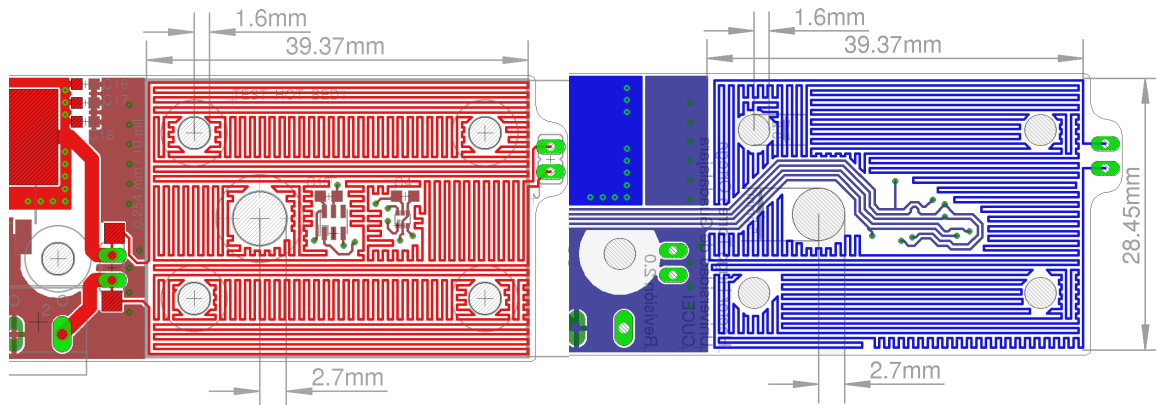


Fig. 6. Design layout of the copper traces in the upper (left) and lower (right) layer of the thermal bed stage, generated with the EAGLE™ CAD program.

5. Summary

The integrated circuit TMP102 was the sensor that was selected fulfilling the compatibility and resolution requirements, $\Delta T = 0.0625$ C. Its precision is 0.5 C, range of temperature operation from -25 C to 85 C, and its size 1.6 mm by 1.6 mm². Its depth is 12 bits.

This device has been build and tested thermally. Next, the complete Lab-On-Chip will be evaluated for its functional performance as a DNA amplifier.

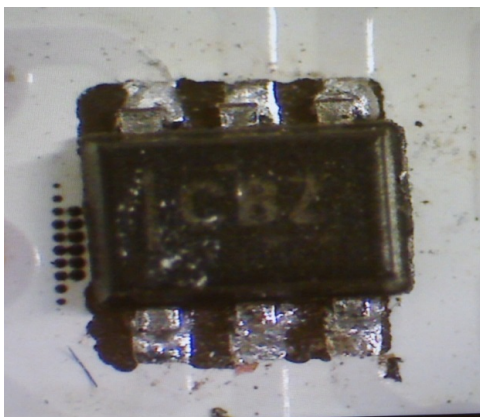


Fig. 7. Temperature sensor mounted over the PCB.

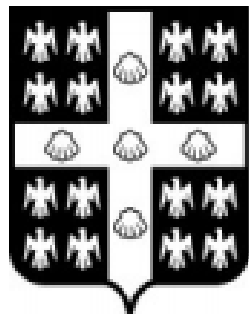
References

1. A. F. Collings and F. Caruso, "Biosensors: Recent advances," *Reports on Progress in Physics* **60**(11), 1397-1445 (1997).
2. E. A. Jamil, P. K. Sorger and K. F. Jensen, "Cells on chips," *Nature* **442**(7101), 403-411 (2006).
3. S. Dittrich, K. Tachikawa and A. Manz, "Micro total analysis systems. Latest advancements and trends," *Anal. Chem.* **78**(12), 3887-3908 (2006).
4. Y. Sun, X. Wang and K. Wang, "A Programmable Thermal Controlling Array for Microfluidic Lab-on-a-chip Systems," in *Proceedings of IEEE International Conference on Bioinformatics and Biomedical Engineering (IEEE, 2007)*, pp. 1230-1233.
5. Y. Zheng and M. Sawan, "Planar Microcoil Array Based Temperature-Controllable Lab-on-Chip Platform," *IEEE Transactions on Magnetics* **49**(10), 5236-5242 (2013).
6. P. Streit, J. Nestler, A. Shaporin, et al, "Thermal Design of Integrated Heating for Lab-on-a-Chip Systems," in *Proceedings of IEEE International Conference on Thermal, Mechanical and Multi-Physics Simulation and Experiments in Microelectronics and Microsystems (IEEE, 2016)*, pp. 1-6.
7. H. Torres-Ortega, M. Strojnik, G. Garcia-Torales, M. K. Scholl, "Design of Sample Chamber for DNA amplification at given temperature ($T = 62$ C)," elsewhere in these AITA proceedings.
8. H. Torres-Ortega, "Modelado de un Dispositivo Para Cuantificación de Amplificación de ADN (A device for Quantification of DNA Amplification)," *Doctoral Tesis, University Of Guadalajara, Guadalajara, Jalisco, Mexico* (2017).

Thermal Properties

AITA 2017

Québec City, Canada
September 27th - 29th, 2017



UNIVERSITÉ
LAVAL

WIND TUNNEL MEASUREMENTS OF LOCAL HEAT TRANSFER COEFFICIENTS AND LOCAL AIR TEMPERATURES IN AN URBAN STREET CANYON USING IR THERMOGRAPHY

J. Allegrini^{1,2}, D. Derome¹, J. Carmeliet^{1,2}

¹ Laboratory for Multiscale Studies in Building Physics, Empa, Überlandstrasse 129, 8600 Dübendorf, jonas.allegrini@empa.ch, dominique.derome@empa.ch, jan.carmeliet@empa.ch

² Chair of Building Physics, ETH Zürich, Stefano-Franscini-Platz 1, 8093 Zürich

Air temperatures in urban areas are higher due to the urban heat island effect, which can have a negative impact on comfort and health and energy demand of buildings. Solar and longwave radiation is absorbed on building and ground surfaces and increases the local air temperature due to convective heat transfer at the surfaces. This heat can most efficiently be removed by wind driven ventilation, which is not well understood for urban areas, especially for mixed convective cases. In this paper, we present a wind tunnel physical model, where we can measure the local convective heat transfer coefficients in a street canyon based on IR thermography. The local air temperatures are measured with IR thermography using a mesh placed inside the street canyon and the flow field in the same plane is measured with PIV (particle image velocimetry). The results of these measurements are used to improve the understanding of the local heat island formation and its mitigation.

Introduction

Air temperatures are normally higher in urban areas compared to rural areas due to the urban heat island effect. Due to densification and climate change, temperatures in cities will keep on increasing in the future. Another effect of climate change will be that the frequency and intensity of heat waves will increase. The urban heat island effect has an impact on the comfort and health of inhabitants of urban areas, and on the energy demand for heating and cooling of buildings. Urban heat island mitigation measures are needed to improve the outdoor and indoor thermal comfort and to decrease space cooling demands in buildings in summer. Heat can effectively be removed from urban areas by wind. Wind flows in urban areas are highly turbulent and form coherent structures. Shear layers are formed at building edges due to flow separation and they interact with the atmospheric boundary layer. A further

complexity is induced by buoyancy effects. These complex flow interactions and their impact on urban heat removal are until now not fully understood.

The primary objective of this study is to get insights in the complex heat removal processes in urban areas. Studies in literature mainly focus on flow structures to give insight in the wind driven heat removal (e.g. [1]), but heat fluxes cannot be determined directly from the flow fields of highly turbulent flows. Therefore we designed a scaled street canyon wind tunnel model, with which we can measure the temperature field and the local connective heat transfer at the building and ground surfaces, in addition to the air flow field as normally done in wind tunnels. One of the main heat sources in urban areas are the solar and longwave radiation exchanges, which are absorbed at building and ground surfaces and are transferred to the air by convective heat transfer. We use building models and ground surfaces consisting of aluminum panels whose

surface temperatures are controlled by heating elements. The aluminum is covered with a thin layer of epoxy that, due to its low conductivity, allows to establish temperature differences over the outside surface which are measured with high accuracy by infrared thermography. These temperature differences are used to determine the local convective heat transfer. The same technique was used by Meinders et al. [2] to determine the convective heat transfer coefficients of a cube. The measured convective heat transfer, on one hand, is used to study how the heat is removed from an urban street canyon. On the other hand, the same results are used for building energy simulations to get more accurate convective heat transfer coefficients (e.g. [3]) for buildings in urban areas. The air temperature distribution within the urban street canyon is measured by placing a non-conductive mesh in the plane of interest and acquiring its temperature by means of infrared thermography [4]. Finally the flow field is measured in the same plane with PIV (particle image velocimetry). The analysis of this extended data set will lead to a better understanding of urban heat island effects and the necessary mitigation measures. Further this data set can also be used to validate CFD (Computational Fluid Dynamics) simulations.

Configurations

A street canyon geometry is chosen to represent a typical urban area (Fig. 1). The two buildings forming the street canyon have different heights to avoid a strong shear layer, which separates the air volume between the buildings from the air flowing over the buildings. The wind direction is here normal to the street canyon axis, but other wind directions could later be studied. The wind is either flowing first over the taller or first over the lower building. The dimensions of the wind tunnel model and the wind speeds are chosen to reach Reynolds numbers between 4000 and 15000 to be in the Reynolds number independent flow regime. Upstream of the model, a series of barriers, spires and roughness elements ensures the

development of an atmospheric boundary layer. The heat removal process in urban areas strongly depends on the strength of buoyancy [5]. Therefore this study is conducted for different forced and mixed convective flow regimes (Richards number: 0 -7). To reach sufficiently high Richardson numbers to induce mixed convective flow regimes, surface temperatures up to 165 °C are needed. As mentioned above, the wind tunnel model is made out of aluminum plates, which are heated with electrical heating elements designed to reach such temperature. Furthermore, each surface can be heated individually and controlled to be at different temperatures if desired.

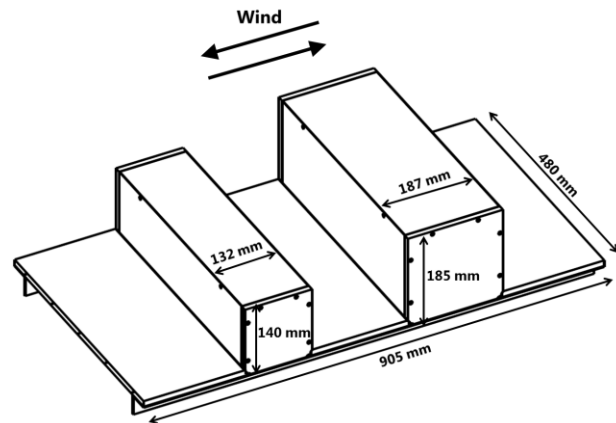


Fig. 1. Dimensions of the wind tunnel model.

Measurement Techniques

Convective Heat Transfer

The local heat fluxes at the building and ground surfaces are measured indirectly by measuring the surface temperatures at the inside and outside of the wind tunnel model. The inside surface temperatures are measured with thermocouples while the outside surface temperatures are measured with infrared thermography. The wind tunnel model consists of aluminum plates which are covered with a thin layer of epoxy with low thermal conductivity to get temperature differences at the outside surfaces of the wind tunnel model. Using aluminum plates heated with electrical heating elements ensures that the inside surface of epoxy can be kept at almost uniform and constant temperature. The conductive heat flux

in the epoxy layer and the radiative heat flux out of each surface can be computed through Finite Element Analysis knowing the exact thermal properties of the epoxy layer. This technique is described by Meinders et al. [2]. Fig. 2 shows a sketch of the setup, which is used to measure the convective heat transfer, which is measured on the building walls, building roofs and ground surfaces. Two infrared cameras (Optris PI 640) are installed on the ceiling for the wind tunnel to be able to measure the convective heat fluxes of all heated surfaces simultaneously.

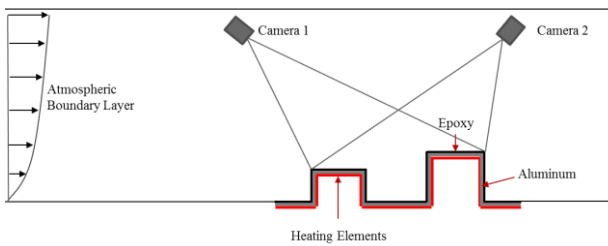


Fig. 2. Sketch of the setup to measure the convective heat fluxes.

Air temperatures

The air temperature is measured in the symmetry plane of the street canyon. In the same plane also, the flow field is measured (see below). To measure the air temperatures, a mesh is installed in the street canyon. This mesh has a low thermal conductivity to assure that the mesh is only heated by convective heat transfer from the air and not by heat conduction. To improve the accuracy of the air temperature measurements small non-conductive patches are glued on the mesh, where temperatures are measured with infrared thermography (Fig. 3). At two locations, the temperature is also measured with thermocouples. One location is used for the calibration of the infrared camera and the second location is used to evaluate the accuracy of the measurements. With this measurement technique, the air temperatures can be measured with a high spatial resolution in one plane.

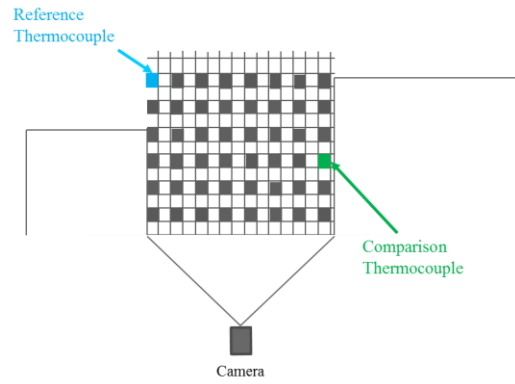


Fig. 3. Sketch of the setup to measure the local air temperatures.

Flow Fields

The flow field is measured with PIV (particle image velocimetry) in the same plane as the air temperatures. The measured velocity fields have therefore a similar spatial resolution as the air temperature measurements and therefore heat fluxes can be determined. A stereoscopic setup with two PIV-cameras is used to measure all three velocity components in the same plane.

Results

Fig.4 shows the measured air temperatures for a fully buoyant and a more forced convective flow regime. Here only the windward wall of the street canyon was heated to 110 °C. The high spatial resolution of the applied measurement technique can be seen.

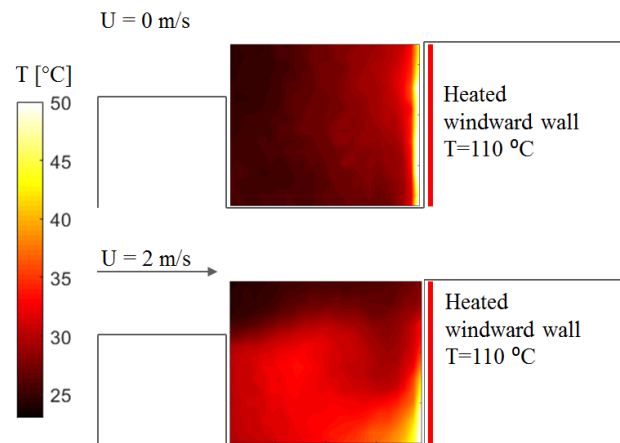


Fig. 4. Measured air temperatures for two cases with different Reynolds numbers.

Further the results show that the air temperatures are lower for the fully buoyant compared to the more forced convective case. For the more forced convective case, the heat is trapped within the vortex, which is formed in the center of the street canyon, while more heat is removed due to buoyancy for the fully buoyant case.

The vortex structure in the center of the street canyon can be seen in Fig. 5 for an isothermal case. The streamlines show the formation of a vortex, which is driven by the air flowing over the two buildings forming the street canyon. The same flow structure can also be found for the more forced convective case in Fig. 4. Comparing the results of the two figures shows that most of the cold air is flowing over the street canyon while only small amounts of cold air enter the street canyon and are therefore available to reduce the temperature inside the street canyon.

In terms of surface temperature measurements, the set-up is being tested and calibrated. We will be in position to present all up-dated measurement at the conference. Using the whole datasets, the local convective heat transfer coefficients over all the surfaces of the physical model can be determined.

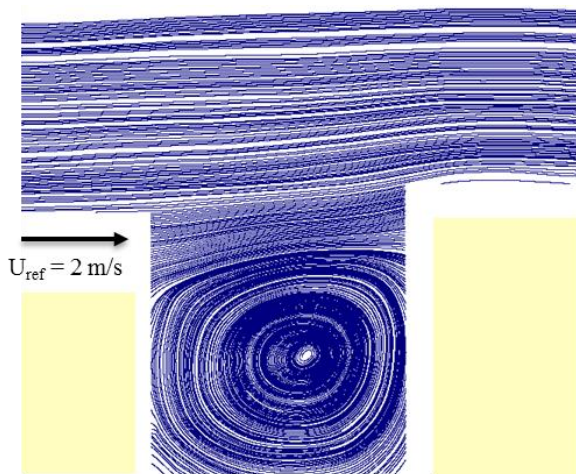


Fig. 5. Streamlines determined from PIV measurements.

Conclusion

In this paper a measurement campaign is presented where, in addition to the air flow fields, the air temperature fields and convective

heat fluxes are measured for a street canyon geometry. The results help to improve the understanding of heat removal from urban areas and therefore to develop urban heat island mitigation measures. Infrared thermography is used to measure all surfaces of the canyon streets. In addition, infrared thermography is used to indirectly measure the air temperature by implanting a mesh in the street canyon. From this extensive dataset, the convective heat transfer at the urban surfaces can be determined. With these measurement techniques it is possible to measure the air temperatures and convective heat transfer coefficients with a very high spatial resolution for a wide range of surface temperature, wind velocities and turbulence levels.

The results show a strong correlation of the measured temperature field with the measured flow field. The results are highly needed to understand in the interactions at play in the phenomenon of urban heat island effect.

References

1. J. Allegrini, V. Dorer, J. Carmeliet. Wind tunnel measurements of buoyant flows in street canyons, *Building and Environment*, 59, pp. 315-326, 2013.
2. E.R. Meinders, K. Hanjalic, R.J. Martinuzzi. Experimental study of the local convection heat transfer from a wall-mounted cube in turbulent channel flow. *Journal of Heat Transfer*, 121, pp. 564–573, 1999.
3. J. Allegrini, V. Dorer, J. Carmeliet J. Analysis of convective heat transfer at building facades in street canyons and its influence on the predictions of space cooling demand in buildings. *Journal of Wind Engineering and Industrial Aerodynamics*, 104–106, pp. 464–473, 2012.
4. M.B. Dufour. Quantification of air leaks through the building envelope using infrared thermography, Master thesis, Concordia University, Montreal, Canada, 2005.
5. J. Allegrini, V. Dorer, J. Carmeliet J. Coupled CFD, radiation and building energy model for studying heat fluxes in an urban environment with generic building configurations. *Sustainable Cities and Society*, 19, pp. 385-394, 2015.

In-plane and through-plane laser flash measurements of thermal diffusivity degradation induced by heavy ion irradiation in thin graphite samples

A. Prosvetov^{1,2}, C. Trautmann^{1,2}, M. Tomut¹

¹ GSI Helmholtz Center for Heavy Ion Research, Planckstr.1, 64291 Darmstadt, Germany, a.prosvetov@gsi.de

² Technische Universität Darmstadt, Alarich-Weiss-Straße 2, 64287 Darmstadt, Germany

Thermal diffusivity is one of the most important characteristics of material exposed to extreme radiation conditions. Components of particle accelerators or nuclear reactors have to withstand the deposition of the highest energy densities. The functional materials involved have to efficiently dissipate energy in order to avoid overheating or even failure. Radiation-induced degradation of thermal properties of graphite is studied using laser flash analysis in planar and transversal orientation. Isotropic polycrystalline graphite samples were irradiated with approximately 1-GeV Au ions of 60-70 μm range. The empirical dependence of thermal diffusivity on the thickness was obtained for thermally thin samples. The diffusivity degradation of the irradiated graphite estimated via thermal resistance formalism of 2 layer sample shows the similar trend as for in plane measurements.

Introduction

The development of new high-power ion accelerators and nuclear reactors requires materials which guarantee high reliability under extreme radiation environments. Graphite is considered as one of the best candidates for such applications because of its resistance to high temperatures, thermal and mechanical stresses, as well as low activation by the beam. However, for application in particle accelerators, the exposure to ion beams may cause structural defects and phase changes finally causing degradation of the initially good thermo-mechanical properties [1], [2].

When high-energy ions hit a target, a large amount of energy is deposited within a small volume and a short time interval, resulting in fast heating of the material. The efficiency how this heat is dissipated is determined by the thermal diffusivity and conductivity of a given material. For reliable application, it is of great importance to investigate and quantify the degradation of these properties under ion beam exposure.

Additional challenge in studying the radiation induced defects is the microscopic scale of the investigated system. For ions in the MeV to GeV energy regime, each ion produces a cylindrical damaged region that has a length of few tens of microns and a radius of several nm. The material we tested typically consists of the thin irradiated layer (in our case $\sim 60 \mu\text{m}$) and the non-irradiated substrate. With increasing exposure to the beam, the properties of the samples continuously change from pristine to homogeneously damage at high accumulated ion fluences, when ions tracks start to overlap.

In this work in-plane and through-plane laser flash analysis were applied to measure the thermal diffusivity degradation of polycrystalline graphite irradiated with 950 and 1160 MeV Au ions.

Experimental

Polycrystalline graphite samples were cut and lapped to discs of 10 and 20 mm in diameter and thicknesses of 500 and 50 μm , respectively. The density of the material is

1.84 g/cm³ and the average grain size equals 8 μm. The samples were irradiated with 950 and 1160 MeV Au ions at the linear accelerator UNILAC of the GSI Helmholtzzentrum (Darmstadt, Germany). According to the SRIM-2010 code, the range of the ions in graphite is 57 μm and 68 μm, respectively, while the stopping power is almost the same for both cases and equals 21 keV/nm [3]. 50-μm thick discs were completely penetrated by the ion beam whereas in the case of the thicker samples, the ion beam stopped at a depth corresponding to the range. This leads to a 2 layer system consisting of a thin irradiated layer on top of a pristine graphite substrate.

In-plane and through-plane thermal diffusivity measurements were performed on LFA427 by NETZSCH at 20°C. The laser wavelength was 1064 nm and the pulse length equaled 0.3 ms. Laser flash analysis as common method for the estimation of the thermal diffusivity of a material was originally developed by Parker et al [4]. For thin and high conductive materials the in plane LFA was introduced in [5].

Results and discussion

As graphite has high thermal diffusivity (~70-85 mm²/s depending on the production process), graphite samples of thickness less than 1 mm show a deviation of the through-plane measured values from the bulk material data. In order to quantify this thickness effect, the thermal diffusivity of thin Cu, Al and Ti samples was measured as a function of their thickness varying between 0.4 and 2.6 mm (Fig.1).

The evolution of the thermal conductivity with increasing sample thickness was fit (dashed line) by a function (1) used in the following to extrapolate the measured values of thin graphite samples to bulk values.

$$\alpha_{meas.} = \alpha_{bulk} \cdot \left(1 - \frac{1}{1 + \left(\frac{l}{l_0}\right)^p} \right) \quad (1)$$

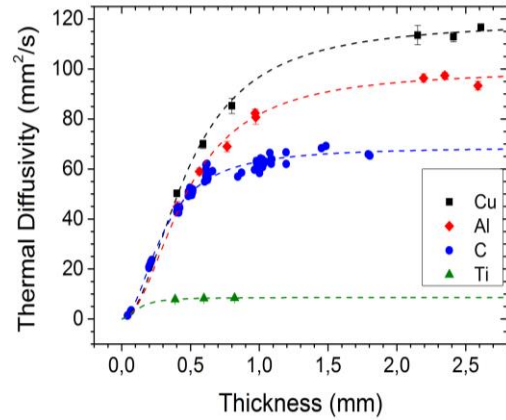


Fig. 1. Through-plane thermal diffusivity as a function of the sample thickness for Cu, Al, C and Ti. Rear and front surfaces of the metal samples were coated with 100-150 μg/cm² of carbon.

Here α_{bulk} and l_0 are free parameters, and p equals 2 for all curves.

In the case of the thick samples, a two-layer system of the irradiated and pristine part of the sample was considered in terms of thermal resistance $R_{th}=l/\lambda$, where l is the thickness of the layer and λ is its thermal conductivity. Assuming that the density and specific heat of graphite stay constant during irradiation, one can estimate the thermal diffusivity α of the irradiated layer using equation (2):

$$\alpha_{irr} = \frac{l_{irr}}{\frac{l_{total}}{\alpha_{eff}} - \frac{l_{total} - l_{irr}}{\alpha_{pristine}}} \quad (2)$$

where the thickness of the irradiated layer l_{irr} equals the Au ion range. The effective thermal diffusivity α_{eff} is the measured diffusivity of the entire sample.

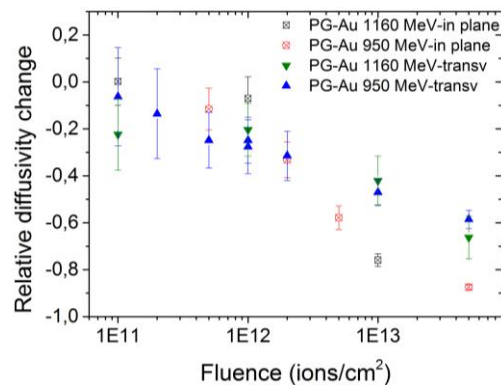


Fig. 2. Relative change of the thermal diffusivity (compared to virgin graphite) as a function of applied ion fluence for in-planar and through-plane measurements.

The in-plane LFA measurements of the irradiated graphite samples show an exponential decay of the thermal diffusivity with increasing ion fluence. The through-plane estimations demonstrate a similar behavior, however the drop is not as pronounced as for the in-plane setting (Fig. 2).

Conclusion

The irradiation of polycrystalline graphite with swift heavy ions leads to a significant degradation of the thermal diffusivity. Within the tested fluence regime, the in-plane LFA measurements show a continuous drop of the thermal diffusivity to approx. 15% of the initial values. By applying the empirical thickness correction function a similar trend is obtained for the two-layer through-plane measurements of thin samples.

References

- [1] S. Fernandes, F. Pellemoine, M. Tomut, M. Avilov, M. Bender, M. Boulesteix, M. Krause, W. Mittig, M. Schein, D. Severin, and C. Trautmann, “In-situ electric resistance measurements and annealing effects of graphite exposed to swift heavy ions,” *Nucl. Instruments Methods Phys. Res. Sect. B Beam Interact. with Mater. Atoms*, vol. 314, pp. 125–129, 2013.
- [2] C. Hubert, K. O. Voss, M. Bender, K. Kupka, A. Romanenko, D. Severin, C. Trautmann, and M. Tomut, “Swift heavy ion-induced radiation damage in isotropic graphite studied by micro-indentation and in-situ electrical resistivity,” *Nucl. Instruments Methods Phys. Res. Sect. B Beam Interact. with Mater. Atoms*, vol. 365, pp. 509–514, 2015.
- [3] J. F. Ziegler, M. D. Ziegler, and J. P. Biersack, “SRIM – The stopping and range of ions in matter (2010),” *Nucl. Instruments Methods Phys. Res. Sect. B Beam Interact. with Mater. Atoms*, vol. 268, no. 11, pp. 1818–1823, 2010.
- [4] W. J. Parker, R. J. Jenkins, C. P. Butler, and G. L. Abbott, “Flash method of determining thermal diffusivity, heat capacity, and thermal conductivity,” *J. Appl. Phys.*, vol. 32, no. 9, pp. 1679–1684, 1961.
- [5] A. B. Donaldson and R. E. Taylor, “Thermal diffusivity measurement by a radial heat flow method,” *J. Appl. Phys.*, vol. 46, no. 10, pp. 4584–4589, 1975.

FLAME INFRARED RADIATION MEASUREMENT AT A MODEL GAS TURBINE COMBUSTOR

S. Park¹, Y. B. Ji², S. V. Ekkad³

¹ Virginia Tech, Blacksburg, Virginia, USA, suhyeon.park@vt.edu

² Shanghai Jiao Tong University, Shanghai, China, ybjj@vt.edu

³ Virginia Tech, Blacksburg, Virginia, USA, sekkad@vt.edu

This paper demonstrates a non-intrusive technique to measure infrared radiation of swirl stabilized flame in an optical model gas turbine combustor. Schott KG glass filtering enabled flame measurement through a quartz combustor wall within wavelength of 1-2.7 μm . Initial measurements have shown feasibility of using this technique. The infrared radiation image was reconstructed with Abel transformation. Infrared radiant energy density was spatially resolved, and inner structures of the reacting swirl flow were identified. This novel technique will be useful to investigate flow structures and thermal properties in gas turbine combustors and other high temperature flows.

Introduction

The study of flow field characteristics in reacting flow in a harsh environment at high temperatures is very challenging. Experimental data are important in combustor studies especially for turbulent reacting flows, due to their inherent complexities. Numerical analysis of complex turbulent reacting flows is technically difficult, and the accuracy of characterizing such flows is limited compared to non-reacting cases. Measuring infrared emission of reacting flow with an infrared thermographic camera can provide information about thermal properties inside combustor-simulator under reacting conditions.

Measuring infrared radiation is a non-intrusive time resolved technique which does not affect the flow field compared to a probe based technique. The proposed experimental setup is relatively simple and inexpensive compared to other optical measurement techniques such as laser induced fluorescence (LIF), Rayleigh scattering, Raman scattering, thermographic phosphor etc. [1-5]. Infrared measurements of flame are available in the literature to correlate with temperature for laminar flames and sooty

diffusion flames [6-10]. Applying these techniques to turbulent flows within swirl stabilized gas turbine combustor is the focus of this work.

Optical windows are necessary to measure the reacting flows under realistic condition. Quartz glass (fused silica) for the window has high transmissivity in visible light range, however the transmissivity is low in the infrared range. Zinc-Selenide (ZnSe) is infrared transmissive window material, but it is significantly expensive compared to quartz glass. The proposed technique in this paper utilizes quartz glass wall as a combustor liner. KG glass filters were installed in front of the IR camera lens to measure infrared radiation from the reacting flows. A similar technique was recently developed for wall temperature and heat transfer measurement on quartz liner using the same combustor test rig [11].

Measurement

The measurements were conducted on the model optical combustor (Figure 1) operated at Advanced Propulsion and Power Laboratory at Virginia Tech. The combustor is equipped with a premixed swirl fuel nozzle

made by Solar Turbines Inc. The test section is a single-can type combustor model, made of quartz glass to ensure visibility for both regular visual cameras and infrared cameras. The entire combustor liner wall is made with quartz glass tube (GE 214) with full optical access from its sides.

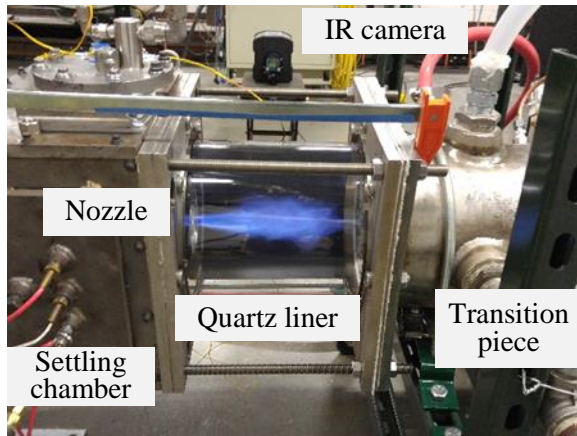


Figure 1. Optical gas turbine combustor test section showing a pilot flame.

Air and fuel (methane) are mixed in the fuel nozzle before it enters the test section. As air passes through the annular main nozzle, vanes generate swirl in the flow. The swirl flow from the main nozzle stabilizes a conical main flame with central recirculation and corner recirculation flows. A pilot flame at the center ensures flame stability. Air and fuel flow at the pilot is a few percent of the total flow.

The IR camera measured the signal from one side of the test section through the quartz glass liner. A FLIR SC6700 camera was used with a 3 mm thick Schott KG2 filter (Figure 2). The KG glass is a heat absorbing filter and can also be an optical short pass filter. The wavelength range of measurement was determined by the response range of infrared camera and absorption curve of quartz material. The camera sensor responds to infrared signal from a wavelength range of 1-5 μm . Infrared signals with wavelengths longer than 2.8 μm are blocked by the KG filter. Transmittance curves accounting for the material absorption and surface reflection are shown in Figure 3. Material property data was obtained from [12]. This filtering enables the camera to

measure the IR signal through the quartz glass window. Fused silica material typically does not show resonance bands at near infrared, but OH band of small amount of water content (less than 5 ppm in GE 214 quartz) emits infrared longer than 2.8 μm at high temperature [13, 14]. When the long wave quartz radiation is sufficiently blocked, the quartz is transparent in the camera view. Thus the flame physically contained in the combustor can be measured without an optical barrier in the measured wavelengths. Another advantage of using KG filter is to prevent saturation of camera sensor by reducing infrared signal strength.

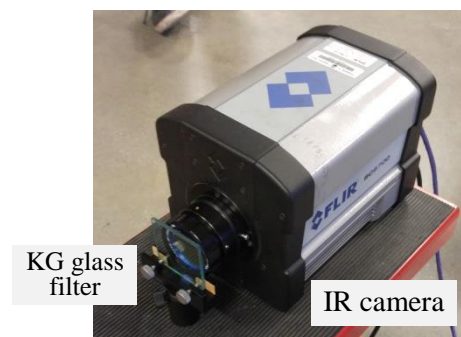


Figure 2. Thermographic camera and KG glass filter for flame measurement

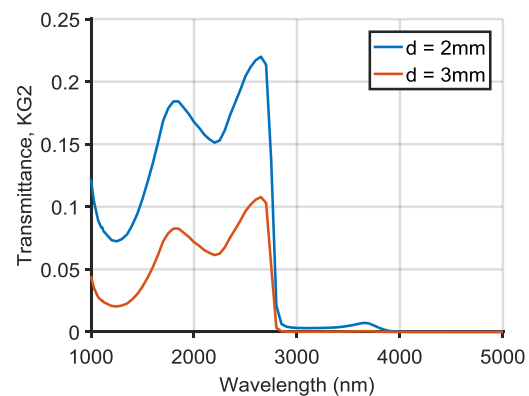


Figure 3. Transmission curves of KG2 glass filters with different thicknesses. [12].

Sources of optical radiation from chemically reacting flow can be soot particles or excited molecules or radicals [15]. Blackbody radiation from soot particle dominates in a rich flame with high carbon ratio in the fuel. For a land-based power generation gas turbine engine, lean and stable flame is required for higher performance and lower pollutant emission. Light radiations from

molecules or radicals are in narrow bands, in a lean flame. Strong bands are commonly observed in ultraviolet and visible ranges, which are out of the measurement range of the infrared camera. The source of the infrared seems to be H₂O or CO₂ bands at the measurement range.

Proof-of-concept result

A proof of concept measurement was conducted with a propane torch flame. TS-1500 low profile torch was used to form a flame. The flame was fuel lean without visible soot radiation. The camera measured infrared radiation from the flame through a quartz glass. Frame rate was 5 Hz and the data was averaged for 30 seconds. Infrared radiation from the flame dominated over radiation signals from surfaces and weak radiation was measured at metal part of the torch. Measured infrared emission and structures inside flame are shown in Figure 4. The filter reduced intensity of infrared radiation received by the camera. Measured infrared radiation distribution represents distribution of high temperature combustion product.

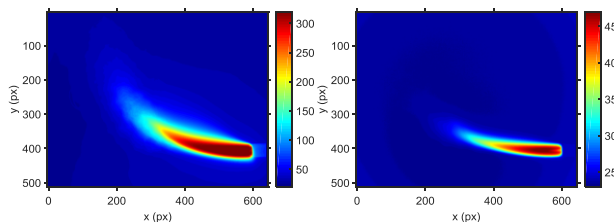


Figure 4 Proof of concept measurement with propane torch flame; (left) without filter (right) with KG2 filter. Color scales represent measured infrared intensity (a.u.).

Combustor flame measurement

Figure 5 shows a typical RGB camera image of a flame in the model combustor rig. Flow direction is left to right. The fuel nozzle is installed at the center of a round dome plate shown on the left side. The main flame is anchored at the hub of the fuel nozzle as a cone. Burnt gas enters a transition zone on the right side, and then exits the combustor.

Measured infrared radiation of the reacting flow in the combustor is shown in

Figure 6. Data was measured at 7.5 Hz rate for 60 s duration. Length scale was normalized with the fuel nozzle diameter (D_N). Flow characteristics observed in the infrared data agree with the Fig. 5 in general. The main flame was observed as a cone, and strong intensity was radiated from the central recirculation zone. Radiation from corner recirculation zone was relatively weaker as expected from the characteristics of swirl flow.



Figure 5. RGB image of flame luminosity showing a swirl stabilized flame inside the combustor.

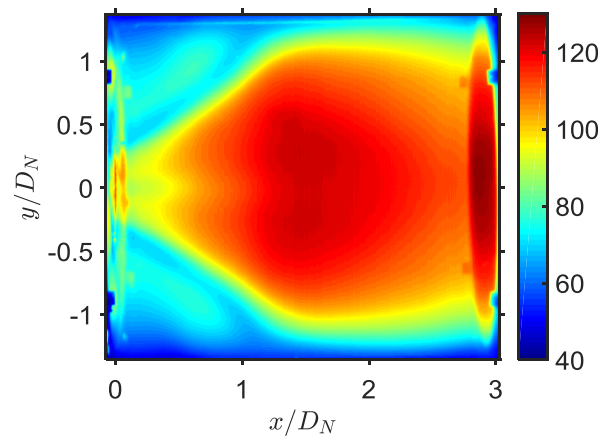


Figure 6. Averaged projection image of infrared radiation from reacting flow at the combustor Color scales represent measured infrared intensity (a.u.).

There are several features observed from the infrared measurement that could not be seen in flame luminosity image in visible light. Two shear layers were observed from the infrared measurement. The layer between corner recirculation and incoming cold jet ($x/D_N \sim 0.5$, $x/D_N \sim \pm 0.8$) was observed only in the infrared measurement and not visible in the regular image. Between those layers, fresh fuel air mixture incoming from the nozzle is shown as low signal gaps. Another relatively low intensity region was captured at the center near

the fuel nozzle ($x \sim 0, y \sim 0$) due to fuel air mixture injected through a circular pilot nozzle at the center of the fuel nozzle hub.

Abel transformation

Assuming axially symmetric geometry, the data was further analyzed with a tomographic reconstruction. Abel transformation is useful technique to convert line-of-sight averaged projection images from axisymmetric objects to cross-section distributions at central axis. Similar techniques were applied to infrared measurements of various laminar flames [6, 8]. In this study, averaged symmetric image of a turbulent flame was reconstructed with Abel inversion.

The combustor is divided into concentric layers of different radiance densities (X_i). A matrix (\mathbf{A}) was obtained from path length segments ($l_{i,j}$) and radial location (r_i). Multiplication of inverse matrix to the line-of-sight averaged projection (\mathbf{P}) gives radial distribution of radiant energy density (\mathbf{X}).

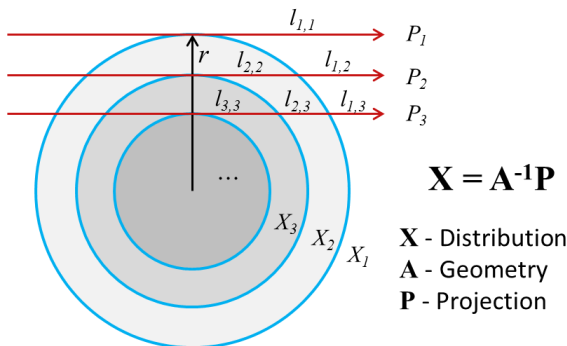


Figure 7 Principle of Abel transformation.

The reconstructed image shown on Figure 8 shows the infrared radiant energy density in radial axis. The inner structures of swirl flame are more distinct compared to the projection image. The most interesting observation is the flame front between incoming fresh mixture and central recirculation zone. It is shown as a high gradient curve starting from $x \sim 0, r/D_N \sim 0.3$ towards upper right direction, until impingement on the liner wall at $x/D_N \sim 1.2, r/D_N \sim 1.4$. The flame front divides the image into two zones, one with low radiation that

includes incoming main jet and corner recirculation zone, and the other with high radiation at central recirculation zone. The highest density region was observed near the nozzle and lowest was at incoming fresh mixture at main jet. The high density region was located at where heat is transported from the flame front. The radiant energy density from the flame decreases as the flow moves to the downstream. On the other hand, total radiant energy increases due to increase in total volume along the radial axis. The density at the corner recirculation zone is very low, but higher than the incoming jet. Structure of the pilot jet at the center of the flame ($r \sim 0$) is shown better than the projection.

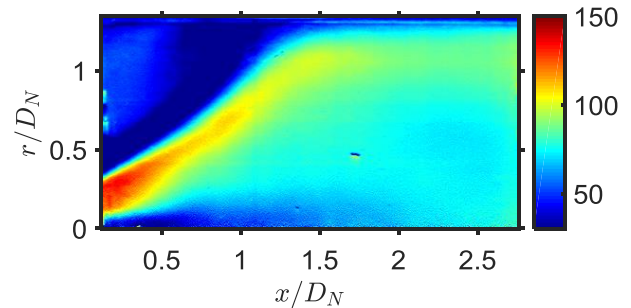


Figure 8. Reconstructed infrared radiant energy density (a.u.).

Further comparison of the infrared radiant energy density with other diagnostic methods will help better understanding of the infrared diagnostics of turbulent reacting flow.

Conclusion

A concept of novel infrared radiation measurement was demonstrated for a model gas turbine combustor. Initial experiments showed the feasibility of the technique and potential value of similar measurements for combustor systems. Flow characteristics in the infrared measurement agreed with flame luminosity observation. Features including double shear layers, fresh mixture flows could only be captured with infrared measurement.

Abel transformation was applied to the measured projection. Infrared radiant energy distribution was spatially resolved, and inner structures of the reacting swirl flow could be

identified. The high density region was observed near flame front where recirculated flow is mixed with fresh mixture. Area of incoming mixture of main jet showed lowest density.

Future study will focus on the quantification of the infrared measurement and comparison with other types of diagnostic techniques. The optical emissivity of the partially transparent flow should be quantified to correlate the infrared measurement to other thermal properties such as temperature distribution. Long term goal of the infrared technique is to measure thermal properties in the flow. If quantitative correlation can be established, the infrared technique will be more useful in the gas turbine research and other high temperature harsh environments.

References

1. P. Weigand, W. Meier, X. R. Duan, W. Stricker, and M. Aigner, "Investigations of swirl flames in a gas turbine model combustor," *Combustion and Flame*, vol. 144, no. 1–2, pp. 205–224, Jan. 2006.
2. U. Stopper, W. Meier, R. Sadanandan, M. Stöhr, M. Aigner, and G. Bulat, "Experimental study of industrial gas turbine flames including quantification of pressure influence on flow field, fuel/air premixing and flame shape," *Combustion and Flame*, vol. 160, no. 10, pp. 2103–2118, Oct. 2013.
3. R. Giezendanner-Thoben, U. Meier, W. Meier, J. Heinze, and M. Aigner, "Phase-locked two-line OH planar laser-induced fluorescence thermometry in a pulsating gas turbine model combustor at atmospheric pressure," *Applied optics*, vol. 44, no. 31, pp. 6565–6577, 2005.
4. R. L. Gordon, A. R. Masri, and E. Mastorakos, "Simultaneous Rayleigh temperature, OH- and CH₂O-LIF imaging of methane jets in a vitiated coflow," *Combustion and Flame*, vol. 155, no. 1–2, pp. 181–195, Oct. 2008.
5. M. Aldén, A. Omrane, M. Richter, and G. Särner, "Thermographic phosphors for thermometry: A survey of combustion applications," *Progress in Energy and Combustion Science*, vol. 37, no. 4, pp. 422–461, Aug. 2011.
6. H. Uchiyama, M. Nakajima, and S. Yuta, "Measurement of flame temperature distribution by IR emission computed tomography," *Applied optics*, vol. 24, no. 23, pp. 4111–4116, 1985.
7. Y. R. Sivathanu and G. M. Faeth, "Infrared radiation statistics of nonluminous turbulent diffusion flames," *Ann Arbor*, vol. 1050, pp. 48109–2140, 1991.
8. C. Jir-Ming and Y. Jun-Hsien, "The measurement of open propane flame temperature using infrared technique," *Journal of Quantitative Spectroscopy and Radiative Transfer*, vol. 56, no. 1, pp. 133–144, 1996.
9. S. K. Jha, S. Fernando, and S. D. F. To, "Flame temperature analysis of biodiesel blends and components," *Fuel*, vol. 87, no. 10–11, pp. 1982–1988, Aug. 2008.
10. G. Parent, Z. Acem, S. Lechêne, and P. Boulet, "Measurement of infrared radiation emitted by the flame of a vegetation fire," *International Journal of Thermal Sciences*, vol. 49, no. 3, pp. 555–562, Mar. 2010.
11. David Gomez-Ramirez, "Heat Transfer and Flow Measurements in an Atmospheric Lean Pre-Mixed Combustor," Virginia Tech, 2016.
12. http://www.schott.com/advanced_optics/english/products/optical-components/optical-filters/optical-filter-glass/index.html
13. A. V. Dvurechenskii, V. A. Petrov, V. Y. Reznik, V. V. Kornev, and G. Y. Levenfel'd, "Investigation of spectral absorption coefficient of KI and KV quartz glasses in IR region to upper temperature limit," *Journal of Applied Spectroscopy*, vol. 31, no. 3, pp. 1157–1160, 1979.
14. E. C. Beder, C. D. Bass, and W. L. Shackelford, "Transmissivity and Absorption of Fused Quartz Between 0.22 μ and 3.5 μ from Room Temperature to 1500° C," *Applied Optics*, vol. 10, no. 10, pp. 2263–2268, 1971.
15. R. O. Buckius and C. L. Tien, "Infrared flame radiation," *International Journal of Heat and Mass Transfer*, vol. 20, no. 2, pp. 93–106, 1977.

Optical temperature measurement of the rotating plate in PVD system

F. Montagner¹, S. Deambrosis¹, E. Miorin¹, G. Ferrarini^{2*}, P. Bison²

¹ CNR-ICMATE, C.so Stati Uniti 4, 35127 Padova, Italy

^{2*} CNR-ITC, C.so Stati Uniti 4, 35127 Padova, Italy

^{1*} Tel: +39-049-829-5722, E-mail: giovanni.ferrarini@itc.cnr.it

In this paper IR thermography is used to measure the temperature of a rotating sample holder (a circular plate) inside a vacuum chamber of a PVD system, used to coat specimens that are laid on the plate. The plate temperature is paramount for the correct deposition process and until now, it was determined by a thermocouple. Looking through an IR transparent window, IR thermography allows measuring the temperature field of the plate surface and accounting for its uniformity.

Introduction

A Physical Vapour Deposition (PVD) system is utilized to deposit thin films on different substrates (see Figure 1).

The sample holder consists in a circular plate made of Inconel, with diameter of 125 mm and thickness of 4 mm.



Fig. 1. PVD apparatus.

The specimen on which the film should be deposited (i.e. the substrate) is placed on the plate that rotates during the deposition process to improve homogeneity. The chamber is evacuated and the sputtering steps start.

The temperature of the plate is very important to obtain good quality thin films. On this purpose, the plate is heated by a heat flux generated by a system of halogen lamps. The temperature of the plate has always been controlled and measured by a thermocouple. In order to achieve a better temperature monitoring, a SnZn windows has been installed in the PVD vacuum chamber, which allows looking at the plate surface by an IR camera.

IR thermography

In order to evaluate correctly the temperature measurement in a range of temperature between 200 to 500 °C a calibration process has been carried out. It consisted in heating a sample of Al₂O₃ with an electrical heater and comparing the temperature obtained by a thermocouple with the one measured by the thermographic camera. The camera used in this case is a FLIR SC660, equipped with a microbolometric detector in the range between 8 and 14 μm, producing an image of 640 by 480 pixels. The picture of the calibration setup is shown in Figure 2.

Experiments

IR thermography is finally utilised to observe the alumina specimen placed on the rotating sample holder, through the ZnSn window. The lamps heating the plate are switched on and supplied with current until the nominal set point is reached. At the equilibrium an IR image is captured as shown in Figure 4, where the apparent temperature on top of the alumina sample is 280 °C. The apparent temperature of the rotating plate is quite inhomogeneous due to the different material deposited on it (just notice the highest value in the scale reaches 400 °C).

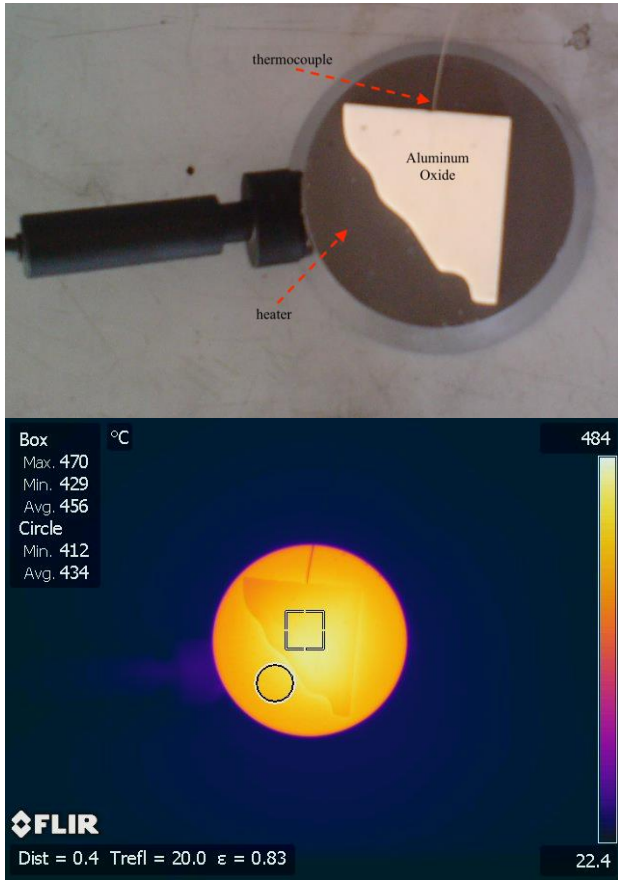


Fig. 2. Experimental setup for calibration of the IR camera (top) and corresponding IR image (bottom).

In the following Figure 3 the calibration line is shown. It allows to convert the measure obtained with the IR camera to the right temperature obtained with the thermocouple in contact with the sample, taking into account the possible problem of emissivity [1,2] and its variation with temperature.

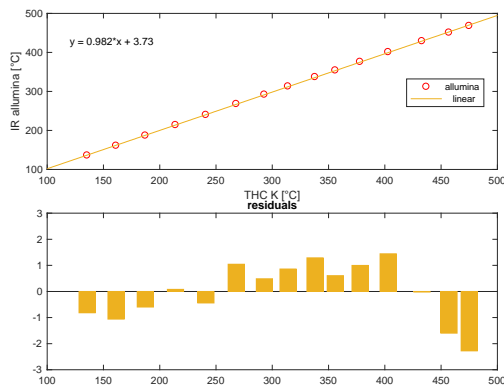


Fig. 3. Calibration line connecting the Thermocouple measurement with that obtained by IR thermography.

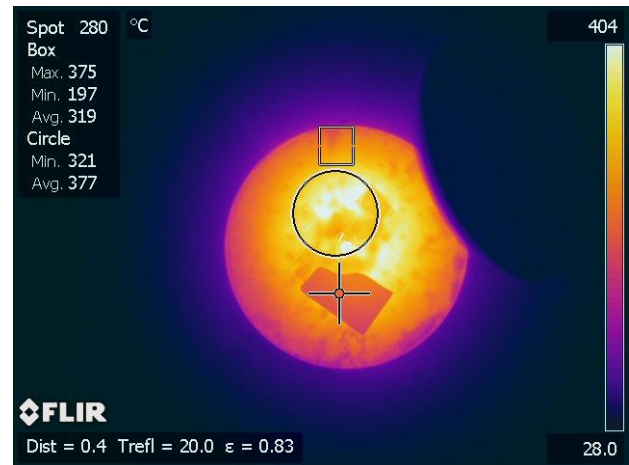


Fig. 4. IR image of the circular sample holder heated from below by a set of halogen lamps. The thermographic camera looks at the plate through a ZnSn window as the PVD chamber is evacuated. The apparent temperature on top of the alumina sample is 280 °C. The apparent temperature on the plate is quite inhomogeneous due to the different coating materials covering the sample holder.

Conclusions

The thermographic camera evidenced that the sample holder temperature is generally below the one measured by the thermocouple. This is an important achievement, which lead to improve the heater system and the temperature control as well in order to obtain better quality depositions.

References

1. R.P. Madding. Emissivity measurement and temperature correction accuracy considerations, volume 3700 of Proceedings of SPIE. SPIE, 1999.
2. Bison, P., Bortolin, A., Cadelano, G., Ferrarini, G., Grinzato, E., Emissivity measurement of semitransparent textiles, (2012) Advances in Optical Technologies, art. no. 373926.

Monte Carlo Ray-Trace Diffraction Based On the Huygens-Fresnel Principle

J. R. Mahan¹, N. Q. Vinh², Nazia B. Munir³, Vinh X. Ho⁴

¹ Department of Mechanical Engineering, Virginia Polytechnic Institute and State University, Blacksburg, VA 24061 USA, jrmahan@vt.edu

² Department of Physics, Virginia Polytechnic Institute and State University, Blacksburg, VA 24061 USA, vinh@vt.edu

³ Department of Mechanical Engineering, Virginia Polytechnic Institute and State University, Blacksburg, VA 24061 USA, nmunir@vt.edu

⁴ Department of Physics, Virginia Polytechnic Institute and State University, Blacksburg, VA 24061 USA, vinhxo1@vt.edu

The goal of this effort is to establish the conditions and limits under which the Huygens-Fresnel principle accurately describes diffraction in the Monte Carlo ray-trace environment. This goal is achieved by systematic intercomparison of dedicated experimental, theoretical, and numerical results. We evaluate the success of the Huygens-Fresnel principle by predicting and carefully measuring the interference fringes produced by both slit and circular apertures. We then compare the results from the analytical and numerical approaches with each other and with dedicated experimental results. We conclude that use of the MCRT method to accurately describe diffraction requires that careful attention be paid to the interplay among the number of aperture points, the number of rays traced per aperture point, and the number of bins on the screen.

Introduction

The Monte Carlo ray-trace (MCRT) method has long been utilized to model the performance of optical systems in the absence of diffraction and polarization effects [1-5]. Heinisch and Chou [6], and later Likeness [7], were among the early proponents of treating diffraction in the MCRT environment. However, their approach, which is based on a geometrical interpretation of the Heisenberg uncertainty principle, relies on empiricism to obtain adequate agreement with theory [8]. More recently the Huygens-Fresnel principle [9] has been implemented to describe diffraction and refraction effects in the MCRT [10] and wavefront tracing [11] environments. The goal of the current effort is to establish the conditions and limits under which the Huygens-

Fresnel principle accurately describes diffraction in the MCRT environment. This goal is achieved by systematic intercomparison of dedicated experimental, theoretical, and numerical results.

Experiment Apparatus and Procedure

Figure 1 is a schematic diagram of the apparatus used to obtain the experimental results reported here. A 351-nm beam from a Coherent Enterprise II 653 Argon Ion Laser is steered through mirrors to a chopper, after which it passes through a beam expander and a 4-by-4 mm beam former before falling on the aperture. The beam expander consists of two convex lenses whose focal lengths are 3.5 and 15 cm. The relatively large dimensions of the beam former ensure that the center of the beam does

not include a significant amount of diffracted light. The aperture consists of either a precision slit or a circular hole. The diffracted beam is incident to a 2.0- μm pinhole at the entrance aperture of a Newport Model 918:UV detector. This pinhole determines the spatial resolution of the fringe measurements.

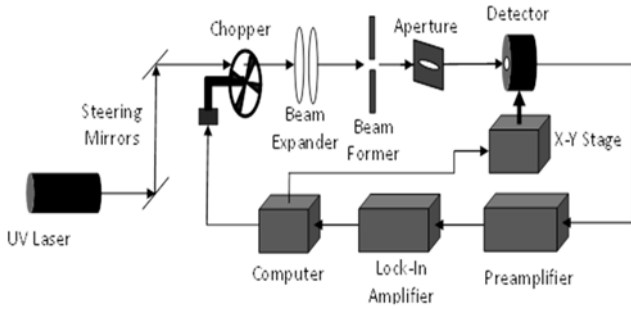


Figure 1. Schematic diagram of the experimental apparatus.

Low-noise operation is assured by passing the detector output successively through a preamplifier and a lock-in amplifier, which in turn controls the chopper speed. The shape and size of the aperture and the aperture-to-pinhole spacing, z , are parameters of the study. A Labview code controls the chopper and the vertical and horizontal positioning of the detector, and records the detector output as a function of position.

Theory

Diffraction is considered to be in the Fresnel regime when either the light source or the observing screen, or both, are sufficiently near the aperture that the curvature of the wave front becomes significant. Thus, we are no longer dealing with plane waves. Consider an aperture at $z = 0$ in the xy -plane illuminated with a monochromatic light of wavelength λ and a field distribution, $E_0(x,y)$, within the aperture, as illustrated in Figure 2. The field for the point S' in the plane of observation ($x'y'$), parallel to the xy -plane but at a distance z to the right, is given by adding together spherical waves emitted from each point in the aperture,

$$E(S') = \frac{1}{i\lambda} \iint_{\Sigma} E_0(x,y) \frac{e^{ikr}}{r} \cos \theta \, dx dy. \quad (1)$$

In Eq. (1), θ is an angle between a vector perpendicular to the xy -plane and the vector \vec{r} joining S and S' , thus $\cos \theta = z/r$. The distance between the points S and S' is given by

$$r = \sqrt{z^2 + (x' - x)^2 + (y' - y)^2} \approx z \left(1 + \frac{1}{2} \left(\frac{x' - x}{z} \right)^2 + \frac{1}{2} \left(\frac{y' - y}{z} \right)^2 \right). \quad (2)$$

Thus, we obtain the Fresnel approximation (near field),

$$E(x', y') = \frac{1}{i\lambda z} e^{ikz} e^{i\frac{k}{2z}(x'^2 + y'^2)} \times$$

$$\iint_{\Sigma} E_0(x,y) e^{i\frac{k}{2z}(x^2 + y^2)} e^{-i\frac{k}{z}(xx' + yy')} \, dx dy. \quad (3)$$

When both the source and the observation point are situated sufficiently far from the aperture (i.e., $z \gg k(x^2 + y^2)/2$), the term $e^{i\frac{k}{2z}(x^2 + y^2)}$ can be dropped from Eq. (3), yielding the Fraunhofer approximation (far field)

$$E(x', y') = \frac{1}{i\lambda z} e^{ikz} e^{i\frac{k}{2z}(x'^2 + y'^2)} \times$$

$$\iint_{\Sigma} E_0(x,y) e^{-i\frac{k}{z}(xx' + yy')} \, dx dy. \quad (4)$$

We employ the Fourier transform to find the solution for both approximations.

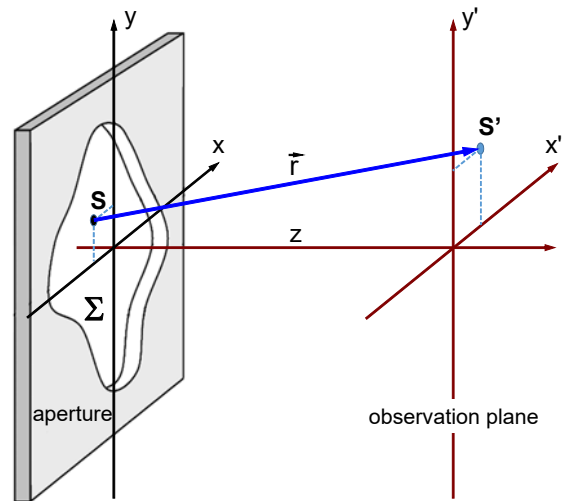


Figure 2. Transmission through an aperture.

MCRT Diffraction Model

According to the Huygens-Fresnel principle, light propagates as a succession of self-replicating wave fronts. At its origin ($t = 0$) the wave front for a plane wave is considered to consist of an array of equally spaced point disturbances. Each point disturbance produces an outward-propagating pattern of concentric spherical waves. Then, for a given order of each spherical wave front ($t + \Delta t$), a tangent plane is passed parallel to the original plane wave front, with each point of tangency now considered to be a new point disturbance. As pointed out by Volpe, Létourneau, and Zhao [11], “the construction should be regarded as a mathematical abstraction that correctly reproduces the physics without necessarily being physically rigorous.”

Figure 2 illustrates equally well the geometry for both the infinite slit and the circular aperture diffraction problems. The following discussion is for the case of an infinite slit aperture, but extension to the circular aperture is straightforward. We consider a source point S in the plane of the slit or circular aperture and a field point S' lying on the screen. Then, referring to Figure 2, the phase φ of the ray when it arrives at screen point S' will depend only on the wavelength, λ , of the light and the length, r , of the line connecting source point S with field point S' ; that is,

$$\varphi = \vec{k} \cdot \vec{r} = \frac{2\pi}{\lambda} r = \frac{2\pi}{\lambda} \frac{z}{\cos\theta}, \quad (5)$$

where z is the horizontal distance between the slit or aperture and the screen and θ is the angle between the ray makes with the horizontal. The electric field strength of the ray at field point S' is then

$$E(x', y') = \frac{E_0(x, y)}{r} e^{i\varphi}. \quad (6)$$

We seek the distribution of intensity on the screen. To within an arbitrary constant this is given by

$$I(x', y') = E(x', y') * E(x', y'). \quad (7)$$

where $E(x', y')$ is the local electric field due to all of the rays incident to a given field point and the symbol $*$ indicates multiplication by its complex conjugate. This calculation requires that the screen surface be divided into bins since it is unlikely that two rays will be incident at exactly the same point. Then the electric field strength in bin n is the algebraic sum of the contributions by the individual rays that are incident within the bin.

Results

Figures 3 and 4 show representative results obtained during this investigation. Figure 3 is a comparison of fringe patterns obtained for a 200- μm slit with a screen distance of 7.60 mm using the MCRT method (green curve), Fresnel theory (red curve), and experimental technique (blue curve). The Fresnel number for all three results is 5.48 ($\lambda = 0.351 \mu\text{m}$). Figure 4 represents a similar comparison for the 200- μm -diameter circular aperture with a screen distance of 7.60 mm.

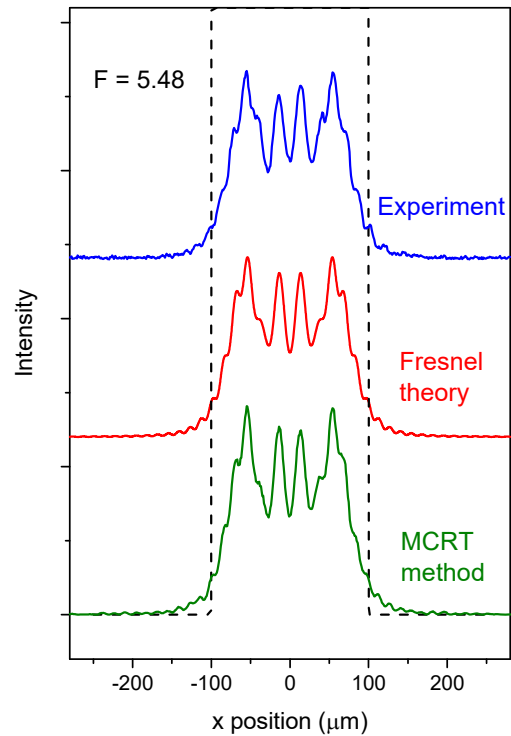


Figure 3. Comparison of fringe patterns produced by a 200- μm slit with a screen distance of 7.60 mm ($\lambda = 0.351 \mu\text{m}$, $F = 5.48$).

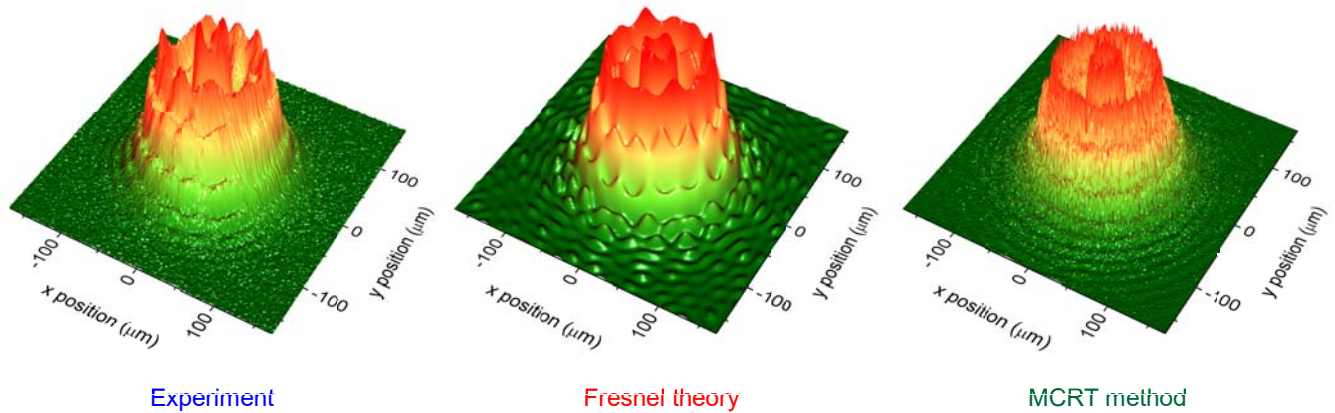


Figure 4. Comparison of fringe patterns produced by a 200- μm -diameter circular aperture with a screen distance of 7.60 mm ($\lambda = 0.351 \mu\text{m}$, $F = 5.48$).

Conclusion

We conclude that the MCRT method is a capable tool for modeling diffraction and interference using the Huygens-Fresnel principle, provided that adequate attention is paid to interplay among source distribution, ray density, and binning resolution.

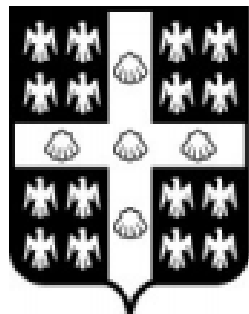
References

1. Chou, Tien S., A Monte-Carlo approach to optical analysis, **Optical Engineering**, Vol. 13, No. 4, 1974, pp. 299-302.
2. Tira, N. E., J. R. Mahan, Robert B. Lee III, and R. J. Keynton, Linear-array apertures for inflight dynamic solar calibration of radiometric channels for Earth radiation budget applications, **Applied Optics**, Vol. 33, No. 24, August 20, 1994, pp. 5617-5637.
3. Haeffelin, M. P. A., J. R. Mahan, and K. J. Priestley, Predicted dynamic electrothermal performance of thermistor bolometer radiometers for earth radiation budget applications, **Applied Optics**, Vol. 36, No. 28, 1 October 1997, pp. 7129-7142.
4. Mahan, J. R., **Radiation Heat Transfer: A Statistical Approach**, John Wiley & Sons, New York, 2002, ISBN 0-471-21270-9.
5. Mahan, J. R., Walker, J. A., and Stancil, M. M., Bidirectional Reflection Effects in Practical Integrating Spheres, **Applied Optics**, Vol. 54, No. 30, 2015, pp. 8951-8956.
6. Heinisch, R. P. and Chou, T. S., Numerical experiments in modeling diffraction phenomena, **Applied Optics**, Vol. 10, No. 10, 1971, pp. 2248-2251.
7. Likeness, Barry K., Stray light simulation with advanced Monte-Carlo techniques, SPIE, Vol. 107, 1977, pp. 80-88.
8. Coffey, Katherine Leigh, Next-Generation Earth Radiation Budget Concepts, Master of Science Thesis, Department of Mechanical Engineering, Virginia Polytechnic Institute and State University, Blacksburg, VA, November 30, 1998.
9. Huygens, Christian, **Traité de la Lumière**, Gautier-Villars et Cie., Editeurs, Paris.
10. Mahan, J. R., A. R. Barki, K. J. Priestley, Diffraction and Polarization Effects in Earth Radiation Budget Measurements, **Applied Optics**, Vol. 55, No. 34, 2016, pp. D54-D59.
11. Volpe, F. A., Létourneau, P.-D., and Zhao, A., Huygens-Fresnel Wavefront Tracing, **Computer Physics Communications**, Vol. 212, March 2017, pp. 123-131.

Posters

AITA 2017

Québec City, Canada
September 27th - 29th, 2017



UNIVERSITÉ
LAVAL

AIRCRAFT FUSELAGE TESTING USING VIBROTHERMOGRAPHY TECHNIQUE

A. Saboktakin¹, X. Maldague², G. Rus³

¹Department of Mechanical Engineering, University of Sistan and Balochestan, Zahedan, Iran

¹Center of advanced lightweight materials, University of Sistan and Balochestan, Zahedan, Iran

²Department of Electrical Engineering, Laval University, Quebec, Canada

³Department of Structural Mechanics, University of Granada, Granada, Spain

Email: Saboktakin@eng.usb.ac.ir

Vibrothermography is a promising non-destructive technique that uses ultrasonic elastic waves to detect damages and is typically applied in the aerospace and automotive industries. This technique allows for defect selective imaging using thermal waves that are generated by ultrasound waves. In this paper, vibrothermography technique was applied to the aircraft fuselage to detect its damage. The influence of the damage on the temperature distribution at the damage region on the aluminum was investigated by finite element technique. Comprehensive understanding in edge crack in fuselage heating caused by local friction between crack surfaces was obtained.

Introduction

In the aerospace industry one of the most important subjects is guaranteeing the certification of an aircraft. Every aircraft companies require that the quality of every component be accepted as ready to fly. This requirement makes it compulsory to inspect every component specifically the fuselage to detect potential defects before it is assembled into the aircraft. The complexity of the fuselage geometry makes it obligatory to have an automated system to inspect it using promising NDT techniques. Many researchers have turned their attention to researching high frequency ultrasonic elastic waves. Elastic waves are capable of propagating over long distances in specimens, and tend to interact with changes such as cracks and delaminations in a workpiece[1]. Vibrothermography based on ultrasonic waves is a non-destructive testing method in which cracks in an object are made visible through heating caused by high frequency ultrasounds wave. In this technique the heat is generated through the dissipation of mechanical energy at the crack

surfaces by ultrasonic waves. The frequency range used for excitation of structures is typically in the range 20 kHz to 100 kHz. The presence of the crack may result in a temperature rise around the damage area and the surface close to the crack. The temperature rise is measured by a high sensitivity infrared imaging camera whose field of view covers a large area. The method can cover large areas from a single excitation position so it is much faster than conventional ultrasonic testing or eddy current inspection, which requires scanning over the whole surface. In addition, vibrothermography can be a more convenient and reliable inspection technique for structures with complex geometries that are difficult to inspect by conventional methods [2,3]. The technique is also particularly well-suited to the detection of cracks that can cause problems with other techniques such as conventional ultrasound and radiography. In fact, in this technique when waves are induced into the defects, mechanical energy will decay rapidly because of the friction between the crack surfaces, the elastic properties of the crack areas which are much more different than any other areas; consequently, thermoelastic and hysteresis effects are generated.

Finite element modeling (FEM) is useful technique to understand the effect of induced sound pulses on damaged zones and the principles behind crack detection using vibrothermography. FEM is also used to investigate effect of complex parameters, such as geometry, material properties, loads and nonlinearities [4,5]. FEM can be used to investigate heat generation which can be generated within the fuselage structure because of thermoelastic damping and friction effects. In this paper finite element modeling of elastic wave propagation was carried out in aluminum fuselage to understand how the waves propagate inside of the fuselage during vibrothermography technique. In this research, the fuselage was excited by dynamic loading at frequency of 20 KHz and then influence of excitation on defect area was evaluated.

Modeling procedure

In our research, we model an aircraft fuselage with a very small crack near the window of aluminum fuselage sector. The analysis for aluminum fuselage is performed using material properties presented in the table with different amplitudes and frequencies to observe the temperature rise in the crack area based on frictional heating.

| Item | Unit | Qty |
|-------------------------------|------------------------|-------------------------------|
| Young's Modulus E | GPa | 73 |
| Poisson Ratio ν | --- | 0.33 |
| Density ρ | Kg/m ³ | 2780 |
| Coefficient of friction μ | --- | 1.4 |
| Yield stress σ_Y | MPa | 345 |
| Loss factor η | --- | 0.3 to 10 $\times 10^{-5}$ |
| Thermal conductivity k | W/m ² °C | 121 |
| Specific heat capacity C_p | J/Kg. °C | 875 |

A time-dependent sinusoidal displacement load is applied in on a circle partition fuselage. The applied displacement had amplitude of 0.05mm

with a frequency of 20 kHz, and was applied for duration of 10 ms.

In all our models, the convection heat transfer coefficient was set at 10 W/m².k, on all sides of the modeled fuselage.

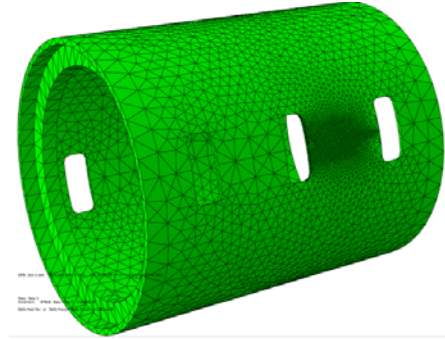


Figure 1.Geometry model for the FEM.

Modeling results

Based on the modeling procedure mentioned above, the temperature distribution in a damaged fuselage under dynamic loading was investigated. In such case, the amount of temperature rise is proportional to the excitation frequency and material property and also to the applied loads. It is observed that the highest temperature increase is in the point of crack tip that is modeled by combining stress-strain analysis with the heat equations to calculate heat generated (see Fig. 2).

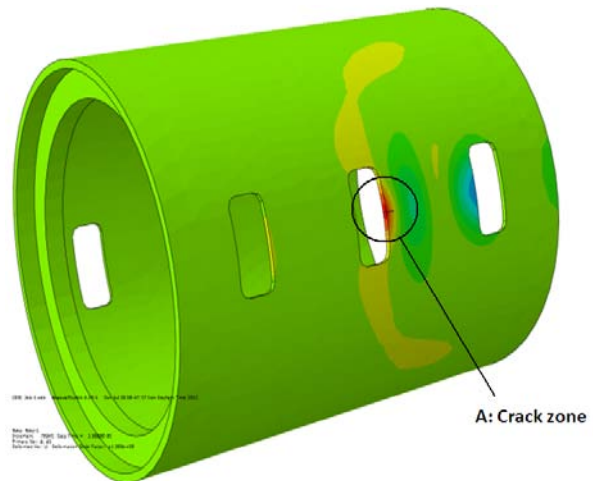


Fig.2. Displacement distribution at fuselage subjected to 20 KHz excitation load (Fuselage diameter: 3300mm, length of fuselage model: 4200mm).

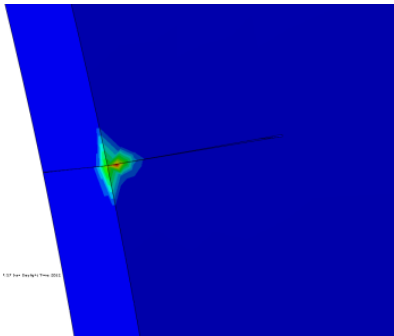


Fig.3. Temperature distribution in defect area of fuselage due to hysteresis heating (Magnification of zone A depicted in figure 2).

The displacement and temperature distribution in defected fuselage subjected to 20 kHz-0.05mm excitation load are illustrated in Figure 3. It is clear that as the excitation time increases the temperature rise at the crack area in aluminum fuselage increases gradually with the exception that the temperature shows a low reduction which is probably due to wave energy dissipation (see Fig 4).

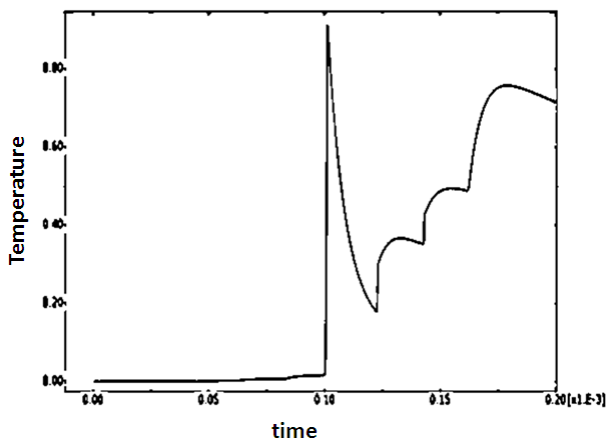


Fig. 4. Temperature rise at edge crack tip versus time at 20 KHz excitation load.

This delay occurs due to the reason that we are capturing the temperature rise at a node on the top of the upper plate and there is a distance between the data node and the heat source. It means that if the delamination was modeled at a location closer to the surface, this time delay would be decreased. Based on modeling results we observed that there is a limit for frequency and amplitude during vibrothermography such that dynamic loading above this limits can cause plastic deformation and also prevent the

wave propagation inside the specimen. It should be noticed that plastic deformation in crack tip could cause a large temperature rise which is expected to have crack propagation and fatigue damage and nonlinear behavior in the frequency response. So this point have considered during dynamic loading by high amplitude excitation during all steps of our modeling.

Conclusion

We developed a finite element method for damage heating in fuselage and learned how to obtain sufficient vibrations. The mechanism of friction and hysteresis and its relation with temperature rise was examined in small edge crack in aluminum fuselage. By such these finite element analysis we studied the mechanism behind this technique to use it more effectively in fuselage inspection. At the next stage of our research, the integration and synchronization of the experimental vibrothermographic data along with FEM results will be used to design a fully-automated system to inspect the whole aircraft fuselage.

References

1. D. T. Wu, G. Busse, "Lock-in thermography for nondestructive evaluation of materials", *Revue Generale De Thermique* 37(8), p. 693-703. 1998
2. A. Gleiter, G. Riegert, T. Zweschper, G. Busse, "Ultrasound lockin thermography for advanced depth resolved defect selective imaging", in *European Conference on Nondestructive Testing, ECNDT Conference Proceedings (Berlin, Germany)*, p. 25-29, 2006.
3. X. Han, M. S. Islam, G. Newaz, L. D. Favro, Thomas R. L., "Finite- element modeling of acoustic chaos to sonic infrared imaging", *Journal of Applied Physics* 98(1), 2005.
4. F. Mabrouki, M. Genest, A. Thomas, "Frictional Heating Model for Efficient Use of Vibrothermography" *NDT & E International*, Vol. 42, No. 5, p. 345-352, 2009.
5. X. Han, M. Islam, G. Newaz, L. Favro, R. Thomas, "Finite element modelling of the heating of cracks during sonic infrared imaging" *journal of Applied Physics*, Volume 99 (7), p. 074905-074905, 2006.
6. ABAQUS user manual version 6.5-1.

7. M. A. Biot, "Thermoelasticity and irreversible thermodynamics", *Journal of Applied Physics*, p. 240-253, 1956.
8. Richard B., Eslami M., "Thermal Stresses: Advanced Theory and Applications", Springer, Berlin, Germany, 2008
9. J. M. Piau, A. Bendada, X. Maldague, J. G. Legoux, "Nondestructive testing of open micro-cracks in thermally sprayed coatings using ultrasound excited vibrothermography", *Nondestructive Testing and Evaluation*, Vol.23, No. 2, p.109-120, 2008.

DETECTION OF EXTERNAL STRUCTURES OF ANTI-PERSONNEL MINES BY MEANS OF THERMOGRAPHIC INSPECTION OF SOIL

Bryan García¹, Andrés D. Restrepo-Girón², Humberto Loaiza-Correa³

¹ Universidad del Valle, Calle 13 # 100-00, Campus Meléndez, Cali, Colombia.
bryan.garcia@correounivalle.edu.co

² Universidad del Valle, Calle 13 # 100-00, Campus Meléndez, Cali, Colombia
andres.david.restrepo@correounivalle.edu.co

³ Universidad del Valle, Calle 13 # 100-00, Campus Meléndez, Cali, Colombia
humberto.loaiza@correounivalle.edu.co

Anti-Personnel Landmines (APL) detection protocol by means of thermographic inspection, digital image processing and learning machines, is presented. The proposed system detects PVC from external structures of the most common type of landmines used in Colombia's armed conflict, buried in dry soil and under outside environmental conditions. The best performance obtained with a Multilayer Perceptron neural network (MLP) was 93.8% in successful detection of PVC-made APL presence.

Introduction

During armed conflict in Colombia, the use of APLs has been frequent, in despite of being prohibited by Ottawa Treaty, signed and ratified by Colombia on 1997. APLs are usually buried between 5 and 10 cm depth, individually or in groups, in order to control land extensions or diminish the attacks from regular military forces.

Several methods had been developed for APL detection, like *metal detectors* [1], *impact acoustic analysis* [2], *ground-penetrating radar* (GPR) [3] and *thermography* [4]. Excepting some research, most works about thermography application in APL detection present results obtained from simulations or experiments performed under controlled laboratory conditions of relative humidity and illumination levels. In the other side, the use of *Artificial Neural Networks* (ANN), *Support Vector machines* (SVM) and *Bayesian Networks* bring good results, but again under those controlled environmental conditions [4], [5].

This report shows APL detection results obtained by the design and implementation of a thermographic inspection protocol, and application of artificial vision and machine

learning techniques, under uncontrolled environmental conditions.

Methodology and system description

The proposed detection system is represented by the diagram of figure 1, and each stage is described in the following paragraphs.

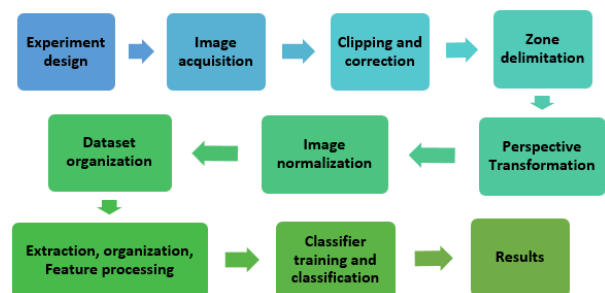


Figure 1. Diagram of the proposed APL detection system

Experiment design

The APL structure considered was the so called *queiebrapatras*, due to its intensive use during the armed conflict in Colombia. Like a craft APL, the final structure of our landmine was fabricated with PVC, is 12 cm height, 7.6 cm diameter, and has a 5 ml syringe as the bomb fuse (figure 2) [6]. 400 g of anthracite coal was used in order to simulate the presence of explosive, because their similar properties

[7]; also, 20 g of iron nails were added to the landmine inside.



Figure 2. APL structure and inside content

According to previous works, thermographic inspection gives better results in low moisture or dry soils [8]. Nevertheless, for this research a natural terrain was selected and no control of temperature, moisture or wind was taken, in order to have similar conditions to those in real situations. This terrain had an area of 3 m × 4 m, and did not exhibit superficial vegetation or appreciable rocky material.

Distribution of APLs through the terrain is shown in figure 3. In addition to PVC APLs, brass landmines were also buried in moist soil.

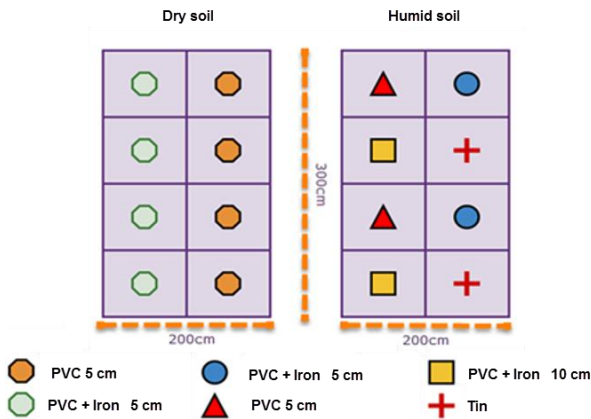


Figure 3. Spatial distribution of APLs over inspected terrain

Image acquisition

Thermal images were acquired by using a FLIR E320 camera, 2.1 ± 0.01 m from the surface where it is located, and 3 ± 0.01 m from the analysis area (figure 4) [9]. The camera was configured with an emissivity of 0.94 and a greyscale color palette with white as the highest temperature point. Figure 5a

shows the actual positions of the MAPs under the terrain.

In total, 26 thermographic sequences were collected: 10 from dry soil without APLs, 10 from dry soil with APLs and 6 from moist soil with APLs, each sequence consisting of 19 images acquired at 15-minute intervals during the period between the 5:00 p.m. and 8:00 p.m. (sunset).

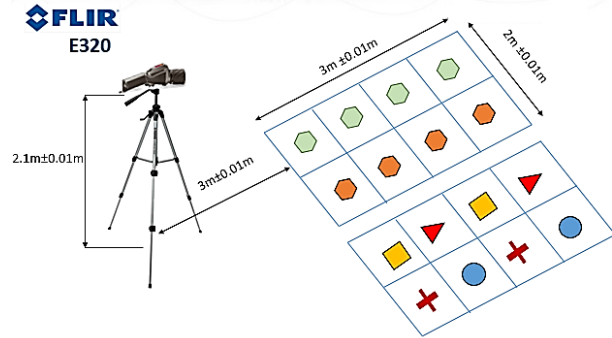


Figure 4. Localization of the FLIR camera, and size of the inspected terrain

Image processing

Each image of the dataset was trimmed to eliminate useless information, modifying its dimension to 320×200 pixels; in addition, a 3×3 medium filter was used to correct for defective pixels in the camera's optical sensor [10].

Then, a perspective transformation was made to compensate for the effect of the capture angle (<90 °) (Figure 5c and d), selecting four points that delineate the area of interest (Figure 5b) and four others that defined the size of the transformed image.

The automatic adjustment of image intensity executed by the FLIR camera introduces an undesired effect (figure 6), which is corrected by subtracting from the values of each image S_k the mean intensity \bar{S}_k of all its pixels, to obtain a normalized image \hat{S}_k :

$$\hat{S}_k = S_k - \frac{1}{N_c N_f} \left[\sum_{i=1}^{N_f} \sum_{j=1}^{N_c} S(i, j, k) \right], \quad \forall k \text{ con } k = 1, 2, \dots, 19 \quad (1)$$

Finally, a dataset was obtained with 494 images (19 for each day of capture): 190 for dry soil without APLs, 190 for dry soil with APLs, and 114 for moist soil with APLs, each segmented into eight equal parts.

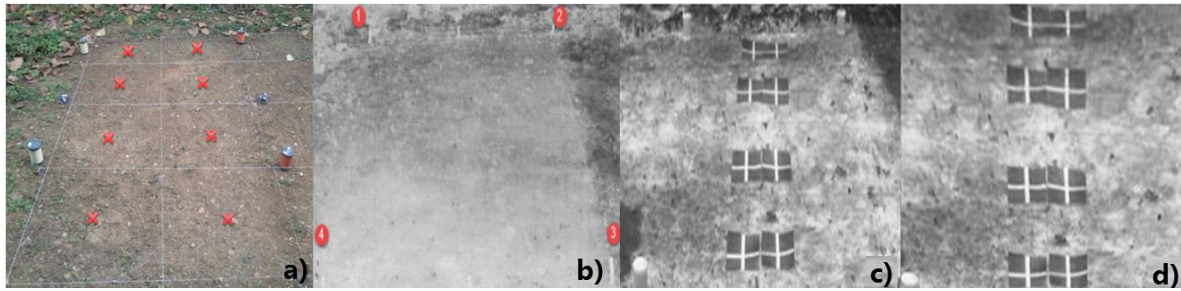


Figure 5. Real images from terrain: (a) APLs localization; (b) terrain delimitation; (c) terrain with perspective; (d) terrain image after perspective transformation

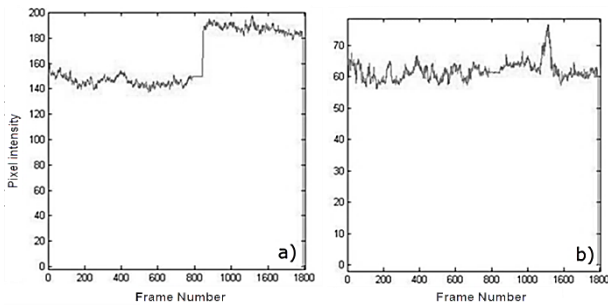


Figure 6. Effect of the automatic contrast adjustment: a) abrupt fluctuation; b) fluctuation compensation

Feature extraction, organization and processing

The four statistical moments of the first order, and the maximum and minimum values, were the features extracted from each image segment stored in the dataset, then organized into a single row vector for all frames, in order to preserve the temporal evolution of the temperature.

To avoid that some of the features adversely influence the cost function of the classifiers, the previous set of standards was normalized with a mean of zero and a standard deviation of 1 for each column of features. In addition, Principal Component Analysis (PCA) was applied to these data in order to construct a new dataset of 160 segments, with the first 30 principal components, retaining 99.62% of information.

Learning machines for classification

To evaluate the performance of classification, the RNA structure was modified both, about the number of neurons in the hidden layer, and the activation function of the output stage. For

its part, the SVM was modified about the training method and the Kernel, and the Bayesian classifier was of Naives-Bayes type. Later, 50% of the normalized dataset was used for training, and the remaining 50%, for validation. The same proportion of data was taken for training and validation with the PCA dataset. The input data (114 values) of the classifier corresponds to 6 features taken from a single segment along the 19 frames that make up a sequence. The total number of training segments was 190.

Results

The performance of the best classifier configurations, regarding the variation in their structure, is presented in Table 1. It can be seen that the MLP network, with 15 neurons in the hidden layer, presents the best performance in APL detection. Also, it is clear that PCA was not decisive for classification performance, as tests showed a 10% less than success obtained without this feature transformation.

| Classifier | Method | Kernel | Neurons in the hidden layer | Success rate (%) | | |
|------------|--------|-----------------------|-----------------------------|--------------------|------------|-------------|
| | | | | Dataset | | |
| | | | | Without processing | Normalized | PCA (30 PC) |
| ANN MLP | - | - | 10 | 93.8 | 88.8 | 80.0 |
| | - | - | 15 | 94.1 | 93.8 | 77.5 |
| SVM | SMO | MLP | - | - | 65,0 | 76,9 |
| | SMO | Quadratic | - | - | 66,3 | 63,1 |
| | SMO | Polynomial (degree 3) | - | - | 64,4 | 62,5 |
| | SMO | RBF | - | - | 65,0 | 71,3 |
| | LS | MLP | - | - | 78,1 | 39,4 |
| | LS | RBF | - | - | 69,4 | 71,9 |
| Bayes | Naives | - | - | 53,9 | 50,6 | 73,1 |

Table 1. Relevant results in classification for the 3 different learning machines tested

Once the learning machines were trained and tested, each image of the sequence was segmented according to the average APL diameter (8 cm) and its ratio in pixels / cm. The image was scanned vertically and

horizontally, using a window of 160×50 pixels height. For the horizontal displacement, steps of 32 pixels were defined, and for the vertical, 25 pixels (Figure 7).

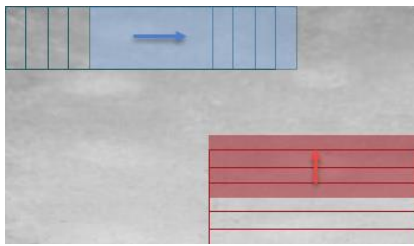


Figure 7. Segmentation of samples to classify

As the window slid through the image, a new segment was generated in each displacement, from which the same 6 features were extracted. For this reason, the dataset for classification consisted of 798 sliding segments that were submitted to the MLP network. From here, each segment classified as suspected of APL presence, was filled with 1; then, with successive displacements, a cumulative image was generated, similar to that of Figure 8, in which the regions with the highest repetition of detection (greater probability of presence of APL) are brighter.

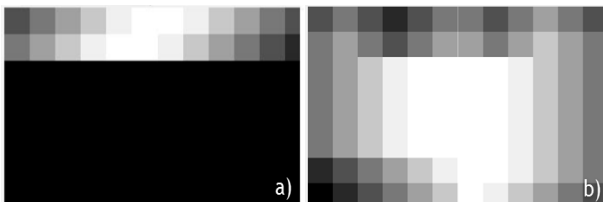


Figure 8. Detection results using the sliding window: a) for a segment without APL; b) for a segment with APL

Conclusions

An APL detection protocol was developed by the acquisition of IR thermal images, its digital processing, extraction of features, and classification with learning machines, in order to discriminate the presence of the most common materials in the structures of these mines. The protocol developed allowed the detection of APLs in soil with low moisture, and uncontrolled environmental conditions. In addition, the construction of large structures around the selected terrain was not required to acquire the images.

It was possible to detect materials commonly used in the external structure of APLs, mainly

PVC (95.6% in dry soil and 45% in humid soil), using infrared thermographic images at distances between 3 and 6 meters at the point of analysis. It should be noted that the classifiers were trained with information from dry soil, exclusively; the moisture represents a great difficulty for the thermographic inspection, which constitutes a motivation for future works.

References

- [1] L. G. Gutiérrez, "Diseño y construcción de exploración de campos sembrados," no. 13, pp. 49–55, 2008.
- [2] P. D. Gader, M. Mystkowski, and Y. Zhao, "Landmine detection with ground penetrating radar using hidden Markov models," *IEEE Trans. Geosci. Remote Sens.*, vol. 39, no. 6, pp. 1231–1244, 2001.
- [3] D. G. Beetner and R. J. Stanley, "Landmine Detection and Discrimination Using High-Pressure Waterjets," pp. 1973–1984, 2004.
- [4] N. Trung Thành, H. Sahli, and D. Nho Hào, "Infrared thermography for buried landmine detection: Inverse problem setting," *IEEE Trans. Geosci. Remote Sens.*, vol. 46, no. 12, pp. 3987–4004, 2008.
- [5] A. Filippidis, L. C. Jain, and N. M. Martin, "Using genetic algorithms and neural networks for surface land mine detection," *IEEE Trans. Signal Process.*, vol. 47, no. 1, pp. 176–186, 1999.
- [6] Ministerio De Posconflicto - Centro Nacional Contra AEI y Minas, "Tipos De Minas Antipersonal En Colombia," 2014.
- [7] W. De Jong, H. Lensen, and Y. Janssen, "Sophisticated test facility to detect landmines," pp. 0–9, 1999.
- [8] A. Muscio and M. A. Corticelli, "Land mine detection by infrared thermography: Reduction of size and duration of the experiments," *IEEE Trans. Geosci. Remote Sens.*, vol. 42, no. 9, pp. 1955–1964, 2004.
- [9] I. R. R. Olave and H. A. R. Garcia, "Estudio de factibilidad para la detección de minas antipersonales mediante el uso de la técnica de termografía," *J. Chem. Inf. Model.*, vol. 53, no. 9, pp. 1689–1699, 2013.
- [10] C. I. Castanedo, S. Member, D. A. González, H. Bendada, and X. Maldague, "Análisis de imágenes en Termografía Infrarroja." Proc. X Simposio de Tratamiento de Señales, Imágenes y Visión Artificial, Cali, Colombia, 14-16 Septiembre, 2005.

THERMAL DIFFUSIVITY MEASUREMENTS WITH FLASH METHOD AT DIFFERENT DEPTHS IN A BURNED COMPOSITE MATERIAL

Serge-Olivier Gnessougou¹, Clemente Ibarra², Xavier Maldague³, Alain deChamplain⁴

¹Université Laval, serge-olivier-adam.gnessougou.1@ulaval.ca

²Université Laval, clemente.ibarra-castanedo@gel.ulaval.ca

³Université Laval, Xavier.Maldague@gel.ulaval.ca

⁴Université Laval, Alain.DeChamplain@gmc.ulaval.ca

We measured the thermal diffusivity (TD) with the flash method for two kind of composite materials. With two heat lamps and an infrared camera, we briefly heat and observe the evolution of the temperature as function of time (following the classical Parker's method). With this temporal signal, we calculate the TD. The first samples of composite material are burnt (two samples) and the second are unburnt samples (six samples). For each kind, we first calculate the TD at the surface and after using a drilling machining we measured again the TD to observe the variations as function of the depth. For the first burnt sample, TD at the burning area were $1.229 \times 10^{-7} \text{ m}^2/\text{s}$ and $2.405 \times 10^{-7} \text{ m}^2/\text{s}$ respectively at the surface and 0.7cm deeper. For the second burnt sample, TD at the burning area were $2.103 \times 10^{-7} \text{ m}^2/\text{s}$ and $2.218 \times 10^{-7} \text{ m}^2/\text{s}$ respectively at the surface and 0.7cm deeper. For the six unburnt samples, we modified the calculation procedure to have the TD for each pixel. We measure the TD at the surface and 0.7cm deeper and observe a variation of the TD between $2 \times 10^{-7} \text{ m}^2/\text{s}$ and $6 \times 10^{-7} \text{ m}^2/\text{s}$.

A Novel FPGA-based Data Reconstruction Method for Synchronous Real-time DMD Display with High Frame Rate

Weike Dong, Long Liu, Zhenqing Song, Xinglang Xiang

School of Physics and Optoelectronic Engineering, Xidian University, Xi'an, Shaanxi, China,
wkdong@mail.xidian.edu.cn

Abstract—With the development of the imaging IR (Infrared) guidance technique, DMD (Digital Micro-mirror Device) is widely used in semi-physical simulation which is a key part of the imaging IR guidance technique. By focusing on the requirement of semi-physical simulation in the imaging IR guidance technique, a novel FPGA (Field Programmable Gate Array) based data reconstruction method for synchronous real-time DMD display with high frame rate is presented. Since the timing of DMD load data is different from the VESA (Video Electronics Standards Association) timing. It is necessary to convert the format of the data streams in real-time. The serial-to-parallel conversion method is used in order to convert VESA timing to satisfy the timing of DMD loading. And then the converted data is stored in DDR2 SDRAM (Double-Data-Rate Two Synchronous Dynamic Random Access Memory). The Ping-pang operation is used to ensure the continuity of data write and read of DDR2 SDRAM. In the process of data output, the system also uses the parallel-to-serial converter to converse the data to reduce the working frequency of the FPGA while ensure that DMD can display normally. The experimental results show that the 8-bit grayscale video is displayed on DMD in real-time synchronously and the frame rate is up to 200Hz.

Keywords: DMD, PWM, FPGA, Data reconstruction, High frame rate

1 Introduction

Simulation technique is an especially important component in imaging IR guidance technique. And the scene simulation instrument uses DMD as its kernel component to realize the Infrared radiation modulation [1]. But, when using a DMD for semi-physical simulation, it is difficult to realize DMD to display the image in real-time with high frame rate [2]. So it is important to design a new method to overcome this limitation. Data reconstruction technique has opened up a new path to realize DMD real-time display. According to this technique, the data from the VESA timing format of the host computer can be converted to the timing of DMD loading in real-time [3]. The diagram of system block is shown in Figure 1.

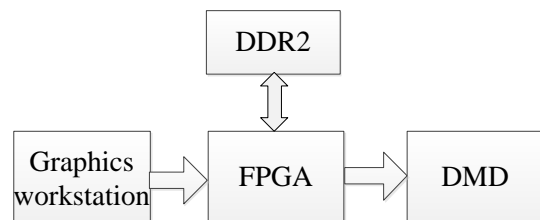


Fig. 1 The diagram of system block

But the real-time dynamic display of 8-bit grayscale video with high frame rate on DMD is still a challenge. For DMD, simple operation on DMD can only display a binary image. To display grayscale video on single-chip DMD, the grayscale modulation must be used [4]. The traditional grayscale image display is difficult to realize the frame rate higher than 150Hz [5], [6]. So it is necessary to optimize the traditional PWM (Pulse-width Modulation) algorithm to improve the frame rate.

In this paper, the method to implement and improve the performance of synchronous

real-time DMD display with high frame rate will be introduced. Firstly, the method to optimize the traditional PWM algorithm will be given. Secondly, FPGA-based data reconstruction is designed to ensure real-time conversion of data format. Finally, the 8-bit grayscale video is displayed on DMD in real-time synchronously and the frame rate is up to 200Hz.

2 Optimization of PWM Algorithm

It is necessary to do grayscale modulation for DMD due to the fact that DMD can only show binary image. PWM method can not only ensure the spatial resolution of the image, but also can ensure a higher image display frame

rate [7], so it is the preferred way to achieve DMD grayscale modulation.

PWM means pulse-width modulation which is also known as duty cycle modulation, solving the problem of image grayscale from the aspect of time [8]. By controlling pixels in different bright and dark time, it achieves a variety of grayscale values. The frame time of the image display is divided into several "bit-planes" (BP) display time. The display time of the "bit plane" is binary-weighted and corresponds to the binary "bit" of the pixel grayscale value. The high "bit plane" display time is twice that of the adjacent low "bit-plane"[9]. The bit-plane representation of the grayscale value in the PWM algorithm is shown in Figure 2.

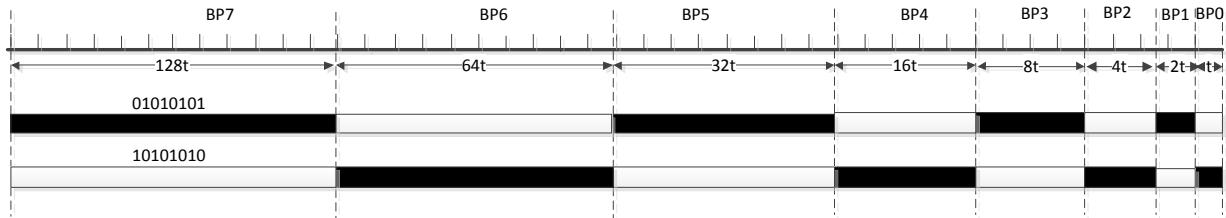


Fig. 2 The diagram of grayscale modulation by using PWM algorithm

The main factor limiting the frame rate of DMD is the time that it takes for DMD to load and "reset". The data transmission clock of DMD used in this paper is up to 400Mhz. The time DMD completed a complete data update is at least 30.72 μ s. The reset operation takes 5 μ s

after receiving the "micro-mirror timing pulse". After reset, 8 μ s of micro-mirror stabilization time is required, and new data cannot be loaded during reset and micro-mirror settling time [10], [11]. The process in which DMD continuously loads the data is shown in Figure 3.

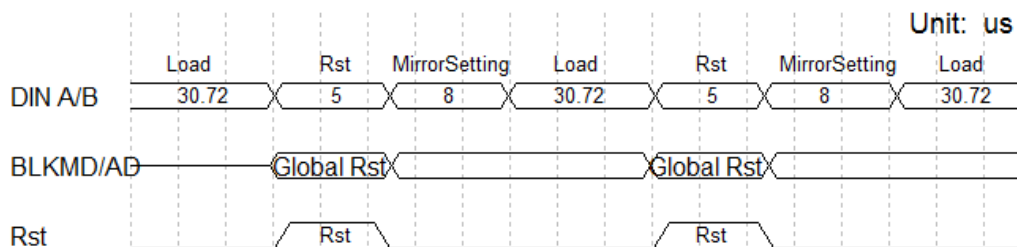


Fig. 3 Process for DMD to operate

If the traditional PWM algorithm is used to display 8-bit grayscale image, it is necessary to divide the original image into eight "bit-planes". And 8 times "data loading" and "reset" are needed for DMD. To ensure the continuity of the image display, it is necessary to complete the data loading of the next bit-plane in the

display time of the current bit-plane. So the display time of the "basic bit-plane" must satisfy $t \geq 38.72\mu$ s. To calculate the frame rate of the 8-bit image, we assume $t = 38.72\mu$ s. The traditional PWM algorithm timing is shown in Figure 4.

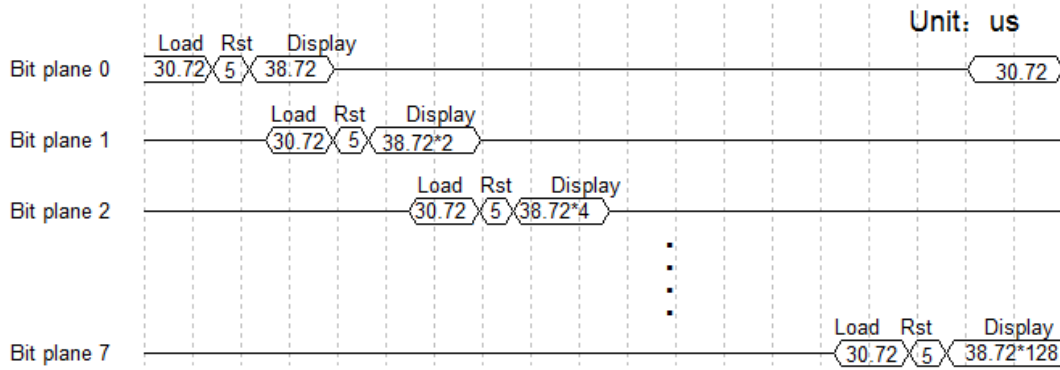


Fig. 4 Traditional PWM algorithm timing

DMD has a "block clear" function, and it allows DMD to clear the value in the memory in a very short time. The purpose of TI's addition of this operation is to allow DMD to be suitable for applications where the image display time is lower than the data loading time. The display time of the "base bit-plane" is set to 19.11us, and using the "block clear" operation to clear the entire DMD needs to consume 0.64us [12]. The micro-mirror settling time of 8us is consumed after each reset, during which DMD cannot load the data. To satisfy the

loading time of the next bit-plane data during the current bit-plane display, the display time of the current bit-plane must be greater than 38.72us. If the display time of the current bit-plane is not greater than 38.72us, the data of the micro-mirror needs to be cleared and reset at the end of the bit-plane display time to make sure that the micro-mirror is in the off state and the image display is in the blanking area. The timing of the optimization using the clear reset mode is shown in Figure 5.

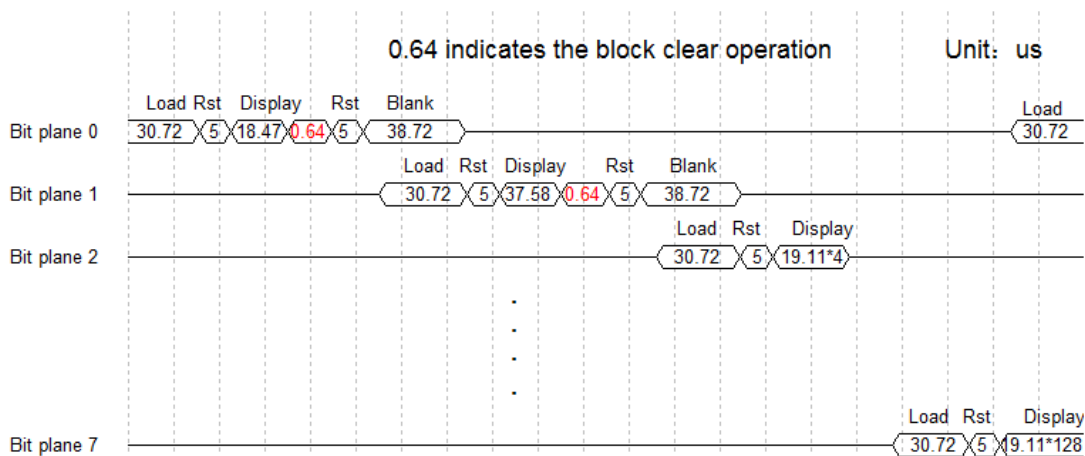


Fig. 5 Optimized PWM algorithm timing

| Algorithm | t_r (us) | t_d (us) | t_p (us) | f_p (Hz) |
|---------------------|------------|------------|------------|------------|
| Traditional PWM | 40 | 9873.6 | 9913.6 | 100.9 |
| Optimization of PWM | 40 | 4960.49 | 5000.49 | 200.0 |

Table 1 Comparison of traditional PWM algorithm and optimized PWM algorithm

In table 1, t_r indicates the time of 8 resets, t_d indicates the total display time of eight “bit-planes”, t_p indicates the time of a frame, f_p indicates the frequency of a frame. From the table 1, we can find that the f_p of the optimization PWM algorithm is about twice of the traditional of PWM algorithm.

3 FPGA-based data reconstruction

The optimized PWM algorithm ensures that DMD displays grayscale image with a higher frame rate. But the data format conversion is the premise of the normal work of the algorithm. To make the image format conversion in real-time synchronously, FPGA is used in data reconstruction method.

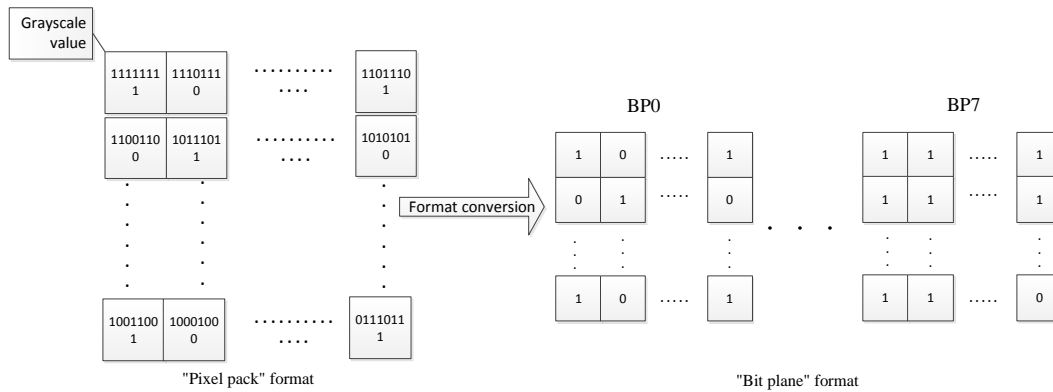


Fig. 6 The diagram of format conversion

Image format conversion means to reorganize the image data. And it is inevitable to cache data during the data reorganization process. One DDR2 SDRAM is used for data storage with 64-bit widths memory data bus. In the case of block storage, it is necessary to split the data by bit before the data is stored and store the split data separately in DDR2 SDRAM. To take full advantage of DDR2 SDRAM access bandwidth, the split data is also required a serial-to-parallel conversion before the data is written into the memory, merging 64 consecutive 1-bit data into a 64-bit data for read operation.

The system uses two-level ram cascade to achieve the serial-to-parallel conversion of the input data. The first level ram conversion ratio of 1:16 and the second level ram conversion ratio of 1: 8. The diagram of the

3.1 Format Conversion

The video data fetched from the host computer is encoded with the VESA display standard. But the data sent to DMD is loaded in a bit-plane manner during the display. So, it is necessary to convert the format of the data streams in real-time. An image with 8-bit widths and a "pixel pack" format that follows the VESA timing is formatted to obtain 8 planes for DMD grayscale modulation. The format conversion process is shown in Figure 6. Here, plane 0 contains the lowest order bit of all the pixels in the image and plane 7 contains the highest order bit of all the pixels in the image [13].

serial-to-parallel conversion module is shown in Figure 7.

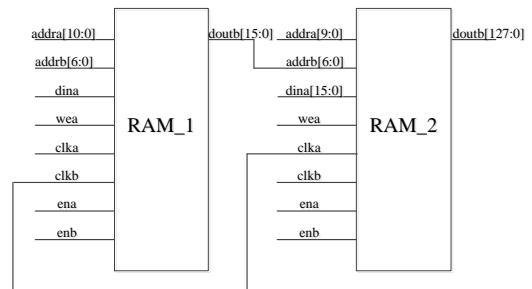


Fig.7 Serial-to-parallel conversion

In this Figure, the ram include the data write and read address, port a and port b clock signal, port a and port b enable signal. “wea” is always valid. The “clkb” in the RAM_1 is the “clka” divided by 16. So we can get 16-bit data. The “clka” in the RAM_2 is connected with “clkb” of RAM_1. And the input of the RAM_2 is

connected to the output of the RAM_1. By controlling the “enb” enable state, we can achieve 128-bit data bit width conversion. After the data bit width conversion, the 128-bit data is split into two 64-bit data and then sent into DDR2 SDRAM.

3.2 Block Storage

This paper uses Ping-pang storage to keep the continuity of data processing. The read and write operations are performed simultaneously in two channels under this mode. Ping-pang technology successively sends the buffered data stream to the post processing module through the rhythmical switch between the “input data stream selector unit” and the “output data stream selector unit”. Due to this, we can ensure that DDR2 SDRAM has sufficient data and DMD can display the image in real-time. In order to make DMD load data efficiently, the entire memory is divided into two subspaces. The previous frame data of the subspace 2 is read during the writing of the data to the subspace 1, and the current frame data of the subspace 1 is read during the writing of the data to the subspace 2. Two subspaces are alternately read and written to ensure continuity of data processing. And each subspace is divided into eight “bit-planes” in the plane

space. Figure 9 shows the storage space for DDR2 SDRAM in case of block storage.

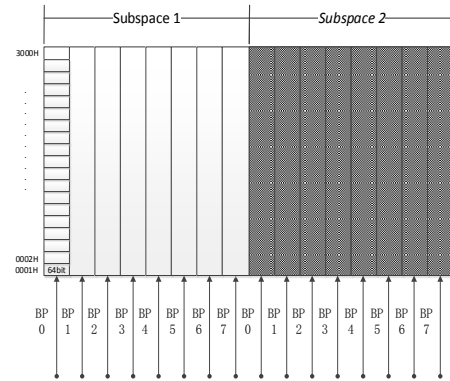


Fig 8 Mapping of blocked storage in DDR2 SDRAM

When loading data into DMD, the DDR2 SDRAM data transfer rate reaches its peak. In the case of block storage, the original data is divided and reconstruction so that when data for DMD is loaded, the data in DDR2 SDRAM is all valid. The bit width in DDR2 SDRAM memory is 64-bit, in order to store a bit plane data in a bit plane space, we need access 12288 addresses. The data transfer rate of DDR2 SDRAM in this process is 400MHz. This rate is less than the upper limit of DDR2 SDRAM data transfer. Although the way of block storage is logically complex, but it can greatly reduce DDR2 SDRAM data transmission bandwidth pressure. The data flow block diagram is shown in Figure 9.

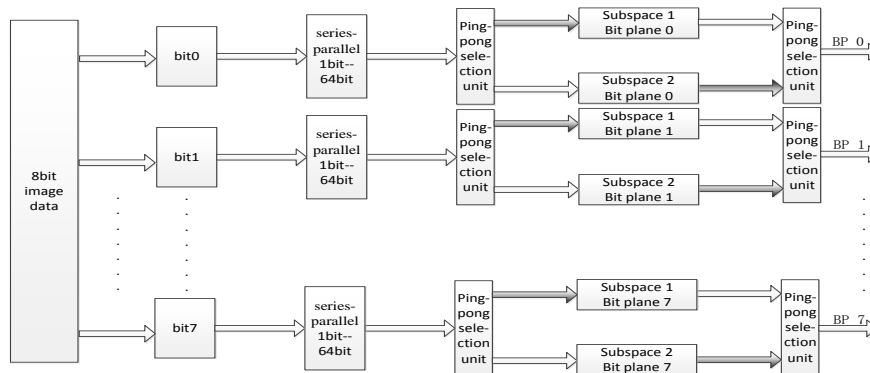


Fig.9 Block caching data flow block diagram

Firstly, each bit of the 8-bit data which from the host computer should be serial-to-parallel converted. This process can be implemented in RAM. Then, the serial-to-parallel conversion data should be sent to DDR2 SDRAM. The Ping-pang operation selection unit selects the

free subspace to store the data. The eight “bit-planes” in the selected subspace are accessed one by one. And the eight 64-bit data obtained by serial-to-parallel conversion are stored in the corresponding bit-plane space. When the current frame data is being stored in

DDR2 SDRM, the other subspace also outputs the bit-plane. The output also has a Ping-pang operation selection unit which selects the subspace that has updated the data and stops the input and outputs the subspace, each time a data of a bit plane space is output to DMD. During the 8-bit plane loading of one frame, the bit space is sequentially read from the bit plane space 0 to the bit-plane space 7.

3.3 Parallel-to-serial conversion

Serial-to-parallel conversion and parallel-to-serial conversion are a concrete manifestation of area and velocity interchange. In the case of data write and read rate is unchanged, we can reduce the speed of the FPGA by copying multiple processing modules, but the overall data processing rate will not be reduced. In this paper, the parallel conversion is done before the image data and control signal output and the conversion ratio is 4:1. The DMD data is loaded one row at a time with two LVDS buses into DMD SRAM pixels. Each bus contains 16 differential pairs of LVDS signals. In the process of FPGA internal operation, the two bus corresponding to the two 64-bit width data DATA_B [63: 0] and DATA_B [63:0]. After the parallel-to-serial

conversion, FPGA only need 200MHz clock can meet the 800MHz data output. The schematic block diagram of the parallel-to-serial conversions is shown in Figure 10.

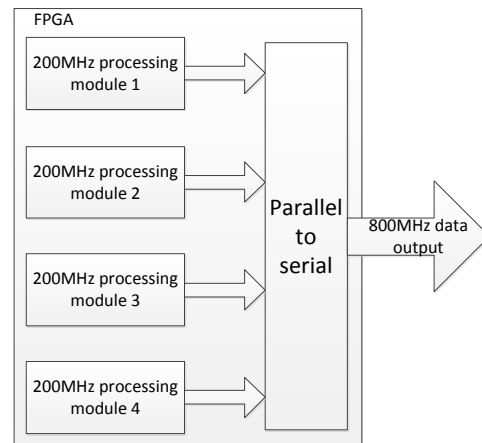


Fig.10 The parallel-to-serial conversions

We can achieve parallel-to-serial conversion of data by using Output Serializer and Deserializer (OSERDES). During the serialization of the OSERDES module, it can also ensure that the OSERDES output data and clock path consistent. This not only keeps the timing relationship between the data and the clock constant and improves the timing stability of the design. The parallel-to-serial timing of OSERDES in DDR mode is show in Figure 11.

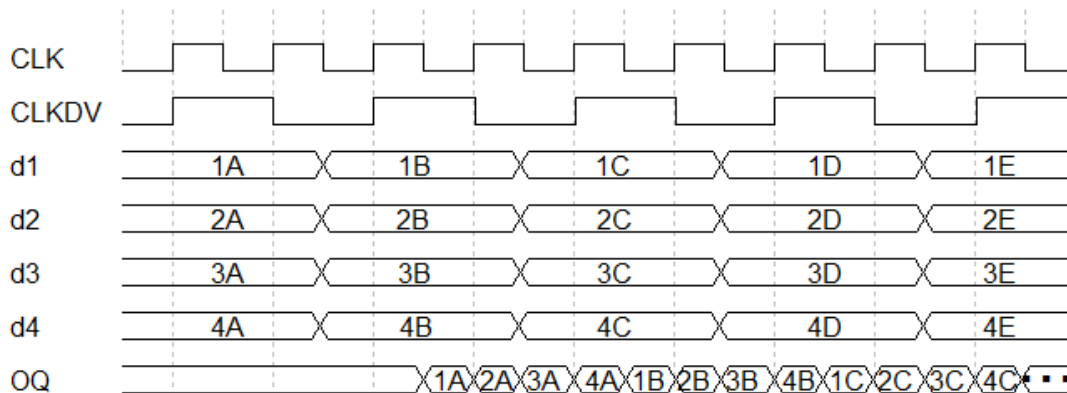


Fig.11 DDR4:1 parallel-to-serial conversion timing

In Figure 11, “CLK” indicates the working clock of OSERDES. The frequency of “CLKDV” is twice of “CLK”. At the input port, the 1-bit data d1, d2, d3 and d4 are sent to OSERDES on the rising edge of “CLKDV”. At the output port, d1, d2, d3 and d4 are output on

the rising edge and falling edges of “CLK”. So data are input on a rising edge of “CLKDV”, and the OQ output port requires two “CLK” cycles to output data. Among them, d1 d2 correspond to the first “CLK” cycle of two edge

data, d3 d4 correspond to the second “CLK” cycle of two edge data.

4. Results

The goal of the system is to display the 8-bit grayscale video in real-time with a frame rate of 200Hz. In this paper, an image of 8-bit grayscale gradient fringe pattern is used for test. The comparison between DMD display results and the original image is shown in Figure 12.



Fig.12 The comparison effect between DMD display results and the original image

From the results we can see that the effect on DMD is consistent with the original image. Grayscale changes significantly, uniformity is good, the display in line meets expectations and the image grayscale level reaches the design goal. The waveform of the RST_ACTIVE signal fed back by DMD when using the clear reset method for DMD drive is shown in Figure 13(a). It can be seen from the figure that one frame of the image contains two clear operations. The micro-mirror resets 10 times, and the time between each two reset signals represents the display time of the bit-plane. The bit-plane display time ratio also meets the design requirements of the algorithm.



Fig.13(a) The waveform of the RST_ACTIVE signal fed back by the DMD

The image display frame rate of DMD is shown in Figure 13(b). The time between two brown

dashed lines indicates the display time of a frame. The result shows that the frame rate is in line with the design requirements.



Fig.13(b) DMD displays the image frame rate

5 Conclusion

Semi-physical simulation requires Synchronous Real-time DMD Display with High Frame Rate. In this paper, to realize the display effect of 8-bit grayscale video on DMD, the traditional PWM algorithm is optimized and a FPGA-based data reconstruction method is proposed. The traditional PWM algorithm is improved by clear reset operation, and the FPGA-based data reconstruction approach is implemented by DDR2 SDRAM based block storage data cache. Ultimately, the real-time synchronized effect of display of the 8-bit grayscale video is realized on DMD and the frame rate is up to 200Hz.

6 References

1. Zhang Kai,Huang Yong,Yan Jie,Sun Li. Dynamic infrared scene simulation using grayscale modulation of digital micro-mirror device[J]. Chinese Journal of Aeronautics,2013,(02):394-400.
2. Sheng Bi, Ning Xi, King Wai Chiu Lai, Xuwei Pan. Design and implementation for image reconstruction of CompressiveSensing using FPGA. 2013 IEEE International Conference on Cyber Technology in Automation, Control and Intelligent Systems, Nanjing, 2013, pp. 320-325.
3. Vishal Markandey, Todd Clatanoff, Robert Gove, Kazuhiro Ohara, Motion adaptive deinterlacer for DMD (digital micromirror device) based digital television, *IEEE Transactions on Consumer Electronics*, vol. 40, no. 3, pp. 735-742, Aug 1994.
4. Y. Liu and L. Sun, "Multi-blocks scheme for high definition video display based on digital micro-mirror device," in *Electronics Letters*, vol. 50, no. 22, pp. 1593-1595, 10 23 2014.

5. Knipe R L. Challenges of a digital micromirror device: modeling and design[J]. Proc. SPIE, 1996, 2783: 10.1117/12.248483.
6. Zhou Hao, Zhang Tao, Cui Wen-nan, Research on Improving Display Frame Rate of Gray Scale Image[J]. Science Technology and Engineering 2014(21):257-261.
7. V. Markandey, T. Clatanoff, R. Gove and K. Ohara, "Motion adaptive deinterlacer for DMD (digital micromirror device) based digital television," in IEEE Transactions on Consumer Electronics, vol. 40, no. 3, pp. 735-742, Aug 1994.
8. Xichao Mo and Yuanyue Zhang, "Consecutive PWM driving video LED display system," Circuits and Systems, 1997. ISCAS '97., Proceedings of 1997 IEEE International Symposium on, 1997, pp. 1437-1439 vol.2.
9. Xu Jialin, Li Bingyu, Liu Yang Gray scale modulation and synchronization of infrared scene projector based on DMD [J]. Infrared and Laser Engineering, 2014, 43(4):1062-1067.
10. Texas Instruments. DLP7000 DLP® 0.7 XGA 2x LVDS Type A DMD [M]. America: TI, 2009
11. Texas Instruments. DLP®Discovery™ 4100 Digital Controller [M] America TI, 2012.
12. Lee Benjamin. Introduction to Digital Micromirror Device (DMD) Technology [M] America TI, 2008
13. Hunny Mehrotra, Badrinath G.S., Banshidhar Majhi, and Phalguni Gupta, "Bit Plane Slicing Technique For Iris Based Biometric System", 1st International Conference on Parallel, Distributed and Grid Computing (PDGC - 2010),pp.350-355, IEEE 2010.

Follow-up of restoration of works of art of the patrimony by infrared thermography.

Mouhoubi Kamel⁽¹⁾, Taram Abdoulaye⁽¹⁾, Bodnar Jean-Luc⁽¹⁾

Infrared thermography is a non-destructive testing technique that has found acceptance in many areas including works of art. This technique of analysis is, for example, very interesting in the field of restoration and conservation of heritage works. The possibilities of active thermography can help in the early detection of defects in works of art and their characterization. In this work we will demonstrate that it is possible to detect old restorations in frescoes and murals by flash method. This new possibility offered by thermography will make it possible, for example, to verify the compatibility of a restoration with the original work, which can prevent the appearance of a defect and may allow the conservator to follow up on restoration. In first we will demonstrate the feasibility of this approach on a laboratory specimen containing different types of clogging materials and then present results of analyzes carried out in situ at two restoration sites that demonstrate the possibility of locating these restorations but also to characterize the pictorial technique used in this one.

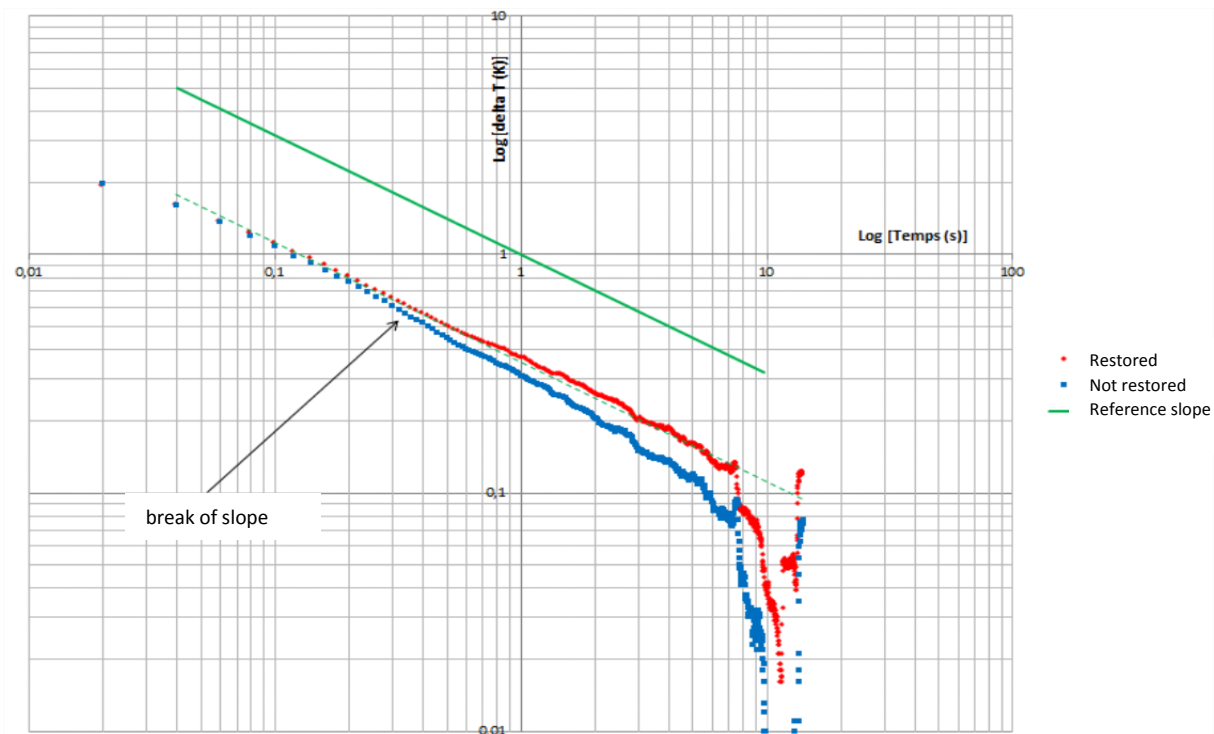


Figure 1 : Comparison of the thermal responses of a restored and non-restored zone

⁽¹⁾ GRESPI / CATHERM, UFR Sciences Exactes et Naturelles, BP 1039, 51687 Reims cedex 02